Infra-Red Spectroscopy of Anthropogenic Atmospheric Gases and Natural Aerosols

Thesis

Infra-red Spectroscopy of Anthropogenic Atmospheric Gases and Natural Aerosols

Sarah Webb MSci PGCE

A Thesis Submitted in Partial Fulfilment of the Degree of Doctor of Philosophy

15 September 2012
Department of Physics and Astronomya

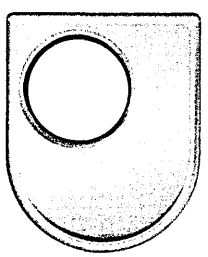

DATE of SUBMISSION : 30 SEPTEMBER 2012
DATE of AWARD : 29 August 2013

ProQuest LLC.
789 East Eisenhower Parkway
P.O. Box 1346
Ann Arbor, MI 48106 – 1346

To my Family

Abstract

Characterisation of the mechanisms and consequences of global warming is one of the most important topics in modern science. It requires a detailed investigation of the infrared properties of the constituents of the terrestrial atmosphere: gaseous, particulate and liquid. In this thesis Fourier-Transform Infra-Red (FTIR) Spectroscopy is used to provide data on the absorption and scattering cross sections needed to evaluate the radiative forcing of several substances present in the terrestrial atmosphere.

CF_3I is being considered as replacements for some of the highly global warming and ozone depleting gases currently used in industry. High-Resolution FTIR spectra has been recorded for CF_3I over a range of temperatures and pressures and used to calculate approximate values of its global warming potential.

Aerosols may affect the terrestrial radiation budget in two ways: i) they may induce global cooling due to scattering and reflection of incident solar radiation and ii) global warming due to absorption of terrestrial infrared radiation. The effects can either be directly due the aerosols themselves or due to indirect effects such as the aerosols acting as cloud concentration nuclei or nuclei for ice particles in the atmosphere. Furthermore, soluble aerosols, such as sulphates and sodium chloride, will affect the radiative properties of these water droplets once formed. To assess the net contribution of these aerosols one must know the concentration and location of any aerosol and also absorption and scattering coefficients. One method of monitoring the amount of aerosol in the atmosphere is to use satellites such as the Michelson Interferometer for Passive Atmospheric Sounding (MIPAS) or Meteostat Second

Generation (MSG). Both the satellite retrieval of aerosol concentrations and the calculation of their scattering and absorption coefficients require knowledge of the optical properties of these aerosols. Studying the spectroscopy of aerosols has proven to be a difficult problem since aerosols settle out quickly under the influence of gravity and so have short residence times in aerosol chambers thus radiative properties of aerosols provide one of the largest uncertainties in atmospheric modelling.

In this thesis an 'acoustic trap' has been developed to counteract gravity allowing us to record spectra of some common atmospheric aerosols: volcanic ash, coal soot and sand. Descriptions of the design of this novel trap and methods for its effective use are presented along with suggestions for further improvements.

Table of Contents

List of Figures

Chapter 1: Introduction

In recent years there has been much evidence to suggest that the average global temperature has been increasing and that a significant proportion of this increase could be due to anthropogenic changes in the atmosphere. In order that the Earth remains at a constant average global temperature, i.e. that the Earth is in radiative equilibrium, it must radiate back into space the same amount of energy that it receives from the Sun. The incoming solar radiation is a blackbody spectrum peaked in the optical part of the spectrum however the terrestrial radiation re-emitted by the Earth is peaked in the infrared. The Earth's atmosphere contains many species that absorb in the infrared, indeed it is the atmosphere that keeps the Earth at a temperature high enough for human habitation. Anthropogenic gases added to the atmosphere may absorb further in the infrared causing additional heating. Aerosols, naturally present or added to the atmosphere, may cause heating due to absorption or cooling due to scattering depending on their size and composition but can also act as cloud and ice condensation nuclei. Soluble aerosols such as sulphates and sodium chloride can then affect the radiative properties of these liquid aerosols. In order that these effects can be managed and damaging consequences prevented models that predict such effects must be as accurate as possible. This is a very complex task and there are many different variables to consider such as local concentrations of gases, how each gas affects the radiative balance, atmospheric lifetimes of gases as well as global variations in temperature and pressure.

Experimentalists can help in this task by providing high resolution spectroscopic data. In this thesis infrared spectroscopic data is reported for the industrial gas: CF_3I. The

iodofluorocarbon (IFC), Tri-fluoro-methyl iodide, CF_3I, has been proposed as a good candidate for the replacement of the potent greenhouse gas, Hexafluoroethane (C_2F_6), used for chamber cleaning in the plasma etching industry. Also investigated in this thesis are a range of particulate aerosols: soot, volcanic ash and sand. The Intergovernmental Panel for Climate change has identified the radiative forcing of aerosols as one of its key uncertainties but because of their short residence time in spectrometer sample chambers (due to settling out under gravity) it has proven extremely difficult to obtain the spectra needed to calculate these values directly from aerosols. In this thesis we have utilised an acoustic trap to levitate the aerosols allowing their infrared spectra to be obtained.

Chapter three of this thesis contains an overview of the theories relating to the interaction of infrared light with matter. In this chapter the complex refractive index is derived first for the simple case of a diffuse medium such as a gas, then these ideas are developed further into an understanding of the refractive index of a dense medium and then further still to scattering and absorption from aerosols particles. This chapter then discusses absorption from molecules in terms of their ro-vibrational energy levels. The final part of this chapter is concerned with the application of Fourier transform Infrared (FT-IR) Spectroscopy to our samples.

Chapter four of this thesis aims to give the reader an account of ultrasound and how it is applied in the phenomena of ultrasonic levitation. It describes the creation of ultrasonic fields by the application of various types of transducers with particular reference to piezoelectric methods. The chapter then goes on to describe the interactions of this field with particulate aerosols. The different "drift" forces that act

on the samples are discussed and the relative importance these have on particles with sizes relevant to atmospheric chemistry. The mechanisms of levitation and agglomeration of aerosols are discussed in depth.

Chapter five presents the results of a study of the infrared transmission spectroscopy of the gas CF_3I over a range of different temperatures and pressures of the gas. The peaks in the spectrum were identified and assigned including the assignment of two previously unseen peaks, the calculated integrated absorption intensities (IAIs) of these peaks are then reported. The simple approximation proposed by Pinnock et al. (Pinnock et al., 1995)to estimate the radiative forcing of an optically thin gas in the atmosphere is then applied to our data and the results presented. The analysis section of this chapter discusses the limitations and rigorousness of assumptions made in this chapter for example those of the Pinnock approximations e.g. that the gases are optically thin and those of the IAI calculations e.g that the gas behaves ideally.

The sixth chapter in this thesis gives the specifics of the design of our ultrasonic trap and how it was made suitable for collecting spectra of particulate aerosols. The trapping chamber had to be able to be evacuated, filled with an infrared inactive gas which was able to be heated and cooled, contain the trap itself and allow for the retrieval of our samples. Significant technical difficulties were overcome in the design of this trap and this chapter aims to present some of the practical considerations that must be taken in to account and how this research tackled them. The seventh chapter then goes on to describe results of the application of this chamber to FT-IR spectroscopy of aerosols and how the data collected can be used to obtain values for

the complex refractive index at many wavelengths. The extinction cross sections obtained are presented as are the refractive indices.

Chapter eight, the final conclusions, brings together the results and findings of the whole. The results for the gas spectroscopy are restated in a concise form and ideas for further analysis of the data are proposed. With regards to the acoustic trap, an analysis of the techniques used is given and an array of ideas for further improvement and application of the ultrasonic levitator are proposed. Since this research has been largely an initial test of feasibility of the suitability of the ultrasonic trap for these purposes; an analysis of its success is put forward.

Chapter 2: An Introduction to Atmospheric Chemistry

"All things good to know are difficult to learn."

Greek Proverb

This chapter aims to give a succinct overview of the underlying theory relevant to the physics and chemistry of the global climate. It will begin with a discussion of the incoming radiation from the Sun and radiation emitted from the Earth in terms of a simple blackbody approximation. It will then discuss the shortcomings of this simple model and how the atmosphere affects this balance. A more formal, mathematical description of the interaction of different components of the atmosphere with radiation will then be introduced. It will then discuss how these are transcribed into a climate model in order to demonstrate where responsibility lies for current climate change and how it may be used to predict future changes.

2.1 The Radiation Balance of the Earth

In order that the Earth remains at a constant average global temperature, i.e. that the Earth is in radiative equilibrium, it must radiate back into space the same amount of energy that it receives from the Sun. The incoming solar radiation may be approximated to a black body spectrum that peaks in the optical part of the spectrum. The average solar power incident on the Earth's averaged over its whole surface is equal to;

$$E = \frac{E_{SUN}(1-A)\pi R^2}{4\pi R^2} \qquad (1)$$

where E_{Sun} is the solar power per unit area intercepted at the mean Earth-Sun distance (1,367 Wm^{-2} (Bailey, 1997)), A is the Earth's albedo which is defined as the fraction of the solar energy reflected back into space and R is the radius of the Earth. The

average solar energy incident on the Earth's surface is 198 Wm^{-2} (IPCC, 2007) which constitutes 99.97 % of the Earth's total available energy with the remainder coming mainly from radioactive heating within the core. If the whole Earth was covered by ocean and no energy was radiated away, such an energy influx would cause a temperature rise of about 20 K/year, since the average temperature rise over the last 100 years is measured to be 7.4×10^{-2} K/decade (IPCC, 2007), thus the assumption of radiative equilibrium is a valid one.

Assuming that the Earth is in radiative equilibrium the mean temperature of the Earth is determined by the balance between the absorbed solar energy and the emitted terrestrial energy by the steady state equation;

$$E_{SUN}(1-A)\pi R^2 = \sigma_B T^4 4\pi R^2$$
$$T^4 = \frac{E_{SUN}(1-A)}{4\sigma_B} \quad (2)$$

where σ_B is the Stefan-Boltzman constant. The Stefan-Boltzman law is used to determine the outgoing energy, this law states that the total energy radiated per unit surface area of a black body in unit time is directly proportional to the fourth power of the black body's absolute temperature. The mean surface temperature is then calculated without the presence of the atmosphere to be 254 K. However this temperature is below the measured average global surface temperature (288 K) because this simple picture does not include the effects of the atmosphere which does not re-radiate all of the energy it receives.

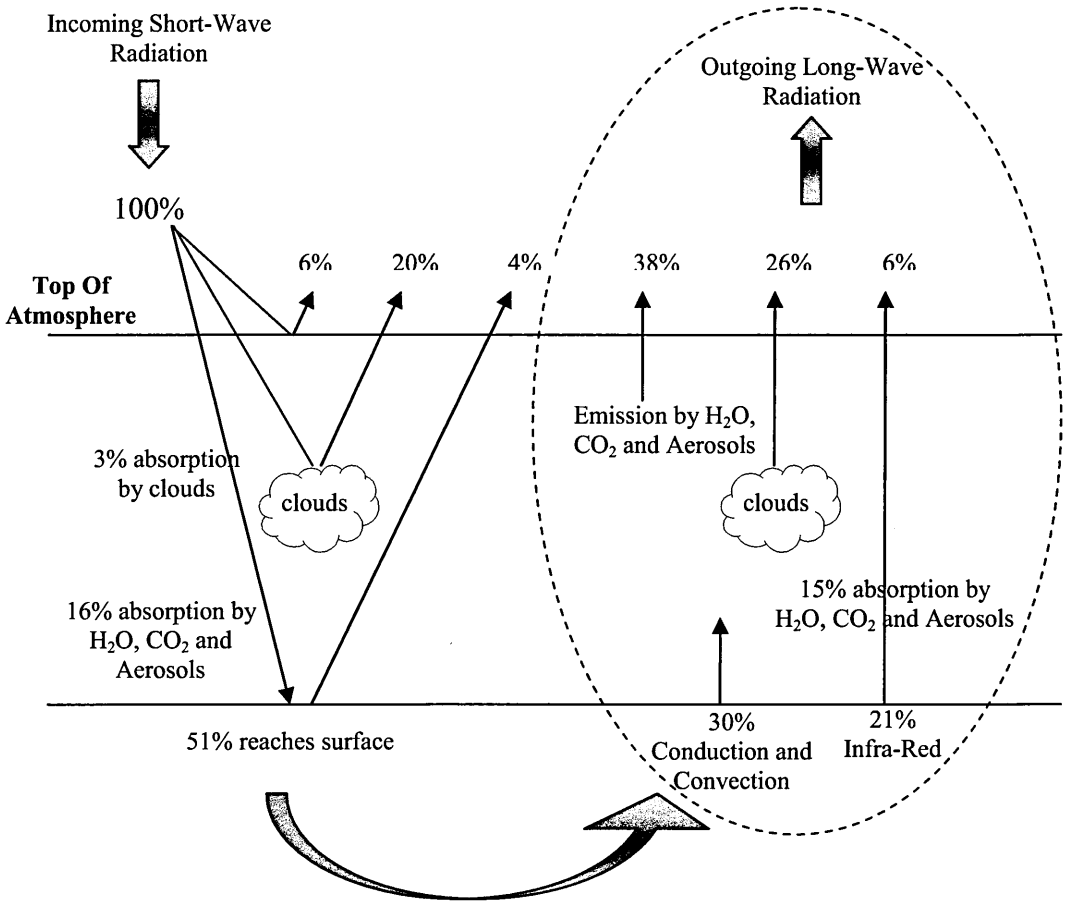

Figure 2-1 : The Main Processes Involved in the Earth's radiation budget (Satheesh and Krishnamoorthy, 2005)

The main processes involved in the Earth's radiative balance are shown in Figure 2-1. The incoming optical and UV solar radiation is reflected from clouds and by the surface of the Earth (especially snow or ice covered surfaces) and is also backscattered by aerosols. These phenomena have the effect of increasing the Earth's albedo such that more of the energy is reflected back into space causing global cooling. The incoming shortwave radiation can also be absorbed by ozone and by other gases in the atmosphere causing heating of the atmosphere. Thus only about 51 % of the total solar energy reaches the Earth's surface. The spectra of incoming solar radiation at different places in the atmosphere is shown in Figure 2-2, the Earth re-

radiates this energy back in the form of longer wavelength infra-red radiation, the calculated blackbody spectra of incoming solar radiation and outgoing terrestrial radiation is shown in Figure 2-3. Some gases in the Earth's atmosphere, whilst largely transparent to the incoming solar radiation, strongly absorb the infrared radiation which has been re-radiated by the Earth thus warming the atmosphere. This is known as the "Greenhouse Effect". There are several naturally occurring greenhouse gases in the atmosphere; under a clear sky about 60-70 % of the natural greenhouse effect is due to water vapour, with carbon dioxide, methane, ozone and nitrous oxide accounting for most of the rest.

Any additional substance introduced into the atmosphere has the potential to affect the radiative balance so, in order that the Earth's equilibrium temperature remains at a safe and comfortable level for human habitation, we must find a way to quantatively monitor the effect a compound will have on the radiation balance when released into the atmosphere.

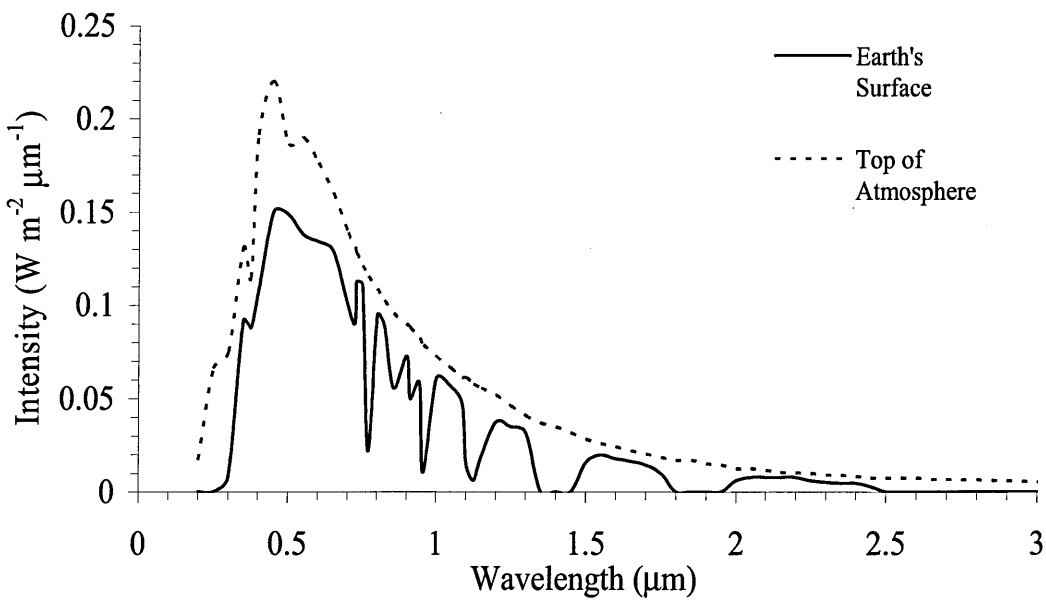

Figure 2-2: Intensity of Radiation Reaching Various Stages of the Earth's Atmosphere (Kendall et al., 2003)

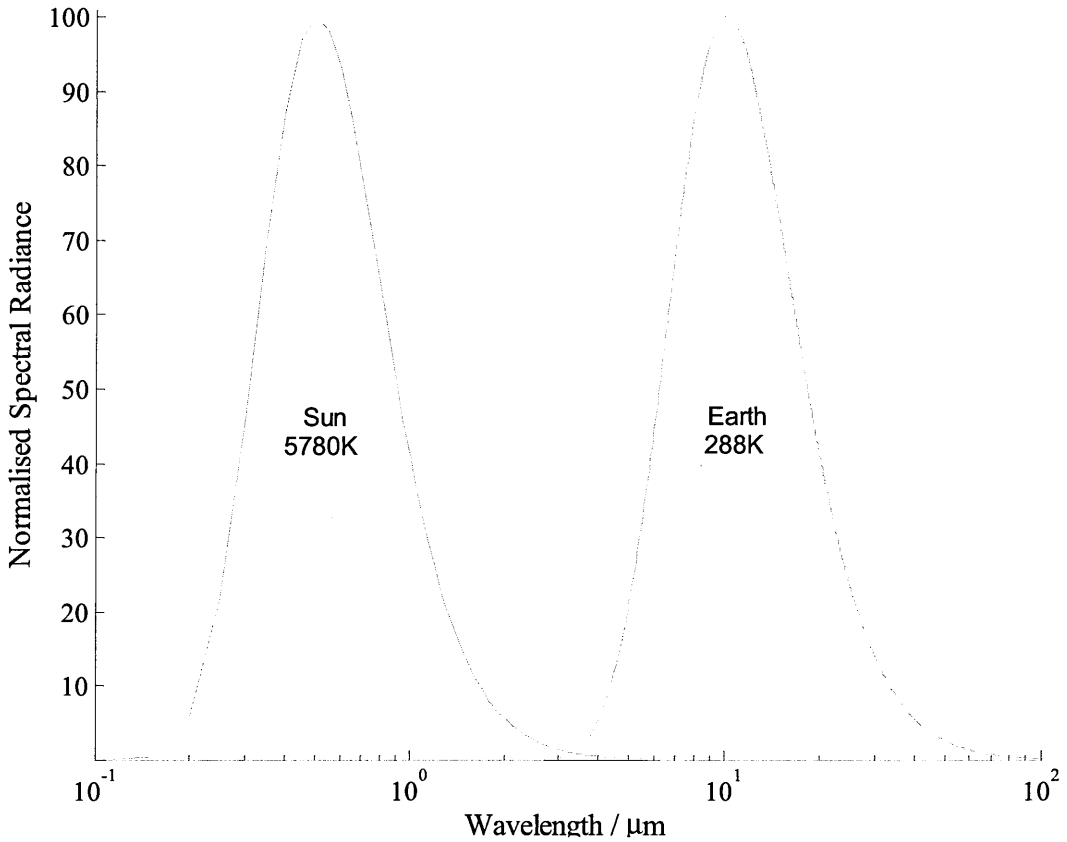

Figure 2-3: Calculated Normalised Blackbody Curves for the Earth and Sun.

2.2 Quantative Descriptions of the Radiation Balance

2.2.1 Radiative Transfer

The fundamental equations describing the propagation of electromagnetic radiation are the radiative transfer equations. Light travelling through a scattering and absorbing medium, such as the atmosphere, that is in thermal equilibrium with its environment will be attenuated by absorption and scattering but will be enhanced by thermal emission and light scattered into the beam, Figure 2-4. The actual mechanisms of these processes will be discussed in more detail in Chapter 3.

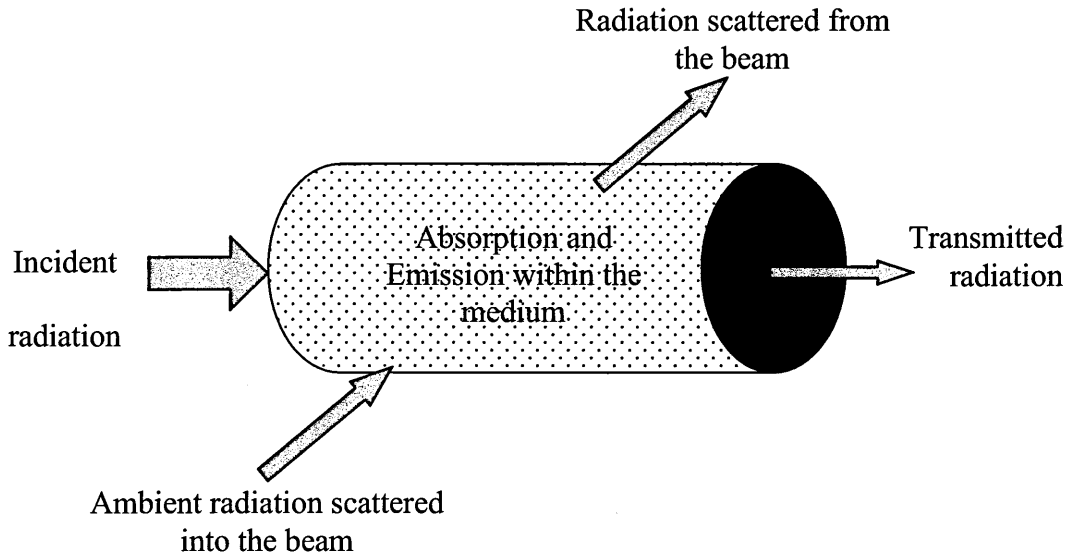

Figure 2-4: A light beam travelling through a medium

The spectral radiance of an electromagnetic source, L_ν, is defined as the power delivered in a certain direction, s, per unit area, per unit solid angle for a frequency interval at a certain point in space, r. The change of the spectral radiance of a beam through a volume element ($\delta L_\lambda(r,\nu)$) is given by the differential form of the radiative transfer equation

$$\partial L_\nu(r,\nu) = -\beta_{ext} L_\nu(r,\nu)\partial s + \beta_{sca} L_\nu^*(r,\nu)\partial s + \beta_{abs} B_\nu(r,\nu)\partial s \qquad (3)$$

where L_ν^* is the spectral radiance of the ambient field and B_ν is the spectral radiance emitted by the sample itself. The first term represents the radiation lost due to scattering and absorption within the volume element, the second term is the radiation gained by scattering into the beam and the last term represents the radiation gained by thermal emission of the surroundings into the volume element. β_{sca} is known as the volume scattering coefficient, β_{abs} is known as the volume absorption coefficient and β_{ext} is the volume extinction coefficient which is given by:

$$\beta_{ext} = \beta_{abs} + \beta_{sca} \tag{4}$$

To calculate the radiative transfer over the whole Earth requires long paths through the atmosphere and integration over the whole surface and all frequencies, the mathematics for which is so complicated that exact solutions are not possible however approximations may be made.

The fraction of radiation transmitted through a sample is given by the Beer-Lambert law;

$$\tau(\lambda) = \exp[-\beta_{ext}(\lambda)x] \tag{5}$$

where τ is the transmission through the sample being equal to the ratio of transmitted to incident intensity, β_{ext} is the volume extinction coefficient, λ is the wavelength of the radiation and x is the distance through the sample. The volume extinction coefficient is given by;

$$\beta_{ext}(\lambda) = \int_0^\infty \sigma_{ext}(r,m,\lambda)n(r)\partial r = \int_0^\infty \pi r^2 Q_{ext}(r,m,\lambda)n(r)\partial r \tag{6}$$

where σ_{ext} is the single particle, spectral extinction coefficient (also known as the extinction cross section), r is the particle radii, n(r)dr is the number of particles of radii between r and r + dr per unit volume and m is the particles complex refractive index. Q is known as the extinction efficiency and is the ratio of the cross-section to the projected area of the particle. The projected area is defined as the rectilinear projection of a surface of any shape onto a plane normal to the unit vector. The particles are most often modelled as being spherical and thus the projected area of the particle is the cross sectional area of the particle at is largest point and is therefore a circle.

The single particle spectral extinction cross-section is given by

$$\sigma_{ext} = \sigma_{abs} + \sigma_{sca} \tag{7}$$

where σ_a is the absorption cross section and σ_{sca} is the scattering cross section which in turn are derived from the real and imaginary parts of the complex refractive index. The complex refractive index is given by:

$$m(\lambda) = n(\lambda) - ik(\lambda) \tag{8}$$

where m is the complex refractive index of the particle and k is the bulk absorptivity and n is the bulk refractivity. A more complete discussion of the mechanisms of absorption and scattering and the refractive index are given in Chapter 3.

2.2.2 Radiative Forcing

The measure of any individual compound's effect on the radiative transfer over the whole surface of the Earth is known as its radiative forcing, there are two definitions of radiative forcing: instantaneous radiative forcing and the adjusted radiative forcing. The instantaneous radiative forcing is the radiative flux change caused instantaneously by an imposed change in radiative forcing agent (greenhouse gases, aerosol, solar radiation, etc.). The adjusted radiative forcing of a compound is defined as the change in net irradiance at the tropopause due to its presence in the atmosphere, after stratospheric temperatures have been allowed to return to radiative equilibrium (Hansen et al., 1997) i.e. the effect on the radiation budget of the surface/troposphere system. For trace gases this is usually calculated for a change in concentration from 0 to 1ppbv. The stratosphere is included as the response time of the stratosphere is of the order of a few months whereas the surface-troposphere systems response time is of the order of decades because of the thermal inertia of the oceans (Jain et al., 2000).

The radiative forcing of a compound is conventionally calculated using the integrated absorption intensities (IAI) between the wavenumbers of 800 and 1100 cm^{-1} as there is little absorption in this region from the most common greenhouse gases (CO_2, H_2O and O_3). Therefore, it is in this region that trace gases have the potential to make their largest contribution to global warming hence, a gases potential for adding to global warming depends on both the wavelength and the strength of the absorption features. However, absorption at wavenumbers below 800 cm^{-1} has also been shown to have an impact on the radiative forcing of a gas (Pinnock et al., 1995) especially in the extra-tropics and at higher latitudes where there is less absorption from water vapour. There are a wide range of radiative forcing models currently in use ranging from line-by-line models to broadband approaches (that calculate the forcing over bands of 100 cm^{-1} width) with differences in CO_2 radiative forcing of as much as 10 % being found between the different models (Luther and Fouquart, 1985). Although line-by-line calculations are acknowledged to give the most accurate values they are computationally expensive and it has been shown that the narrow band models (typical resolution 10 cm^{-1}) give radiative forcings that agree to within a few percent (Freckleton et al., 1998). The most rigorous models of the adjusted radiative forcing are calculated with reference to a model atmosphere and account for altitudinal and temporal changes in cloud cover, water vapour, pressure and temperature in different regions of the globe as well as different vertical profiles of H_2O, CO_2, O_3, CH_4 and N_2O (Houghton and Group, 1995). It is common to divide the globe into three regions: the extra-tropics of each hemisphere and the tropical belt. Models that do not account for seasonal, latitudinal and vertical changes in gas concentrations and cloudy skies (clear sky models) have each been shown to result in errors of several percent with the greatest error being seen in radiative forcing from halocarbons (Jain et al.,

2000). The methods are computationally expensive and require access to a radiative transfer model. Radiative forcings for different compounds vary greatly in the literature indeed part of the difficulty in comparing radiative forcing calculations made by different authors is that each author uses a different model and differences in the models often cause a greater variation in the forcings than those ensuing from any spectroscopic uncertainties. The accuracy of these models can be tested by comparing the calculated and observed fluxes at the top of the atmosphere (TOA).

2.2.3 Climate Modelling

Radiative transfer models calculate the effect that a standard increase in concentration of a substance in the terrestrial atmosphere will have on the global radiation budget. In order to predict the actual impact of compounds we introduce into the atmosphere we must be able to compute the long-term effect on the radiative transfer of the levels that we introduce. These models must also account for parameters such as the positions of sources, the lifetime of the substance in the atmosphere, its movement through the atmosphere and the sinks of the compounds.

There are many different levels of complexity in climate modelling, GCMs, which stands for either "Global Climate Models" or "General Circulation Models", currently have the highest temporal and spatial resolution on the global scale. These models discretise the equations for fluid motion and integrate these forward in time, they also parameterise processes such as convection that occur on timescales too small to be resolved directly. More sophisticated models may include representations of the carbon and other cycles. Atmospheric GCMs (AGCMs) model the atmosphere and impose sea surface temperatures. AGCMs consist of a dynamical core which integrates the equations of fluid motion, typically for:

- surface pressure
- horizontal components of velocity in layers within the atmosphere
- temperature and moisture in layers within the atmosphere

Oceanic GCMs (OGCMs) model the ocean (with fluxes from the atmosphere imposed) and may or may not contain a sea ice model. Coupled atmosphere-ocean GCMs (AOGCMs e.g. Hadley Centre Coupled Model Version 3 (HadCM3) (Pope et al., 2000)) combine both of these models and are the most complex and advanced models to date. These models are the basis for sophisticated model predictions of future climate. Most of these recent simulations show plausible agreement with measured temperature anomalies (see Figure 2-5).

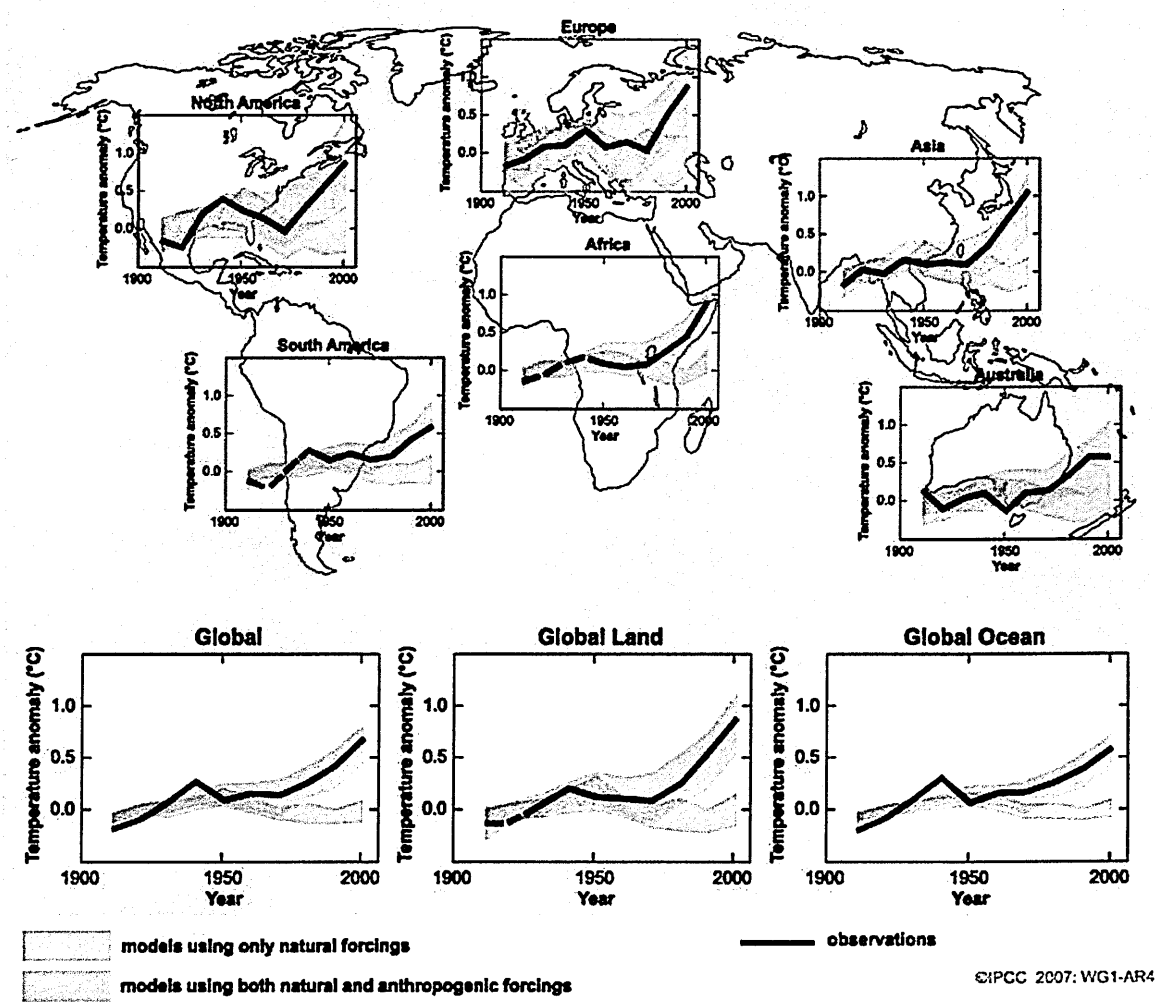

Figure 2-5: Comparison between observed and modelled deviations of Earth surface temperature from the mean since 1906 (IPCC, 2007)

2.2.4 Climate Modelling and the Debate over Global Warming.

Temperature records since 1850 show that eleven of the twelve years between (1995–2006) are among the 12 warmest years in the instrumental record of global surface temperature (IPCC, 2007) and in the last 50 years the temperature has risen by about (0.13 ± 0.03) °C per decade (IPCC, 2007). Although there was some suggestion that these results could have been biased by urban growth close to the sites where temperatures are measured, researchers at the Met Office (Parker, 2006) have recently re-analysed the temperature data taking consideration of the wind conditions. Windy conditions would have the effect of dispersing the heat generated by urban areas and so a bias would be seen in the data, no such bias was seen. The IPCC stated that "urban heat island effects are real but local, and have a negligible influence (less than 0.006 °C per decade over land and zero over the oceans) on these values." (IPCC, 2007).

Temperature records have been estimated going back thousands of years using proxy measurements such as air bubbles in ice cores from permafrost in Siberia or separations of growth rings in trees (Huang, 2004, Mann and Jones, 2003) but there are systematic problems with these measurements e.g. change in growth rate of trees with age, and so they are not considered here.

It has also been shown that (IPCC, 2007):

- The average temperature of the global ocean has increased to depths of at least 3000 m and that the ocean has been absorbing more than 80 % of the heat added to the climate system.

- Global average sea level rose at an average rate of (1.8 ± 0.5) mm per year over 1961 to 2003.
- Average arctic temperatures increased at almost twice the global average rate in the past 100 years.
- Satellite data since 1978 show that annual average arctic sea ice extent has shrunk by (2.7 ± 0.6) %.
- The frequency of heavy precipitation events has increased over most land areas and that more intense and longer droughts have been observed over wider areas since the 1970s, particularly in the tropics and subtropics.

There are several possible natural causes for this climatic variation; for example, solar cycles mean that there is significant variation in the intensity of radiation reaching the Earth. Sceptics of anthropogenic global warming claim that much more of the temperature rise seen is attributable to solar variation. There is a difference in outcomes between the two hypotheses in that an increase in energy received from the Sun would also cause warming in the stratosphere whereas warming due to increased levels of global warming gases is thought to cause a cooling of the stratosphere. Temperatures in the stratosphere, which contains the ozone layer, have been measured and found to be lower than average, some of this can be attributed to the destruction of the ozone layer by CFCs (Brasseur and Hitchman, 1988) (the ozone layer absorbs UV light which heats the stratosphere) but it is thought that stratospheric cooling due to global warming is also being observed (Ramaswamy et al., 1996). A second natural cause is a change in the frequency of volcanic eruptions since; the dust that is thrown up into the air during eruptions can reflect and scatter radiation back into space causing global cooling. However, most scientists believe that most of the dramatic

rise seen in the temperature is due to the increased levels of global warming gases in the atmosphere arising from human activity (Oreskes, 2004). In fact using the most up to date global warming models the observed increases can only be explained by including both the anthropogenic and natural radiative forcings (see Figure 2-5).

Since industrialisation there has been a sustained year on year rise in the CO_2 concentrations and the levels are now thought to be as much as 36 % higher than pre-industrialisation levels reaching a level of 379 ppm in 2005 (IPCC, 2007). This seems to be having a measurable effect on the planet's energy budget; in the year 2000 researchers at Imperial College London (Harries et al., 2001) examined nearly 30 years of satellite data and charted the changes in the amount of infrared radiation escaping the atmosphere. They discovered that less and less radiation was escaping which is indirect evidence for atmospheric heating.

There are several important feedbacks that also need to be considered when thinking about global warming (IPCC, 2007). There are positive feedbacks that will tend to warm the atmosphere further and negative feedbacks that will tend to dampen down the warming. An example of positive feedback is; the melting of the Siberian permafrost may result in the release of huge quantities of methane, which is a very potent greenhouse gas. Warming also enhances evaporation which increases the water vapour concentration in the atmosphere which amplifies the warming of the atmosphere. Snow and ice reflect much of the incident light back into space, an increase in the average temperature would cause a reduction in global snow/ice cover and thus would also amplify the heating effect. However some of the water vapour will form clouds, clouds can absorb heat radiated from the surface but they also reflect

light back into space, the dominant effect of the cloud depends on the type and height of clouds. A possible negative feedback, with increased temperature would come from stronger average winds, suspending more crustal material, thus increasing average aerosol concentrations and possibly increasing the Earth's albedo thus reducing temperatures.

One further problem of note is that of "inertia", the resistance of atmospheric systems to change. For example stabilisation of the emission rate of CO_2 will not lead to an immediate stabilisation of the atmospheric CO_2 concentrations because of its long atmospheric lifetime (this is not the case for shorter lived substances such as CH_4). Stabilisation of CO_2 levels requires the emission rate to be a fraction of the current rates and even if the necessary reductions were made in the rate of greenhouse gas emissions the slow transfer of heat into the oceans and the slow reaction of ice sheets means that global surface temperatures will continue to rise for over a century and sea levels will continue to rise for many centuries. The uptake of CO_2, the CO_2 sinks, also suffer from such effects, for example the enhanced growth rate in trees, a valuable CO_2 sink, is partly due to increased levels of CO_2 and partly due to increased use of fertilisers but these effects will decline as those forests reach maturity. Warming will also reduce the uptake of CO_2 into the oceans but this effect is not predicted to take effect until the end of the 21st century.

The Intergovernmental Panel on Climate Change (IPCC) was established in 1988 by two United Nations organizations, the World Meteorological Organization (WMO) and the United Nations Environment Program (UNEP) to assess the "risk of human-induced climate change". IPCC reports are widely cited in almost any debate related

to climate change. Their reports have been influential in forming national and international responses to climate change. The IPCC has projected six future scenarios of socio-economic development (Table 2-1) and predict the resulting climate change allowing for no environmental policy change and all of the scenarios show climatic changes which increase further by the year 2100. They project that there will be both beneficial and adverse affects on both environmental and socio-economic systems but the larger the climatic change and the rate of change the greater the likelihood that the adverse affects will predominate. Assessing the relative impacts of atmospheric feedbacks has been one of the "key uncertainties" identified by the IPCC and clouds have been identified as the largest source of uncertainty in their models.

Table 2-1: The six future emissions scenarios as framed by the IPCC and their projected temperature and sea level rises in the year 2099 compared to 1999 (IPCC, 2007).

Scenario Name	Description	Temperature Change / °C	Sea Level Rise / m
A1F	Very rapid economic growth, global population that peaks in mid-century and declines thereafter, substantial reduction in regional differences in per capita income and rapid introduction of new and more efficient technologies which are fossil intensive.	4.0	0.26 – 0.59
A1T	Same as above but with an emphasis on non-fossil intensive technologies	2.4	0.20 – 0.45
A1B	Same as above but with a balance between fossil and non fossil intensive technologies	2.8	0.21 – 0.48
A2	A very heterogeneous world with continuously increasing global population and regionally oriented economic growth that is more fragmented and slower than in other storylines.	3.4	0.23 – 0.51
B1	A convergent world with the same global population as in the A1 storyline but with rapid	1.8	0.18 – 0.38

	changes in economic structures toward a service and information economy, with reductions in material intensity, and the introduction of clean and resource-efficient technologies		
B2	A world in which the emphasis is on local solutions to economic, social, and environmental sustainability, with continuously increasing population (lower than A2) and intermediate economic development	2.4	0.20 – 0.43

2.3 Gases in the atmosphere

2.3.1 The Radiative Effects of Atmospheric Gases

Gases affect the radiation budget mainly through absorption and so a convenient measure of the optical properties of a gas is its absorbance. The Beer-Lambert law in the case of gases reduces to.

$$\tau(\lambda) = \mathrm{e}^{-\sigma_a(\lambda)nx} \tag{9}$$

where the absorbance is given by

$$Absorbance = -\ln(\tau) = \sigma_a \times n \times x \tag{10}$$

where τ is the transmittance of the sample, σ_a is the absorption cross section in cm^2 $molecule^{-1}$, n is the number density and x is the path length through the sample. The absorbance of a gas is easily measured in spectroscopic experiments and from it the absorption cross-section is easily calculated.

In this thesis we use a simple approximation for estimating instantaneous radiative forcing of trace gases by Pinnock et al. (Pinnock et al., 1995). This model assumes

that there are no intense spectral features that become saturated even at low concentrations and that the concentrations of the gas under investigation are small enough for it to be considered optically thin meaning that the radiative forcing is proportional to the product of a molecule's column density, the number of molecules per unit area in a vertical column through the atmosphere, and its absorption cross section.

Using this approximation the instantaneous radiative forcing (RF) for a 1-ppbv increase in a concentration of a gas is

$$RF = \sum_{i=1} \sigma_i F_i^{\sigma} \tag{11}$$

where F_i^{σ}, in units of W $m^{-2}(cm^{-1})^{-1}$ $(cm^2\ molecule^{-1})^{-1}$, is the radiative forcing per unit cross section per wavenumber for the spectral interval *i* for the average Earth sky and σ_i (with units $cm^2\ molecule^{-1}\ cm^{-1}$) is the photoabsorption cross section integrated over spectral interval *i*. Pinnock et al. found that the difference between instantaneous forcings and adjusted forcings of most halocarbons was an increase of about 7 % but it was not a steadfast rule. Pinnock et al. used a narrow band model to calculate the instantaneous, cloudy-sky, radiative forcing per unit cross section as a function of wavenumber for a Global and Annual Mean Earth-Sky radiative forcing including clouds in 10 cm^{-1} intervals (see Figure 2-6).

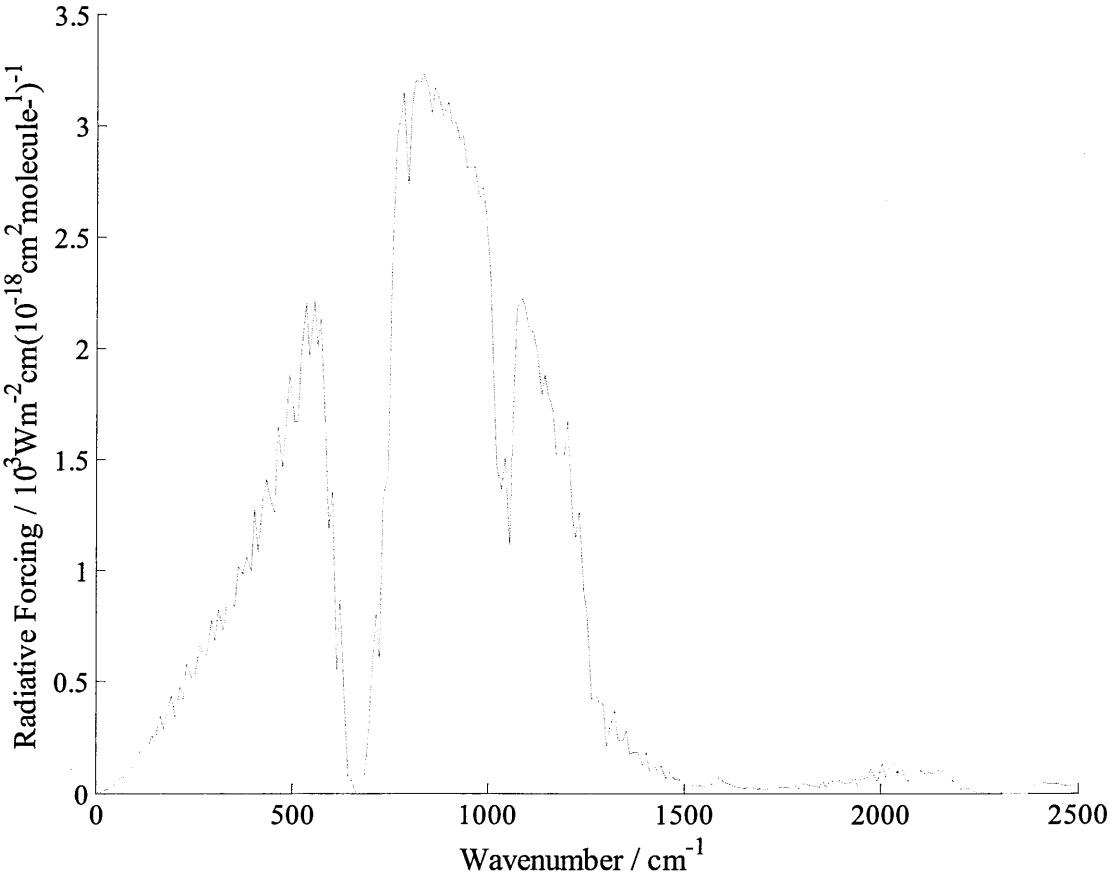

Figure 2-6: Global Annual Mean (GAM) Earth-Sky radiative Forcing including clouds (Pinnock et al., 1995).

Radiative forcings consider only the effect on the radiation budget but in order to compare the actual long term effects the residence time of the substance must also be considered. A common way of estimating this complete effect of a gas is to use its "Global Warming Potential". The Global Warming Potential (GWP) of any gas is a monitor of its role in the atmosphere after release, the effect of 1 kg of the gas is usually compared with the effect of 1 kg of a reference gas over a desired time horizon. The reference gas is usually carbon dioxide. The global warming potential is defined by the IPCC (IPCC, 2007) as:

$$GWP = \frac{\int_0^T \Delta F_{gas}(c_{gas}, t)\partial t}{\int_0^T \Delta F_{CO_2}(c_{CO_2}, t)\partial t} \tag{12}$$

where ΔF is the change in radiative forcing over time as a function of the species concentration, c. An approximate form of the equation was published by the IPCC in 1990 (IPCC, 1990).

$$GWP = \frac{\int_0^T A_{gas} c_{gas} \partial t}{\int_0^T A_{CO_2} c_{CO_2} \partial t} \tag{13}$$

where A is the instantaneous radiative forcing of a gas due to a unit increase in concentration of the gas and T is the desired time horizon. This approximation assumes that the radiative forcing is linear with gas concentration. The concentration of a gas in the atmosphere can be approximated by an exponential decay function

$$c = c_0 e^{(t/\tau)} \tag{14}$$

where c_0 is the initial concentration and τ is the atmospheric lifetime of the gas. This results in the expression.

$$GWP = \frac{\int_0^T A_{gas} c_{0gas} \exp(-t/\tau_{gas})\partial t}{\int_0^T A_{CO_2} c_{0CO_2} \exp(-t/\tau_{CO_2})\partial t} \tag{15}$$

the concentration of a gas can be given by

$$c = \frac{m}{VM} \tag{16}$$

where m is the mass of gas, M is the molar mass of the gas and V is the volume of gas, since the GWP values compare the change in radiative forcing of equal masses of each gas the initial concentrations of the gases will be inversely proportional to their molar mass. Assuming that A is a constant and using an approximation for the integration of the exponential, the GWP of a gas can be approximated to:

$$GWP = \frac{A_{gas} M_{CO_2} \tau_{gas} \left(1 - \exp(t/\tau_{gas}\right)}{A_{CO_2} M_{gas} \tau_{CO_2} \left(1 - \exp(t/\tau_{CO_2}\right)} \tag{17}$$

Table 2-2 lists the global warming potentials of several greenhouse gases commonly used in industry relative to that of CO_2. Since the GWP allows for the lifetime it offers a better measure of the relative impacts of greenhouse gases than radiative forcing alone. However, some caution should be used when using GWPs as they do not take into account the relative quantities of gases that are released into the atmosphere.

Table 2-2: Estimated Global Warming Potentials (GWPs) relative to that of CO_2 (taken from Jain et al. 2000)

Gas	Time Horizon in Years		
	20	100	500
	Global Warming Potential		
CH_4	72	28	9
N_2O	296	340	188
CFC-11	6100	4700	1700
CFC-12	9800	10600	5200
CCl_4	2700	1800	600
CH_3CCl_3	500	160	50
HCFC-22	4900	1900	590
SF_6	14600	22500	33200
CF_4	4400	6800	10600

The radiative forcing of a gas is conventionally calculated using the integrated absorption intensities (IAI) between the wavenumbers of 800 and 1100 cm^{-1} as there is little absorption in this region from the most common greenhouse gases (CO_2, H_2O and O_3). Therefore, it is in this region that trace gases have the potential to make the greatest contribution to global warming hence, the GWP depends on both the wavelength and the strength of the absorption features (see Table 2-3 for the radiative forcings of several common greenhouse gases). However, absorption at wavenumbers below 800 cm^{-1} has also been shown to have an impact on the radiative forcing of a gas (Pinnock et al., 1995) especially in the extra-tropics and at higher latitudes where there is less absorption from water vapour. In order to calculate the possible effect any compound will have on the radiation budget it is therefore necessary to have detailed information about both the integrated absorption cross-section at these wavelengths and the atmospheric lifetime of the species.

In an initial attempt to mitigate global warming, the Kyoto Protocol, which was signed in 1998 and came into force in February 2005, is an amendment to the United Nations Framework Convention on Climate Change. Countries that ratify this protocol are committed to reducing their emissions of carbon dioxide and five other greenhouse gases (methane, nitrous oxide, sulfur hexafluoride, HFCs, and PFCs) by 5.2 % compared to the levels of 1990 (which corresponds to a reduction by 29 % of the predicted levels in 2010) or engage in emissions trading if they maintain or increase emissions of these gases. The objective is the "stabilization of greenhouse gas concentrations in the atmosphere at a level that would prevent dangerous anthropogenic interference with the climate system" (UNFCCC, 1991).

Table 2-3: Narrow band model (NBM)-Estimated Adjusted Cloud-Sky Radiative Forcing due to changes in Greenhouse concentrations from pre-industrial times to the present day (taken from Jain et al. 2000)

Gas	Concentration (ppbv)		Radiative Forcing (Wm^{-2})	
	Pre-industrial (1765)	Current (1992)	Model-based concentration	Observation-based concentration
CO_2	278 000	356 000	1.308	1.3083
CH_4	700	1714	0.578	0.604
N_2O	275	311	0.117	0.121
CFC-11	0	0.268	0.064	
CFC-12	0	0.503	0.152	0.148
CCl_4	0	0.132	0.017	
CH_3CCl_3	0	0.135	0.009	
HCFC-22	0	0.100	0.020	
SF_6	0	0.032	0.016	
CF_4	0	0.070	0.006	
Total			*2.287*	

2.3.2 The Industrial Gas CF_3I

In response to the Kyoto protocol the plasma etching industry has been seeking replacements for the high global warming potential (GWP) perfluorocarbons (PFC) used in their industrial reactors e.g. CF_4, C_2F_6 and C_3F_8. These potent greenhouse gases (1 kg of C_2F_6 is equivalent to 9200 Kg of carbon dioxide) are known to have very long atmospheric lifetimes (10,000 years for C_2F_6). The Kyoto protocol to the UN framework convention to climate change and the U.S. Environment Protection Agency's (EPA) pollution prevention framework both place emphasis on finding replacements for these gases that have lower GWPs and do not form by-products with significant GWPs. The Massachusetts Institute of Technology under the sponsorship of the Semiconductor Research Corporation and Sematech has produced a long list of

possible alternatives, they are categorised in three groups: Hydrofluorocarbons (HFC), iodofluorocarbons (IFC) and unsaturated fluorocarbons. The iodofluorocarbon (IFC), Tri-fluoro-methyl iodide, CF_3I, has been proposed as a good candidate for the replacement of the potent greenhouse gas, hexafluoroethane (C_2F_6), used for chamber cleaning in the plasma etching industry. CF_3I/O_2 mixtures have been shown to be efficient at etching silicon oxide and nitride films in a PECVD (Misra et al., 1998, Ohtake et al., 2003) but there has been some concern because of chemisorption onto the surface resulting in low-energy electron-activated chemistry which attacks the substrate surface. This has been demonstrated on mono- and multi-layers of CF_3I on Ag(111) (Fieberg et al., 1996) and on silicon dioxide (Sanabia et al., 2002) on which it has a sticking co-efficient of 0.34, this does not occur with etch gases such as CF_4 for which the sticking coefficient is very small (10^{-7}).

It is known that CF_3I is chemically and photochemically active due to the weak C-I bond (bond enthalpy 209 $KJmol^{-1}$ compared with that of C-F at 552 $KJmol^{-1}$) and readily undergoes photolysis in direct sunlight through the reaction pathway;

$$2CF_3I \rightleftharpoons^{h\upsilon} 2CF_3^{\bullet} + 2I^{\bullet} \longrightarrow C_2F_6 + I_2 \qquad (18)$$

C_2F_6 is also a potent greenhouse gas but a review of its reaction kinetics indicates that the reformation of CF_3I is almost twice as fast as the production of C_2F_6 however the reaction chemistry is dramatically affected by the presence of oxygen i.e. in tropospheric conditions (Atkinson et al., 1992). The products of the photolysis of CF_3I in the troposphere result in reservoirs of such iodocompounds as HI, $IONO_2$, and HOI. These readily exchange between one another by photochemical processes. HI has been shown to have near unit absorption in water and $IONO_2$ hydrolyses in water, also, with near unit efficiency, this means that the atmospheric lifetime of iodine is of

the order of a few weeks. As a result CF_3I has a very small steady state ozone depleting potential (ODP), ODP is the extent of ozone depletion the chemical can cause relative to CFC-11 which has an ODP of 1. The ODP of CF_3I is estimated to be less than 0.0008 for surface releases (Solomon et al., 1994). However, if any iodine reached the stratosphere it would be very effective as an ozone depleting substance but its extremely short atmospheric lifetime limits its transport to the stratosphere. The half life of CF_3I photolysis was found to be less than a few days even at sea level (Solomon et al., 1994, Rattigan et al., 1997).

CF_3I is also seen as a possible replacement for halon in fire extinguishers due to its low steady state ozone depleting potential (ODP) relative to halon. Halon fire extinguishers function by interrupting the chemical reactions that take place during burning, they have been popular in the past because they leave no residue and so have been particularly useful in extinguishing fires near expensive equipment. Halon, however, has been banned from production and import since January 1994 and banned from use since December 2003 in response to the Montreal protocol and EC regulation 2037/2000 as it is known to be an ozone depleting substance. Only those deemed as critical users are still permitted to use halon e.g. fire extinguishers onboard aircraft and in crew compartments in military vehicles. CF_3I has also been shown to be an effective combustion quenching gas; although its effectiveness varies greatly with the type of fuel used (Glass et al., 1999) but in some cases it matches the effectiveness of halon. CF_3I has also been investigated as a possible replacement for the halon 1301 inerting agent inside F16 aircraft fuel tanks but was found to be unsuitable for many reasons including its higher boiling point and resulting reduced delivery pressure and because it was believed that CF_3I could be more strongly ozone

depleting than halon 1301 if released at altitude (Gann et al., 1994). CF_3I blends have also been commercially approved for use by SNAP (The Significant New Alternatives Policy) for use as a refrigerant. There have, however, been some concerns with the cardiotoxicity data of CF_3I in case of emergency release which show a greater risk than halon.

2.4 Aerosols in the atmosphere

2.4.1 The Nature of Atmospheric Aerosols

Atmospheric aerosol particulates are either solid or liquid particles that are suspended in the air and have sizes less than 100 μm. Particle sizes can be classified according to their method of creation. Those larger than 1 μm are "coarse-mode" particles, those between 0.1 μm and 1 μm are "accumulation-mode" particles and those <0.1 μm are referred to as "nucleation-mode" particles (IPCC, 2007). It has been estimated that the burden of dust aerosols with diameters below 10 μm is between 1000 and 3000 $Tgyr^{-1}$ (Cakmur et al., 2006) and that seven to twenty percent of the dust emissions are less than 1 μm in diameter (Cakmur et al., 2006). Aerosols can also be divided into two categories by their source, "anthropogenic" - those which are due to human activity and industry e.g. carbon black (soot) from coal burning power stations or vehicle exhausts and "natural" - those which occur naturally e.g. volcanic ash, dessert sand lifted into the atmosphere by wind or secondary organic aerosols from interactions between biogenic compounds. Each of these categories can be subdivided into two further categories; "Primary" – those that have the same physical and chemical form in the atmosphere as when they were introduced and "Secondary" – those that physical and/or chemical form has changed since introduction to the atmosphere. The most common atmospheric aerosols and their categorisations are shown in Table 2-4,

where the emission is the total global emission and the column burden is the mass of a substance contained in a column of atmosphere with an area of one square meter.

Table 2-4: Common Atmospheric Aerosols (Satheesh and Krishnamoorthy, 2005)

Source	Emission / $Tgyr^{-1}$	Column Burden / mgm^{-2}	Optical Depth
Natural			
Primary			
Soil Dust	1500	32.2	0.023
Sea-Salt	1300	7.0	0.003
Volcanic Dust	33	0.7	0.001
Biological Debris	50	1.1	0.002
Secondary			
Sulphates	102	2.7	0.014
Organic matter	55	2.1	0.011
Nitrates	22	0.5	0.001
Total Natural	3060	46	0.055
Anthropogenic			
Primary			
Industrial Dust	100	2.1	0.004
Black Carbon	20	0.6	0.006
Secondary			
Sulphates	140	3.8	0.019
Biomass Burning	80	3.4	0.017
Nitrates	36	0.8	0.002
Organic Matter	10	0.4	0.002
Total Anthropogenic	390	11.1	0.050
Total	3450	57	0.105
Anthropogenic Fraction	**11 %**	**19 %**	**48 %**

Aerosols remain in the atmosphere until they are removed by either settling out under gravity or by incorporation into raindrops. The efficiency of these deposition processes, and hence the time spent in the atmosphere by an aerosol particle, is a complex function of the aerosol's physical and chemical characteristics (e.g. particle

size) and the time of year and location of its release. Average lifetimes are of the order of a few days to a week. For fine sulphate aerosols (0.01 to 0.1 mm) released into or formed near the Earth's surface, an average lifetime is typically of the order of several days (Tegen and Miller, 1998). This time scale is dominated mainly by the frequency of precipitation. Particles transported into or formed in the upper troposphere are likely to remain there for weeks or months because of the less efficient precipitation scavenging (Balkanski et al., 1993). Stratospheric aerosols, formed as a consequence of large volcanic eruptions can remain there for one or two years (Sigurdsson, 1990). Clearly therefore the lifetime of any particular particle depends on its size and location. Larger aerosols settle out of the atmosphere very quickly under gravity and some surfaces are more efficient at capturing the aerosol than others. These aerosols must coagulate in some way before being removed by conventional deposition mechanisms. The most common deposition methods are outlined below.

- **Wet deposition:** Wet deposition is the name given to deposition pathways involving water. The main mechanisms are;
    - Rainout: Aerosols can act as nuclei for the condensation of cloud droplets. The aerosol is removed from the atmosphere when the droplet falls.
    - Washout: If an aerosol is incorporated into an already existing cloud drop, and that drop grows large enough to fall as rain, the particle is said to have been washed out.
    - Sweepout: falling raindrops can collide with aerosols below the cloud base. If the impact leads to incorporation of the aerosol into the drop the aerosol is deposited with the raindrop.

The three processes, although similar, are distinct because the efficiencies and the sizes and amounts of aerosol swept out by each process are different. It is the total deposition due to all three processes that is of interest to climate scientists in order to determine a residence time in the atmosphere.

- **Dry Deposition:** Deposition without the assistance of precipitation.
    - Gravitational Settling**:** The settling out of a particle under the influence of gravity. The velocity at which particles, greater than 1μm, settle out from the atmosphere under the influence of gravity alone is given by Stokes Law. For spherical particles this law takes the form:

$$v = \frac{gd^2(\rho_1 - \rho_2)}{18\eta} \tag{19}$$

      where d is the diameter of the particle, g is the acceleration due to gravity, η is the viscosity of air and ρ_1 is the density of the particle and ρ_2 is the density of air.
    - Turbulent Deposition: The most effective dry vertical transport mechanism.

Owing to the short lifetime of aerosol particles in the atmosphere, particularly in the troposphere and the non-uniform distribution of sources, their geographical distribution is highly non-uniform. The highest concentrations are usually found in urban areas reaching up to 10^8 and 10^9 particles/cm^3 (Seinfeld et al., 2000). As a consequence the relative importance of the aerosols varies considerably over the globe. In certain areas of the Northern Hemisphere, for example Europe and North America, anthropogenic sources are relatively much more important than natural sources whilst in Africa and South America natural sources currently dominate.

2.4.2 The Radiative Effects of Aerosols

Aerosols can affect the radiative balance of the atmosphere both directly through absorption and scattering but also indirectly by acting as cloud condensation nuclei. Hence the integrated effect of aerosols depends on the absorption and scattering characteristics. The transmission of radiation through an aerosol is given by the Beer-Lambert equation and since aerosols scatter and absorb the full function must be used (equation (5)).

The radiative effects of aerosols are poorly understood, indeed they were noted as part of at least three key uncertainties in the IPCC Third Assessment Report (IPCC, 2001). The net radiative effect of an aerosol depends on whether it acts overall to increase the albedo of the earth or decrease it. Aerosols that only scatter radiation will increase the albedo whereas strongly absorbing aerosols will act to reduce the Earth's albedo. It is estimated that the global-mean net direct effect of aerosols at the top-of-the-atmosphere (TOA) is a reduction in the incident intensity of 0.5 Wm^{-2} with a 95 % confidence range of (0.1 - 0.9) Wm^{-2} (IPCC, 2007). Aerosols also affect the radiation budget through indirect mechanisms a summary of which are given in Table 2-5.

Table 2-5: Overview of the different aerosol indirect effects, the sign and potential magnutide of the net radiative flux change at the top of the atmosphere (TOA) and the level of scientific understanding about the process (IPCC, 2007).

Effect	Cloud Types Affected	Process	Sign of Change in TOA Radiation	Potential Magnitude	Scientific Understanding
Cloud albedo effect	All clouds	For the same cloud water or ice content more but smaller cloud particles reflect more solar radiation	Negative	Medium	Low
Cloud lifetime effect	All clouds	Smaller cloud particles decrease the precipitation efficiency thereby presumably prolonging cloud lifetime	Negative	Medium	Very low
Semi-direct effect	All clouds	Absorption of solar radiation by absorbing aerosols affects static stability and the surface energy budget, and may lead to an evaporation of cloud particles	Positive or negative	Small	Very low
Glaciation indirect effect	Mixed-phase clouds	An increase in IN increases the precipitation efficiency	Positive	Medium	Very low
Thermodynamic effect	Mixed-phase clouds	Smaller cloud droplets delay freezing causing super-cooled clouds to extend to colder temperatures	Positive or negative	Medium	Very low

The reduction of the intensity due to the indirect effects of aerosols acting as condensation nuclei was estimated as 0.7 Wm^{-2} with a 95 % confidence range of (0.3

- 1.8) Wm^{-2} (IPCC, 2007). The large uncertainties in these values accounts for a large fraction of the uncertainty in the total anthropogenic radiative forcing (Haywood and Schulz, 2007). These effects are usually evaluated by computer models as a radiative flux perturbation (RFP) (Haywood et al., 2009) which is defined as the difference in the top-of-the-atmosphere radiation budget between a present-day simulation and a pre-industrial simulation using the same sea surface temperatures in both cases. These effects are not currently included in the IPCC reports but Lohman (Lohmann et al., 2010) argues that feedbacks and interactions that are fast as compared to the time scale of global warming should be included when estimating the total anthropogenic aerosol effect and that the total anthropogenic aerosol effect cannot be evaluated precisely enough as a radiative forcing.

A term called Single Scattering Albedo (SSA) is used to define this. The SSA is the ratio of scattering to extinction (extinction includes both scattering and absorption) of radiation by a particle.

$$\varpi = \frac{\sigma_s}{\sigma_{ext}} = 1 - \frac{\sigma_a}{\sigma_{ext}} \tag{20}$$

where ϖ is the single scattering albedo, σ_a is the absorption coefficient and σ_s is the scattering coefficient. High SSA implies the aerosol species mainly scatters radiation; lower SSA implies absorbing aerosols for example Sea-salt aerosol has a SSA of 1, implying that a sea-salt particle only scatters, whereas soot has a SSA of 0.23 making it one of the most important and dominant aerosol absorbers in the atmosphere. Menon et al. (Menon et al., 2002) noted that while most regions of the earth have been experiencing increasing surface temperatures the picture in newly industrialized countries has been more complicated e.g. there have been increased summer floods in

south China, increased drought in north China, and moderate cooling in China and India during recent decades. They used a global climate model to investigate possible aerosol contributions to these trends and found that precipitation and temperature changes predicted by the model were comparable to those observed if the aerosols included in the model had a large proportion of absorbing black carbon.

The next generation of atmospheric models must include the interaction of the biosphere with the rest of the atmosphere and the affects of the chemical reactions that take place within the atmosphere. Many of these processes are still poorly understood but aerosols are thought to have a significant contribution e.g. anthropogenic (soot), volcanic dust, salt from the sea and secondary organic aerosols. Secondary organic aerosols are formed when volatile organic compounds (VOC) e.g. terpenes released from trees, undergo photochemical reactions to form condensable compounds (Takekawa et al., 2003). It is estimated that they could be anything from 10-70 % of the total dry aerosol mass.

As well as being damaging to the environment aerosols can directly affect human health. Particles less than 10μm are easily inhaled and are small enough to pass through the cilia and penetrate deep into the lungs. If these particles are present in significant numbers they can line the air sacs reducing their efficiency or can release chemicals known to cause bronchitis or emphysema (Schwartz and Neas, 2000). Aerosols produced from coal burning are also known to be effective nuclei for fog formation; a correlation between the resulting "smog" and temporary increases in the mortality rate has been noted. The most extreme incidence of this being in London in

December 1952, when increased concentrations of sulphur oxide gases and soot particles resulted in some 40000 premature deaths (Wilkins, 1954).

2.5 Conclusions

One can see that it is of great importance to be able to ascertain the extent of the interaction of every component of our atmosphere with the incoming and outgoing radiation.

This thesis aims to measure high resolution infra-red spectra for one important industrial gas, CF_3I, and for some important atmospheric particulate aerosols: soot, sand and volcanic ash. The next chapter will discuss the relevant interactions of these substances with infra-red light and the techniques used to measure their spectra.

Chapter 3: Interactions of Light with Matter

"Never regard study as a duty, but as the enviable opportunity to learn to know the liberating influence of beauty in the realm of the spirit for your own personal joy and to the profit of the community to which your later work belongs."

Albert Einstein

In order that we may calculate the radiative forcing of a compound we must know its scattering and absorption cross sections. These are derived from the compounds complex refractive index. In order to calculate the complex refractive index a combination of experimental data and models are required.

This chapter aims to give the reader a succinct guide to the interaction of light with molecules and particles and how we investigate this using spectroscopy. The first part of the chapter will formalise the idea of the complex refractive index it will be explained first in its most simple form, light passing through a low density gas. This model is included as it shows how the ideas of absorption and scattering can be described using the classical theory of electromagnetic waves. It then discusses how this model must be amended for dense materials before extending the classical view of the complex refractive index to the more complex situation of aerosol particles using Mie theory. In the latter part of this chapter the interactions of infra-red light with molecules in a gas and the quantum mechanical rules that govern them will be discussed. The last part of the chapter will describe the theory and application of Fourier transform spectroscopy and its advantages over other forms of spectroscopy.

3.1 The Complex Refractive Index

The derivations for these theories are largely followed from the published versions of the Feynman lectures (Feynman et al., 1971); the reader is referred to volumes 1 and 2 of these works for a more complete derivation.

3.1.1 In a diffuse medium

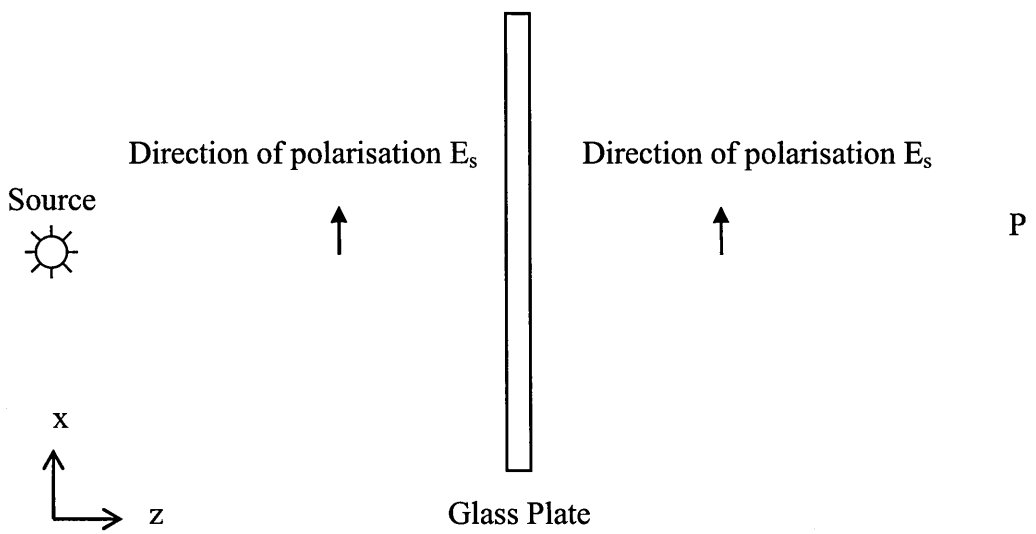

Figure 3-1: Electromagnetic waves passing through a glass plate

If light is incident upon a thin plate of a transparent material with a different density to air, such as glass, (Figure 3-1) there is an apparent phase shift in the wave exiting the plate. This apparent shift of the incoming phase is usually attributed to a difference in the speeds of electromagnetic (EM) radiation in the more dense material to that of air. This ratio is the refractive index such that;

$$v_{material} = \frac{c}{m} \tag{21}$$

where v is the speed of EM radiation in the material, c is the speed of EM radiation in a vacuum and m is the refractive index of the material. If the incoming electric field has the form

$$E_s = E_0 e^{i\omega(t-z/c)} \tag{22}$$

when it has passed through a plate of thickness Δz it will be delayed by an amount of time given by $\Delta t = (m-1)\Delta z/c$ which changes the emerging field to the form

$$\begin{aligned} E_{\text{after plate}} &= E_0 e^{i\omega\left[\left(t-\frac{(m-1)\Delta z}{c}\right)-\frac{z}{c}\right]} \\ &= e^{-\omega(m-1)\Delta z/c} E_0 e^{i\omega(t-z/c)} \end{aligned} \tag{23}$$

If Δz is small we may use the equality $e^x = 1+x$ in equation (23) to give us

$$E_{\text{after plate}} = E_0 e^{i\omega(t-z/c)} - \frac{i\omega(m-1)\Delta z}{c} E_0 e^{i\omega(t-z/c)} \tag{24}$$

This shows us that the field far from the plate is equal to the source field (the first term in equation) with an added field due to the movement of the charges in the material (second term in the equation). This mathematical model describes that wave very well, however, it is not valid when the wave travels more slowly. Electromagnetic radiation can be considered to be a simple harmonic oscillation of electric and magnetic fields (Figure 3-2) and as such will interact with every charge and dipole within the medium leading to acceleration of these charges. These induced motions of charges and dipoles will in turn induce their own electric field each moving at the speed of light but as we shall show the total field of each moving charge superimposes to create a wave shifted by c/n. The next task is to show what form the refractive index takes when we consider the field produced by each of the charges.

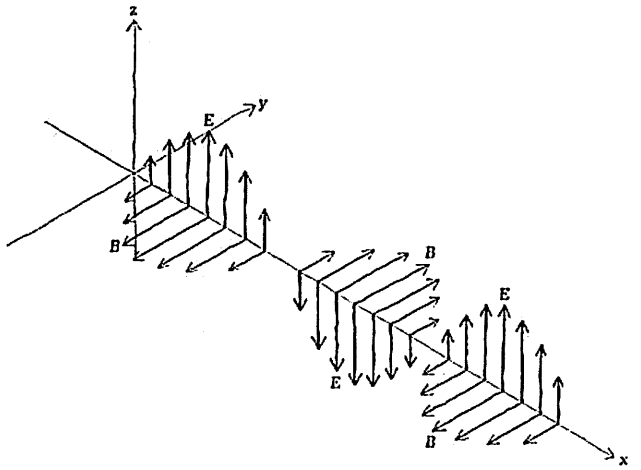

Figure 3-2: Diagram of the electric and magnetic field polarisations in electromagnetic radiation

For simplicity the case will be considered when the density of atoms in the material is low enough that the only electric field each atom experiences is that of the source and that reflections are limited i.e. that the refractive index is very close to 1. In the far field approximation the total electric field due to the source and moving charges is just the vector sum of the electric fields produced by each charge.

$$E = E_s + \sum_{\text{all charges}} E_{\text{each charge}} \tag{25}$$

where E_s is the electric field from the source. If we assume that the plate is far from the source then we can say that electric field is the same phase over that whole of the plate and if we take z = 0 at the plate the source wave becomes

$$E_s = E_0 e^{i\omega t} \tag{26}$$

Each electron in the material will be driven by a force equal to qE_s in the direction of the electric field vector, x. If we assume that the electrons in the atoms are elastic, damped harmonic oscillators then the equation of their motion will be given by

$$m_e\left(\frac{\partial^2 x}{\partial t^2} + \omega_0^2 x + \gamma\frac{dx}{dt}\right) = F = q_e E_0 e^{i\omega t} \tag{27}$$

where m_e is the mass of the electron, q_e is the charge on the electron, ω_0 is the natural frequency of oscillation of the electron and γ is the damping factor. The displacement of the electron will then be given by

$$x = x_0 e^{i\omega t} \tag{28}$$

by finding the differentials and substituting into equation (27)

$$x_0 = \frac{q_e E_0}{m_e(\omega_0^2 - \omega^2 + i\gamma\omega)} \tag{29}$$

$$\begin{aligned} x &= \frac{q_e E_0}{m_e(\omega_0^2 - \omega^2 + i\gamma\omega)} e^{i\omega t} \\ x &= \frac{q_e E}{m_e(\omega_0^2 - \omega^2 + i\gamma\omega)} \end{aligned} \tag{30}$$

The electric field from a point charge at a distance r is given by

$$E(t) = \frac{-q}{4\pi\varepsilon_0}\left(\frac{e_{r'}}{r'^2} + \frac{r'}{c}\frac{d}{dt}\left(\frac{e_{r'}}{r'^2}\right) + \frac{1}{c^2}\frac{\partial^2}{\partial t^2} e_r\right) \tag{31}$$

where e_r is the unit vector of the direction between the point of measurement and the oscillating charge. The first term is Coulomb's law however, since EM radiation cannot travel faster than the speed of light, the field is determined by the behaviour of charges in the past and as such the second and third term allow for a change in the field and unit vector in the time it takes for the information to reach the point at which we are measuring the field. This time is given by r'/c which is known as the retardation time. Variables with a prime signify the values of the variables when the field left the charged particle. At large r only the third term is significant as the others fall off as $1/r^2$, this term is the radiation term and it is proportional to the rate of change of the unit vector between the point, P and the charge.

$$E = \frac{-q}{4\pi\varepsilon_0 c^2}\frac{\partial^2 e_{r'}}{\partial t^2} \tag{32}$$

If the charges are not moving relativistically and if the distances moved along r are small compared to r then the rate of change of the unit vector as seen at P will just equal the acceleration of the charge at the retardation time.

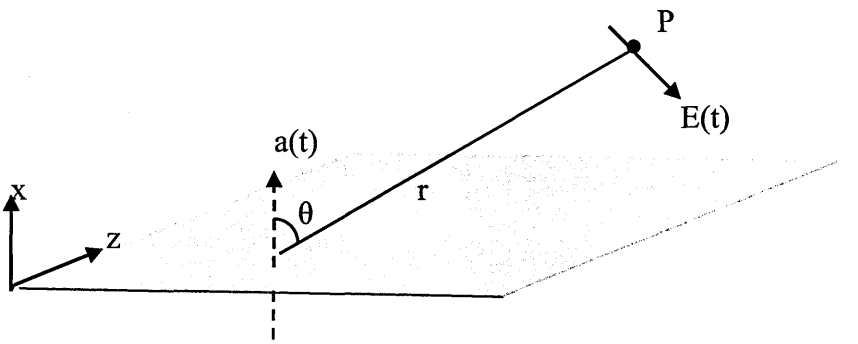

If the acceleration of the charge is in the x-direction then the field at point P at right angles to the line of sight, r, will be given by

$$E(t) = \frac{-qa(t - r/c)\sin\theta}{4\pi\varepsilon_0 c^2 r} \tag{33}$$

where $a(t - r/c)$ is the acceleration of the charge at the retardation time, the so called retarded acceleration and θ is the angle between the line of motion of the charge, x, and r. We can now use this equation to find the total field produced by a plate of such radiators such as found in a glass plate.

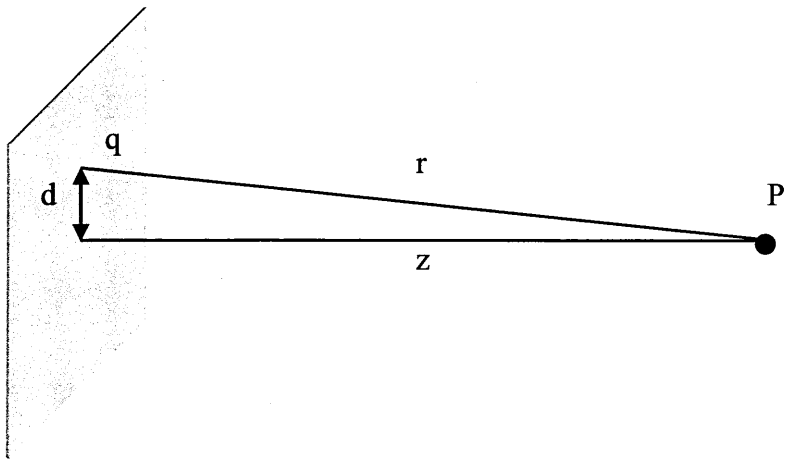

Figure 3-3: Field from a sheet of atoms in a plate

Since the charge is being oscillated by a field that varies as equation (22) the acceleration will be equal to $a_0 e^{i\omega(t-r/c)}$ where $a_0 = -\omega^2 x_0$. If we assume that r is very large compared to d then we can assume that $\theta \approx 90°$ and therefore the complex term tends to 1. The field due to the whole plate of charge at point P is then the integral of the effect of each charge over the whole area of a plate with a charge per unit area of η. This is found to be

$$E = -\frac{\eta q_e}{2\varepsilon_0 c} i\omega x_0 e^{i\omega(t-z/c)} \tag{34}$$

where η is the number of charges per unit area and ε_0 is the permittivity of free space. which is then, by substituting equation (29), found to be

$$E = -\frac{\eta q_e}{2\varepsilon_0 c}\left(i\omega \frac{q_e E_0}{m_e(\omega_0^2 - \omega^2 + i\gamma\omega)} e^{i\omega(t-z/c)} \right) \tag{35}$$

one can see that this equation for the field due to the movement of the electrons is now of the form found in equation (24) with

$$(m-1)\Delta z = \frac{\eta q_e^2}{2\varepsilon_0 m_e(\omega_0^2 - \omega^2 + i\gamma\omega)} \tag{36}$$

if we now say that $\eta = N\Delta z$ where N is the number of atoms per unit volume we can equate the refractive index to be

$$m = 1 + \frac{Nq_e^2}{2\varepsilon_0 m_e(\omega_0^2 - \omega^2 + i\gamma\omega)} \tag{37}$$

In a "real" atom there are several different modes of oscillation and so we must modify this equation to be a sum of all of the modes. In the quantum mechanical view each electron has more than one resonant frequency mode and each mode must have a factor called the oscillator strength, f_k, which indicates how strongly each resonance is exhibited. The equation then becomes

$$m = 1 + \frac{q_e^2}{2\varepsilon_0 m_e}\sum_k \frac{Nf_k}{(\omega_k^2 - \omega^2 + i\gamma_k\omega)} \tag{38}$$

This form of the refractive index **is complex**. If we separate the real and imaginary parts of the refractive index by saying $m = n + ik$ where n and k are real numbers and insert it into equation (23) we obtain

$$E_{\text{after plate}} = e^{-\omega k\Delta z/c} e^{-i\omega(n-1)\Delta z/c} E_0 e^{i\omega(t-z/c)} \tag{39}$$

The last two factors are just a phase delayed wave as predicted but the first factor is a real term. Since this term is a negative exponential it describes an attenuation of the wave as it travels through the plate which is proportional to Δz. If we look at (37) we can see that as the frequency of light equals the natural frequency of that mode then the complex refractive index becomes completely imaginary and absorption is the dominant effect. The form of the attenuation is

$$Intensity \propto e^{-2\omega k\Delta z/c} \tag{40}$$

This can be compared with the Beer Lambert law for absorption (equation (5)) in a gas and it is seen that the absorption coefficient is given by

$$\beta_{abs} = 2\omega k / c \tag{41}$$

The imaginary part shows that a wave shifted by a certain phase is created by the movements of the electrons inside the atoms due to the source field. This field travels in the same direction as the incoming wave. This description only holds if the atoms are arranged in a regularly spaced pattern.

The radiation added to the field by the plate is accounted for by the real component of the complex refractive index, n, this is the scattered radiation. In the simple example above the radiated energy at any direction other than z was minimised by letting $\sin\theta \to 1$ but in many real situations this is not the case. Radiation will be scattered in all directions. The power radiated by a field per square meter is given by

$$S = \varepsilon_0 c E^2 \tag{42}$$

using equation (33) the power radiated in the θ direction is

$$S(t) = \frac{-q^2 a'^2 \sin^2\theta}{16\pi 2\varepsilon_0 c^3 r^2} \tag{43}$$

To find the average power scattered in all directions we integrate over the whole area and substitute for the acceleration found in equation (34)

$$P = \frac{q^2 \omega^4 x_0^2}{12\pi\varepsilon_0 c^3} \tag{44}$$

substituting in equation (29) for x_0 results in an expression for the scattered power that is proportional to the incoming intensity. The constant of proportionality is known as σ_s, the scattering cross section and in this example is given by

$$\sigma_s = \frac{8\pi r_0^2}{3} \frac{\omega^4}{(\omega^2 - \omega_0^2)} \tag{45}$$

3.1.2 In a dense medium

In gases the electric field polarises the molecules producing oscillating dipoles, the acceleration of which produce a new radiation field. This new field interferes with the source field and produces a change in the source field equivalent to a phase change. In diffuse media the effects of the fields of these oscillating dipoles on the other oscillating charges are neglected. This effect cannot be ignored in dense media, the next step to forming a description of the scattering of aerosol particles is to discuss how this effect changes the result. Many of the ideas used are similar to those in section 3.1.1 however we must now solve Maxwell's equations in order to formalise this theory. Again we assume that charge in the isotropic dielectric material acts as a damped harmonic oscillator and as such the displacement of the charge parallel to E, x, is given by equation (30). The induced dipole moment of an atom is given by

$$p = q_e x \tag{46}$$

however the electric field now has to include polarisation due to the effects of the molecules in the vicinity, this new field is called the local field. Providing that the separation of the molecules is much smaller that the wavelength of the field this local field is given by

$$E_{local} = E + \frac{P}{3\varepsilon_0} \tag{47}$$

which now gives the polarisation as

$$p = \frac{q_e^2}{m}(\omega^2 + i\gamma\omega - \omega_0^2)E_{local}$$
$$p = \varepsilon_0 \alpha(\omega) E_{local} \tag{48}$$

where α(ω) is a collection of the other terms and is known as the atomic polarisability. In the quantum mechanical view, allowing for the multitude of resonant modes in an atom and for the effective oscillator strength of each mode the atomic polarisability can be represented by

$$\alpha(\omega) = \frac{q_e^2}{\varepsilon_0 m}\sum_k \frac{f_k}{\omega^2 - \omega_{0k}^2 + i\gamma_k\omega} \tag{49}$$

The polarisation of the material is then equal to

$$P = Np = \varepsilon_0 N\alpha E_{local}$$
$$P = \varepsilon_0 N\alpha\left(E + \frac{P}{3\varepsilon_0}\right) \tag{50}$$
$$P = \frac{N\alpha}{\left(1 - \frac{N\alpha}{3}\right)}\varepsilon_0 NE$$

where N is the number of atoms per unit volume. This induces polarisation charges and currents which must be included. The charge density caused by polarisation is given by

$$\rho_{pol} = -\nabla \cdot P \tag{51}$$

this is sufficient for the static case but as the electric field is changing with time we also need to consider the polarisation currents.

$$j = Nq_e \frac{dx}{dt} \tag{52}$$

which we can see from equations (46) and (50) is just equal to

$$j_{pol} = \frac{dP}{dt} \tag{53}$$

If we assume there are no extra charges present then we can write Maxwell's equations to be;

$$\nabla \cdot E = -\frac{\nabla \cdot P}{\varepsilon_0} \tag{54}$$

$$\nabla \times E = -\frac{dB}{dt} \tag{55}$$

$$\nabla \cdot B = 0 \tag{56}$$

$$c^2 \nabla \times B = \frac{d}{dt}\left(\frac{P}{\varepsilon_0} + E\right) \tag{57}$$

If we manipulate these equations by taking the curl of equation (55), using the vector identity $\nabla \times (\nabla \times E) = \partial / \partial t (\nabla \times B)$ and then substitute for $\nabla \times B$ using equation (57) and for $\nabla \cdot E$ using equation (54) then we can find the equation

$$\nabla^2 E - \frac{1}{c^2}\frac{\partial^2 E}{\partial t^2} = \frac{1}{\varepsilon_0 c^2}\frac{\partial^2 P}{\partial t^2} - \frac{1}{\varepsilon_0}\nabla(\nabla \cdot P) \tag{58}$$

for isotropic dielectrics P is always in the same direction as the electric field vector, E and so $\nabla \cdot P = 0$. If we consider a wave of the form

$$E_x = E_0 e^{i(\omega t - kz)} \tag{59}$$

which can be written

$$E_x = E_0 e^{-ik\left(z - \frac{\omega}{k}t\right)} \tag{60}$$

this describes a wave with a phase velocity of $v_{ph} = \omega / k$ which can also be expressed as in equation (21). This means that the refractive index can also be expressed by

$$m = \frac{kc}{\omega} \tag{61}$$

To find the complex refractive index we must now find the form of the wavenumber that satisfies equation (58). If the substance is a linear dielectric then $\partial^2 P_x/\partial t^2 = -\omega^2 P_x$, $\partial^2 E_x/\partial t^2 = -\omega^2 E_x$ and $\partial^2 E_x/\partial z^2 = -k^2 E_x$. Substituting these equalities into the above equation gives

$$-k^2 E_x + \frac{\omega^2}{c^2} E_x = \frac{\omega^2}{\varepsilon_0 c^2} P_x \tag{62}$$

if we now substitute equation (50) in to this equation then

$$-k^2 E_x + \frac{\omega^2}{c^2} E_x = \frac{\omega^2}{c^2} \frac{N\alpha}{\left(1 - \frac{N\alpha}{3}\right)} N E_x \tag{63}$$

we can then rearrange the equation to give

$$k^2 = \frac{\omega^2}{c^2}\left(1 + \frac{N\alpha}{1 - N\alpha/3}\right) \tag{64}$$

substituting this into equation (61) we find

$$m^2 = 1 + \frac{N\alpha}{1 - N\alpha/3} \tag{65}$$

this equation can be rearranged to give

$$3\frac{m^2 - 1}{m^2 + 2} = N\alpha \tag{66}$$

this is known as the Claussius-Mosotti equation.

3.2 Particulate Scattering

3.2.1 Types of Scattering

Scattering is the process by which energy is removed from the incident electromagnetic wave and re-radiated at a solid angle centred at the particle. Scattering can be either elastic, as found in the cases discussed in this thesis, or inelastic, such as Raman scattering. There are different mathematical descriptions of elastic scattering processes depending on the shape of the particle and the size of the particle relative to the wavelength of light. If we consider spherical particles and the diameter of the particle is much greater than the wavelength of light then geometric optics is used, but if the diameter of the particles is of the order of the size of the wavelength of light the scattering is best described by "Mie Theory". Mie theory provides rigorous solutions for light scattering by an isotropic ***sphere*** embedded in a homogeneous medium. This is generally the case for atmospheric aerosol and cloud particles at visible and infra-red wavelengths. If the diameter of the particle is much smaller than the wavelength of light "Raleigh Scattering" is the best mathematical description, this type of scattering is usually seen from large gas molecules in the atmosphere. The scattering regime used depends mathematically on what is known as the size parameter:

$$x = \frac{2\pi r}{\lambda} \tag{67}$$

where x is the size parameter, r is the radius of the particle and λ the wavelength of light. The regime boundaries are shown in Figure 3-4.

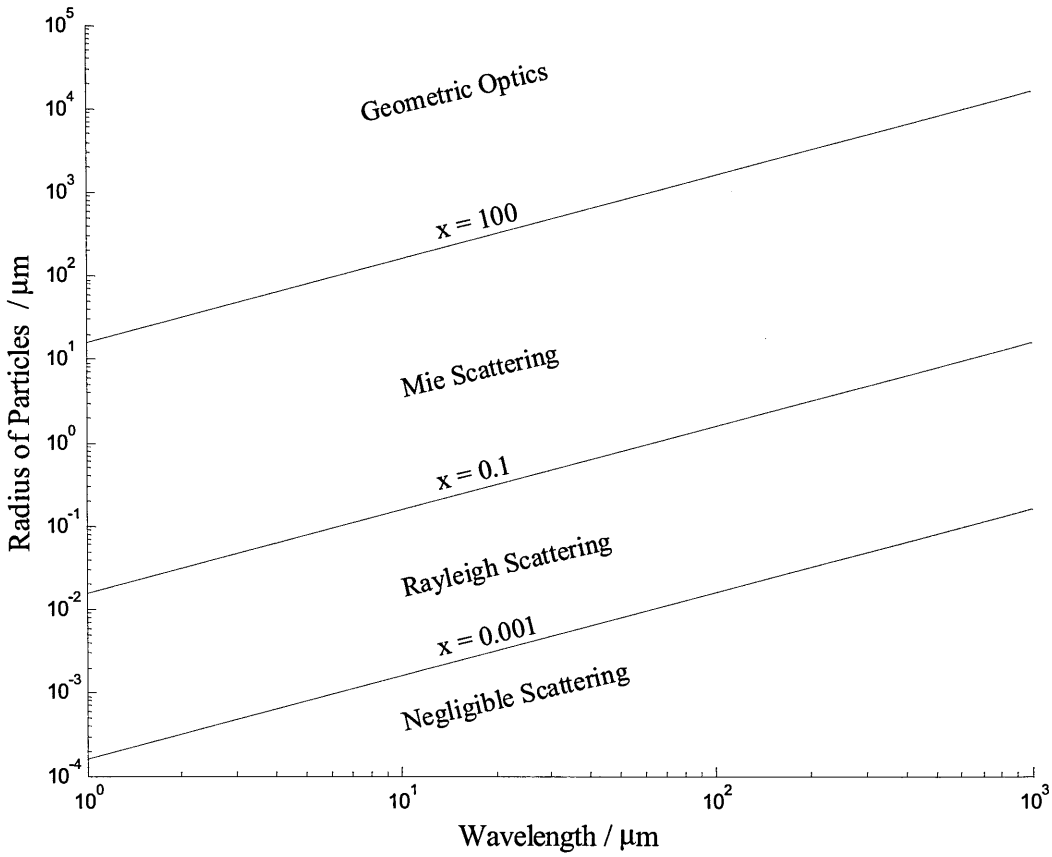

Figure 3-4: A diagram to show the scattering regime as a function of wavelength and particle radius.

Aerosol particles are usually assumed to be spherical in models, Pilinis et al. (Pilinis and Li, 1998) developed a model which calculates all the optical properties relevant to direct forcing for particles are homogeneous spheres, stratified spheres, and spheroids and compared the model with measurements. They found that the relative contribution from their model was found to be 0.98 of measured properties for normal concentration and 0.86 for the low dust concentrations. Their model indicated that the scattering and extinction coefficients and thus the single-scatter albedo are insensitive to the shape and the structure of the particles throughout the measurement period however the difference in the backscatter and upscatter fractions can be large.

Electromagnetic (EM) radiation is an oscillating electromagnetic field and as it encounters a medium it will interact with any electric charges within the medium. If a particle is much smaller than the wavelength of light, i.e. in the Rayleigh regime, the electric field over the particle can be thought of as homogeneous.

The dipole within the particle modifies the applied field within the particle. The applied field generates oscillations in the dipole in a particular direction which in turn produces an oscillating EM field i.e. the scattered wave. If the full EM equations are solved it shows that the radiation is preferentially scattered in certain directions and shows a dependence on wavelength of λ^4. The scattering cross section is given by;

$$\sigma^{sca} = \frac{8\pi^3}{3\lambda^4 N^2}(n^2 - 1)^2 \tag{68}$$

The phase function of scattering for un-polarised light is defined as the ratio of the energy scattered per unit solid angle in a particular direction to the average energy per solid angle in all directions and a qualitative description of the phase functions for different regimes is shown in Figure 3-5.

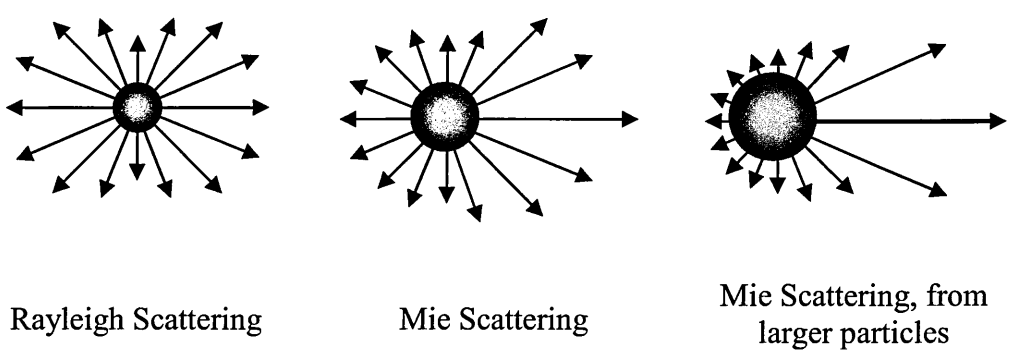

Figure 3-5: A qualitative diagram of the phase function for different sized particles

However, the regime of scattering of interest to this work is "Mie Scattering" and this is discussed in greater detail in the next section.

3.2.2 Mie Scattering

For particles sizes of the order of the wavelength of light the best description is Mie scattering. In a gas molecule there is only a single dipole, however an aerosol particle is a compact array of molecules and therefore produces an array of dipoles resulting in an array of multipoles. These multipoles are set into oscillation by the incoming EM radiation. Each multipole gives rise to a second oscillating field called a "partial wave" and the superposition of these waves in the far field is the scattered wave. Due to the size of the particle the incoming electric field can not be thought of as homogeneous and so there are spatial and temporal differences between the phases of the partial waves. The combined scattered wave therefore can be shown to have a high dependence on the angular position of detection as well as the wavelength of light and the size and refractive index of the particle.

Mie theory is the theory that describes the scattering of light from isotropic, homogeneous, dielectric spherical objects where the particle is of a similar size to the wavelength of light. The field at a point in the far field in this case is given by

$$E = E_{incident} + E_{internal} + E_{scattered} \tag{69}$$

where $E_{incident}$ is the field of the incoming EM wave, $E_{internal}$ is the field inside the particle and $E_{scattered}$ is the field of the scattered wave. Each of these electric fields must be computed and the boundary condition satisfied in order that we might find a solution to the problem. The boundary condition to be satisfied is that the components of the electric field must be matched at the boundary between the particle and the

surrounding medium. Matching in this case means that the total of the electric and magnetic fields must be equal to zero at the surface i.e. the sum of the scattered and incident field minus the internal field must equal zero.

From Maxwell's equations it can be shown that the transverse components of the electric fields have to satisfy the Helmholtz equation

$$\nabla^2 E + k^2 E = 0 \tag{70}$$

$$\nabla^2 H + k^2 H = 0 \tag{71}$$

where H is the magnetic field strength. For this symmetry of particle the equations are best solved in spherical polar co-ordinates. This includes the incoming plane wave, which must be expressed as a vector spherical harmonic expansion. To determine each of the fields Laplace's equation in spherical polar co-ordinates is separated into its variables R(r), $\Theta(\theta)$ and $\Phi(\varphi)$. The result is a partial differential equation; one solution of these equations is to express the function as an infinite power series. If the equal powers of the series are collected in the partial differential equation the series may be reduced to two power series each with their own co-efficients. The fields must then be put into the boundary conditions from which expressions are obtained for each component (transverse and parallel) of the internal and scattered fields. Expressions for the constants for these series a_n and b_n can then be determined. These coefficients, which are functions that include the complex refractive index, can then be used to find scattering and extinction efficiencies and the scattering amplitude and phase functions.

The electric field in the far field is

$$\begin{bmatrix} E_{\parallel} \\ E_{\perp} \end{bmatrix}_{sca} = \frac{\exp(-ikR+ikz)}{ikR} \begin{bmatrix} S_2 & S_3 \\ S_4 & S_1 \end{bmatrix} \begin{bmatrix} E_{\parallel}^0 \\ E_{\perp}^0 \end{bmatrix} \tag{72}$$

where the matrix containing the values of S_n, the scattering amplitudes, is the unitless amplitude scattering matrix. For spheres S_3 and S_4 are equal to zero. The other scattering amplitudes are given by

$$\begin{aligned} S_1(\theta) &= \sum_{n=1}^{\infty} \frac{2n+1}{n(n+1)} \left[a_n \pi_n \cos\theta + b_n \tau_n \cos\theta \right] \\ S_2(\theta) &= \sum_{n=1}^{\infty} \frac{2n+1}{n(n+1)} \left[b_n \pi_n \cos\theta + a_n \tau_n \cos\theta \right] \end{aligned} \tag{73}$$

where $\pi_n(\cos\theta) = \frac{1}{\sin\theta} P_n^1(\cos\theta)$ and $\tau_n(\cos\theta) = \frac{d}{d\theta} P_n^1(\cos\theta)$. Each of these categories is found for a single size parameter and must then be averaged over the size distribution. The scattering, σ_s, absorption, σ_a and extinction, σ_e cross-sections can then be given by

$$\sigma_e = \frac{2\pi}{k^2} \sum_{n=1}^{\infty} (2n+1) \operatorname{Re}(a_n + b_n) \tag{74}$$

$$\sigma_s = \frac{2\pi}{k^2} \sum_{n=1}^{\infty} (2n+1) \left(|a_n|^2 + |b_n|^2 \right) \tag{75}$$

$$\sigma_a = \sigma_e - \sigma_s \tag{76}$$

these values are for a single particle of a specific size parameter, x, for a size distribution of particles the overall cross section will be averaged over the whole size distribution and will be expressed as

$$\sigma = \frac{\int_{r_1}^{r_2} \sigma(r) n(r) \partial r}{\int_{r_1}^{r_2} n(r) \partial r} \tag{77}$$

3.3 Molecular Absorption

3.3.1 Molecular Energy Levels

The total energy of a molecule is the sum of its kinetic and potential energies. The molecule's potential energy depends on distances between charged particles and is usually grouped as nuclear and electronic energies. A molecule can have a continuum of translational kinetic energies if it is moving in space but it can also take discrete values of vibrational and rotational energies. Vibrational energies are seen as periodic bending and stretching of the intra-molecular bonds and rotational energy arising from a molecule's rotation about its centre of mass.

Within the Born-Oppenheimer approximation we assume that the nuclear, electronic, rotational and vibrational parts of the molecular wavefunction can be treated separately. Using the idea of the centre of mass of the molecule we can also separate the continuous translational part of the wavefunction from the ro-vibrational parts.

$$\Psi_{total} = \Psi_{nuclear} \Psi_{electronic} \Psi_{vibrational} \Psi_{rotational} \Psi_{translational} \tag{78}$$

In this approximation the energy components can be separated to give

$$E_{total} = E_{nuclear} + E_{electronic} + E_{vibrational} + E_{rotational} + E_{translational} \tag{79}$$

Except for translational motion the above energies can only take discrete quantised values unique to each molecule. Transitions between energy levels can occur but

require an input of energy. Photons can provide this energy but only those with energy equal to that of the transition will allow it to occur. The energy needed for each type of transition varies in magnitude but guidelines are given in Table 3-1

Table 3-1: Common frequencies for molecular transitions

Transition	Light Frequency	Wavenumber / cm^{-1}
Nuclear	Gamma Rays	$>10^8$
Electronic	Optical / Ultraviolet	10^4-10^8
Vibrational	Infra Red	10^2-10^4
Rotational	Radio/Microwaves	10^0-10^2

Since this work is concerned with atmospheric absorption of the infrared radiation re-radiated by the Earth we will be primarily concerned with ro-vibrational transitions. Wavelengths of light absorbed or emitted by the gas will correspond to energy changes during a single transition.

$$E_{photon} = \Delta E_{transition} = \Delta E_{vibrational} + \Delta E_{rotational} \tag{80}$$

3.3.2 Vibrational transitions

If a molecule has N atoms then to fully describe the position of all of the atoms you need three Cartesian co-ordinates, if they are allowed to move independently the molecule will have 3N degrees of freedom. Three of these will be translational degrees of freedom and three will be rotational about three perpendicular axes, unless the molecule is linear in which case it will be reduced to two, this leaves 3N-5 vibrational degrees of freedom for linear molecules and 3N-6 for all others. If the molecule is non-cyclic there are N-1 bonds between its atoms so of the vibrational

modes N-1 will be bond stretching and the remaining will be bond bending modes. The details for the modes for the molecule CF_3I is given in Table 3-2.

Table 3-2: Designations of degrees of freedom of molecules used in this work

	Generic	CF_3I
No of Atoms	N	5
Degrees of freedom	3N	15
Translational	3	3
Rotational	3	3
Vibrational	3N-6 (N-1 2N-5)	9 (4 bond stretching 5 bond bending)

These nine vibrations are knows as the fundamental modes of vibration and are given the designation υ_1- υ_9. The manifestations of these vibrations for a linear tri-atomic molecule are shown in Figure 3-6

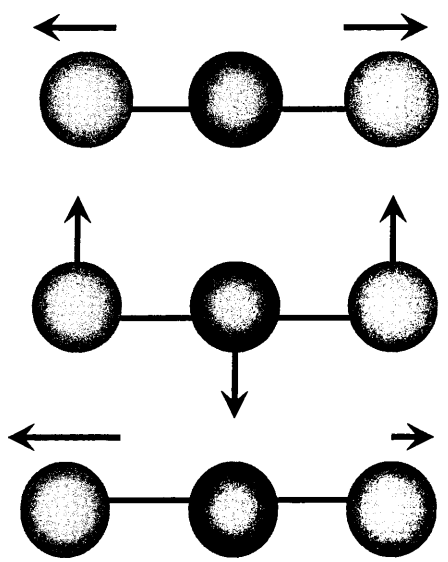

Designation	Type of vibration
υ_1	Symmetric stretch
υ_2	Symmetric bend
υ_3	Asymmetric stretch

Figure 3-6: Examples of fundamental mode vibrations for a linear tri-atomic molecule

Vibrational rotations may be simplistically treated using the simple harmonic approximation. In the simple harmonic oscillator approximation the restoring force obeys Hooke's law which states that the restoring force is proportional to the extension. The resulting electric potential between nuclei in the molecule is modelled as being symmetric about the minimum potential:

$$V(r) = \frac{1}{2}k(r - r_e)^2 \tag{81}$$

where V is the potential, r is the inter-nuclear distance, k is the force constant which is given by $k = \left.\frac{\partial^2 V}{\partial r^2}\right|_{r=r_e}$ and r_e is the separation that gives the minimum potential this results in quantised vibrational energy levels given by:

$$E_\upsilon = \left(\upsilon + \frac{1}{2}\right)h\omega \tag{82}$$

where h is Planck's constant, υ is the vibrational quantum number, which can take integer values, ω is the oscillator frequency determined by the mass of the atoms and strength of the bonds. Each of the fundamental modes of vibration are excited in this way and as higher levels are designated as $1\upsilon_1$, $2\upsilon_1$, $3\upsilon_1$ etc.

The total vibrational energy for a molecule is the sum of the energies for each of the vibrational modes. For non-linear molecules this is given by;

$$E_\upsilon = \sum_{k=1}^{3N-6}\left(\upsilon_k + \frac{1}{2}\right)h\omega_k \tag{83}$$

It can be seen that a molecule can never have zero vibrational energy, the lowest energy it can have is $\frac{1}{2}h\omega$. This is called the zero point energy and is a result of the

uncertainty principle. Selection rules for this approximation state that only transitions of $\Delta\upsilon = \pm 1$ are allowed.

One of the limitations of this simple harmonic motion approximation is that it predicts that infinite vibrational levels are possible. This is not observed since at some point Hooke's law is no longer obeyed and the bond breaks. Another limitation is that it predicts that the vibrational energy levels are evenly spaced at hω intervals. This is not seen in experiment as the spacing get smaller for higher υ i.e. the difference in energy levels becomes progressively smaller. An empirical potential, known as the Morse potential, is therefore used to give an anharmonic oscillator potential, Figure 3-7 shows both the harmonic and Morse potentials. The Morse potential is given by;

$$V(r) = D_e(1 - e^{-a(r-r_e)})^2 \tag{84}$$

where D_e is the dissociation energy, r_e is the equilibrium separation of the nuclei, r is the instantaneous inter-nuclear distance and a is a constant. This results in vibrational energy levels given by;

$$E_\upsilon = \left(\upsilon + \frac{1}{2}\right)h\omega_{eq} - \left(\upsilon + \frac{1}{2}\right)^2 h\omega_{eq}x \tag{85}$$

where ω_{eq} is the equilibrium vibration frequency, which means the frequency of an infinitely small vibration centred at the equilibrium inter-nuclear distance, and x is the anharmonicity constant. The selection rules for this potential allow transitions with changes in the vibrational constant of more than one but in practise the larger the change in υ the smaller the transition probability. Changes in vibrational states are always accompanied by changes in rotational state; this is discussed in section 3.3.3.

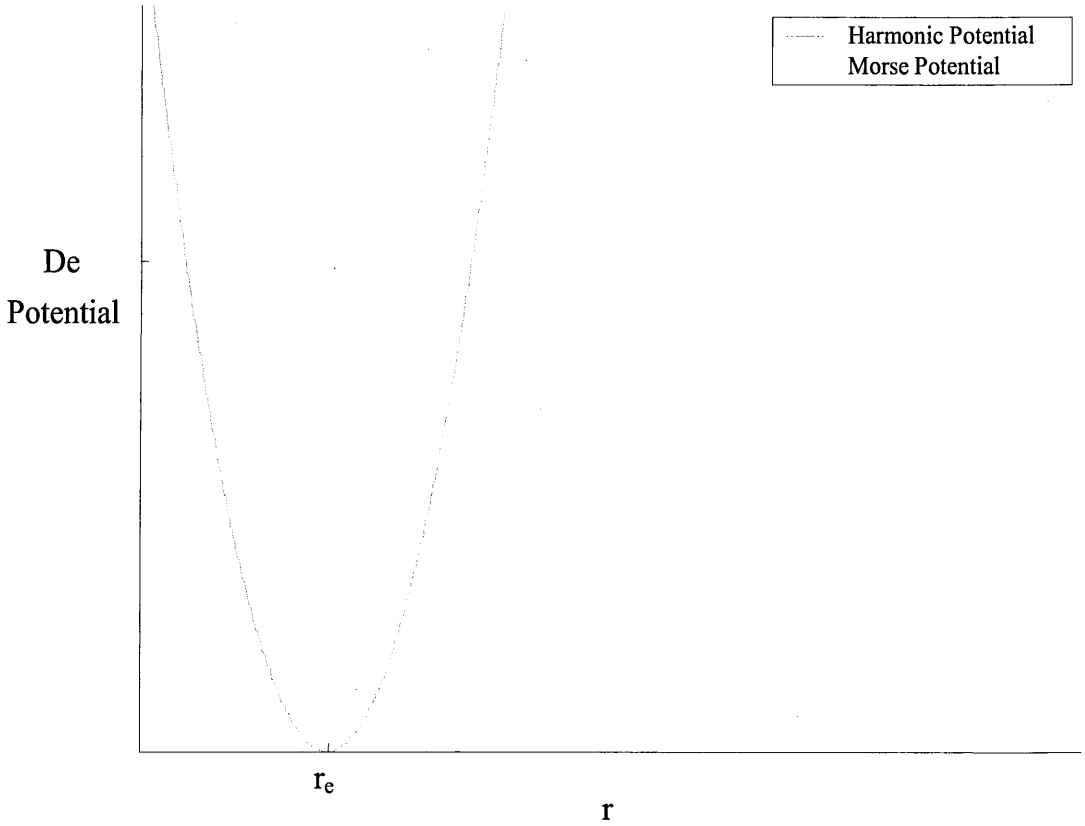

Figure 3-7: Approximate potentials for calculating the energies of vibrational states

The total vibrational energy for a molecule will be the sum of the energy for each active vibrational mode.

3.3.3 Rotational Transitions

In order to consider rotational energies of molecules we must consider the symmetry of the molecule as this determines where the mass lies and thus the moment of inertia, I, around each axis of rotation. There are various types of symmetry illustrated in Table 3-3. Consider moments of inertia around three perpendicular axes A, B and C.

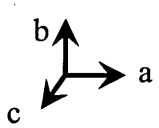

Table 3-3: Illustration of symmetries of molecules

Symmetry	Example molecule shape	Moments of inertia
Linear e.g. hydrogen chloride	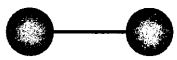	$I_A=0$, $I_B=I_C$
Prolate Symmetric top e.g. chloromethane	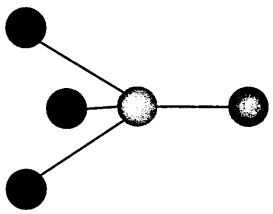	$I_A< I_B=I_C$
Oblate Symmetric top e.g. ammonia	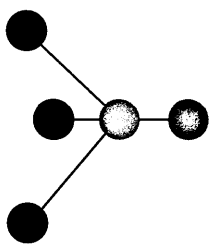	$I_A > I_B=I_C$
Spherical top e.g. carbon tetrachloride	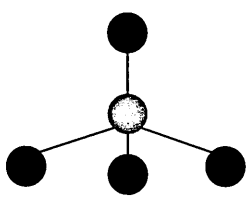	$I_A= I_B=I_C$
Asymmetric top e.g. water	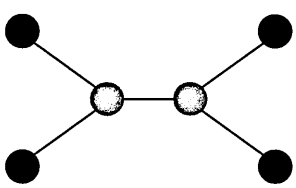	$I_A\neq I_B\neq I_C$

The molecules considered in this work are prolate symmetric tops (see Figure 3-8) so the ensuing theory will be centred on rotations of molecules with this symmetry.

The first approximation considered when considering the rotations of molecules is the rigid rotor in which no change in bond length occurs as the molecule rotates. In this case we consider a diatomic molecule; which will only have one moment of inertia, which is perpendicular to the bond axis and so we need only one quantum number to

describe its rotation. We consider the molecule rotating with a fixed inter-nuclear distance fixed at $r = r_\upsilon$ where r_υ is taken to be the expectation value of r for that vibrational state, this is usually larger than the r_e and increases with υ. The energy of these rotational states is given by

$$E_{rot} = \frac{\hbar^2}{2I_0} J(J+1) \tag{86}$$

where J is the resultant total angular momentum quantum number, I_0 is the moment of inertia of the molecule, $I_0 = \mu r_e^2$, and μ is the reduced mass. This is usually simplified to

$$E_{rot} = B_\upsilon J(J+1) \tag{87}$$

where B_υ is known as the rotational constant. Since r_υ increases with υ, B_υ gets smaller as the vibrational quantum number increases.

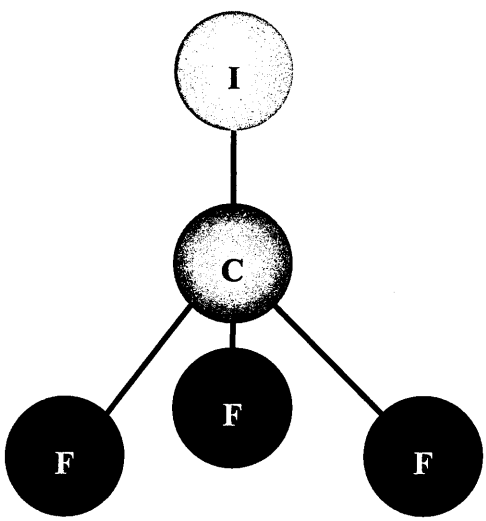

Figure 3-8: A diagram of a molecule used in this thesis: CF_3I (bond lengths d_{CF}=1.326 A and d_{CI}=2.16 A (Sheridan and Gordy, 1950))

If we now consider the symmetric top molecule CF_3I (Figure 3-8) we can see that there are two axes about which the molecule might absorb energy, one along the C-I bond and one perpendicular to this axis. We therefore need two quantum numbers to

describe its rotation. It is usual in this case to use the J quantum number to represent the total angular momentum and K to represent the angular momentum about the top axis i.e. C-F axis in this case. K can then take integer values between J and –J with positive and negative values representing different directions of rotation. If we now assume the prolate symmetric top to be rigid then we find that the energy levels are given by (Banwell and McCash, 1995);

$$E_{J,K} = hc(BJ(J+1)+(A-B)K^2) \tag{88}$$

where

$$B = \frac{h}{8\pi^2 I_B c} \text{ and } A = \frac{h}{8\pi^2 I_A c} \tag{89}$$

The selection rules for these transitions are

$$\Delta J = \pm 1 \text{ and } \Delta K = 0 \tag{90}$$

Another effect worth noting is that of centrifugal distortion; as J increases the bond length increases due to centrifugal forces; these are represented as extra terms in the energy expansion. For a prolate symmetric top molecule the rotational energy levels including first order centrifugal distortion is given by

$$\begin{aligned} E_{J,K} = hc(&BJ(J+1)+(A-B)K^2 - D_J J^2(J+1)^2 \\ &- D_{JK} J(J+1)K^2 - D_K K^4) \end{aligned} \tag{91}$$

Usually the distortion effects are less than one thousandth of the strength of the rigid rotor energy and is really only significant for $J \gg 10$. The effects are larger for molecules with lower force constants. It is possible to include higher order distortion constants (H and L) but these are small.

3.3.4 Ro-vibrational population distributions

The populations of each ro-vibrational state may be derived from the Boltzman distribution. To calculate the populations of all states we must take into account all rotational and vibrational states and their degeneracies.

$$P_{v,J,k} = \frac{g_v g_J g_K g_I e^{-\left(E_{vJK}/k_B T\right)}}{Q} \tag{92}$$

where P is the fraction of the population in the state, g represents the degeneracies, E is the energy of that state, k_B is the Boltzman constant, T is the temperature and Q is the ro-vibrational partition function. The degeneracies listed are vibrational, J state degeneracy ($g_J = 2J+1$), the K degeneracy (for symmetric tops $g_k = 1$ if $K = 0$ and 2 if $K \neq 0$) and the nuclear spin weighting factor. For a symmetric top the energy of each state is then given by the following equation:

$$\begin{aligned} E_{v,J,K} = (v+1)hf - (v+1/2)^2 hfx + BJ(J+1) + (A-B)K^2 \\ - D_J J^2 (J+1)^2 - D_{JK} J(J+1)K^2 - D_K J^4 \end{aligned} \tag{93}$$

where J is the total angular momentum quantum number, K is the projection of J on the molecular axis, v is the vibrational quantum number, f is the band origin and A and B are the rotational constants and D are the higher order centrifugal distortion constants. The partition function is given by

$$Q = \frac{1}{\sigma} \sum_{v,J,K} g_v g_J g_K g_I e^{-\left(E(v,J,K)/k_B T\right)} \tag{94}$$

This of course would be the partition function for one particular mode of vibration but all of the molecules must have at least the zero point motion in all modes of vibration. Therefore this must be summed for all possible energy states for every mode of vibration.

3.4 Infra-red spectroscopy

3.4.1 Operation of spectrometer

In continuous wave spectroscopy light is passed through a monochromator and each individual wavelength selected is then passed through the sample to measure the position and strength of its absorption features. There are several important limitations with this method. The light from the source is incident on a monochromator which splits the light into a continuous spectra and the particular wavelength chosen to illuminate the sample is chosen by letting it fall incident onto a slit. This limits the amount of signal one can get at a particular resolution; to improve resolution, you must narrow the slit and therefore increase the measurement time. The instrument must be repetitively calibrated, because the analogue connection between the monochromator position and the recording device is subject to misalignment and wear.

In FT-IR spectroscopy all of wavelengths are passed through a Michelson-type interferometer (see Figure 3-9) and onto the sample. The continuum of IR light passes through a beam splitter (labelled BS in the diagram); one part of the beam goes to a stationary mirror (M1) then back to the beam splitter. The other is reflected by a constantly moving mirror (M2). The motion of the mirror varies the path length and therefore the phase with which the beam arrives back at the beam splitter. When the two beams meet again at the beam splitter, they recombine, but the constant motion of M2 creates a signal that alternates in time between constructive and destructive interference. If we consider a monochromatic wave and assume that the beam-splitter performs an amplitude division equally between the two paths then the detector would

see a sinusoidally varying signal as the path lengths vary between the conditions for constructive and destructive interference i.e.

$$I = \frac{1}{2} I_S \left(1 + \cos\left(2\pi \frac{L}{\lambda} \right) \right) \tag{95}$$

where I is the intensity of light, I_s is the intensity of the light at the source, λ is the wavelength of light and L is the path difference introduced by the moving mirror. From equation (95) it can be seen that the detector would measure a constant component and a varying component. The signal will be maximised when the path difference is equal to an integer number of wavelengths.

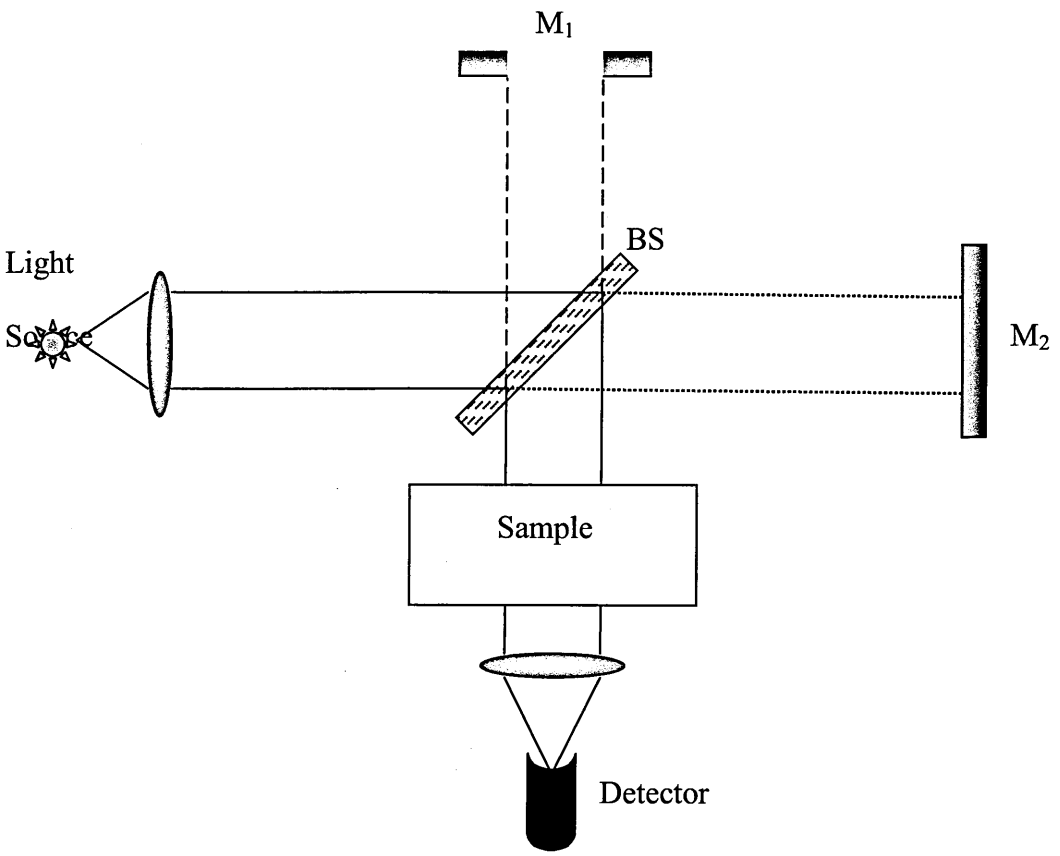

Figure 3-9: Schematic diagram of a Michelson interferometer where M1 and M2 are mirrors and BS is the beamsplitter

When the source is emitting a broadband thermal spectrum (Figure 3-10) the detected signal will be a superposition of many cosine waves with different frequencies and

amplitudes this is called an interferogram. The maximum intensity is seen at zero path difference when all frequency components will have maximum intensity. The spectrum taken as the mirror moves is a time dependent change and so taking the Fourier transform of this interferrogram gives a frequency spectrum of the detected signal.

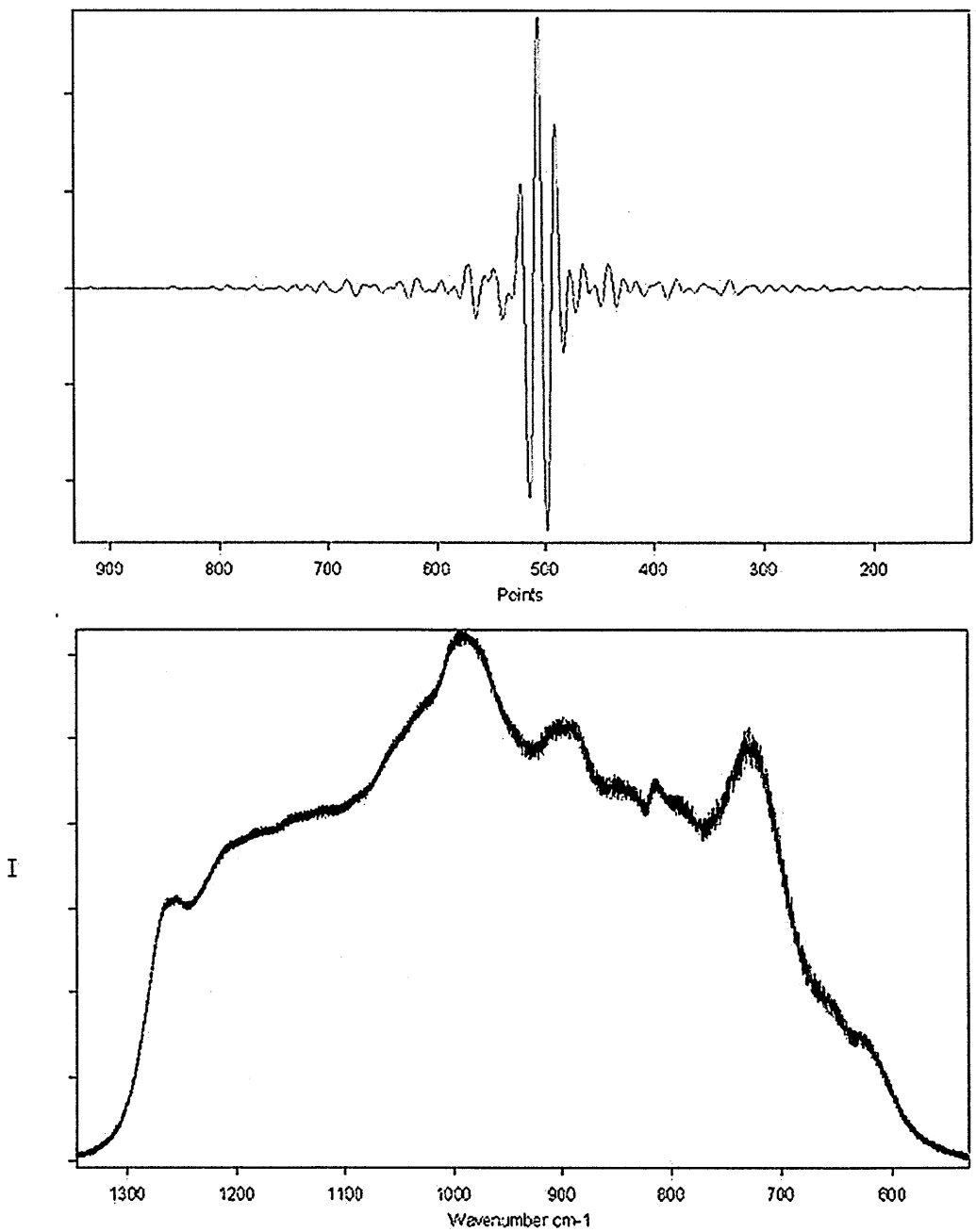

Figure 3-10: An experimentally obtained spectrum of the globar source and the interferrogram that produced it

In any practical FT-IR spectrometer there are, however, several problems that must be compensated for:

- The dispersive effect of the beam splitter: This will alter the apparent position of zero path difference and the symmetry of the interferrogram. Most spectrometers only record one side of the interferrogram but the moving mirror is allowed to overshoot the zero position in order to record both sides of the interferrogram and a phase correction algorithm is used to correct for this. This is known as phase correction.
- Extended source interference: As the source is not a point source the rays will not be perfectly collimated. Off-axis rays will have a different optical path difference and will therefore cause a circular fringe pattern at the detector. Apertures must be included to remove this from the field of view of the detector as it would affect the modulation pattern observed.

There are however significant benefits to using an FT-IR spectrometer the signal to noise ratio is very high and because each wavelength is measure simultaneously a spectrum of a particular resolution can be obtained much more quickly.

To record an infrared spectrum of a sample the recombined beam is passed through the sample. The sample absorbs or scatters at characteristic wavelengths and this alters the strength of specific wavelengths within the interferrogram. The detector measures the variation in energy versus time for all wavelengths simultaneously. A laser beam is superimposed to provide a reference. Fourier transforming the interferrogram allows us to convert an intensity-time spectrum into an intensity-frequency spectrum. To make a measurement of the strength of the absorption a spectrum is taken of the empty cell, I_0, and then of the cell containing a known

amount of the sample, I. Measuring the transmission through the sample and empty cell with the same optics allows us to automatically remove any effect from the optical components when the transmittance is calculated. The transmittance of the sample is then given by:

$$\tau = \frac{I}{I_0} \tag{96}$$

The transmittance is the used in conjunction with the Beer-Lambert law (equation (5)) to derive useful spectroscopic parameters such as σ.

In gas phase spectroscopy a known pressure of a gas is inserted into a sealed sample chamber of known dimensions. From this the number density of the molecules and the path length through the sample can be calculated. From measurements of the transmittance used in conjunction with the Beer-Lambert law the absorption cross section can be found.

In aerosol spectroscopy the transmittance is influenced by scattering as well as absorption. In this case a Mie scattering model must be employed to determine the contributions from the scattering and absorption. These models calculate the a_n and b_n constants for a certain size parameter, x, and use them to calculate the scattering, Q_{sca}, and extinction, Q_{ext}, efficiencies which are then integrated over the whole size distribution to get the volume extinction coefficient, β_{ext}, and the single scattering albedo, ϖ. In this thesis a Fortran routine called Miex written by Stephen Wolf (Wolf and Voshchinnikov, 2004) is used to calculate the extinction efficiencies; as well as the transmittance spectrum, the real and complex refractive index as a function of

wavelength, the size distribution of the sample and number concentration are needed as inputs.

There are several advantages to using FT-IR spectroscopy: all of the source energy reaches the sample, improving the inherent signal-to-noise ratio. The resolution in an FT-IR spectrometer is limited by the design of the interferometer, the longer the path of the moving mirror, the higher the resolution. To illustrate this consider a source with two monochromatic spectral lines. The interference signal produced by the moving mirror depends on a difference in phase between the two signals. If the signals are close in frequency the mirror will have to move further to observe modulation of the signal modulation of the signal. Hence the resolution of the spectrometer is inversely proportional to the maximum optical path difference (OPD) which is twice the distance that the mirror moves, this is known as the Rayleigh criterion. This criterion is affected by post processing of the signal so is not exactly as theory states. The manufacturer of the spectrometers used in this thesis, Bruker, gives a guideline for the resolution of their spectrometers as

$$\text{Resolution} = \frac{0.9}{OPD_{\max}} \tag{97}$$

where OPD_{max} is the maximum distance that the mirrors can move.

3.5 Summary

Radiation interacts with matter in many various and complex ways, energy is transferred to the electrons in molecules resulting in absorption and scattering of the incoming wave.

FT-IR spectroscopy has been chosen to investigate some of interesting interactions of light with matter mentioned in this chapter. To find the transmittance of a gas sample is a relatively simple affair. A sample cell of known dimensions is filled with a known pressure of the gas to be analysed and from this the number density and path length through the sample can be obtained. This can then be used, in conjunction with the Beer-Lambert law to calculate the absorption cross-section of the gas. For aerosols however the case is more difficult. Aerosols are heavier particles than air and so, once inserted into a sample cell start to settle out under gravity. If one wants to take spectra of aerosol particles one must therefore find a way of suspending the aerosols in the sample chamber in order that the sample remain in the beam. Many different methods have been used but the one we are investigating in this thesis is levitation using ultrasound. The methods of levitation of aerosols used and the physics of ultrasonic levitation are the topic of the next chapter.

Chapter 4: Ultrasound and Ultrasonic Levitation

"As far as we can discern the sole purpose of human existence is to kindle a light of meaning in the darkness of mere being".
Carl Gustav Jung

"If nature were not beautiful, it would not be worth knowing, and if nature were not worth knowing, life would not be worth living."
Henri Poincaré

Measuring spectra of atmospheric aerosols has an added complication in that aerosols will settle out under gravity during the time that it takes to collect the data. This chapter aims to give the reader an account of ultrasound and how it is applied in the phenomena of ultrasonic levitation. It describes the creation of ultrasonic fields by the application of various types of transducers with particular reference to piezoelectric methods. The chapter then goes on to describe the interactions of this field with particulate aerosols. The different "drift" forces that act on the samples are discussed and the relative importance these have on particles of sizes relevant to atmospheric chemistry. The mechanisms of levitation and agglomeration of aerosols are discussed in depth.

4.1 A short introduction to sound

The derivations in this section follow those of The Acoustic Bubble (Leighton, 1997).

4.1.1 The sound wave

Sound is a series of compressions and rarefactions, it is a longditudinal wave, meaning that the motion of the particles is parallel to the direction of propagation of the wave, but whilst the wave travels through the medium, the particles only oscillate locally. Figure 4-1 shows how the passing of a sound wave affects the common properties of the medium. For sinusoidal waves of infinite length, propagating in one

dimension there is a simple relationship between the speed of the wave and its wavelength.

$$c = f\lambda \tag{98}$$

where c is the phase speed of the wave and λ is its wavelength. If all the frequencies of sinusoidal waves travel at the same phase speed then the medium is said to be non-dispersive. A wavepacket or pulse, which is localised in space, can be thought of as the summation of many, single frequency, infinite sinusoidal waves which are chosen so as to cancel each other out beyond the bounds of the wavepacket. If the medium that a wave packet is travelling through is dispersive then the different sinusoidal waves will travel through the medium at different phase speeds and thus the wavepacket will change shape over time.

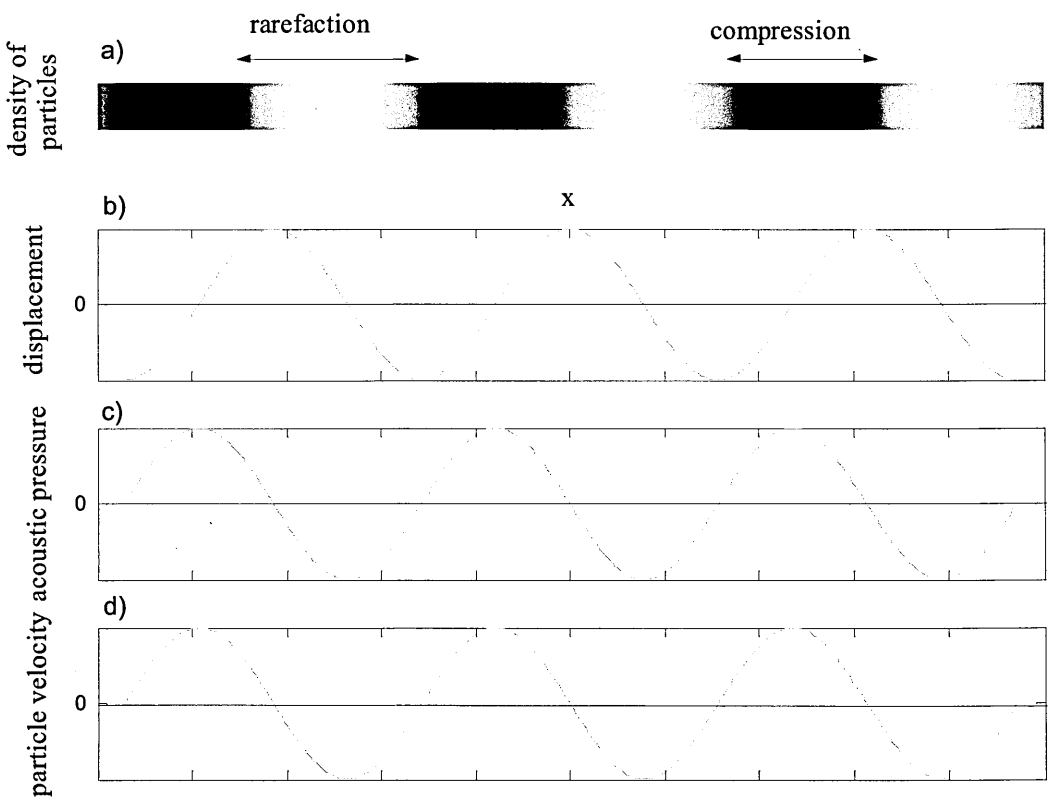

Figure 4-1: A diagram to show how the properties of a sound wave vary respective to each other. a) The density of the medium through which the sound passes; the darker the shading the denser the region b)The displacement of the particles in the medium c) The relative pressure change caused by the passing acoustic wave d) The velocity of the particles through the wave.

4.1.2 The sound spectrum

Average human hearing ranges from 20 Hz to 20 KHz, although sensitivity to the higher frequencies is lost with age. Sound is categorised according to the range of human hearing, sounds of lower frequency are named infrasonic, those within the range, sonic, and those above the range, ultrasonic. Table 4-1 shows the frequencies of some common phenomena. In most cases the medium can be considered to be a continuum since the wavelength of sound is much greater then the mean free path of the molecules. Air at atmospheric pressure becomes unable to transmit sound at about 2 GHz because the mean free path of the air molecules becomes comparable in size to one half-wavelength of the sound and thus the wave will no longer "see" the air as a continuum.

Table 4-1: Some examples of common acoustic phenomena and their typical frequencies

Frequency (MHz)	Phenomena
1-20	Medical Ultrasound
Frequency (KHz)	
25-80	Bat sonar clicks
40-50	Ultrasonic cleaning
18-20	Upper limit of human hearing
2-5	Maximum sensitivity of human ear
Frequency (Hz)	
2048	Highest note of soprano singer
90	Ruby throated hummingbird in flight
64	Lowest note of bass singer
50	Alternating current (Europe)
8-20	Lowest limit of human hearing
1-5	Rotation of tornadoes
<1	Tidal motion, Earthquakes

4.1.3 Sound travelling through different materials

If changes in a material property such as density or pressure satisfy the one dimensional linear wave equation then linear waves of parameter, ε, will propagate at speed, c.

$$\frac{\partial^2 \varepsilon}{\partial t^2} = c^2 \frac{\partial^2 \varepsilon}{\partial x^2} \tag{99}$$

In solids changes in the bulk modulus divided by the density, B/ρ, satisfies this equation, meaning that waves of both the pressure (and thus displacement) will propagate with a phase speed,

$$c = \sqrt{\frac{B}{\rho}} \tag{100}$$

The bulk modulus is the volume response of a material to an applied pressure.

$$B = -V \frac{\partial p}{\partial V} \tag{101}$$

where V is the volume and dp is the change in the pressure from the equilibrium value for a change in volume of dV.

In gases the situation is more complicated, as sound travels through the gas it will be compressed and rarefied. This will cause heating in the compressed regions and cooling in the rarefied regions, which in turn will cause volume and pressure changes in the gas. These temperature differences mean that heat will tend to flow from the hotter parts to the cooler parts i.e. from compressions to rarefactions. There are two extremes of this situation; either the volume and pressure changes occur so rapidly that no heat exchange takes place, an "adiabatic" change, or the heat exchange occurs

almost instantaneously so that the pressure and volume changes take place at constant temperature, an "isothermal" change. These situations results in slightly different bulk modulii and so result in different phase speeds. The conditions for adiabacity are

$$pV^{\gamma} = \text{constant} \tag{102}$$

where γ is the ratio of the heat capacity of the gas at constant pressure to that at constant volume. The adiabatic bulk modulus, B_s, is then given by

$$B_S = \gamma p \tag{103}$$

and the phase speed of the sound by

$$c = \sqrt{\gamma p / \rho} \tag{104}$$

In the isothermal limit the corresponding equations are

$$pV = \text{constant} \tag{105}$$

$$B_T = p \tag{106}$$

$$c = \sqrt{p / \rho} \tag{107}$$

Rarely is a process however fully adiabatic or isothermal and consequently the information is surmised in the following equation

$$pV^{\kappa} = \text{constant} \tag{108}$$

where κ is the polytropic index which has values between 1 and γ depending on the situation. The speed of sound is therefore

$$c = \sqrt{\frac{\kappa p}{\rho}} \tag{109}$$

In air at room temperature and pressure the speed of audible frequencies obeys the adiabatic equation meaning that there is little heat exchange between the

compressions and rarefactions but as the frequency gets higher and the distance between the regions becomes smaller the propagation becomes isothermal and the speed changes. This means that different frequencies will travel through the air at different speeds. Full isothermality is reached at about 7×10^8 Hz. Note: In liquids the situation is complicated by non-linear effects and so is not considered here.

4.1.4 Acoustic Characteristics

"I would rather live in a world where my life is surrounded by mystery than live in a world so small that my mind could comprehend it. "

Harry Emerson Fosdick

4.1.4.1 Acoustic Impedance and Attenuation

The acoustic impedance, z, is an analogous idea to impedance in other branches of physics, it is the ratio of the driving impulse to the velocity response. In acoustics the driving force is the pressure amplitude, p_A, and the velocity response is the velocity of the particles in the medium.

$$z_s = \frac{p_A}{\dot{\varepsilon}} \tag{110}$$

This is known as the specific acoustic impedance, from equation (101) it can be shown that

$$p_A = -iBk\varepsilon \tag{111}$$

substituting this and for $\dot{\varepsilon}$

$$z = \frac{Bk}{\omega} \tag{112}$$

substituting for equation (100) results in the equation

$$z_c = \rho c \tag{113}$$

which is known as the characteristic acoustic impedance. As a sound wave passes through a medium it will lose energy to the medium, some possible methods of energy loss are heat transfer due to viscous forces in the medium or transfer between the rarefactions and compressions as discussed earlier. In a plane wave travelling in the x direction the acoustic pressure can be modified such that

$$p_A = p_{A0} e^{i(\omega t - kx)} e^{-bx} \tag{114}$$

where b is the amplitude attenuation coefficient. Higher frequencies tend to be attenuated more strongly than lower ones.

Travelling waves transmit energy from one place to another, however, if two identical waves travel in opposite directions there is no net flow of energy a standing wave can be formed. In the case where a pressure wave is reflected from a boundary the pressure amplitude varies as

$$p_A = p_I + p_R = e^{i(\omega t - kx)} + Re^{i(\omega t + kx)} \tag{115}$$

where R is the reflection co-efficient, p_I is the incident pressure wave and p_R is the reflected wave. If R=1

$$p_A = 2e^{i\omega t} \cos kx \tag{116}$$

If R is less than one then only partial reflection occurs and then the nodes of the superposition resulting from only partial reflection of the waves do not go to zero and the field can then be thought of as being part standing wave and part progressive wave. The fraction of the field which is a standing wave is given by

$$\frac{P_{\text{antinode}} - P_{\text{node}}}{P_{\text{antinode}} + P_{\text{node}}} \tag{117}$$

Attenuation in a standing wave would be greater in the reflected wave than in the incident wave as it has travelled further through the medium. Thus the standing wave fraction of the field decreases with increasing distance from the reflector.

In general if a process has high losses there will also be a time lag between the driving force and the velocity response. This manifests itself in the mathematical description as a complex impedance, wavenumber and waveform.

$$\begin{aligned} k &= q + ib \\ e^{ikx} &= e^{iqx} e^{-bx} \end{aligned} \tag{118}$$

where the real parts of these functions show the conditions of no attenuation.

4.1.4.2 Acoustic Intensity

Acoustic intensity is the way of categorising the strength of an acoustic wave; the rate of energy transfer per unit area perpendicular to the direction of propagation. If we consider a volume element of density, ρ, exactly one wavelength long in the direction of propagation and of cross sectional area, A, the kinetic energy of this volume is equal to

$$\begin{aligned} \text{K.E.} &= \frac{1}{2} m \cdot |v|^2 \\ &= \frac{1}{2} A\rho \int_{L}^{L+\lambda} \left(\text{Re}(\dot{\varepsilon})\right)^2 dx \\ &= \frac{1}{2} A\rho \int_{L}^{L+\lambda} \omega^2 \varepsilon_0^2 \cos^2(\omega t - kx) dx \\ &= \frac{1}{2} A\rho \int_{L}^{L+\lambda} \omega^2 \varepsilon_0^2 \frac{1}{2}(1 + \cos 2(\omega t - kx)) dx \end{aligned} \tag{119}$$

since the integral of the cosine term over one complete cycle is zero and the volume of each element is Aλ, the mean kinetic energy per unit volume can be expressed by

$$\begin{aligned} K.E._{mean} &= \frac{1}{4}\rho\left|\omega\varepsilon_0\right|^2 \\ &= \frac{1}{4}\rho\left|\dot{\varepsilon}\right|^2_{\max} \end{aligned} \tag{120}$$

In an undamped wave the total energy of the system is twice that of the mean kinetic energy, so the total energy density is given by

$$E_{total} = \frac{1}{2}\rho\left|\dot{\varepsilon}\right|^2_{\max} \tag{121}$$

The total intensity of the wave travelling at speed, c, will be

$$I = \frac{1}{2}c\rho\left|\dot{\varepsilon}\right|^2_{\max} \tag{122}$$

If we now substitute in the values for the specific acoustic impedance we find that

$$I = \frac{p_A^2}{2z} \tag{123}$$

The usual measurement scale for the power transferred by sound is the bel; this is a logarithmic scale to the base ten of the ratio between the sound power to be measured compared to a reference sound power level so if the surface areas of the detectors are kept constant

$$\text{Intensity Level(bels)} = \log\left(\frac{I}{I_{ref}}\right) \tag{124}$$

$$\text{Intensity Level(decibels)} = 10\log\left(\frac{I}{I_{ref}}\right) \tag{125}$$

and since the intensity is proportional to the square of the sound pressure level

$$\text{Sound Pressure level} = 20\log\left(\frac{p}{p_{ref}}\right) \tag{126}$$

A logarithmic scale is used as it can easily represent the vast range of sound intensity that humans can hear.

4.1.4.3 Reflection and Transmission

If sound is incident on an absorber a force will be transmitted to the absorber, this is known as the radiation pressure. If the intensity of the sound field acting on the surface is I, the energy incident on an area, A, in time, Δt, is given by

$$E = IA\Delta t \tag{127}$$

this exerts a force of

$$F_{rad} = \frac{IA}{c} \tag{128}$$

and a radiation pressure of

$$p_{rad} = \frac{I}{c} \tag{129}$$

this pressure is different for different geometries. A wave may also be partially reflected and partially absorbed or transmitted into the media. The property that distinguishes the behaviour of materials under the influence of an acoustic field is known as its acoustic impedance. If a wave is incident on a massless surface between two media of different acoustic impedance the pressure and velocity across the surface must be continuous.

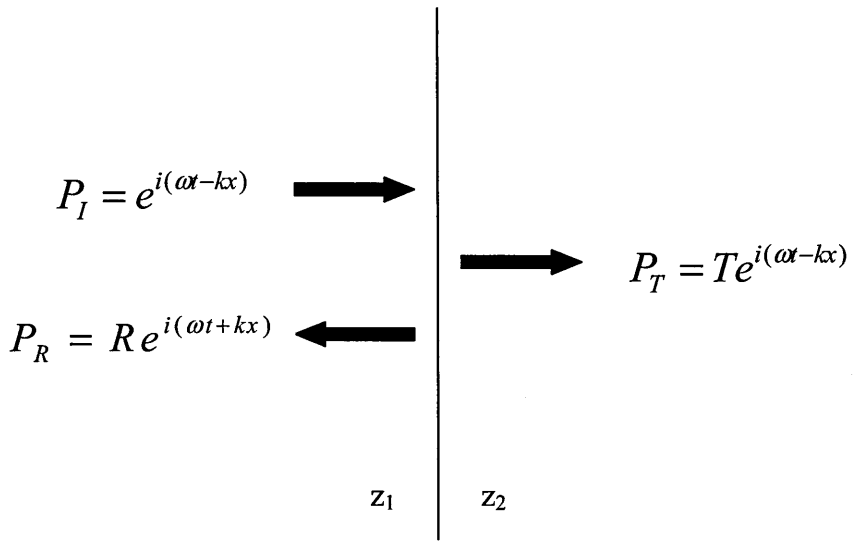

Figure 4-2: A travelling sound wave incident on a surface.

Since pressure must be continuous at the boundary

$$1 + R = T \tag{131}$$

where R is the reflection coefficient and T is the transmission coefficient. The velocities must also be continuous at the boundary and since the acoustic impedance is said to be the ratio of the acoustic pressure to the particle velocity it can be shown that

$$\frac{(1-R)}{z_1} = \frac{T}{z_2} \tag{132}$$

from this it can be shown that

$$T = \frac{2z_2}{(z_1 + z_2)} \tag{133}$$

$$R = \frac{(z_2 - z_1)}{(z_1 + z_2)} \tag{134}$$

if $z_1 = z_2$ the wave is completely transmitted and the materials are said to be "impedance matched".

4.2 Ultrasonic Fields

The fields employed in this thesis are airborne ultrasonic fields and so only the practical implications of finding a suitable ultrasonic transducer for creating ultrasonic fields in air will be discussed.

4.2.1 The Near and Far Sound Field

Each acoustic source can be represented as a collection of point sources radiating spherically symmetric waves. At a point far from the source the properties of the field can be calculated by summing the contributions from each spherical wave. For an extended source the difference in path length results in a phase difference between the waves. If the point of measurement is far from the source this phase difference is vanishingly small. Close to the source, however, the phase differences cannot be ignored in the calculations and the region where this effect is significant is known as the 'near field' and where it becomes negligible it is defined as the 'far field'. The smaller the wavelength the greater the distance over which the near field extends, r_{nf}. The region over which is the near field extends for a cylindrically shaped transducer of radius, r_t, is given by the relation

$$r_{nf} = \frac{r_t^2}{\lambda} \tag{135}$$

4.2.2 Ultrasonic Transducers

Creating a sound field in a medium at any frequency is a case of creating a mechanical oscillation that couples to the medium, causing oscillations in that medium. There are several transducers which create mechanical oscillations at ultrasonic frequencies. Transducers are classified by the principles that cause the mechanical vibrations, the most common types are electrostatic, electrodynamic,

magnetostrictive, piezoceramic and pneumatic transducers. Typical values of properties for these transducers are given in Table 4-2. Piezoelectric transducers are the most commonly used due to their mechanical ruggedness and high efficiency. In any electrically driven transducers, such as piezoelectric transducers, the electro-acoustic efficiency, η, gives the proportion of the input electrical energy that is turned into acoustic energy. The effectiveness of each transducer type depends on the efficiency of driving the mechanical vibrations and the efficiency with which these mechanical vibrations are converted to a pressure wave within the medium. Any energy that is not converted into acoustic energy is reflected back into the transducer and is dissipated as heat - which can be damaging to the transducer.

The work in this thesis requires an ultrasound field to be created in air, from equation (122) we can see that we would need much greater deflections of the mechanical surface to produce sound intensity in gases than we would for liquids or solids at the same frequency. As discussed earlier, gases stop transmitting ultrasound completely at about 2 GHz but for most practical purposes the useful range of ultrasonic transducers in air is limited to 500 kHz, much lower than those used in liquids or solids. This also reduces the energy intensities attainable in airborne ultrasound. Much larger amplitude vibrations of the radiating surface are needed in order to get enough acoustic energy transmitted into air. Much current research in this field concentrates on finding methods of increasing the electro-acoustic efficiency of airborne transducers in order that enough energy can be extracted from transducer (Cochran et al., 1998, Manthey 1992).

Table 4-2: Table of typical values properties of 200 kHz ultrasonic transducers in air

Parameter	Electrostatic	Piezoelectric
Transmitting /mVPa^{-1}	2	1
Receiving /mVPa^{-1}	0.2	1
Range	0.3	0.02
f_{max} /kHz	200	500
Maximum Temperature /°C	80	>100

There are many different ways of modelling the characteristics of transducers in order to improve their efficiency:

- As a "lumped" electrical circuit where the electrical and mechanical oscillatory properties are represented by inductors, capacitors and resistors (Butterworth, 1914)
- using transmission matrices in which the power of the transmitted sound is calculated using the transmission and reflection coefficient of each layer (Hill, 1980)

4.2.3 Piezoelectric transducers

The piezoelectric (PE) effect was first observed in quartz in 1880 by Jacques and Pierre Curie (Duck, 2009), the direct PE effect occurs in particular materials when a pressure is applied and a voltage is generated across the material Figure 4-3. The converse PE effect is when a voltage is applied and an external pressure is generated. The degree of polarization varies almost linearly with the applied stress.

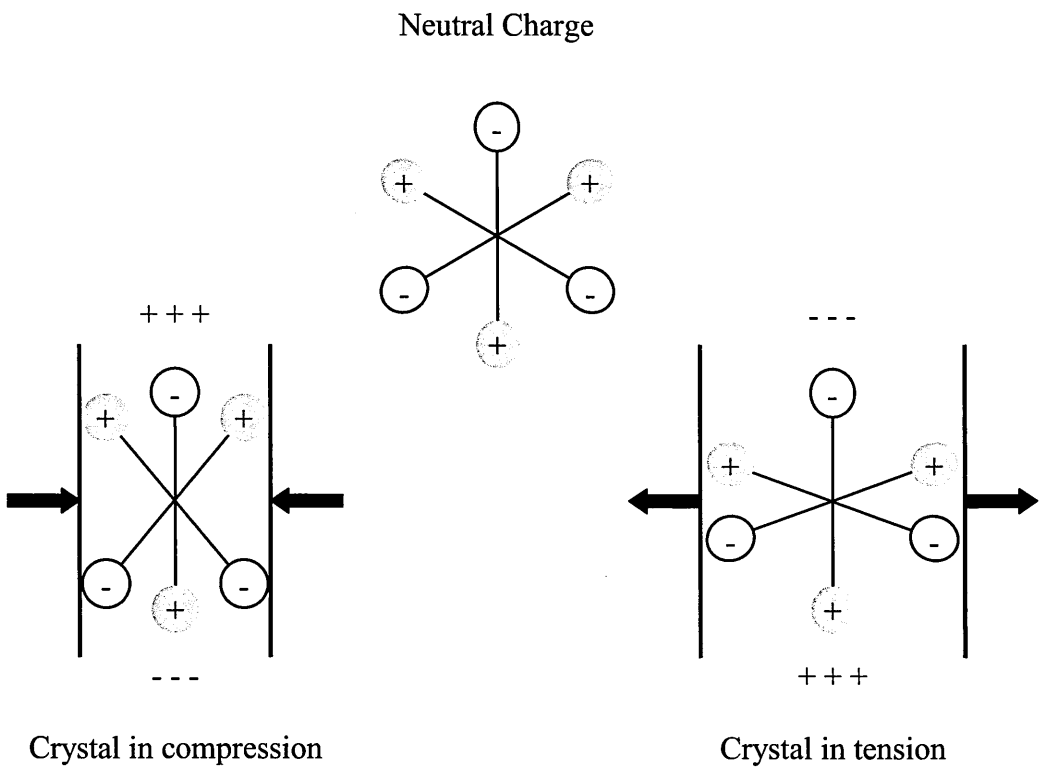

Figure 4-3: The piezoelectric effect as seen in a quartz crystal under the action of forces where + represents silicon and – represents oxygen.

The most common piezoceramic materials are ceramics with the perovskite crystal structure, the dominant type being lead zirconium titanate (PZT). Piezoceramic crystals can be thought of as a mass of crystallites; above the Curie temperature of the crystals there are no dipoles present in the crystallites but below the Curie point the crystallites take on a different symmetry causing each elementary cell of the crystal to have a dipole. In the crystal these dipoles align in regions called Weiss domains but the Weiss domains themselves are not aligned (see Figure 4-4).

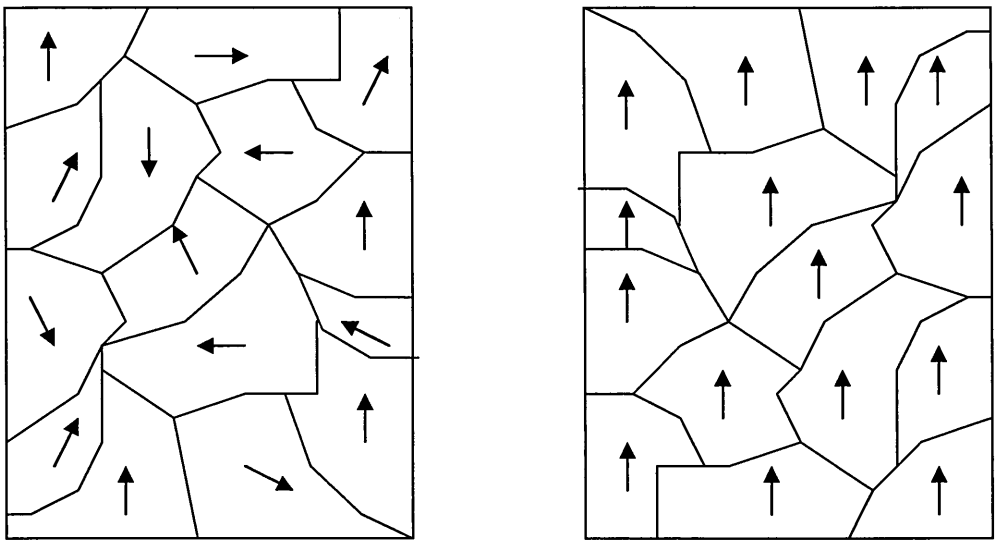

Unaligned Wiess Domains

Aligned Weiss Domains

Figure 4-4: Aligned and unaligned Weiss domains

In order for these crystals to demonstrate the piezoelectric effect they must be poled. During this process a strong electric is applied across the crystal, the Weiss domains that are aligned with the field grow at the expense of the non-aligned domains and the crystal lengthens in the direction of the applied field. When the field is removed the alignment approximately remains; this is known as the permanent polarisation. Once the crystal has been poled piezoelectric phenomena can be observed. If an alternating voltage is applied to the crystal in the same axis of the polarisation it will grow and shrink along the same axis and at the same frequency of the applied voltage to a maximum extension given by the saturation polarisation, which occurs when all of the dipoles are aligned with the field, i.e. they are anisotropic.

Crystals can be designed with a variety of different geometries; with the direction of polarisation in the axial or radial direction e.g. cylinders that expand axially or radially or disks that expand axially or radially. Loss of the polarisation of the crystal results in loss of piezoelectric properties and occurs if the domains become unaligned,

this can happen if mechanical stresses on the crystal are great enough to disturb the orientations, if the crystal is exposed to strong electric fields or if the crystal is heated to above its Curie point.

In the dynamical mode these crystals will have a natural frequency of vibration according to their dimensions, this is known as the mechanical resonance. These crystals behave, electrically, like capacitors and so if driven by a sinusoidal voltage will also have a natural electrical resonant frequency. The electromechanical characteristics of a piezoelectric crystal can be represented by an equivalent electrical circuit. Near the first fundamental resonance of the crystal the recommended standard equivalent circuit by the IEEE is the Van Dyke circuit model (IEEE, 1976). The idea of an equivalent circuit was first proposed independently by Butterworth (Butterworth, 1914) and Cady (Cady, 1922) in these models the mechanical properties of the transducer are modelled as lumped electrical components. The equivalent circuit used to model transmitting piezoelectric transducers is shown in Figure 4-5. In this circuit model the voltage source is an ideal voltage source with its internal resistance instead represented by R_i, C_0 represents the clamped electrical capacitance of the transducer. R_L represents the energy lost to the load i.e. the acoustic energy radiated into the medium; in a vacuum this would be zero. R_l represents the energy loss due to mechanical and dielectric losses in the circuit, C_l and L_l represent the capacitance and inductance of the mechanical circuit respectively. The power given to the load can then be found by calculating the power delivered to the load resistor in this equivalent circuit.

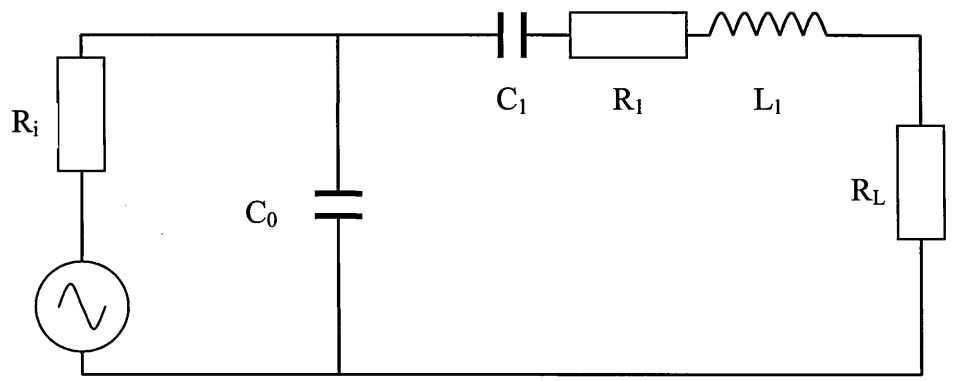

Figure 4-5: Equivalent circuit of a piezoelectric ultrasound transmitter

When capacitors or inductors are introduced into circuits they cause a phase difference between the voltage and the current.

$$V = V_m e^{i\omega t} \tag{136}$$

$$I = I_m e^{i(\omega t - \phi)} \tag{137}$$

where V is the voltage, I is the current, ω is the angular frequency if the voltage, ϕ is the phase angle between the current and voltage and t is the time. The complex impedance is then defined as

$$Z = \frac{V_m}{I_m} e^{i\phi} = R + iX \tag{138}$$

where R is the resistance and X is the reactance, for a capacitor the voltage lags behind the current by a phase of π thus the frequency dependent reactance is given by

$$X_c = -\frac{1}{\omega C} \tag{139}$$

for an inductor the voltage leads the current by a phase of π and thus it's contribution to the reactance is given by

$$X_L = \omega L \tag{140}$$

The resistance and reactance can then be represented on an Argand diagram

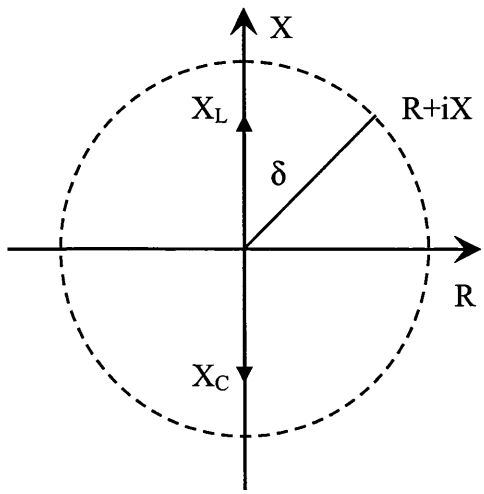

Figure 4-6: Diagram of the complex impedance as an Argand diagram

where δ, the phase angle between the resistance and reactance, is known as the loss angle. From Figure 4-6 it can be seen that if the complex contributions from the inductor and capacitor are equal then the impedance is purely real and the load is acting like a pure resistance, at this point the voltage and current are acting in phase and the system is at resonance.

The complex impedance of piezoelectric transducers is given by

$$\frac{1}{Z} = \frac{1}{Z_C} + \frac{1}{Z_M} \tag{141}$$

where Z_C is the impedance of the static capacitance branch and Z_M is the impedance of the mechanical equivalent branch, this can be shown to be (Svilainis and Motiejûnas, 2006);

$$Z = \frac{\left(R_1 + R_L - i\frac{1}{\omega C_1} + i\omega L_1\right)\bullet\left(i\frac{1}{\omega C_0}\right)}{R_1 + R_L - i\frac{1}{\omega C_1} + i\omega L_1 - i\frac{1}{\omega C_0}} \tag{142}$$

Piezoelectric transducers have a characteristic complex impedance curve as shown in Figure 4-7, where f_s and f_p are the series and parallel resonance respectively.

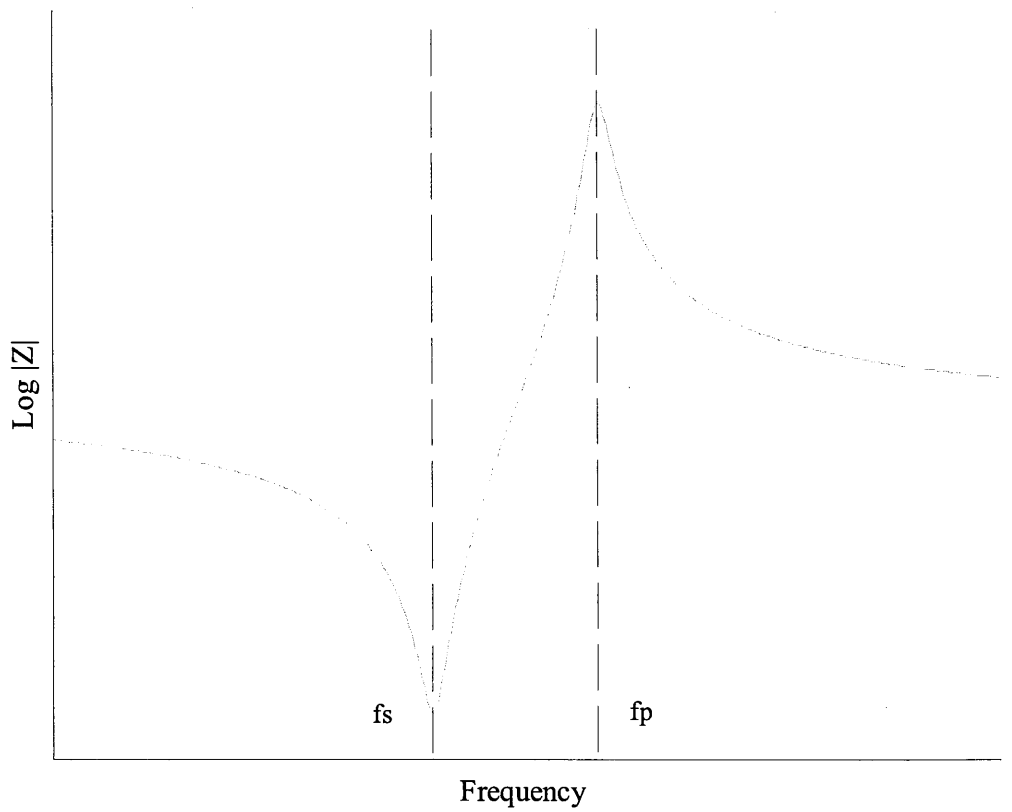

Figure 4-7: Characteristic Impedance curve of a piezoelectric transducer

At f_S the complex impedance, Z, is real, in other words the circuit is acting as a pure resistor. The minimum impedance is in the vicinity of the series resonance, f_s, and is given by (MorganElectroCeramics, 2009)

$$f_s = \frac{1}{2\pi}\sqrt{\frac{1}{L_1 C_1}} \tag{143}$$

At the parallel resonance, f_p, the impedance is close to a maximum and is given by

$$f_p = \frac{1}{2\pi}\sqrt{\frac{C_0 + C_1}{L_1 C_0 C_1}} \tag{144}$$

Apart from these resonance frequencies there is a frequency at which the transducer has a maximum sound output. This is because as the circuit is being driven the internal resistance of the generator cannot be ignored. This frequency is given by

$$f_{\max} = f_s + \frac{f_p - f_s}{1 + 1/Q^2} \tag{145}$$

where

$$Q = \omega_s C_0 R_i \tag{146}$$

In order that the maximum amount of acoustic power is radiated from a transducer for a given voltage it is imperative that the transducer be driven at its resonance with a high mechanical quality (Q) factor. The overall electro-acoustic efficiency factor is given by (MorganElectroCeramics, 2009)

$$\eta \approx 1 - \underbrace{\frac{1}{1 + k_{eff}^2 Q_E Q_L}}_{\substack{\text{dielectric} \\ \text{losses}}} - \underbrace{\frac{1}{1 + \frac{Qm}{Q_L}}}_{\substack{\text{mechanical} \\ \text{losses}}} \tag{147}$$

where k_{eff} is the effective electromechanical coupling factor, Q_m is the mechanical quality factor, Q_E is the electrical quality factor and Q_L is the quality factor due to the acoustic load. k_{eff} is not easily calculated from the material parameters but can be approximated from the impedance vs. frequency curve (MorganElectroCeramics, 2009)

$$k_{eff} = \frac{f_n^2 - f_m^2}{f_n^2} \tag{148}$$

where f_n is the frequency at which the impedance is a maximum and f_m is the frequency at which the impedance is a maximum.

Q factors give us an idea of the damping in the oscillating system and are the ratio of the stored energy per cycle to the energy lost per cycle (Kritz, 1961).

$$Q = 2\pi \times \frac{\text{energy stored per cycle}}{\text{energy lost per cycle}}$$
$$Q = \frac{f_0}{\Delta f} \tag{149}$$

where f_0 is the frequency of the peak of the resonance and Δf is the difference between the frequencies of the points either side of the maximum where the value measured, e.g. Z, reaches, $Z_{max} / \sqrt{2}$.

There are several Q factors to be taken into account when discussing the electro-acoustic efficiency of a transducer. The mechanical Q factor can be calculated by the following equation

$$Q_m = \frac{\omega_r L_1}{R_1} \tag{150}$$

The electrical quality factor ,Q_E, may be calculated by

$$Q_E = \frac{1}{\tan \delta} \tag{151}$$

where tanδ is the tangent of the loss angle δ which is the angle between the parallel resistance and reactance; the phase angle. The power lost in transducers as heat can then be approximated by

$$P \approx \tan \delta (V_{p-p} C_0 f) \tag{152}$$

The quality factor for a single quartz crystal loaded at both ends with air is given by (Kritz, 1961)

$$Q_L = \frac{\pi}{4}\left(\frac{z_{quartz}}{z_{air}}\right) \tag{153}$$

where the z values are the respective characteristic acoustic impedances. At resonance the loss angle should be zero and thus the electrical quality factor should be infinite meaning that there should be no dielectric losses. It can then be seen from equation (147) that the losses would be purely mechanical hence to maximise the efficiency we can see that the mechanical quality factor must be maximised and the quality factor across the load must be minimised. Although these methods may be used to determine the conditions under which the electro-acoustic efficiency is the greatest these are not necessarily the point at which the transducer emits the highest sound output as will be seen later in the chapter.

The quality factor of the series and parallel resonances can be found using equation (149) and Figure 4-8 where the Y, the admittance of the transducer, is the reciprocal of the impedance. These represent the quality factors at constant electric field and constant dielectric displacement respectively.

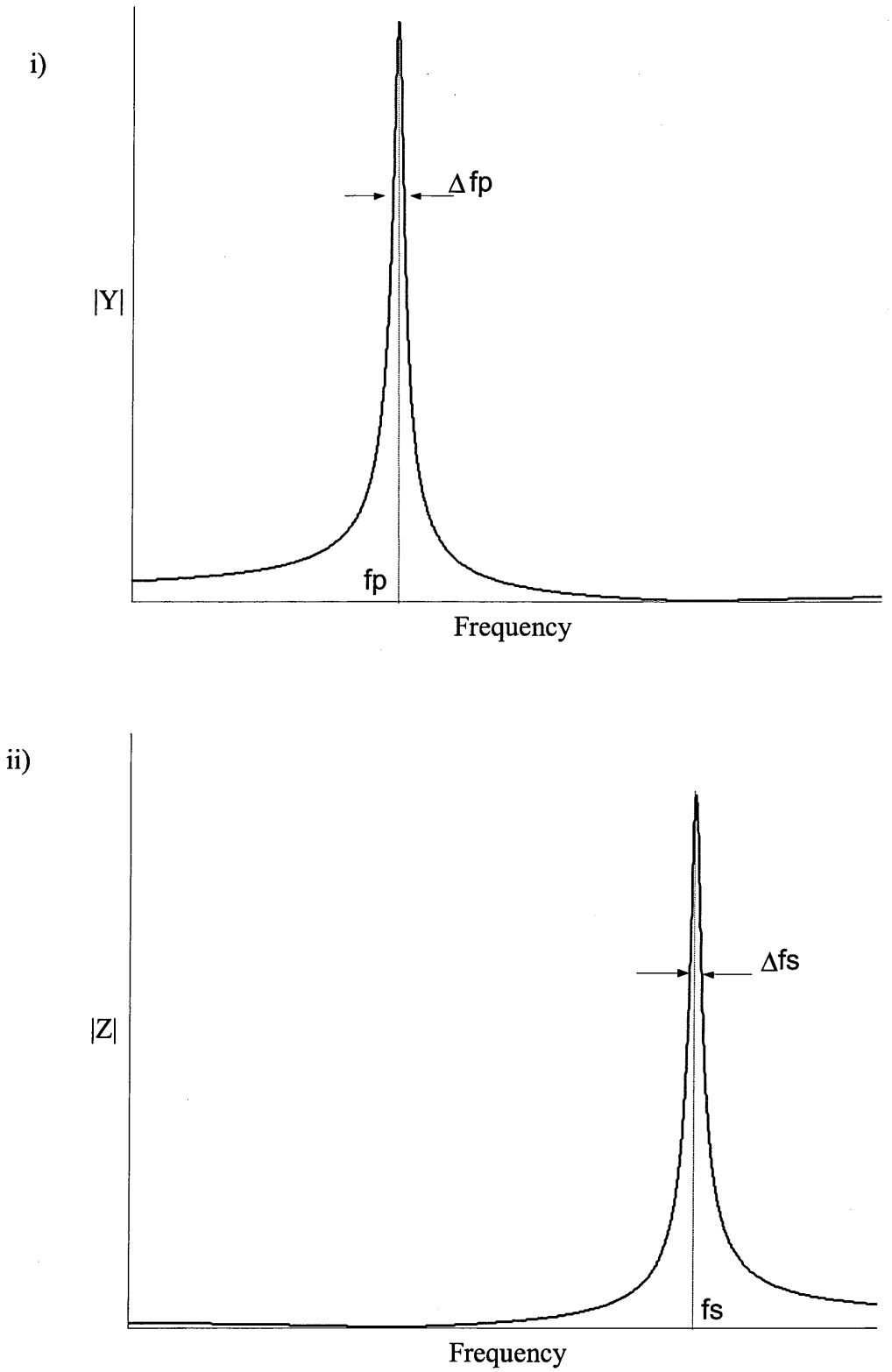

Figure 4-8: Diagrams of i) the admittance and ii) the impedance of a piezoelectric transducer

4.2.4 Piezoelectric Sandwich (Langevin) Transducers

Most ultrasound applications require sound frequencies in the range 18-45 kHz, to achieve the highest electro-acoustic efficiency a transducer should be designed whose mechanical and electrical resonant frequency equalled that of the desired frequency. Since the velocity of sound in the ceramics is about 3200 m/s a single crystal half wavelength transducer would need to be about 9 cm long. Single ceramic crystals of these dimensions are difficult to manufacture and would be inefficient due to the low mechanical Q factor of the crystal. In a transducer the material undergoes maximum stress at the centre with the two end portions acting largely as inert masses they can therefore be replaced by metal parts. Metals also have a higher mechanical Q factor than ceramics and so energy savings can be made.

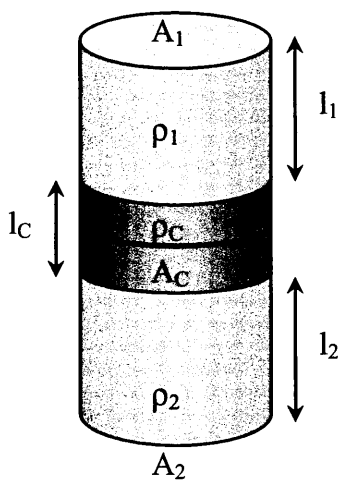

Figure 4-9: A Sandwich (Langevin) half wavelength transducer.

Modelling the transducer as a transmission line the optimum material properties can be deduced. For a transducer to resonate at an angular frequency, ω, the parameters of the slices must adhere to the following equation as detailed in the Morgan Electro

Ceramics technical publication 235 entitled "The design of piezoelectric sandwich transducers" (MorganElectroCeramics)

$$\frac{\omega l_c}{v_c} + \tan^{-1}\frac{A_1\rho_1 v_1}{A_c\rho_c v_c}\tan\frac{\omega l_1}{v_1} + \tan^{-1}\frac{A_2\rho_2 v_2}{A_c\rho_c v_c}\tan\frac{\omega l_2}{v_2} = \pi \quad (154)$$

where l are the lengths of the sections, A are the areas, ρ are the densities and v are the speeds of sound as depicted in Figure 4-9. If we start with a single crystal of ceramic and try to replace each end with a block made of the same metal, the length of the metal sections, l_m, is be shown to be (MorganElectroCeramics, 2012)

$$l_m = l_c\frac{A_m Y_m}{A_c Y_c} \quad (155)$$

where Y are the respective Young's modulii. An improvement to the basic design can be made by using different materials for each end piece (Figure 4-10). The gains of each portion relative to a transducer with both ends made of the same material may then be calculated (MorganElectroCeramics, 2012)

$$G_i = q_i^2 - \left(q_i^2 - 1\right)\sin^2\frac{\omega l_c}{v_c} \quad (156)$$

where G is known as the coefficient of gain and

$$q_i = \frac{\rho_c v_c A_c}{\rho_i v_i A_i} \quad (157)$$

Assuming that there is a load on both faces the maximum intensities allowable at each end are then

$$I_{\max i} = \frac{1}{2}G_i\left(\frac{T_{\max c}}{\rho_c v_c}\right)^2\rho_L v_L \quad (158)$$

where $T_{max\,c}$ is the maximum permissible stress amplitude in the ceramic. In order that damage to the ceramic is avoided $T_{max\,c}$ is recommended not to exceed 4×10^6 Pa. In many high intensity transducers this value can be increased by mechanically pre-stressing the ceramic, by means of a bolt, as the ceramics have a higher strength in compression rather than tension. This is usually a stress of around 20×10^6 Pa.

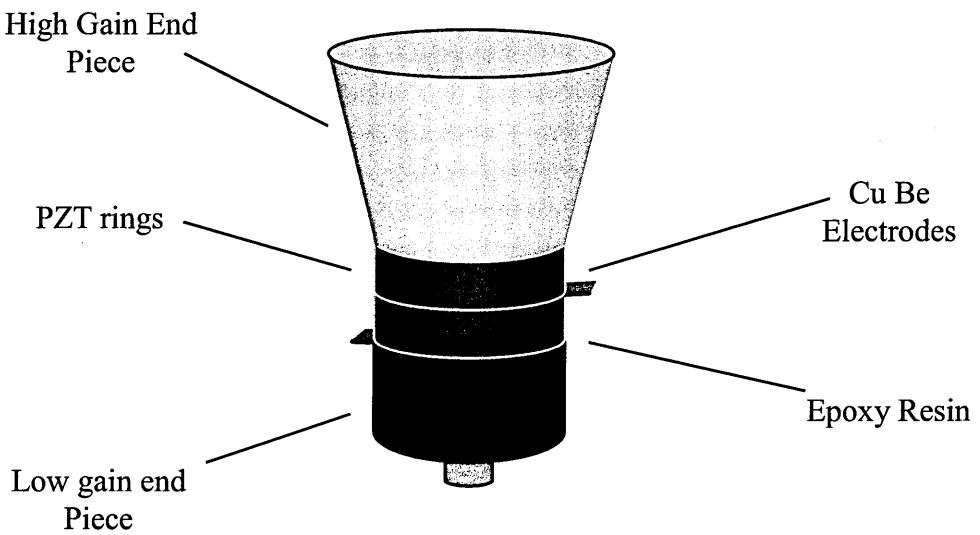

Figure 4-10: Sandwich transducer with different end sections as used for experiments in this thesis.

The transducers are bonded together with epoxy resin which can be a crucial part of the design a thick bond would cause acoustic losses but a bond that is too thin would fracture too easily. The thickness of the bond can be regulated using a wire mesh of known thickness in the bond. The copper-beryllium alloy electrodes are glued between the PZT rings a mesh is also used in this bond to allow electrical conduction between the faces of the PZT rings and the electrodes.

4.2.5 Drive circuits for transducers

The electrical resonance is often tuned to match the mechanical resonance with a variable inductor placed in series or in parallel (Figure 4-11). This creates two coupled resonant LC circuits; the mechanical circuit (L_1 and C_1) and an electrical circuit (L_S or L_P, and C_0) the frequency response of which resembles a band-pass filter (Figure 4-12). The parallel inductance tunes to the series resonance creating an impedance minimum at f_S that is real, the series inductor tunes to the parallel resonance creating an impedance maximum at f_P that is real.

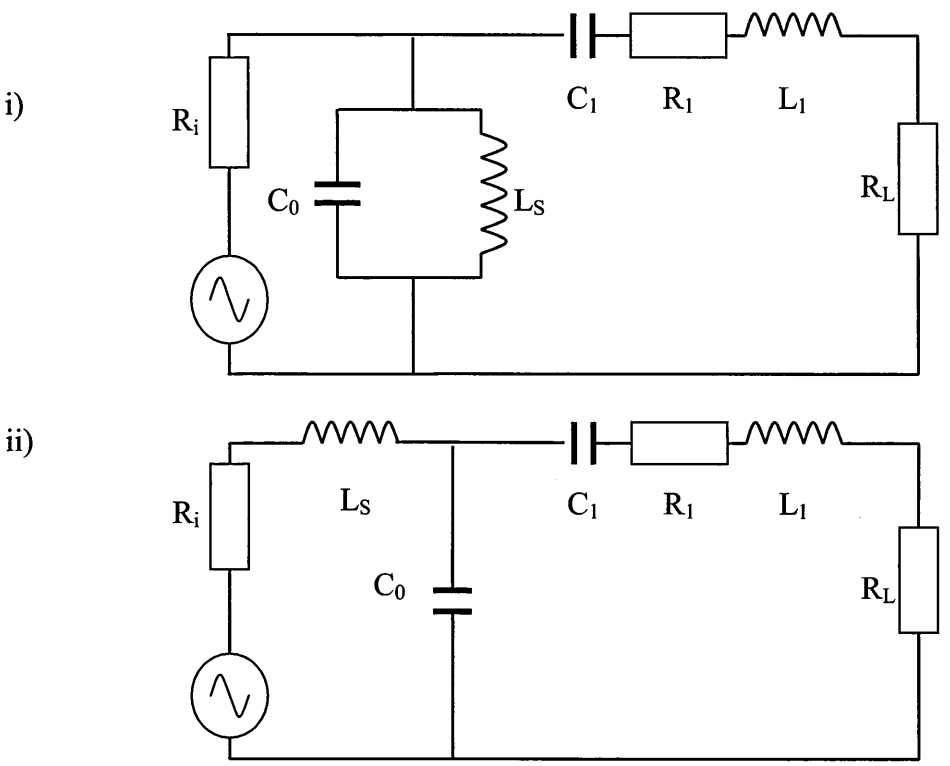

Figure 4-11: Equivalent circuits for i) parallel and ii) series tuned transducers

The values for the series and parallel inductances required to tune to the resonant frequencies are given by the equations

$$L_{par} = \frac{1}{\omega_S^2 C_0} \tag{159}$$

$$L_{ser} = \frac{1}{\omega_P^2 C_0} \tag{160}$$

where $\omega_S = 2\pi f_S$ and $\omega_S = 2\pi f_S$. The choice of whether to use a series or parallel inductor can be made using the respective electromechanical transfer co-efficients (Domarkas and Kazys, 1975). For a transducer with a series inductor this can be taken to be

$$k_s = \frac{z_L / R_i}{1 + R/R_i} \tag{161}$$

where z_L is the characteristic acoustic impedance of the load. For a transducer and parallel inductor the equivalent is

$$k_p = \frac{1}{1 + R \cdot R_i / z_L^2} \tag{162}$$

we can see that

$$\begin{aligned} k_S &\succ k_P \text{ if } z \succ R_i \\ k_P &\succ k_S \text{ if } z \prec R_i \end{aligned} \tag{163}$$

The impedance curves for the tuned transducers are shown in Figure 4-12

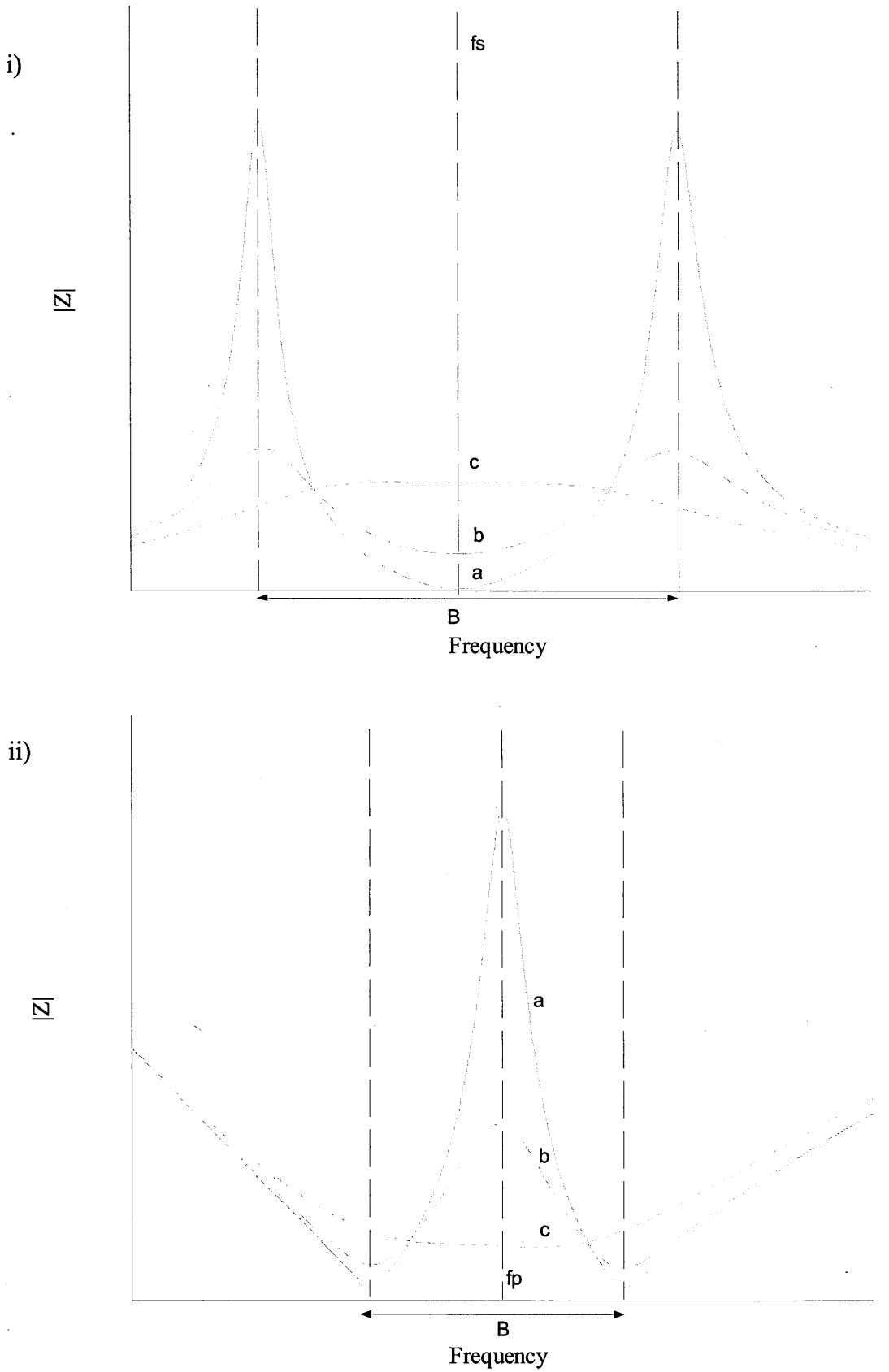

Figure 4-12: Impedance curves for i) parallel and ii) series tuned transducers. a, b and c denote an unloaded oscillator, a medium loaded oscillator and a high loaded oscillator respectively.

4.2.6 Ultrasonic Transducers used in air

The acoustic impedance of the transducer is much greater than that of air and as such a very small proportion of the acoustic energy is transmitted. A matching layer that couples the front end of the transducer to the medium being driven can be used which can greatly increases the amount of energy transferred to the medium driven. One method is to place a matching layer of intermediate acoustic impedance with a quarter wavelength thickness on the front of the transducer to increase transmission. The ideal acoustic impedance for a matching layer should be the geometric mean of the acoustic impedances of the layers to be matched (Alvarez-Arenas, 2004)

$$z_g = \sqrt{z_i z_L} \tag{164}$$

however Nichihira (Nishihira and Imano, 2004) found that the optimum matching layer impedance when the matching layer was directly coupled to the transducer at resonance was given by

$$z_m = 0.7 z_g \tag{165}$$

Plastics have the most suitable acoustic impedances but they have high mechanical losses meaning that the attenuation of the sound is quite significant in the matching layer. Manthay (Manthey 1992) discusses the improvements that stacked quarter-wave matching plates of stepped acoustic impedance might bring. Another method to improve the transmission of sound energy to the load is to taper the front plate of the transducer so that the area of the load that is being driven is larger meaning that the total acoustic impedance of the load (Aρc) is increased thus providing a better impedance match. At the fundamental resonance of the transducer the flexure of the end plates can either be in phase or antiphase with the extension of the ceramic meaning that neither mode has as much energy and as such less energy is transferred

to the load, the extent of the tapering is limited by flexure of the edges of the front plate

The optimum acoustic design for a transducer can be modelled using a transmission matrix, these theories treat the transducer as a series of layers of different materials with different thicknesses and derive the sound field created from the transmission characteristics of each of the layers and the reflection characteristics of each of the boundaries. Transducers were first treated this way by Rayleigh (Rayleigh, 1878) but in this thesis we explain this method in the simplified terms used by Hill (Hill, 1980).

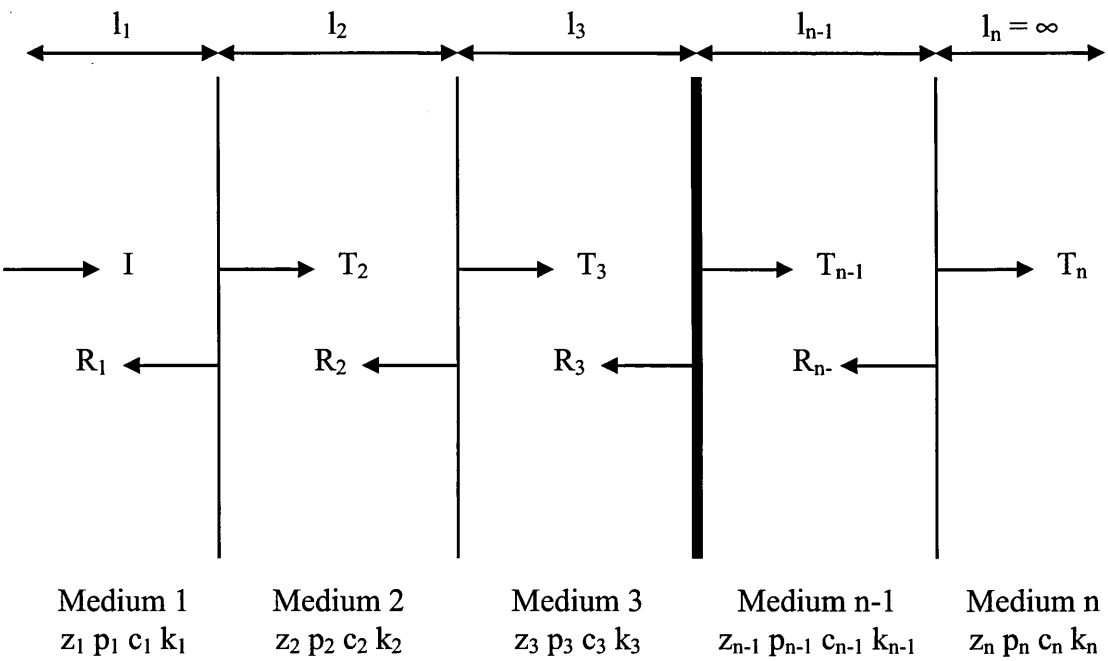

Figure 4-13: The acoustic transmission through a many layered transducer.

Assuming the waves travel at normal incidence to the surfaces of the layers. A plane unattenuated sound wave travels from left to right in the x-direction through n different layers with specific acoustic impedance, z . The sound wave in each layer has a characteristic sound pressure p, speed of sound c and wave number k. The layers are assumed to be infinite in the y and z directions. The wave travels through the

layers and emerges into medium n which is assumed to be infinite and therefore reflectionless. For simplicity only one transmission and reflection is considered at each boundary for which T and R are the respective coefficients. The electrical effects of the piezoelectric layer have been ignored since (Nishihira and Imano, 2004) showed that if there is such a large electrical impedance mismatch between the amplifier and transducer there is little energy lost to the dielectric effects of the transducer.

The values of the pressure in each layer are shown in Table 4-3 where A and B are the amplitudes of the transmitted and reflected wave respectively, these can be real or complex due to phase changes at the boundary.

Table 4-3: Pressure of the transmitted and reflected waves in each of the layers of the transducer.

Variable	Medium 1	Intermediate Media	Medium n
$p_{incident}$	$p_{I1} = A_1 e^{i(\omega t - k_1 x_1)}$	$p_{Tx} = A_x e^{i(\omega t - k_x x_x)}$	$p_{Tn} = A_n e^{i(\omega t - k_n x_n)}$
$p_{reflected}$	$p_{R1} = B_1 e^{i(\omega t + k_1 x_1)}$	$p_{Rx} = B_x e^{i(\omega t + k_x x_x)}$	n/a

The total pressure in each layer will be given by adding both the transmitted and reflected components, for example for layer 2 the pressure will be

$$P_2 = A_2 e^{i(\omega t - k_2 x_2)} + B_2 e^{i(\omega t + k_2 x_2)} \tag{166}$$

The velocities of the particles in the medium are then

$$v_2 = \frac{A_2}{z_2} e^{i(\omega t - k_2 x_2)} - \frac{B_2}{z_2} e^{i(\omega t + k_2 x_2)} \tag{167}$$

These can be represented in matrix form as

$$\begin{pmatrix} P_1 \\ v_1 \end{pmatrix} = \begin{pmatrix} e^{-ik_2x_2} & e^{ik_2x_2} \\ \frac{1}{z_2}e^{-ik_2x_2} & -\frac{1}{z_2}e^{ik_2x_2} \end{pmatrix} \begin{pmatrix} A_2 \\ B_2 \end{pmatrix} e^{i\omega t} \tag{168}$$

If we now state that x = 0 at the boundary between medium 1 and 2 the pressure and particle velocity at this boundary are represented by the matrix equation

$$\begin{pmatrix} P_{12} \\ v_{12} \end{pmatrix} = \begin{pmatrix} 1 & 1 \\ \frac{1}{z_2} & -\frac{1}{z_2} \end{pmatrix} \begin{pmatrix} A_2 \\ B_2 \end{pmatrix} e^{i\omega t} \tag{169}$$

At the boundary between media 2 and 3 x = l_2 and the equations become

$$\begin{pmatrix} P_{23} \\ v_{23} \end{pmatrix} = \begin{pmatrix} e^{-ik_2l_2} & e^{ik_2l_2} \\ \frac{1}{z_2}e^{-ik_2l_2} & -\frac{1}{z_2}e^{ik_2l_2} \end{pmatrix} \begin{pmatrix} A_2 \\ B_2 \end{pmatrix} e^{i\omega t} \tag{170}$$

We can now form an equation of the pressure at the 2-3 boundary in terms of the pressure at the 1-2 boundary

$$\begin{pmatrix} P_{12} \\ v_{12} \end{pmatrix} = \begin{pmatrix} 1 & 1 \\ \frac{1}{z_2} & -\frac{1}{z_2} \end{pmatrix} \begin{pmatrix} e^{-ik_2l_2} & e^{ik_2l_2} \\ \frac{1}{z_2}e^{-ik_2l_2} & -\frac{1}{z_2}e^{ik_2l_2} \end{pmatrix}^{-1} \begin{pmatrix} P_{23} \\ v_{23} \end{pmatrix} \tag{171}$$

Evaluation of the inverse and subsequent multiplication yields

$$\begin{pmatrix} P_{12} \\ v_{12} \end{pmatrix} = \begin{pmatrix} \cos k_2l_2 & iz_2 \sin k_2l_2 \\ \frac{i\sin k_2l_2}{z_2} & \cos k_2l_2 \end{pmatrix} \begin{pmatrix} P_{23} \\ v_{23} \end{pmatrix} \tag{172}$$

If we write this equation in a simplified form

$$F_{12} = C_2F_{23} \tag{173}$$

The factor C contains variables that are only dependent on the properties of layer 2 and thus the same equation can be used to describe the changes in each layer

$$F_{23} = C_3F_{34} \tag{174}$$

Substituting equation (174) into equation (173) yields

$$F_{12} = C_2 C_3 F_{34} \tag{175}$$

For a transducer with n layers the transmitted pressure will be $F_{(n-1)n}$ and will be represented by

$$F_{12} = \left(\prod_{i=12,(n-1)n} C_i \right) F_{(n-1)n} \tag{176}$$

Using the solutions of these equations useful parameters of the transducer can be calculated. The sound pressure transmission co-efficient is given by the equation

$$\alpha_{pr} = \left| \frac{A_n}{A_1} \right| \tag{177}$$

Thus the sound power transmission coefficient is given by

$$\alpha_{pow} = \left| \frac{A_n}{A_1} \right|^2 \frac{z_1}{z_n} \tag{178}$$

Solutions for these factors are given for 3, 4 and 5 layered transducers in the paper by Hill (1980).

4.3 Ultrasonic levitation of Aerosols

In this thesis we are interested in using the energy in a standing ultrasound field to trap aerosol particles for spectroscopic analysis. In this section we discuss the methods by which this can be done.

4.3.1 Levitation

Acoustic levitation is achieved by using a sound field to counteract the force of gravity, the sound field being directed along the axis of gravity. Acoustic levitation is most readily achieved in a resonant cavity as the forces acting on the particles are stronger. Levitation can be "single axis" in which there is one resonator and a

reflector or "triple axis" in which there is a reflector and a resonator on each of the three perpendicular axes. Acoustic levitation has found many uses in containerless material processing and non-contact measurement of liquid properties (Gao et al., 1999, Hawkes et al., 1998, Xie and Wei, 2001) It has also found use as a method by which to agglomerate aerosols for ease of removal from power station exhausts (Hoffmann, 2000, Riera-Franco de Sarabia et al., 2003, Temkin, 1994). Such are the forces in these fields that it has been possible to levitate solid materials as dense as iridium and liquid materials as dense as mercury (Xie et al., 2002). In this thesis a single axis ultrasonic levitator has been used to levitate particulate aerosols in order that infra red spectra of aerosols may be recorded.

When a particle is suspended in a sound field the fluid exerts hydrodynamical forces upon it. In a standing wave, within in a linear approximation, the force is proportional to the velocity and so, on average; do not lead to a particle displacement. The velocity of the oscillations in the medium that the standing ultrasound wave is travelling through is given by

$$u_g = u_{g0} \sin(kx) \cos(\omega t) \tag{179}$$

where u_g is the velocity of the gas, u_{g0} is the amplitude of the sound oscillations, k is the wavenumber of the sound, x is the distance measured in the direction of propagation, ω is the angular frequency of the sound and t is time. Nodes of the standing waves are found at x = 0, $\lambda/2$, λ etc and the antinodes are found at x = $\lambda/4$, $3\lambda/4$, $5\lambda/4$. In the approximation of Stokes' law and including the drag force the equation of motion of the particle is

$$m_p \dot{u}_p = 6\pi\eta r_p \left(u_g - u_p\right) \tag{180}$$

where m_p is the mass of the particle, u_p is the velocity of the particle, η is the kinematic viscosity of the gas and r_p is the radius of the particle. The constants can be collected together to give

$$\tau = \frac{m_p}{6\pi\eta r_p} \tag{181}$$

which is a quantity known as the dynamic relaxation time. Equation (180) then becomes

$$\tau \dot{u}_p + u_p = u_g \tag{182}$$

If higher order components are considered directional so called "drift forces" can result in levitation of particles. There are different drift forces that arise from different solutions of hydrodynamic equations all of which act on different sizes of particles with different strengths. There are many papers published that exemplify different drift forces under different experimental conditions (Czyz, 1990, Doinikov, 1994, Gor'kov, 1962, King, 1934), the paper written by Czyz et al. considers drift forces that are most applicable to the work considered in this thesis and so the discussion in this chapter will use the nomenclature and equations from this paper.

The first drift force to be considered is the radiation pressure drift force, this is a first order effect caused by the transfer of momentum from the acoustic wave to the particle

$$F_{rad} = \frac{8}{3}\pi k r_p^3 \mu_g^2 \bar{E} \sin 2kx \tag{183}$$

this is valid for particles that have a far greater density than the gas where μ_g is known as the "flow around" co-efficient and $\bar{E}$ is the mean energy density of the wave. The flow around coefficient is

$$\mu_g = \frac{\omega t}{\sqrt{\left(1+\omega^2\tau^2\right)}} \tag{184}$$

A second drift force to be considered is the asymmetric drift force which arises from the asymmetric motion of the medium in a standing wave.

$$F_{asym} = -\frac{1}{2} m_p \rho_g^{-1} k \mu_p^2 \bar{E} \sin 2kx \tag{185}$$

where μ_p is the particle entrainment co-efficient and is the ratio of the amplitude of the particles oscillation to the sound amplitude.

$$\mu_p = \frac{1}{\sqrt{\left(1+\omega^2\tau^2\right)}} \tag{186}$$

A third drift force of importance is the viscosity drift force arising from temperature dependence of the viscosity

$$F_{vis} = 3\pi(\chi - 3) r_p \mu_g^2 \eta \left(\rho_g c\right)^{-1} \bar{E} \sin 2kx \tag{187}$$

where χ is the ratio of the specific heats of the gas, η is the kinematic viscosity of the gas and c is the wave velocity.

It was observed by Csyz that all of these forces have the same dependence on position, x, and so their equations of motion will all be of the form

$$m_p \ddot{x} + 6\pi\eta r_p \dot{x} = F_{drift} \sin 2kx \tag{188}$$

where F_{drift} is the is now the values of the drift forces at sin2kx = 1. The potential of the force is given by

$$\phi_{drift} = (2k)^{-1} F_{drift} \cos\left(2kx\right) \tag{189}$$

In the sound field the particles will drift to the minimum potential. Forces that have a value greater than zero i.e. F_{vis} and F_{rad} will have their minimum potentials at cos(2kx) = -1 i.e. at sin(kx) = ±1 so their equilibrium position will be at the antinodes of the sound field. Drift forces such as the asymmetry drift force that are less than zero will have their minimum potential at cos(2kx) = 1 i.e. at sin(kx) = 0 so their equilibrium position will be at the nodes of the sound field.

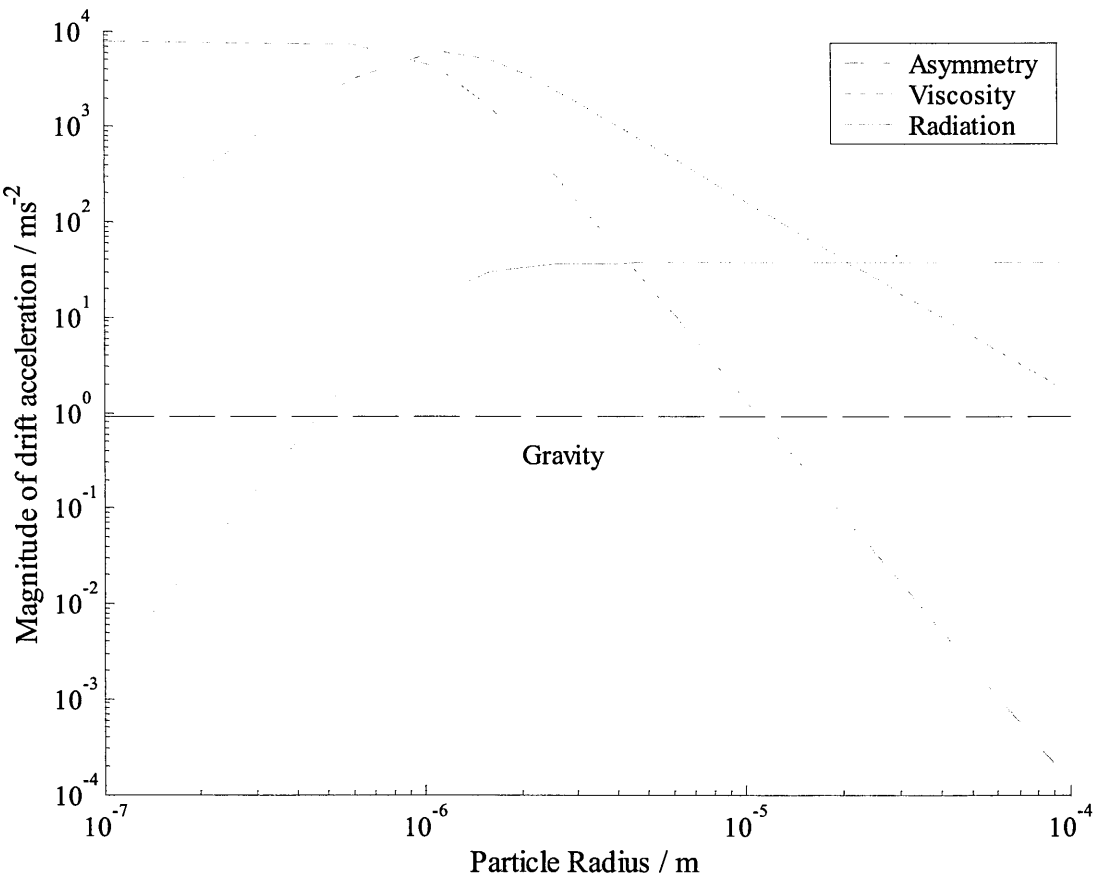

Figure 4-14: Magnitudes of the accelerations of the different drift forces on a particle with density of 1000 kgm^3 in air at 20 °C and 1 atm pressure and a mean energy density of 100 Jm^{-1} and a frequency of 10 KHz, gravity is included as a comparison.

Figure 4-14 shows the magnitudes of the accelerations of the different drift forces which is calculated by dividing equation (188) by the mass of the particle, m_p. The overall position and strength of trapping depends on the cumulative actions of all of the forces. e.g. for large particles (diameter >0.1 mm) the radiation force is much

greater than the viscous drift force and the drift force arising from asymmetries in the field and thus they are trapped at the antinodes of the field whereas the opposite is true of small particles (diameter <0.1 mm) which coagulate in the nodes. To trap particles of a certain size the conditions must be engineered to maximise the drift forces. For a drift force to levitate a particle the force must be greater than that of gravity.

4.3.2 Agglomeration of aerosols

The agglomeration of aerosols occurs when particles in a sound field collide and then stick together to form a single particle. This is therefore dependent on the "sticking coefficients" of the particles as well as the rate at which they collide. There are two categories of agglomeration mechanisms 'orthokinetic' and 'hydrodynamic' (Hoffmann, 2000). Orthokinetic agglomeration is due to particles moving with different velocities through a medium therefore any phenomenon that induces differential motions can cause agglomeration. Sound waves and shock waves can both result in such orthokinetic motions (Alexeev and Gutfinger, 2003). One way for these motions to be induced is for particles of different sizes to be accelerated differently by a sound field however agglomeration is still seen in monodispersed particles. This alerted scientists to another category of agglomeration mechanisms: hydrodynamic. These indirect mechanisms generate particle interactions through viscous interactions between the particle and the surrounding fluid.

The dominant mechanism for agglomeration in aerosols is thought to be the acoustic wake effect (AWE) (Dong et al., 2006), this effect is due to asymmetries in the viscosity due to the flow field around the particle. When a particle travels in the acoustic wake of another it experiences a reduction in drag and therefore the relative

velocity between the particles increases. These hydrodynamic effects are due to the flow around the particles and so are important for low values of acoustic entrainment. The particles also scatter the sound field which in turn interacts with the incident wave resulting in a mutual radiation pressure (MRP). This effect shows a complex dependence on the parameters and is repulsive along the axis of sound but attractive along the axis at right angles to the sound. Hoffman (Hoffmann, 2000) observed particles that came to a certain spacing apart but did not agglomerate, this was named a "pseudo agglomerate", Hoffman hypothesised that these were held in place by a force balance between the MRP and the AWE. Other hydrodynamic affects are thought to contribute to this agglomeration such as turbulence, micro-streaming around larger particle and drift forces resulting from non-linear behaviour. These effects have been studied but are far from being well understood (Temkin, 1994) but what is agreed is that high power sound fields cause greater agglomeration.

Sound fields that maximise the orthokinetic processes, such as progressive saw tooth waves, cause the most pronounced agglomeration effect. In this thesis levitation and increased concentration of the aerosols are desirable but proper agglomeration is an unwanted affect as it will alter the size distribution of our sample over time. There are many different models of widely varying complexity to explain the observed coalescence (Czyz, 1990, Temkin, 1994) these are usually aimed at maximising the agglomeration, in fact in his paper Temkin introduced an optimum frequency for agglomeration of aerosols with narrow size distributuions from orthokinetic processes

$$\omega_{opt} = \frac{1}{\tau_{peak}} \tag{190}$$

where τ_{peak} is the relaxation time of a particle with the maximum diameter. Temkin suggested (Temkin, 1994) that if the frequency of the wave was small enough that the largest particle relaxation time was much smaller than the period of the standing wave then all of the particles would move with the gas and no agglomeration would be seen. The hydrodynamic effects are more difficult to quantify and in his work Gonzales et al. (Gonzalez et al., 2003) concluded that there existed no optimum frequency for agglomeration caused by these effects. In this thesis agglomeration needs to be minimised as the aerosol size distribution should remain constant throughout the measurement, to do this we can use the entrainment coefficient (186). The entrainment coefficient is the ratio of the amplitudes of the acoustic wave oscillation to the particle oscillation. If the particles are completely entrained in the sound field i.e. E = 1 then the particles move completely with the gas, if E = 0 then the particles are unperturbed by the sound field. To maximise the orthokinetic effects and thus maximise agglomeration by these procedures it is estimated that E = 0.5 at the mean of the distribution (Scott, 1975). To minimise the orthokinetic effects whilst still trapping the particles in the field the entrainment coefficient should be as close to 1 as possible for as many particles in the distribution as possible. It is estimated that particles with entrainment coefficients greater than 0.95 and less than 0.05 experience little differential motion between them. Figure 4-15 shows the values of the entrainment coefficient for particles of different radii in sound fields with different frequencies.

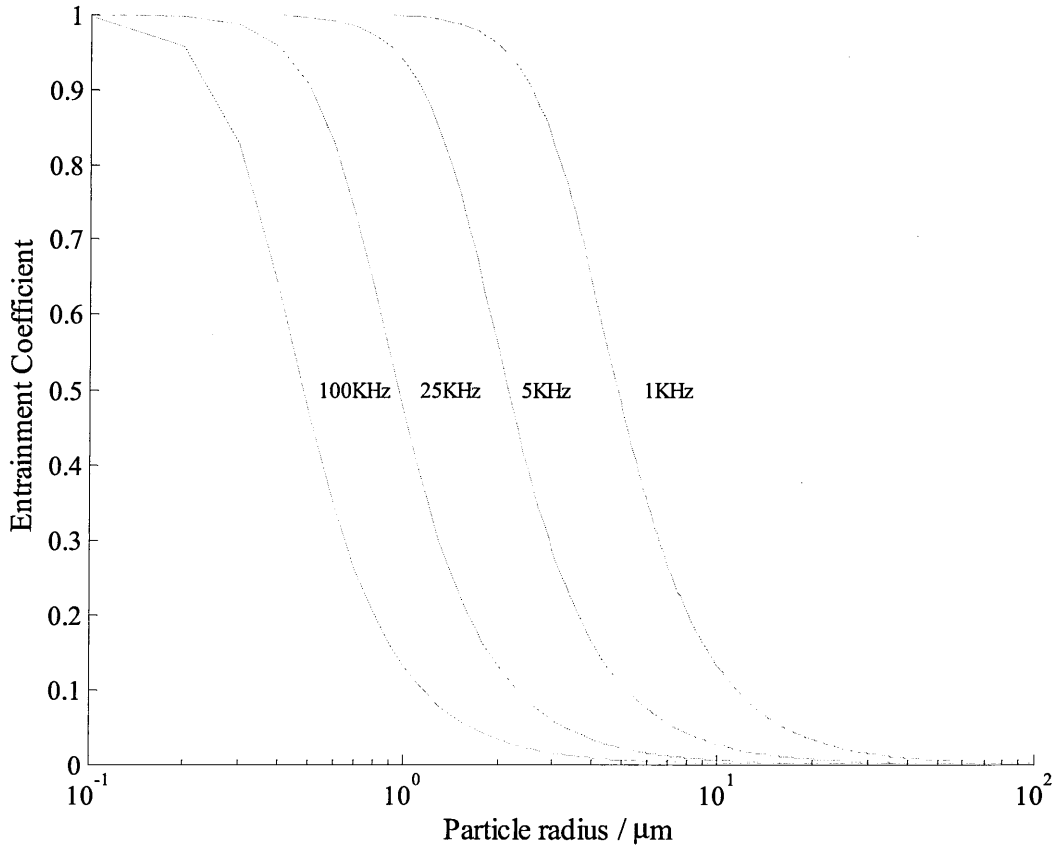

Figure 4-15: Entrainment coefficient as a function of particle radius for different frequencies.

It was noticed by de Sarabia et al. (Riera-Franco de Sarabia et al., 2003) that humidity increases the agglomeration rate of micrometer sized particles in a 21 KHz sound field by over 50 %. The agglomeration effects on a particle distribution can also be minimised by having a narrow range of particle sizes as they would have smaller orthokinetic effects.

4.4 Conclusion

In order to understand how to levitate the aerosol samples we wish to study in this project a wide variety of theories must be encompassed. The ultrasonic field generated is a standing ultrasound field generated by a sandwich (Langevin) piezoelectric transducer. Piezoelectric crystals expand and contract along a poled axis as an electric field is applied across them such that they have a natural resonant frequency which is

determined by their electrical and mechanical properties. If driven at this resonant frequency a high intensity ultrasound field can be produced. However, piezoelectric transducers couple inefficiently to air due to the large mismatch in their acoustic impedances, careful design of the transducers and intermediate matching layers can improve the efficiency.

Aerosols interact with sound fields in very complex ways, in order to levitate the aerosols the forces acting on the aerosol due to the sound field must be greater than gravity, different solutions of the wave equations result in forces with different origins that act on different sizes of particles with different strengths. In order to maximise efficiency we must ensure that the drift forces are tuned to match our aerosol size distribution.

Sound fields also cause agglomeration of aerosols, this is an undesirable factor in the present work as it would change our size distribution. These effects can be minimised by maximising the entrainment co-efficient.

Using this information we designed an ultrasonic trap that was optimised to capture and retain aerosol particles of the size distribution and density that is encountered in the atmosphere, this is discussed in Chapter 6:.

Chapter 5: Gas phase spectroscopy Results for CF_3I.

"None of us has gotten where we are solely by pulling ourselves up from our own bootstraps. We got here because somebody bent down and helped us".

Thurgood Marshall

In order to calculate the radiative forcing of a gas its absorbance at each wavelength must be evaluated. The absorbance of the sample as a function of wavelength was calculated from its transmission using the Beer-Lambert law as described in Chapter 2. An FT-IR spectrometer has been used to obtain infra red spectroscopy of the gas CF_3I and the spectra obtained have been used to calculate values of the radiative forcing. These radiative forcing values are then used to calculate the global warming potential of CF_3I.

5.1 Configuration of the Spectrometer

The experiments were performed in the Molecular Spectroscopy Facility (MSF) at Rutherford Appleton Laboratory (RAL) and this research was published (Webb et al., 2005). The sample cell used was a stainless steel, double walled, cylindrical cell with a 5.0985 cm path length between the two KBr windows. It was held under vacuum within the spectrometer. The temperature of the sample cell could be controlled by flowing ethanol through the outer skins of the cell (Smith et al., 1996). The ethanol was cooled as it flowed through a closed loop of stainless steel pipe which was immersed in liquid nitrogen. The temperature of the ethanol bath was measured with a platinum resistance thermometer and the addition of liquid nitrogen was regulated using a PID controller. The temperature in the cell was measured by an array of eight platinum resistance thermometers with a tolerance of ±0.1 K at room temperature and ±0.2 K at 208 K which were continuously logged during measurement. Air was

removed from the cell by a rotary backed diffusion pump and its pressure was monitored using baratron capacitance vacuum gauges (10 and 1000 Torr full scale MKS type 690).

The spectra were measured on a Bruker IFS 120HR Fourier transform infrared (FTIR) spectrometer. This spectrometer has a resolution of up to 0.0015 cm^{-1} and operates over a wide spectral range (far IR to UV) (Newnham et al., 1996). During the work the spectrometer was configured with a broadband silicon carbide globar source operating at approximately 1000 K and a germanium/potassium bromide (Ge/KBr) beamsplitter. Three detectors were used in this work: a broadband mercury-cadmium-teluride (MCT) detector (500-2000 cm^{-1}) to cover the low wavenumber region, a narrow band high sensitivity MCT for the mid range wavenumbers (1300-2500 cm^{-1}) and an Indium-Antimonide (InSb) detector for the high wavenumber range (1800-8400 cm^{-1}). The wideband MCT detector's non linearity at high intensity was minimised using a 1.3 mm aperture and optical filters to select specific the regions of the spectra that were found to contain features of interest, thus minimising the total overall intensity incident on the detector.

During sampling a number of scans were obtained and co-added. Initially sample readings are collected of 100 scans at a low resolution of 0.25 cm^{-1} to identify the location of the spectral peaks. Following this survey it was decided to concentrate on two spectral regions of interest, one at 700-1250 cm^{-1} which required the broadband MCT D316 detector and a suitable optical filter (400-1400 cm^{-1}) and the second at 1975-2300 cm^{-1} which needed the InSb detector and a suitable optical filter (1900-2500 cm^{-1}). Each of these experiments was sampled with 100 scans at a resolution of

0.03 cm^{-1} for several temperatures (299.4 K, 272.9 K, 251.6 K and 208.0 K) and over a range of pressures (0.1-30 mbar) that allowed several non saturated measurements for each peak. Exploratory measurements were made at higher resolution (0.015 cm^{-1}) but this did not resolve any further structure.

5.2 Spectroscopy of CF_3I

In this part of the chapter we report the results of the FT-IR study of the compound CF_3I. The sample gas was obtained from Argo International Ltd and has a purity of 99 %. The sample was decanted into a clean glass round bottomed flask which was connected to the vacuum system. Several freeze-pump-thaw cycles were performed to remove any dissolved gases.

Since the sample gas is known to photolyse in sunlight the room containing the FT-IR spectrometer was left in the dark and the glass containing the gas was covered in blackout cloth. In order to test whether any of the CF_3I was photolysed during the experiment an initial spectrum was taken of a gas sample and then left for approximately one hour. A spectrum was then recorded to look for the presence of even a small amount of C_2F_6, (the expected product of photolysis) which would be shown as a sharp peak at 1250 cm^{-1}. In addition we observed for a reduction in absorption from the CF_3I peaks. Since the data collection time is much shorter than an hour and neither of these effects were noticed it was assumed that there was no photolysis of the sample during the spectral measurement. As a further precaution the sample cell was evacuated after each measurement and fresh samples of CF_3I inserted. A background reading, used in the calculation of the transmission, was taken after every three measurements.

At the start of each day a leak test was performed to measure the amount of air entering the system. During the sampling the change in pressure of the sample was noted as a function of time the leak rate was fairly stable throughout experimentation at a steady rate of 0.36 mbar/hour. An anomalous rate of pressure change would indicate whether the sample was desorbing onto the walls or perhaps degrading to different products.

The survey spectrum of IR absorption at 19.98 mbar and 299 K revealed several absorption bands (Figure 5-1), a summary of which are shown in Table 5-1 along with their assignments from McGee et al. (McGee, 1952). Two regions of interest were chosen for further analysis (700-1250 cm^{-1} and 1975-2300 cm^{-1}) since they included the strongest absorption peaks. In the first spectral region (700-1250 cm^{-1}) (Figure 5-4) the main spectral bands in the spectra have their most intense bands at 743.2, 1028.0, 1075.1, 1154.2 and 1187.5 cm^{-1}. The bands themselves are complex structures consisting of more than one band. The 743.2 cm^{-1} band is comprised of three sharp bands (743.2, 742.5 and 741.7 cm^{-1}) and two broad side lobes with bands at 737.3 cm^{-1} and 748.2 cm^{-1}. The 1028.0 cm^{-1} band has one other sharp band at 1024.9cm^{-1} and two side lobes centred at 1021.8cm^{-1} and 1032.3cm^{-1} however there are signs of additional structure in these lobes. The 1075.1 cm^{-1} band has two central sharp bands at 1075.1 cm^{-1} and 1074.1 cm^{-1} and again two lobes centred at 1068 cm^{-1} and 1079 cm^{-1} wavenumbers. In this structure there is also a curious spike in one of the lobes at 1080 cm^{-1} wavenumbers. The band at 1154.2 cm^{-1} has two other sharp bands at 1153.3 cm^{-1} and 1156.0 cm^{-1} however the side lobes, as seen in all the other bands, are absent in this band. The last band in this region at 1187.5 cm^{-1} is the most complex consisting of four sharp bands at 1187.5 1187.7, 1186.4 and 1185.8 cm^{-1}, the side

lobes of this band, at 1183.5 cm^{-1} and 1190.8 cm^{-1}, are relatively small and anti-symmetric with the lobe at lower wavenumber being stronger. There seems to be added structure in this lobe with a spike at 1183.8 cm^{-1}.

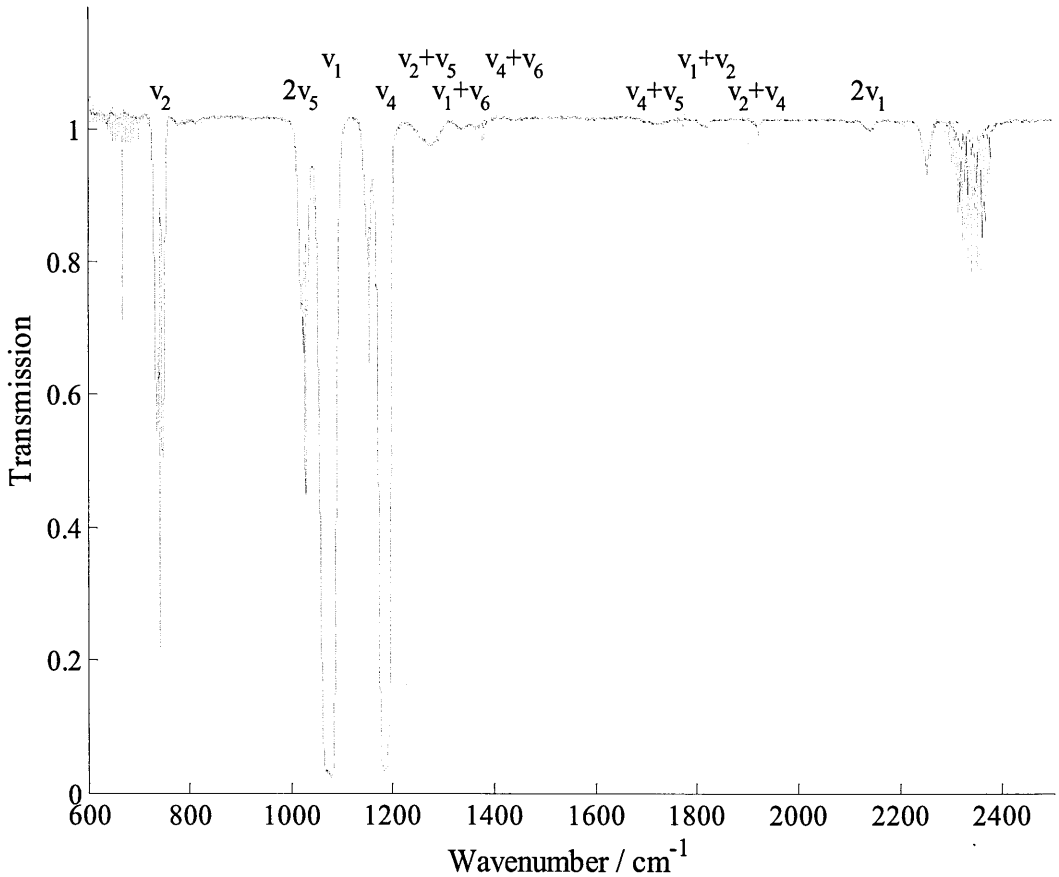

Figure 5-1: A survey spectrum of 19.98 mbar of CF3I at 299 K at 0.25 cm^{-1} resolution the vibrational assignments of the bands have been shown

In the second spectral region three bands are seen centred at 2144.4 cm^{-1}, a very weak band at 2206.0 cm^{-1} and a strong band at 2255.6 cm^{-1} that unfortunately overlapped with some water absorption lines (Figure 5-5). The 2144.4 cm^{-1} band had another sharp band at 2137.7 cm^{-1}. The second very weak band at 2206.1 cm^{-1} had another even weaker band at 2209.2 cm^{-1}. By far the strongest band was that at 2255.64 cm^{-1} which also had a feature at 2260.8 cm^{-1}, there may have been other structures in this band but this was obscured by the water lines that overlap the band.

The peak wavelengths and intensities found in this thesis are in good agreement with the results from the infrared spectrograms of (McGee, 1952) (Table 5-1), although we did not observe the 1271 cm^{-1} band to be "very strong" but rather "weak". Figure 5-4 and Figure 5-5 show typical cross-sections of CF_3I in both spectral regions, these spectra were recorded at (a) 272.9 K and 2mbar for the low wavenumber spectral region and at (b) 272.9 K and 30 mbar for the high wavenumber spectral region. Figure 5-8 shows the three smallest bands on an expanded scale.

Table 5-1: Infrared absorption band assignments for CF_3I from McGee et al. (1952), our corresponding wavelengths are also shown. Assignments shown with an asterix have been added by the authors

Wavenumber / cm^{-1}	Intensity of peak	Tentative Assignment	Symmetry	Wavenumber / cm^{-1} from this study
-	-	-	-	664.1 (CO_2)
747	Very strong	Y_2	A_1	743.2
1030	Very strong	$2\upsilon_5$	$A_1 + E$	1028.0
1080	Very strong	Y_1	A_1	1075.1
-	-	-	-	1154.2
1187	Very strong	Y_4	E	1187.5
1274	Very strong	$\upsilon_2+\upsilon_5$	E	1275.3
1334	Weak	$\upsilon_1+\upsilon_6$	E	1331.1
-	-	-	-	1377.1
1441	Weak	$\upsilon_4+\upsilon_6$	A_1+A_2+E	1448.2
1714	Weak	$\upsilon_4+\upsilon_5$	A_1+A_2+E	1723.2
1814	Weak	$\upsilon_1+\upsilon_2$	A_1	1818.2
1910	Weak	$\upsilon_2+\upsilon_4$	E	1922.1
2132	Very weak	$2\upsilon_1$	A_1	2144.4
-	-	$2\upsilon_1+\upsilon_5$*	-	2206.0
-	-	$2\upsilon_1+2\upsilon_5$*	-	2255.6
-	-	-	-	2276-2380 (H_2O)

The uncertainty on the pressure value is due to both an uncertainty in the accuracy of the baratron gauge, which is quoted as 0.12 % in the manufacturers guide, and due to air leakage into the system whilst CF_3I is inserted and left to reach equilibrium temperature with the cell ($\approx$ 5 mins) with the measured leak rate during this time being approximated to be 3 Pa. The pressure recorded during the measurements for

299.4, 272.9 and 251.6 K changed at the same rate as the measured leak rate (≈ 36 Pa/hour) however the recorded pressures at 208 K only increased by ≈ 18 Pa/hour. This is assumed to be because the CF_3I is desorbing onto the walls at these temperatures and pressures at a rate of roughly 18 Pa/hour giving an additional uncertainty to pressure estimates at 208 K, each measurement took roughly half an hour giving an additional uncertainty of roughly 9 Pa.

5.3 Calculation of the Absorbance and determination of cross sections

The absorbance of the sample as a function of wavelength was calculated using the Beer-Lambert law.

$$Absorbance = \ln\left(I_0(\bar{\upsilon})/I(\bar{\upsilon})\right) = \sigma \times N \times L \qquad (191)$$

where I_0 is the transmitted intensity through an evacuated cell, I is the transmitted intensity through the sample and the cell, σ is the absorption cross section in cm^2 $molecule^{-1}$, N is the number density and L is the path length of the cell in cm. There was a small baseline correction made by averaging the absorbance in a non absorbing region between peaks and then removing this from all data points. A significant amount of channelling was noticed at low temperatures, channelling is seen as a sinusoidal harmonic on the absorbance graphs and is due to multiple reflections from the inner surfaces of the filters. This should cancel out when the ratio of I to I_0 is taken but this was not the case for some of our readings, it is assumed that this is due a change in the thickness of the lens as it adjusts more slowly to the temperature change. If integrated over a whole number of cycles this would cancel out but as this can not be guaranteed by our choice of peak widths a small frequency band corresponding to the frequency of the harmonic was removed using a digital filter.

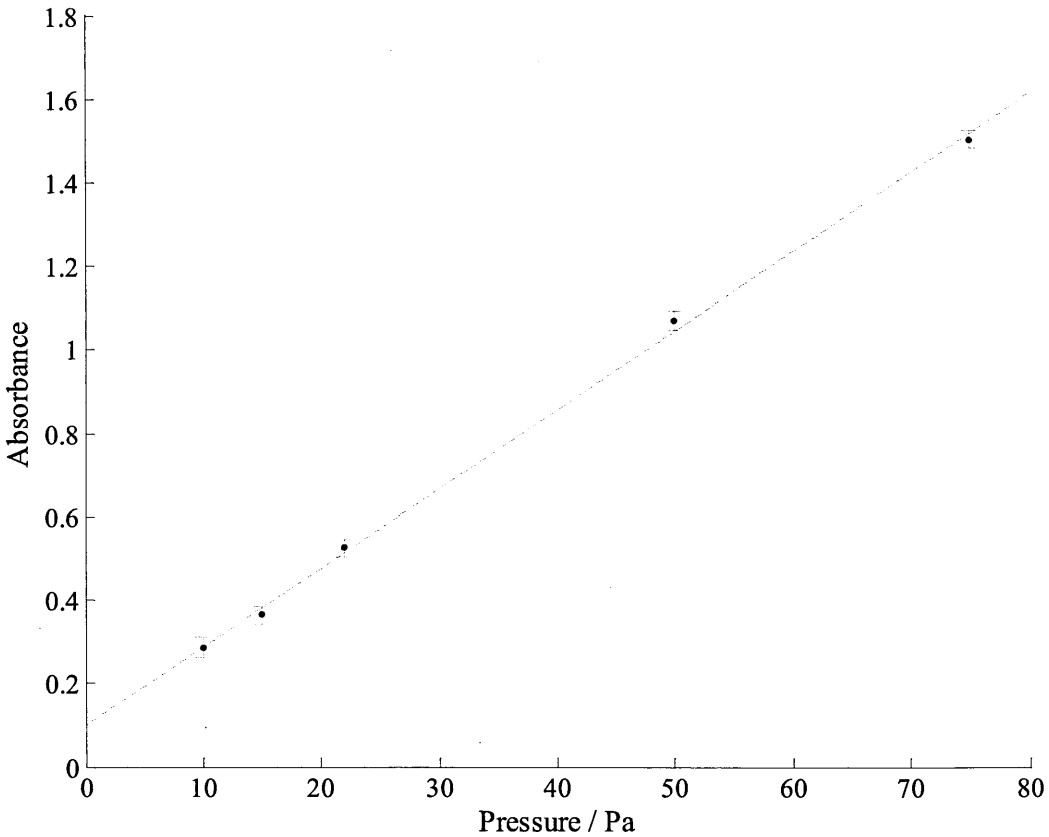

Figure 5-2: Maximum absorbance at 1187.5 cm^{-1} as a function of pressure at 298 K with a linear line of best fit. The error bars shown are calculated from the spectral noise.

The maximum absorbance of each peak was plotted as a function of pressure; those that followed a straight line are unsaturated and can be used to calculate the cross-sections (Figure 5-2). Equation (191) was then used to calculate the cross-section. The ideal gas equation is usually used to find the number density of molecules, N, from the pressure and temperature of the sample cell. The ideal gas equation assumes that the molecules are point masses and that there are no interactions between the molecules, this works best at low temperatures and pressures. At high temperatures and pressures the attractive interactions become significant, which would act to decrease the pressure for a given volume, temperature and number of moles: this would lead to an underestimation of the number of molecules resulting in a larger cross section. The fact that the molecules are not points would affect the cross section in the opposite way. The assumption was validated using a third order virial

expansion where the coefficients have been determined experimentally by Duan et al. (Duan et al., 2000).

$$\frac{P}{\rho RT} = 1 + B\rho + C\rho^2 + D\rho^3 \tag{192}$$

where A, B and C are experimentally determined coefficients that are dependent on the temperature, P is the pressure, R is the molar gas constant, ρ is the density of the gas, and T is the temperature. Over the range of pressures used in this work we can see that the assumption of the ideal gas law would lead to an overestimation of the number density by around 17 % for 298 K and 30 mbar. The number density of molecules was therefore determined from the virial expansion.

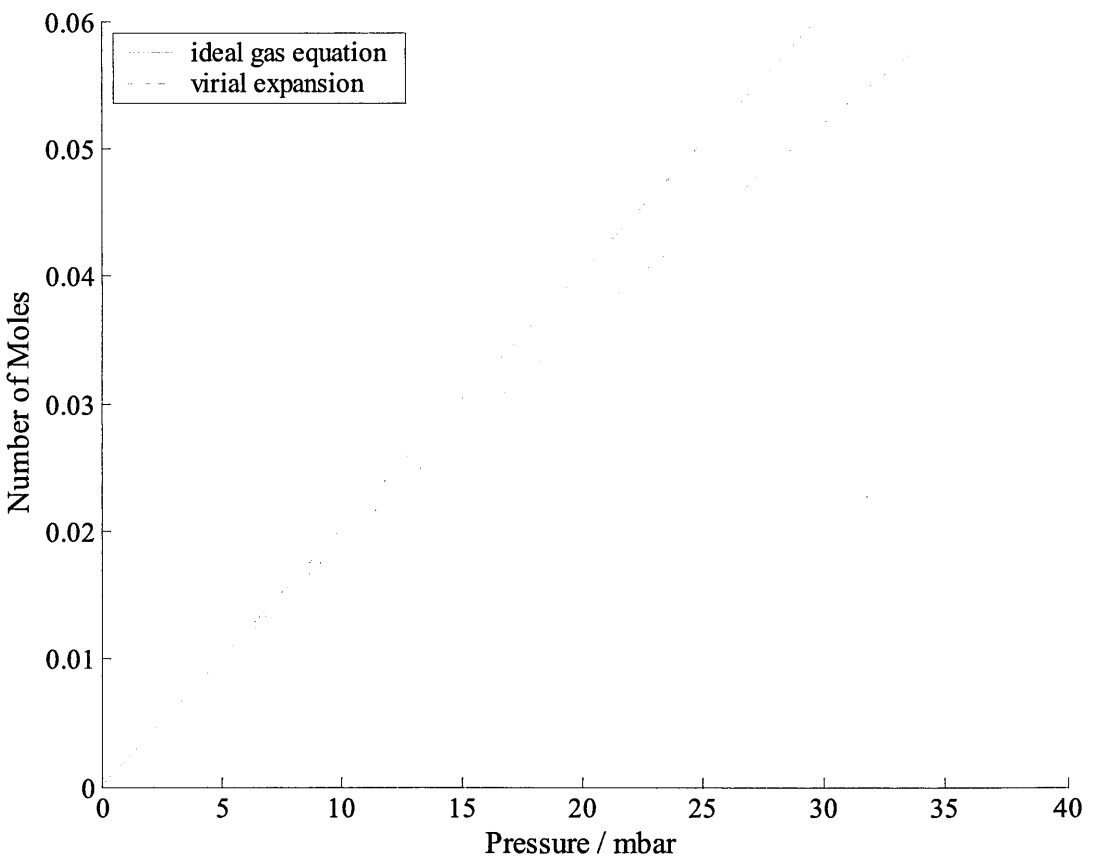

Figure 5-3: Pressure calculated from ideal gas equation and experimental virial expansion for CF_3I at 298 K.

There are several assumptions made in the calculations of the cross-sections that are very accurate for small molecules and low temperatures but cannot be assumed for heavier molecules at high temperatures for example, *that all of the molecules are in the ground vibrational state.* When a vibrational mode is excited at room temperature and pressure the transition is assumed to be $v = 0 \rightarrow v = 1$ but there could be a significant population in the $v = 1$ state resulting in $v = 1 \rightarrow v = 2$ transitions. These are known as 'hot bands'. We can calculate the relative populations of rotational and vibrational states (Table 5-2) with a Boltzman distribution function using the ro-vibrational partition function as described in Chapter 3 section 3.4. the relevant constants for CF_3I have been taken from He at al. (He et al., 2002). It can be seen that the population in higher levels is a very small percentage and so this is not thought to have a significant effect on our measured cross-section.

Table 5-2: Percentage population of Vibrational States

V	% of population in state			
	298 K	**273 K**	**252 K**	**208 K**
0	99.45	99.66	99.79	100
1	0.55	0.34	0.21	0.00
2	0.00	0.00	0.00	0.00
3	0.00	0.00	0.00	0.00

Examples of the cross sections obtained for each of our spectral regions are given in Figure 5-4 and Figure 5-5. The weak peaks shown in Figure 5-4 are expanded in Figure 5-6, Figure 5-7and Figure 5-8.

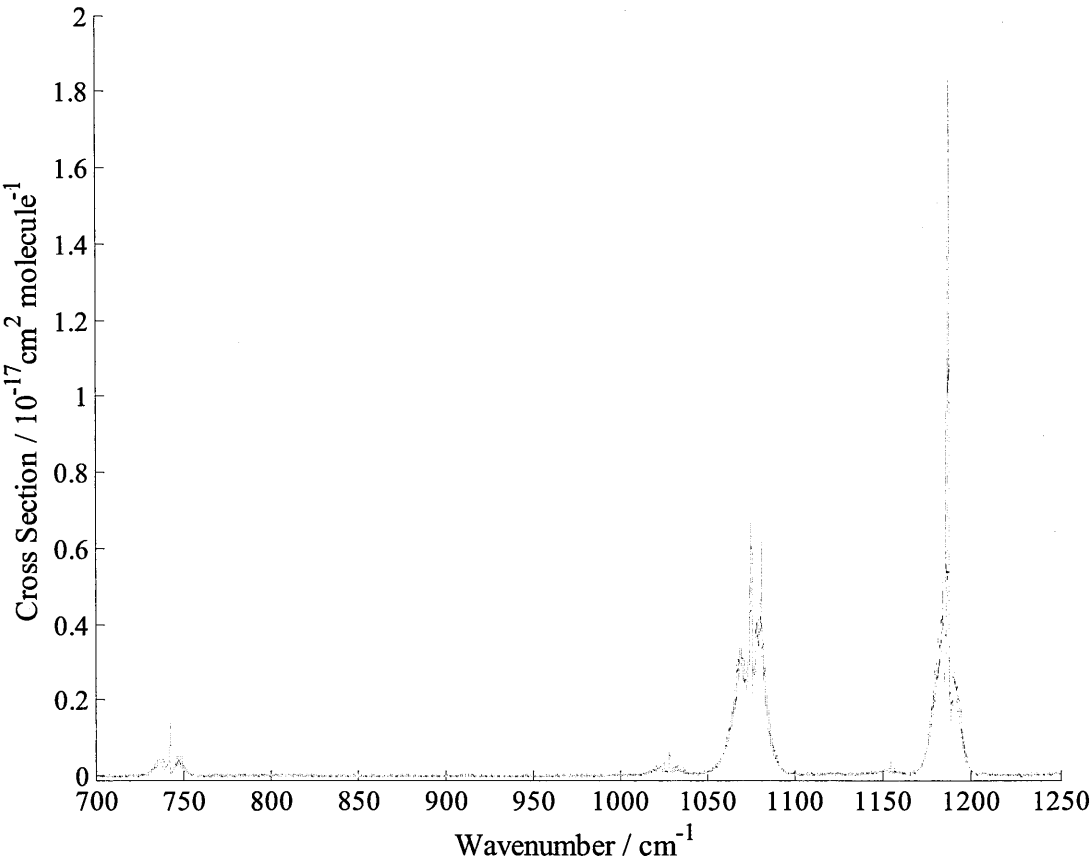

Figure 5-4: Examples of cross-sections obtained for CF_3I; 10 mbar of gas at 298 K

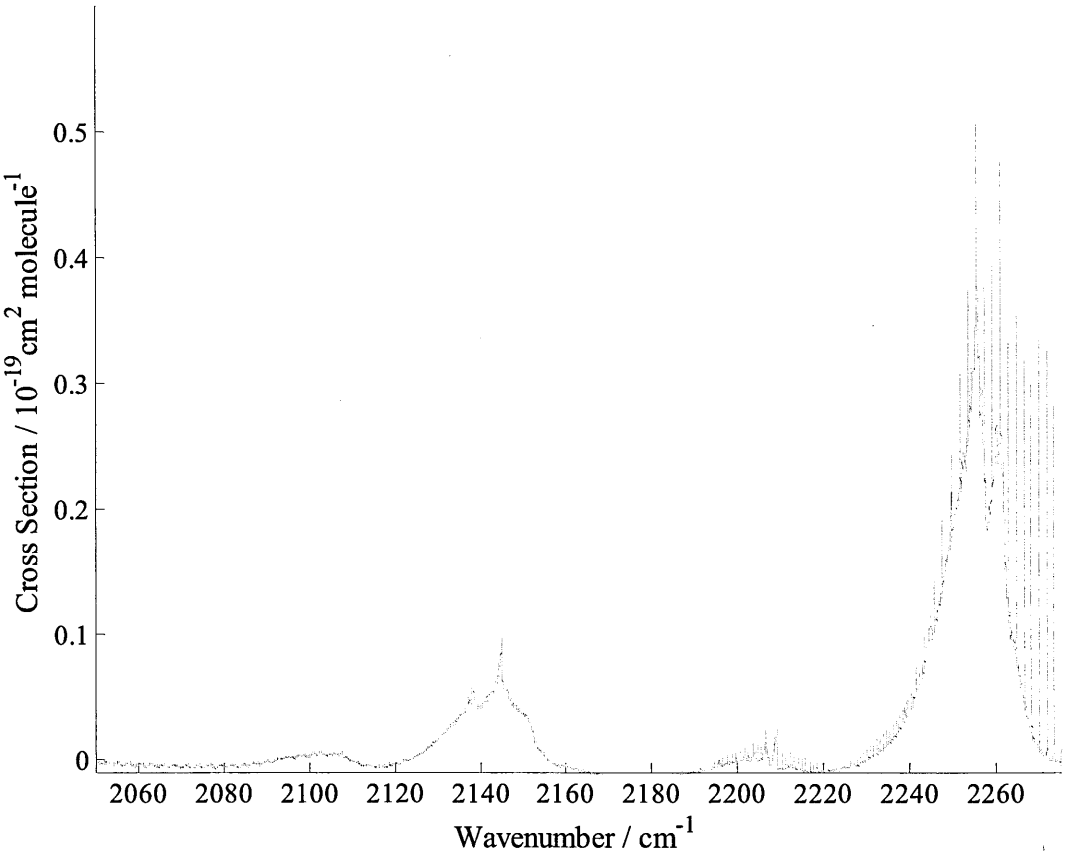

Figure 5-5: Examples of cross-sections obtained for CF3I; 30 mbar of gas at 272.9 K

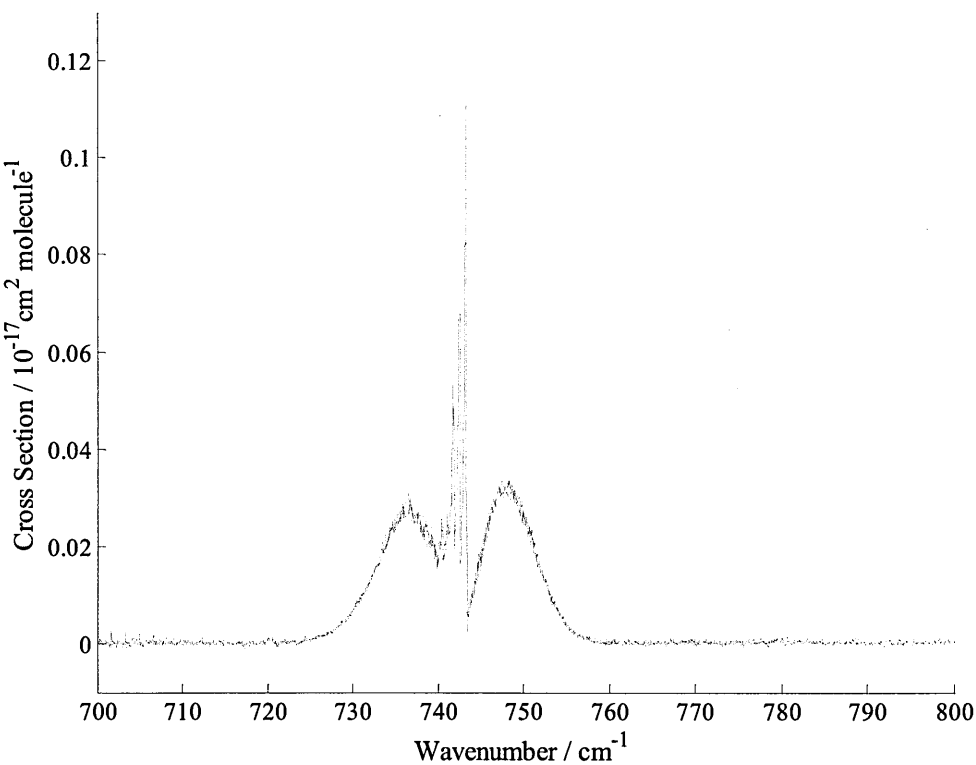

Figure 5-6: An expansion of the weak bands in Figure 5-5 at 10 mbar and 298 K

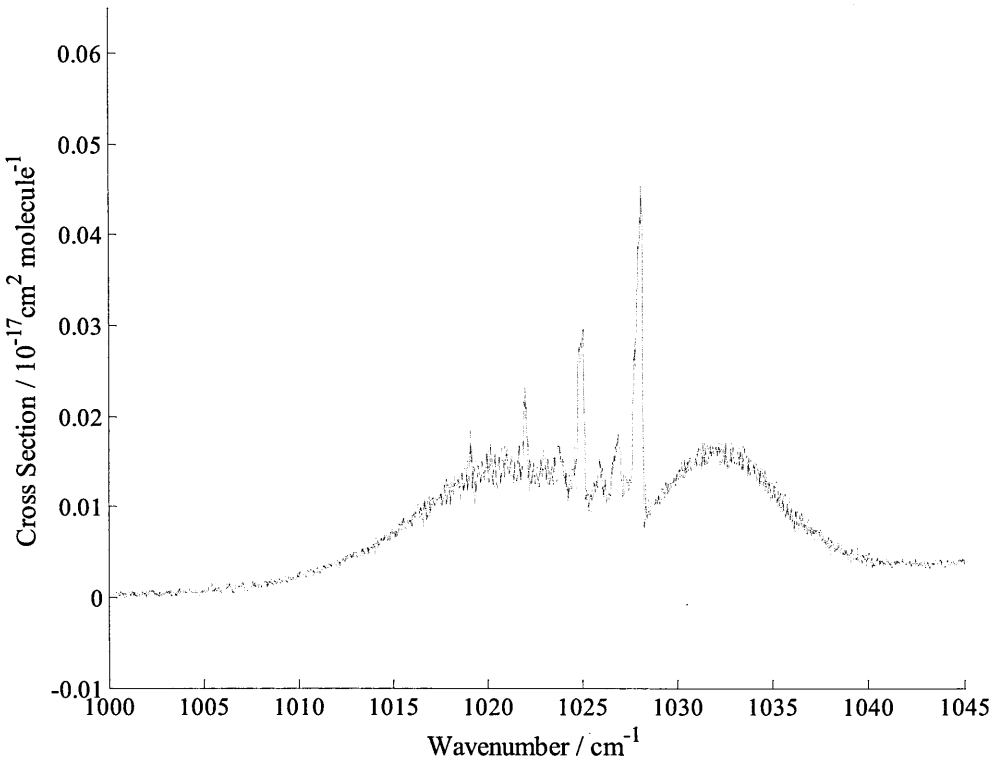

Figure 5-7: An expansion of the weak bands in Figure 5-5 at 10 mbar and 298 K

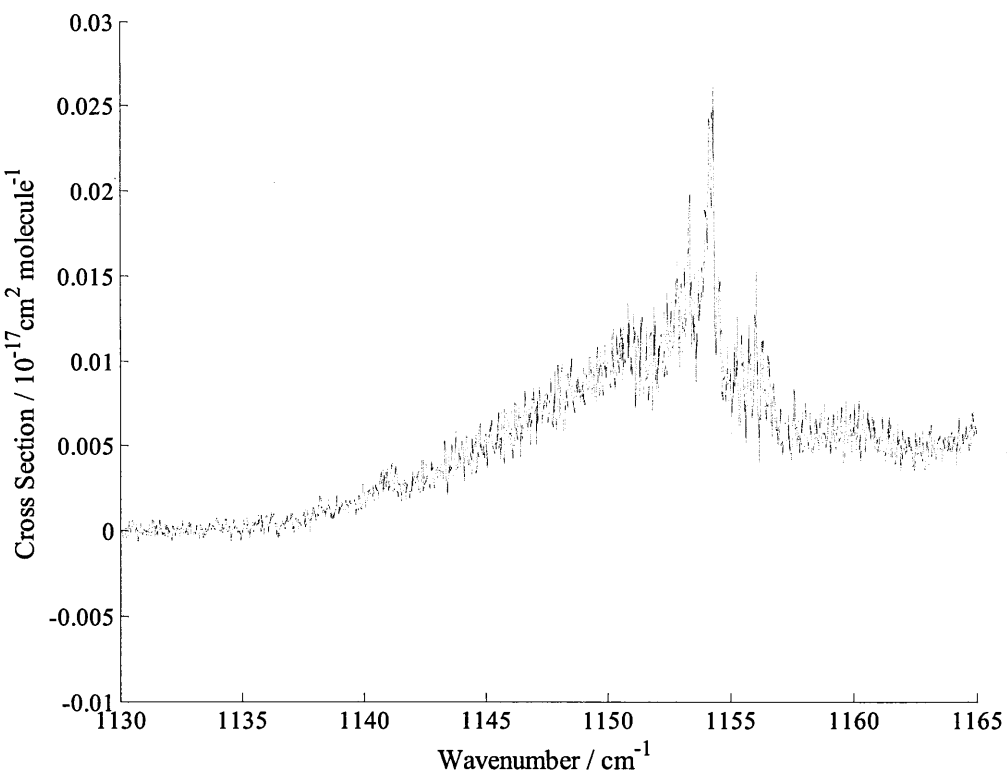

Figure 5-8: An expansion of the weak bands in Figure 5-5 at 10 mbar and 298 K

The average peak cross-sections are shown as a function of temperature in Table 5-3. There appears to be a dependence of the peak cross-sections with temperature, with the cross-section increasing with a decrease in temperature. This is because at higher temperatures more rotational and vibrational states are occupied resulting in a broadening of the bands and a decrease in the intensity of the peak. The temperatures shown are the mean values of the average temperature logged on each thermometer with a standard error on the mean of the average of temperatures logged for each thermometer of around ±0.1 at 299.4 K and ±0.2 at 208.0 K.

Table 5-3: Average peak cross-sections as a function of temperature (the numbers in brackets are the standard deviations).

Temperature	Peak cross-section $\times 10^{-18}$ / cm^2				
/ K	743.2 cm^{-1}	1028.0 cm^{-1}	1075.1 cm^{-1}	1154.2 cm^{-1}	1187.5 cm^{-1}
299.4	1.03 (0.2)	0.46 (0.02)	6.03 (0.4)	0.28 (0.01)	19.2 (0.3)
272.9	1.6 (0.2)	0.63 (0.02)	6.9 (0.5)	0.36 (0.02)	26 (1)
251.6	-	-	2.8 (0.2)	-	12 (1)
208.0	2.3 (0.4)	0.91 (0.02)	8.1 (0.8)	0.45 (0.09)	42 (3)

Integrated absorption intensities (IAI) are then used to calculate the global warming potentials; our values of the IAI are shown in Table 5-4. The integrated absorption cross-section is found by integrating the area under each peak using a five point Newton-Cotes method. The regions used to define our integration regions were as follows (720-760 cm^{-1}), (1010-1044 cm^{-1}), (1044-1105 cm^{-1}), (1140-1165 cm^{-1}) and (1165-1210 cm^{-1}). These regions were chosen to enable the individual resolution of the IAI of each peak. The IAI is extracted for pressures of each peak that were non-saturated but at least three times the peak to peak level of noise. In spectroscopic theory the integrated absorption cross-section is shown to be independent of

temperature for diatomics however it has been shown that the radiative forcings of some heavy fluorocarbons show temperature dependence. This is hypothesised (Highwood and Shine, 2000) to be due to a change in the shape of absorption bands with temperature for these heavy molecules as they have torsional states in the side bands which can become populated at high temperature. Therefore even if the integrated absorption of a band remains constant a change in the shape may effect the radiative forcing as the radiative forcing is wavelength dependent. This is not the case however for CF_3I as there are no possible torsional states so any temperature dependence seen would be due to thermal population of excited states: so called "hot bands". The absorbance was found to be directly proportional to the pressure for all non saturated peaks, this shows that there is no pressure dependence of the cross-sections over the range of pressures studied. We were therefore able, to take an average of our integrated absorption intensities and these are shown in Table 5-4.

Table 5-4: Mean IAI values of each peak as a function of temperature (the numbers in brackets are the standard deviations).

	Average Integrated Absorption Intensity $\times 10^{-18}$ / cm molecule^{-1}					
T / K	720-760 cm^{-1}	1010-1044 cm^{-1}	1044-1105 cm^{-1}	1140-1165 cm^{-1}	1165-1210 cm^{-1}	Total cm^{-1}
299.4	5.4 (0.6)	3.7 (0.1)	72 (4)	1.8 (0.1)	60 (2)	143
272.9	6.0 (0.8)	4.1 (0.2)	72 (18)	2.2 (0.3)	61 (11)	145
251.6	-	-	75 (1)	-	63 (1)	138
208.0	6.9 (1.5)	2.6 (0.7)	79 (17)	1.3 (0.7)	65 (15)	154

In the strongest absorption bands there appears to be a general trend of an increase in the integrated absorption intensity with a decrease temperature. It has been shown (Mills and Whiffen, 1959) that for diatomics the IAI is independent of temperature

and it was assumed that this would be the same for polyatomics. It is thought that this temperature dependence is an experimental uncertainty rather than a physical phenomenon. Smith et al. also noticed a systematic decrease in the integrated absorption intensity at higher temperatures (Smith et al., 1996). Smith et al. have used a program known as CALCAT (Pickett, 1991) to calculate a theoretical spectrum for a vibrational band of trifluoromethane that showed that at higher temperatures there are absorbing bands over a greater wavenumber range from the band centre than at lower temperatures. They noticed that at higher temperatures there was a significant amount of absorption in the tails from these weak absorption lines that were obscured by the effects of noise. Any temperature dependence would be important when calculating the global warming potential of the gas as a function of altitude in the atmosphere. There was no noticeable shift in the position of the peaks with temperature which can also affect the radiative forcing of a species in the atmospheric window. Estimates of the uncertainties in these IAIs have been made using the standard deviation of our individual IAIs and were found to be around ±10 % with the highest uncertainties being associated with the lower temperatures.

In the second spectral region the integrated absorption intensities were 8.75×10^{-20} cmmolecule^{-1} for the peak at 2144.4 cm^{-1} and 4.87×10^{-19} cm molecule^{-1} for the peak at 2255.6 cm^{-1}. Unfortunately because of the small cross-sections of these peaks not enough information about the peaks is available for further, more detailed analysis.

Two studies into the infrared absorption cross-sections of CF_3I have been conducted the results of which are summarised in Table 5-5. The data from this study shown in the table is that recorded at 299.4 K. Solomon et al. (Solomon et al., 1994) recorded

FTIR spectra with a resolution of 0.05cm^{-1} and a temperature of 298 K in an atmosphere of nitrogen. They observed three peaks centred at 743, 1075 and 1187 cm^{-1} with strong Q branch features, which is in very good agreement with our three predominant peaks. This study did not, however, resolve the weaker peaks at 1028 and 1154.2 cm^{-1}. Their values of the integrated absorption intensities are higher than ours for all peaks sometimes by as much as 16 %. Their integration regions are different to ours for the 1075 and 1187 cm^{-1} peak as they did not resolve the weaker peaks in their study and so their chosen regions overlap with the neighbouring weak peaks. This difference in the integration region, however, does not appear to explain the difference in the IAI as the addition of the IAI of both peak does not sum to Solomon et al. values. Christidis et al. (Christidis et al., 1997) also measured FT-IR spectra at a resolution of 0.5 cm^{-1} from 450-2000 cm^{-1}. Their sample was mixed with 933 mbar of ultra-high purity synthetic air and was conducted at 296 ± 2 K. In comparison with Solomon, their IAI are in much better agreement with the results of this study.

Table 5-5: Integrated IAI data for CF_3I from this thesis compared with the work of others

Integration region / cm^{-1}	IAI / cm molecule^{-1}		
	(Solomon et al.)	(Christidis et al.)	(This Study)
720-760	6.8×10^{-18}	6.0×10^{-18}	5.4×10^{-18}
1040-1105	8.4×10^{-17}	7.7×10^{-17}	7.2×10^{-17}
1155-1210	7.1×10^{-17}	6.4×10^{-17}	6.0×10^{-17}

The total integrated absorption over the whole range of our data as shown in Table 5-4 is 143×10^{-18} cm^{2}molecule^{-1} compares well with that of Christidis at 150.6×10^{-18} cm^{2}molecule^{-1}.

5.4 Approximation of the Radiative Forcing and GWP.

Using the approximation of Pinnock et al. (1995) outlined in chapter 2 the instantaneous radiative forcing for a 1-ppbv increase in a concentration in a gas is given by the equation:

$$RF = \sum_{i=1} \sigma_i F_i^{\sigma} \tag{193}$$

where F_i^{σ}, in units of W $m^{-2}(cm^{-1})^{-1}$ $(cm^2\ molecule^{-1})^{-1}$, is the radiative forcing per unit cross section per wavenumber for the spectral interval *i* for the global annual mean atmosphere including cloud (Pinnock et al., 1995) and σ_i (with units cm^2 $molecule^{-1}$ cm^{-1}) is the photoabsorption cross section integrated over spectral interval *i*.

In order to calculate the radiative forcing a suitable cross section must be defined, in this thesis the cross sections have been calculated for several different pressures and so we need to take an average, however the average cross section for each peak may only be taken at non-saturated values. This results in different pressures being suitable for strong and weak peaks making an average over the complete spectrum impossible. In order to calculate an average cross section, therefore, the average cross section has been calculated for each peak separately over a range of pressures suitable for that peak. The radiative forcing for the peaks will then be calculated using the average which have a standard error on the mean of approximately 3 %. The contribution to radiative forcing between the peaks will be assumed to be zero.

Table 5-6: Radiative forcing of CF_3I at different temperatures

Forcing region / cm^{-1}	Radiative Forcing / Wm^{-2}		
	298 K	273 K	208 K
720-760	0.008	0.009	0.017
1010-1044	0.006	0.007	0.004
1044-1105	0.145	0.146	0.150
1140-1165	0.004	0.005	0.029
1165-1210	0.098	0.091	0.094
Total	0.261	0.258	0.291

The uncertainties on these radiative forcing values are difficult to determine however Pinnock et al. found their values to differ from the values calculated using a narrowband model by less than 1 %. Christidis et al. reported a cloudy sky instantaneous radiative forcing of CF_3I of 0.28 Wm^{-2} for a 1 ppbv global increase in gas concentration which agrees with our value to within 10 %.

Using the approximation for the global warming potential derived in Chapter 2

$$GWP = \frac{A_{gas} M_{CO_2} \tau_{gas} \left(1 - \exp(-t/\tau_{gas}\right)}{A_{CO_2} M_{gas} \tau_{CO_2} \left(1 - \exp(-t/\tau_{CO_2}\right)} \qquad (194)$$

the global warming potential for CF_3I can now be calculated. It will be calculated relative to CO_2 and CFC-11 which are the common reference gases but also relative to the gases it is proposed to replace Halon 1301 and C_2F_6. In the interests of comparison with other works the lifetimes and radiative forcing used for the reference gases will be those from the Christidis study.

Table 5-7: Global warming potential of CF_3I relative to a range of gases over three different timescales (20, 100 and 500 years).

Reference Gas	GWP / $\times 10^{-4}$ Time / years		
	20	100	500
CO_2	0.14	0.06	0.05
CFC-11	2.2	0.9	0.8
C_2F_6	500	100	20
Halon 1301	630	210	167

The resultant GWP for a 20 year time horizon from previous studies are $<1\times10^{-5}$ relative to CO_2 and $<1\times10^{-3}$ relative to CFC-11 for the Solomon study and 2×10^{-4} relative to CFC-11 for the Christidis study, both were calculated for a lifetime of two days (Christidis et al., 1997, Solomon et al., 1994).

Even though the radiative forcing of CF_3I is large relative to some other greenhouse gases the extremely short lifetime means that the global warming potential of CF_3I is still small compared to gases presently used in the plasma industry e.g. the global warming potential of CF_3I over a 20 year timescale relative to CFC-11 is 2.2. Moreover, due to the weak CF_3-I bond, iodine is released and found to react in the troposphere to form water-soluble compounds, HI, HOI, $IONO_2$ which are rained out before reaching the stratosphere; CF_3 radicals are found not to react efficiently with ozone.

5.5 Conclusions

High resolution Fourier transform infrared spectra have been obtained for CF_3I at pressures ranging between 0.25 mbar and 30 mbar and for several temperatures

(299.4, 272.9, 251.6 and 208.0 K). Two spectral regions have shown strong absorption bands. In the first spectral region the main bands have their most prominent peaks at 743.2, 1028.0, 1075.1, 1154.2, 1187.5 cm^{-1}. The 1075.2 cm^{-1} and the 1187.5 cm^{-1} are the strongest with IAI of around 10^{-17} cm $molecule^{-1}$. In the second spectral region there are three peaks centred at 2144.4 cm^{-1}, a very weak peak at 2206.0 cm^{-1} and a strong peak at 2255.6 cm^{-1}. The bands themselves are complex structures consisting of more than one peak. Integrated absorption cross-sections have been calculated for non saturated peaks using the Beer-Lambert law with the number density obtained using an experimentally determined virial expansion.

Values of the radiative forcing of CF_3I have been calculated using the approximation of Pinnock et al. and are found to be within 10 % of the values calculated using narrowband models. These radiative forcing estimates were then used to calculate a value for the global warming potential of CF_3I which also shows good agreement with other studies.

Chapter 6: Designing an ultrasonic trap

"The most exciting phrase to hear in science, the one that heralds new discoveries, is not 'Eureka!' (I found it!) but 'That's funny....'"

Isaac Asimov

The author was first involved with ultrasonic trapping through a project into single bubble sonoluminescence (Webb and Mason, 2004), in which small bubbles are trapped in an ultrasound field within a liquid medium and the expansion and collapse of the bubbles heats the bubble to such an extent that the bubble glows. This chapter explains the specifics of the design of our ultrasonic trap and how it was made suitable for collecting spectra of particulate aerosols, the design of the trap has been the subject of a published paper (Mason et al., 2008). The trapping chamber had to be able to be evacuated, filled with an infrared inactive gas, heated, cooled, contain the trap itself and allow for the retrieval of our samples. Significant technical difficulties were overcome in the design of this trap and this chapter aims to present some of the practical considerations that had to be taken in to account and how this research tackled them. The design and building of the transducers and acoustic trap as well as the writing of the data analysis codes was the independent work of the author of this thesis and the preparations of the samples, the spectroscopic and SEM work undertaken was shared with E. A. Drage.

6.1 The Langevin transducer and driving circuit

In order that we might trap each of the four different aerosol materials we had selected at the size range that we were interested in we have to select a frequency of operation and parameters of the levitating medium such that the entrainment coefficient is above 0.95 for as many of the size range of particles we are interested in. In our chamber we

were able to control both the temperature (between 10 °C and 70 °C) and pressure (between 0.5 atm and 1.5 atm) of the levitating medium. To calculate entrainment coefficient (equation (186)) we used the temperature and pressure dependent properties of the gas i.e. the speed of sound (Figure 6-3), the density (Figure 6-2) and the viscosity (Figure 6-1), the data used was from the National Institute of Standards and technology (NIST) online database of Thermophysical Properties of Fluid Systems (NIST, 2011). The range of temperature over which we could hold our chamber had a greater influence over the values of the viscosity and the speed of sound than the range of pressures whereas the density is significantly affected by both factors over their respective possible ranges.

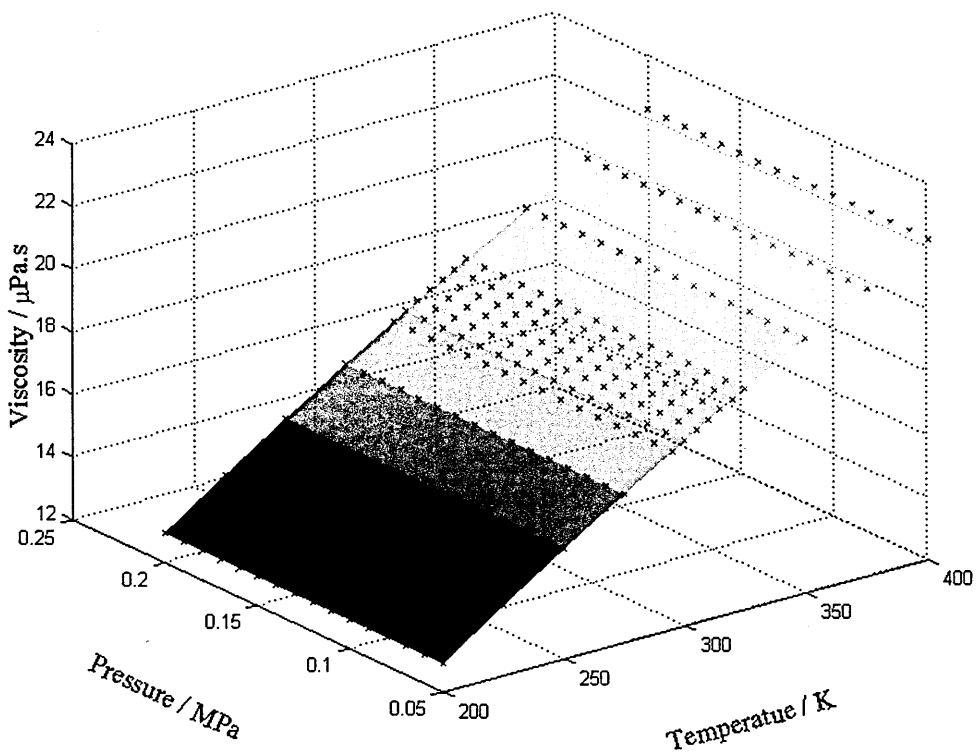

Figure 6-1: A surface plot to show the temperature and pressure dependence of the viscosity of nitrogen gas (data taken from the NIST online database of Thermophysical Properties of Fluid Systems (NIST, 2011))

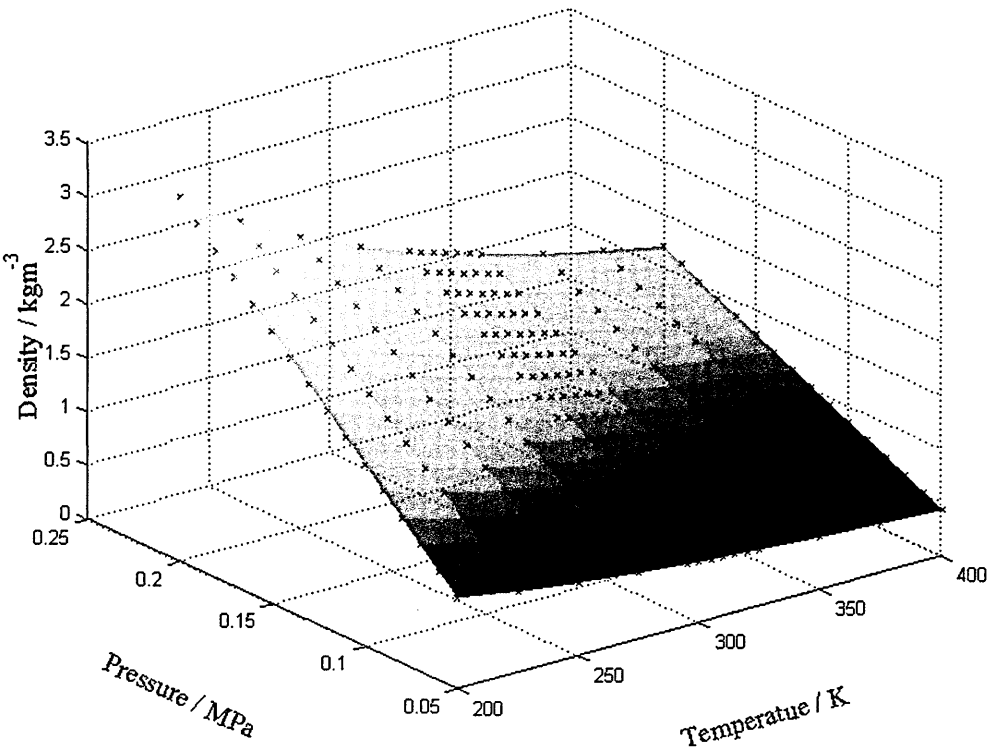

Figure 6-2: A surface plot to show the temperature and pressure dependence of the density of nitrogen gas (data taken from the NIST online database of Thermophysical Properties of Fluid Systems (NIST, 2011))

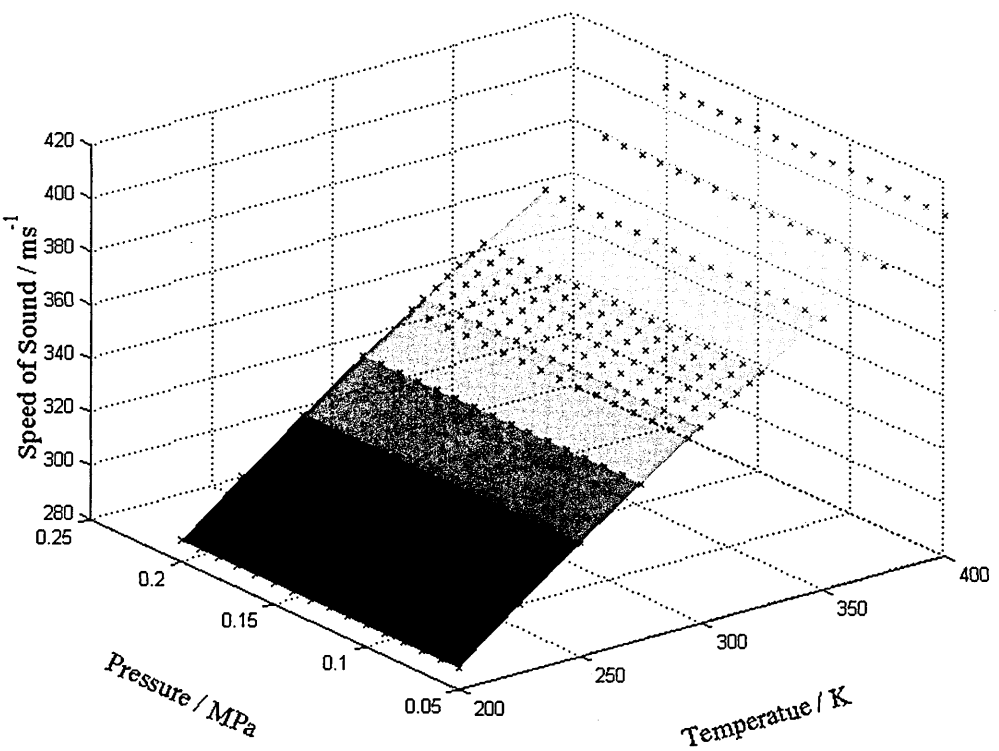

Figure 6-3: A surface plot to show the temperature and pressure dependence of the speed of sound in nitrogen gas (data taken from the NIST online database of Thermophysical Properties of Fluid Systems (NIST, 2011))

The entrainment coefficient was then calculated over the range of different possible values of pressure, temperature and frequency and the maximum radius of particle with an entrainment coefficient of above 0.95 was calculated (Table 6-1). As you can see from the table the size of the maximum particle entrained increases both as the frequency decreases and the temperatures increases. To sustain the most stable levitating node of aerosol particles all of the particles entrained otherwise those particles not entrained would move orthokinetically, collide with the other particles and cause agglomeration thus changing your aerosol over the time of the spectroscopic measurements.

Table 6-1: A table to show how the diameter of the largest particle (μm) with an entrainment coefficient of greater than 0.95 changes as a function of temperature and frequency.

		Temperature / °C					
		10	**20**	**30**	**40**	**50**	**60**
Frequency / kHz	**10**	0.88	0.90	0.92	0.93	0.95	0.95
	15	0.72	0.74	0.75	0.76	0.77	0.77
	20	0.62	0.64	0.65	0.66	0.67	0.67
	25	0.56	0.58	0.58	0.60	0.60	0.60
	30	0.51	0.52	0.53	0.54	0.55	0.55
	35	0.47	0.48	0.49	0.50	0.50	0.50

From Table 6-1 we can see that the frequency is a significant factor in the diameter of the particle trapped and as such we would ant the lowest working frequency possible however several other factors must be taken into account such as: working with high intensity sound levels at audible frequencies would not be a comfortable working environment for the experimenter and also that the size of the transducer that would resonate at those frequencies would not just make mechanical losses much higher but

also would make the physical size of the transducer too large to put into a chamber (using equation (154) the total length of the transducer would be 25.0 cm long with 9.1 cm steel back plate and a 14.6 cm polythene front plate). On balance it was decided to opt for a 25 KHz transducer as it was compact enough to fit in the vacuum chamber, worked at ultrasound frequencies, fully entrained particles of under 0.60 μm and a commercial Langevin style transducer that worked at this frequency was available that we could use as a comparison to our designs. Figure 6-4 shows how the entrainment coefficient changes as a function of particle size for an operating frequency of 25 kHz in an atmosphere of nitrogen at 25 °C and atmospheric pressure.

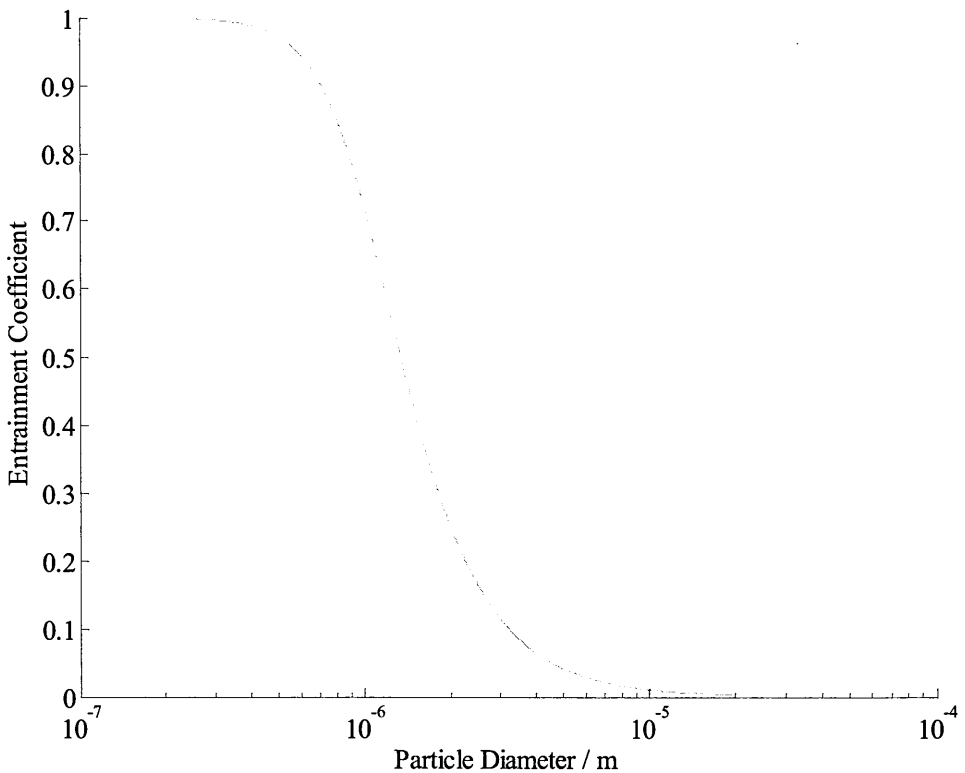

Figure 6-4: A graph to show the entrainment coefficient as a function of particle size for a frequency of 25 kHz, in a nitrogen atmosphere of 25 °C and 0.101 Mpa.

A transducer then had to be designed that operated at this frequency but that was matched to provide that largest power to a gaseous load. Three transducer designs with a resonant frequency of approximately 25 kHz were trialled during the course of

this research, each of them is a Langevin style sandwich transducer the layers of which are glued together with epoxy resin: wire mesh (48 s.w.g. and 250 μm gauge) was put between the layers both to make an electrical connection to the electrodes and to ensure that the spacing between the layers is uniform and thus ensure that charging of the PZT layers was uniform.

Each transducer had to be pre-stressed to prevent fracture of the crystal, to do this we used made use of the characteristic of the PZT material that the charge on the PZT is proportional to the applied stress; we used the stated d_{33} constant of the specific PZT material being used, where

$$d = \frac{\text{short circuit charge/ electrode area}}{\text{applied stress}} \tag{195}$$

and the subscripted numbers represent the axes, the first one being the axis that the electrodes are perpendicular to and the second subscript being the axis along which the stress is applied. The numbers 1, 2 and 3 corresponding to x, y and z and by convention the z axis is the axis along which the ceramic has been poled. The d_{33} constant is therefore the charge per area per unit of applied stress in the direction of the poling of the ceramic measured i.e. that the applied stress, charge measured and poling are all along the same axis. The method used to measure the charge generated in the PZT under short-circuit conditions is to connect a non-electrolytic capacitor of 10 μF and a voltmeter (internal resistance > 10 MΩ) to the electrodes of the ceramic crystals. The voltage can be used to calculate the charge on the capacitor and thus the charge on the PZT using the equation

$$Q = CV \tag{196}$$

Where Q is the charge stored on the capacitor, C is the capacitance and V is the voltage. The applied stress was then calculated using equation (195).

6.1.1 Transducer Designs

6.1.1.1 Transducer 1 – Polythene Front Plate

This design of transducer incorporates a steel back plate and a polythene, high intensity, front plate which increases the acoustic impedance matching between the transducer and the air however the mechanical losses in plastics are high which limits the energy delivered. In addition to this the size of the compression which can be put on the ceramic by the bias bolt is limited to about 16 Nm by the softness of the polythene, this in turn limits the power at which we can drive the transducer before ti will fracture. The front plastic plate is designed to be a quarter wave matching plate of length of ¾ of the wavelength of sound in the polythene, one quarter wavelength was not used as this would not provide sufficient mass to bring the resonant frequency down to the desired order of magnitude. The dimensions of the PZT rings were used to define the areas and the length of the ceramic layer, the length of the plastic layer was determined by the wavelength of sound in polythene. The length of the steel back plate could then be calculated using equation (154). The resulting design can be seen in Figure 6-5.

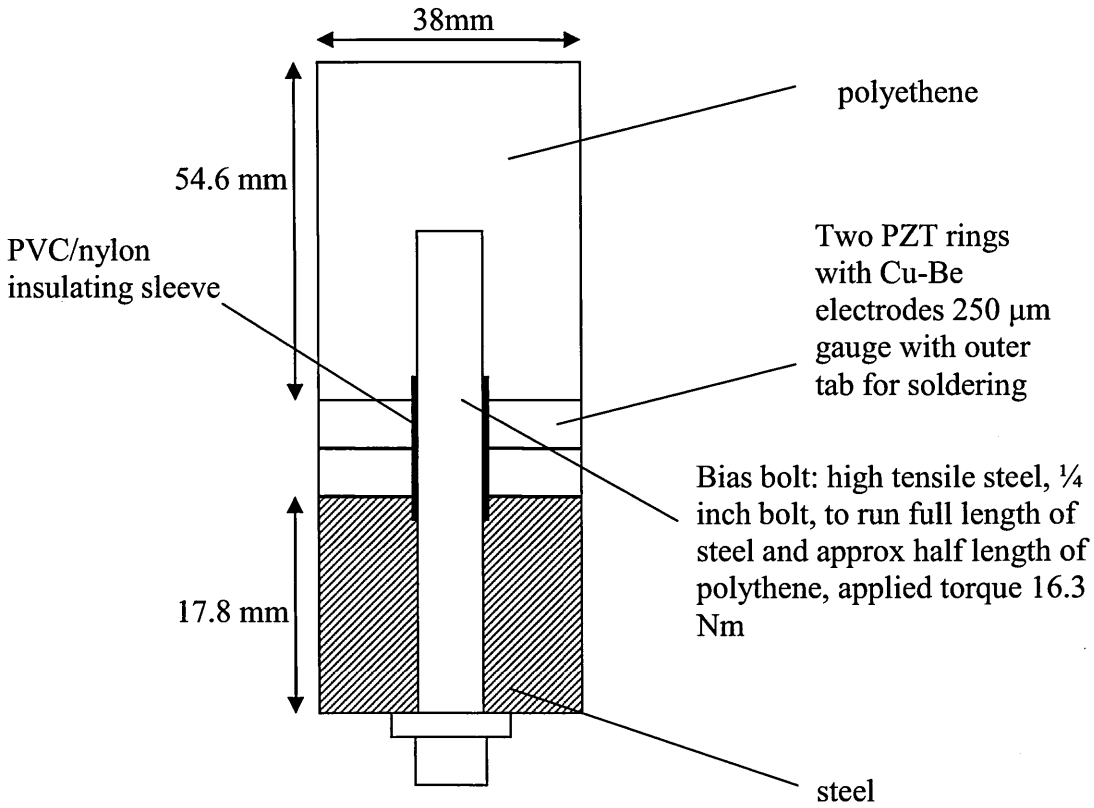

Figure 6-5: A diagram of one of the transducer designs, this transducer design utilised a polythene front plate

This design produced a good level of sound intensity but the transducer became very hot during operation and as such the epoxy resin was altered resulting in a loss of impedance matching and thus sound level intensity. The levitation of the aerosols was also not very stable I believe this is due to the small area of the front face meaning that edge effects close to the levitating node caused instability. This could be improved by attaching a tapered front plate such as in transducer design 3. Threading of the polythene was also a problem during construction and in order that a greater pre-stress be put on the PZT crystals I would use a bolt with a deeper thread or larger thread count per length.

6.1.1.2 Transducer 2 – Transducer with Flexure-Mode Resonator

This design was recommended by Morgan Electro Ceramics as a good air coupled transducer in their online "Guide to Piezoelectric & Dielectric Ceramic" in chapter 6b

(MorganElectroCeramics, 2009) a full technical drawing can be found on page 5. The flexure-mode resonator is an aluminium cap which acts as a membrane clamped on its circumference. The amplitude of the vibration is amplified by the flexure mode resonator which provides a better match to air than a rigid cylindrical resonator. The resonance of the membrane and the resonance of the transducer form a coupled wide bandwidth resonance although it means that it has a wide operational frequency and better matching to air the electroacoustic efficiency will be lower. The pre-stressing force for this is 25×10^3 N (Torque 60-90 Nm).

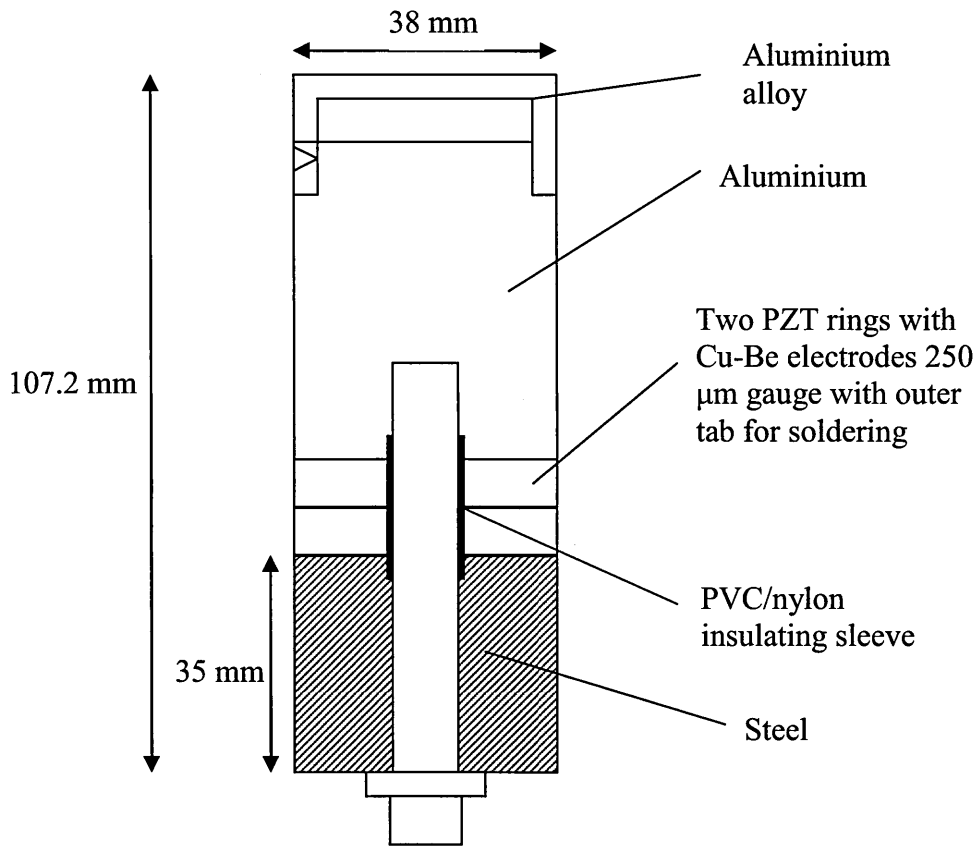

Figure 6-6: A diagram of one of the transducer designs, this transducer design utilised a flexure mode resonator

This design did not provide enough sound level intensity to levitate the aerosols is a consistent and stable node.

6.1.1.3 Transducer 3: Aluminium Front Plate with Matching Layer

The third design trialled was a standard Langevin transducer with a range of different matching layers. The transducer used for the work in this thesis was a Morgan Electro Ceramics sandwich transducer part number 0912. This transducer design was the most successful as it was able to produce a sound field of the necessary intensity and stability to make the most stable levitation of aerosol particles. The stated resonant frequency of this part number is 25 kHz and the typical power output 60 W rms.

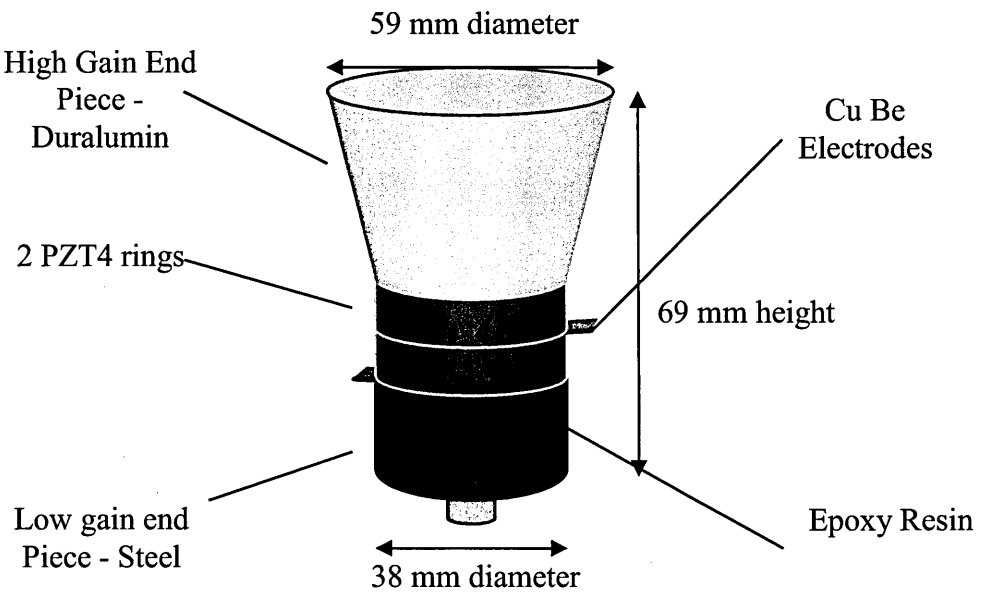

Figure 6-7: Standard Langevin transducer design

The ratings for this transducer are given in Table 6-2 and are quoted from the manufacturers technical specifications delivered with the product.

Table 6-2: Quoted values of transducer properties as given by manufacturer tests

Property	Value
Capacitance, C_0	3896.19 pF
Tan δ	0.0027
Z_{min}	17.0135 Ω
Z_{max}	186229.0000 Ω
F_r	26.7725 kHz
F_a	28.7913 kHz
Activity	0.4019
Q_m	662.7418

The values for C_0 and the series and parallel resonant frequencies can be used in conjunction with equations (143) and (144) to determine the values for the equivalent circuit parameters as shown in Figure 4-5. The calculated values for the equivalent circuit parameters are shown in Table 6-3.

Table 6-3: A table to show the calculated equivalent circuit parameters

Property	Value
C_1	6.1×10^{-10} F
L_1	5.8×10^{-2} H
R_1	14.7
Q_E	37.0
Q_M	6.6×10^{2}
Q_L	41339.9

These circuit parameters were then used in a Matlab simulink model of the equivalent circuit (Figure 6-8) and used to calculate a theoretical curve for both the complex impedance and the phase angle. The impedance analyser function on the Matlab power GUI was used to model the complex impedance as a function of frequency of driving voltage.

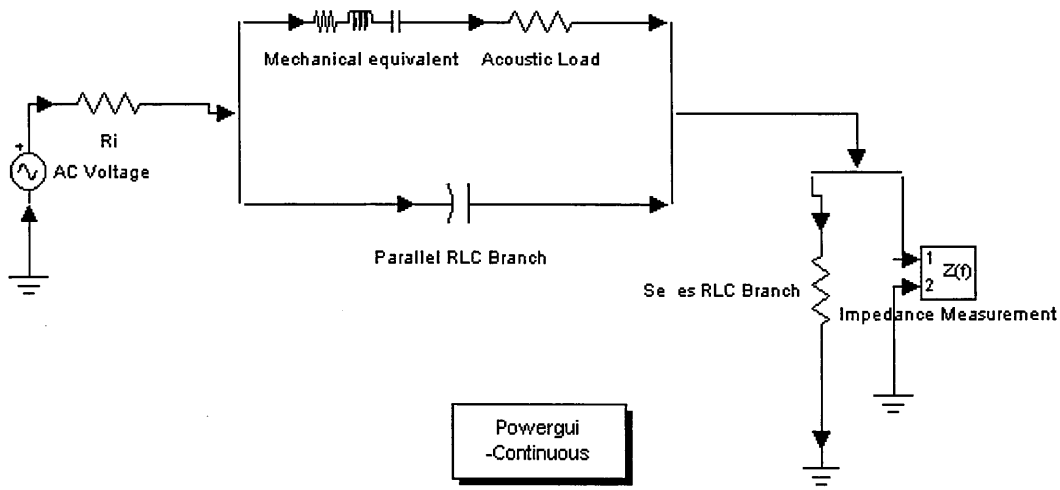

Figure 6-8: Matlab simulink model of the equivalent circuit of a Langevin transducer

The complex impedance and phase angle of the transducer was then measured using a complex impedance analyser and compared with the theoretical values calculated using the electrical circuit model. The measured and modelled impedance are shown as a function of frequency in Figure 6-9. The modelled phase angle of the transducer as a function of frequency is shown in Figure 6-10. The measured and calculated acoustic impedance curves show good agreement. These values could then be use to ascertain whether parallel or series tuning would result in a higher electro-acoustic efficiency.

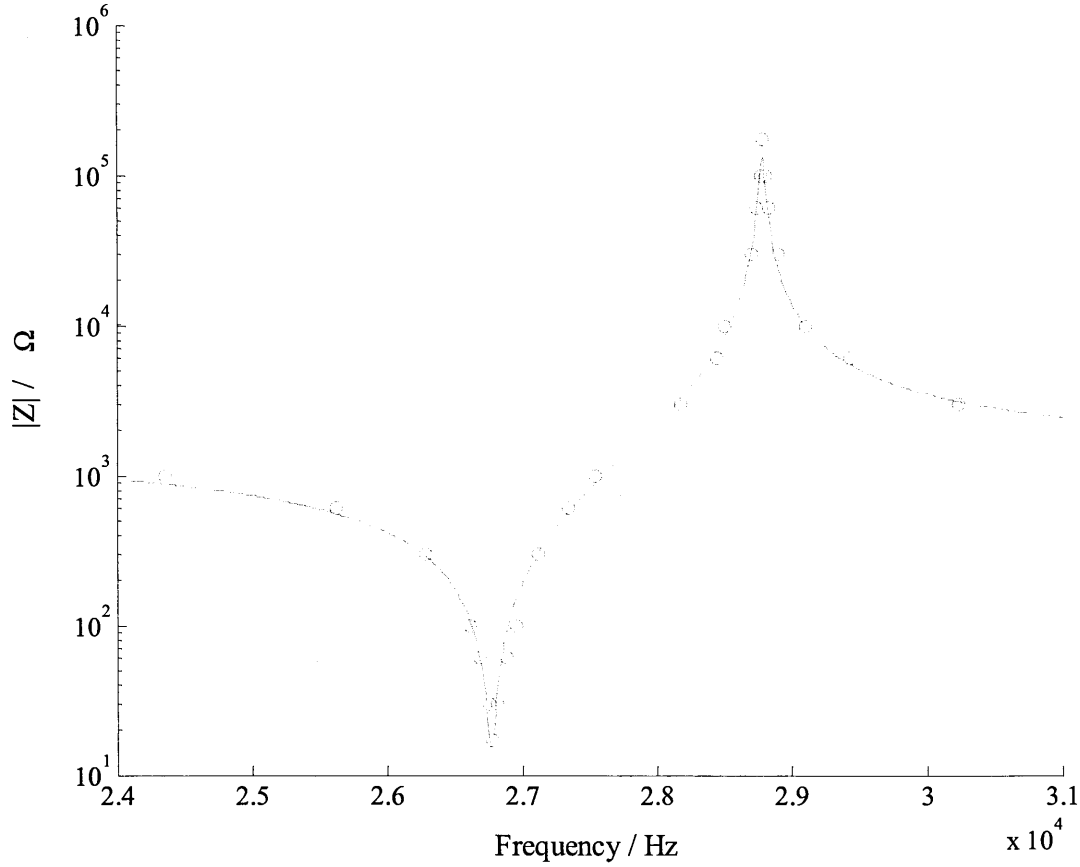

Figure 6-9: The measured and theoretical impedance of the Langevin transducer

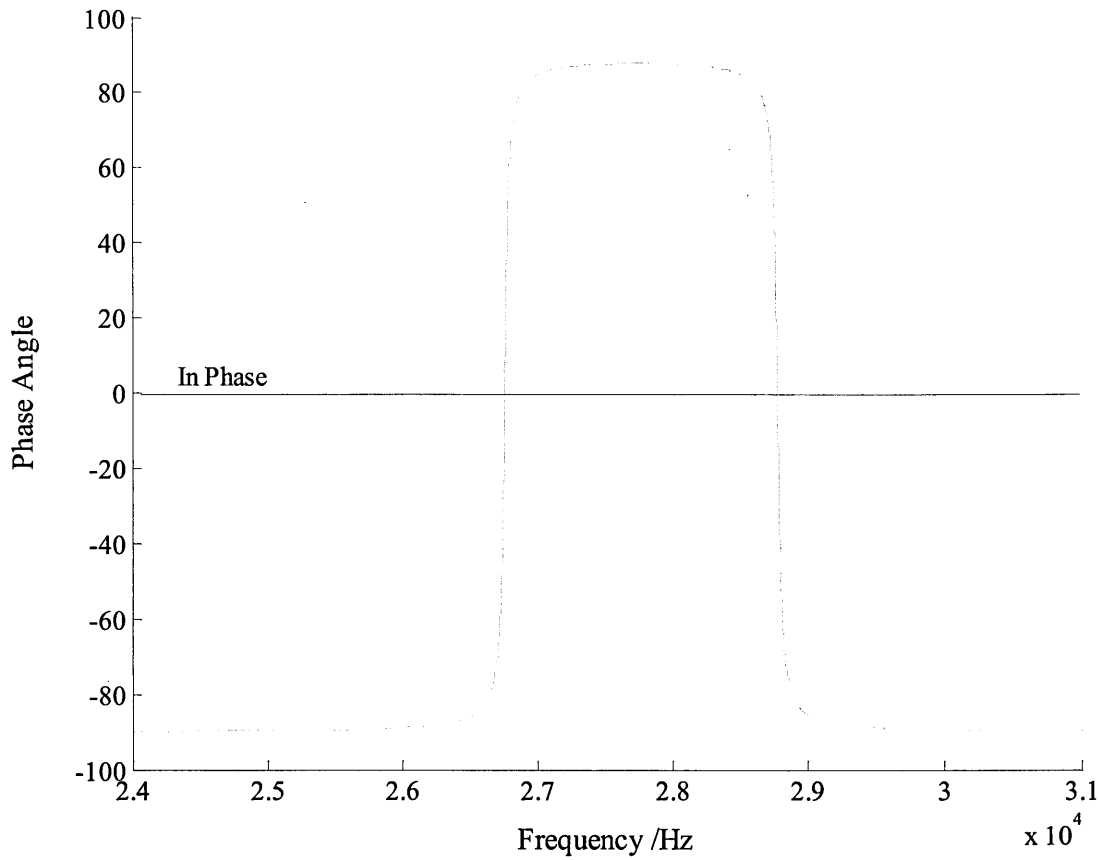

Figure 6-10: The phase angle of the complex impedance

As described in chapter 4 the transducer is driven as part of a LCR circuit tuned either in series or parallel. The values of inductance needed to tune to the series and parallel frequencies of the transducer were calculated using equations (159) and (160). These are shown in Table 6-4.

Table 6-4: Calculated values of inductance needed for resonance

Tuning	Value of Inductor / H
Series	7.9×10^{-3}
Parallel	9.1×10^{-3}

Inductors of these values were then inserted into the Matlab Simulink models (Figure 6-11 and Figure 6-12). As described in chapter 4.2 the energy transferred to the acoustic load is modelled by a resistor (labelled acoustic load in Figure 6-11and Figure 6-12), the power transferred to acoustic load, a gas in the case of this project, can be calculated as the electrical power transferred to this resistor. A Simulink model was run to determine the power transferred to the resistor in each case and thus whether series or parallel tuning resulted in a higher electro-acoustic efficiency. The results are shown in Table 6-5.

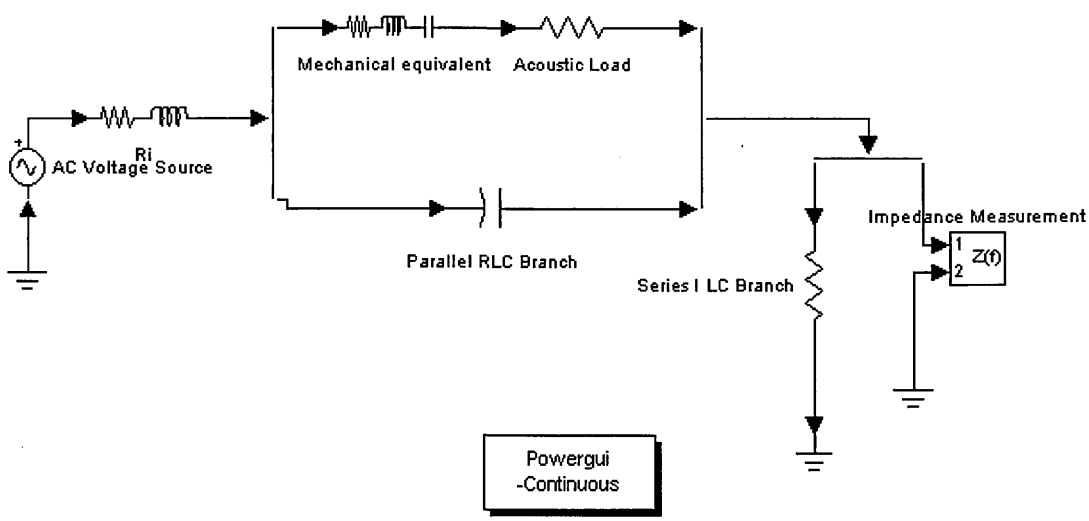

Figure 6-11: Simulink model of a transducer tuned with a series inductor

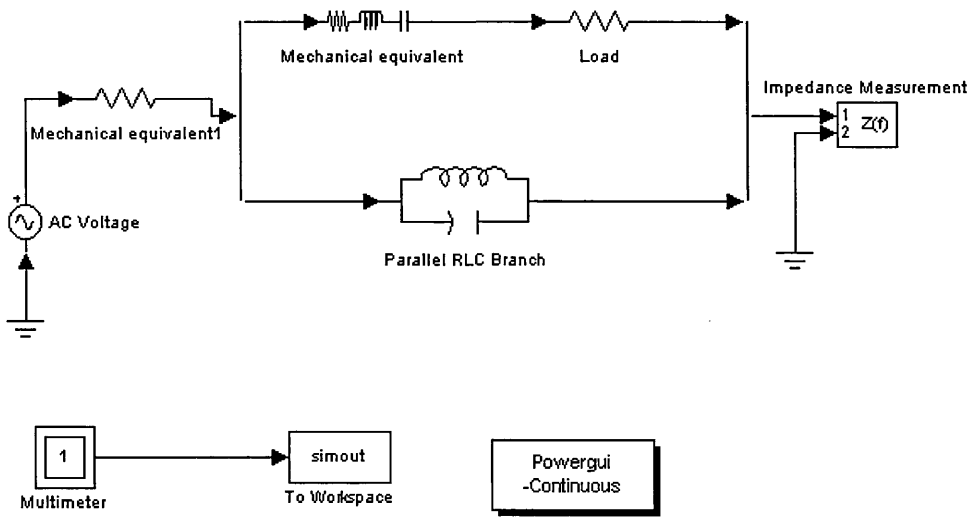

Figure 6-12: Simulink model of a transducer tuned with a parallel inductor

Table 6-5: Transfer coefficients of different inductors showing that the parallel inductor transfers more energy to the sound field

Tuning	Power transferred to load / W	Electroacoustic efficiency / %	Current through the load / A
Series	2.2×10^{-5}	0.034	0.05
Parallel	0.18	0.057	4.45

The overall electro-acoustic efficiency was determined to be approximately 0.1 %

6.2 Designing a matching layer

The transmission of sound energy from the transducer to the ultrasonic field depends on the acoustic impedances of the transducer and the surrounding atmosphere (as described in chapter 4). The acoustic coupling of aluminium-air is 1/200000 so to get enough energy transmitted into the standing ultrasonic field an acoustic matching layer with an intermediate acoustic impedance must be used. A material for the matching layer must be chosen that allows the transmission most of the energy sound out in the direction of the trap. The acoustic impedance of the glue used to attach this matching layer to the transducer must also be matched.

Experiments were conducted with several different matching layers to discover which was most successful in sustaining levitation of our aerosol sample. Using equations (164) and (165) from chapter 4 the ideal acoustic impedances given by the two equations for the transmission of sound between a layer of duralumin and air are Z_g = 78057 Pas/m and Z_m = 54640 Pas/m. There are no common materials with acoustic impedances that match these values and so several alternatives were tried with the comparable acoustic impedances (Table 6-6). Matching layers were machined that had the same radius as the high gain end face of the transducer. Plastics have a high acoustic attenuation and so two different lengths of transducer were tried, one with a length of a quarter of the length of the sound wave at the resonance frequency in that material and one with a length of just a few mm.

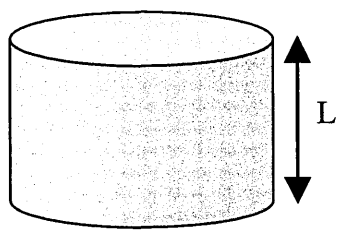

Figure 6-13: Diagram to show the shape and dimensions of the matching layer.

Table 6-6: Matching layer properties

Material	Acoustic Impedance / Pas/m	Length, L / cm
Low density polythene	1755000	1.2
Low density polythene	1755000	0.3
PTFE	3000000	1.2
PTFE	3000000	0.3

The matching layer that provided us with the greatest levitating power was the low density polythene layer with a length 0.3 cm. This layer was glued onto the high gain end face of the transducer with an epoxy resin which acts also as an acoustic couplant.

It was discovered that after a length of time in use the epoxy resin was processed by the ultrasound and the heat from the transducer which meant that levitating power was lost. When this effect was seen the matching layer was removed using acetone and then re-glued and full performance was regained, a heat cured adhesive was found to greatly reduce the frequency with which this needed to be done. Although the heat cured adhesive required a high curing temperature (approximately 130 °C) the Curie temperature of PZT- 4 is approximately 350 °C meaning that no loss of performance of the PZT occurred during the curing process. To maximise the transmission of sound energy through the epoxy some transducer production companies e.g. ONDA Corporation (ONDA, 2012) recommend adding aluminium or tungsten powder to the epoxy resin to increase its acoustic impedance to be the geometric mean of the acoustic impedance of the two layers to be matched. The powder added should be as fine as possible so that it will not sink through the epoxy as it dries. Figure 6-14 shows how the acoustic impedance of epoxy resin changes as you change the percentage by mass of tungsten powder, the acoustic data used to calculate the acoustic impedances was from the ONDA Corporation online database (ONDA, 2012).

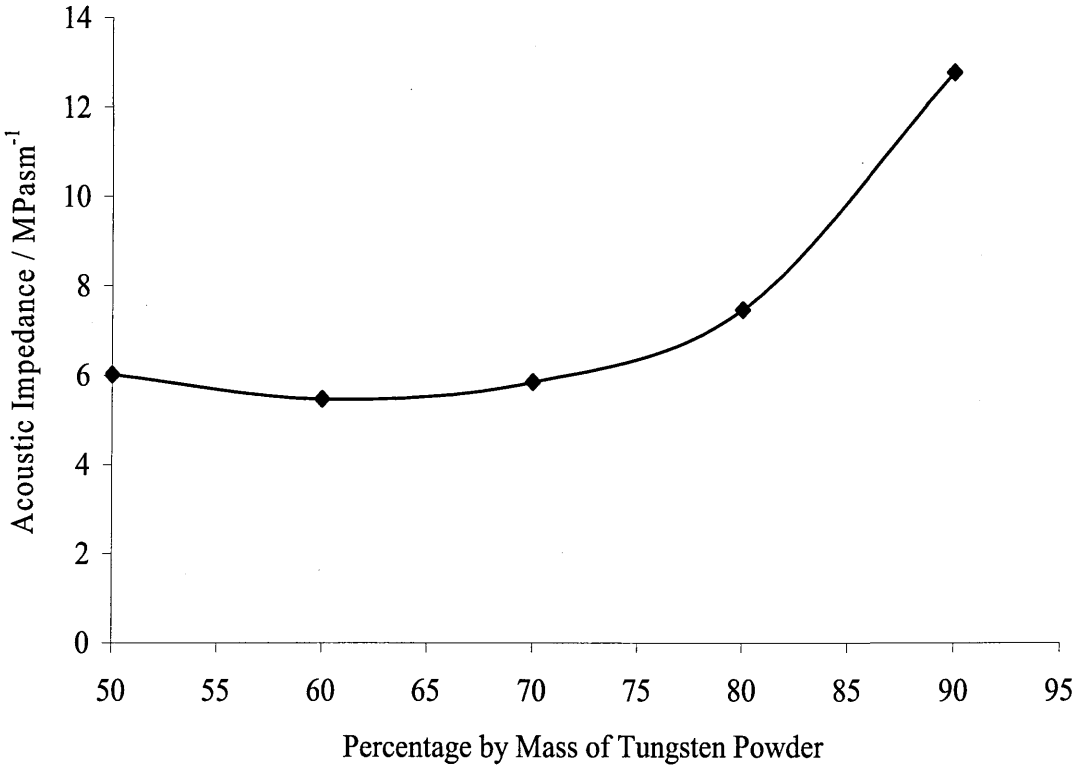

Figure 6-14: A graph to show how the specific acoustic impedance of epoxy resin changes as you vary the percentage by mass of added tungsten powder

The materials involved in the design of our sandwich transducer need to be glued and therefore matched with a suitable epoxy resin. Table 6-7 shows the acoustic properties of the materials used in the design of our transducers(ONDA, 2012).

Table 6-7: A table giving the acoustical properties of materials used in the transducers (ONDA, 2012)

Material	Density / kgm^3	Speed of Sound / ms^{-1}	Acoustic impedance / $Pasm^{-1}$
PZT	7500	4800	36000000
Steel	7800	5900	46020000
Aluminium	2730	6380	17417400
Polythene	920	1950	1794000

Each join between two layers will require a matching layer with acoustic impedance that is the geometric mean of the acoustic impedances of the two layers, these values and the recommended percentages of added tungsten by mass are shown in Table 6-8.

Table 6-8: A table to show the optimum percentage by mass of tungsten added to the epoxy resin for matching different materials

Layer 1	Layer 2	Geometric Mean of Impedances / $Pasm^{-1}$	Optimum Percentage of Tungsten Powder by Mass
PZT	Steel	40702825	As high as possible
PZT	Aluminium	25040495	As high as possible
PZT	Polythene	8036417	80-85
Aluminium	Polythene	5589885	60-65

To glue two surfaces together we first had to use an abrasive sand paper to make the surface rough and then clean the surfaces with alcohol to ensure a strong bond. The layer of glue then needs to be spread evenly and be made as thin as possible. During construction the epoxy resin should be allowed to run freely over the mesh making sure there are no air pockets.

6.3 The resonant ultrasonic field

To levitate high density solids requires a large amount of energy in the standing field so the reflector must be designed that minimises energy loss from the sound field. Empirical guidelines have been found that provide the optimum geometry for maximising levitating forces (Xie and Wei, 2001), the radius of the spherically curved reflector (R_a) should be as large as possible but if the radius is much larger than the wavelength of sound then one should ensure that the curvature of the reflector (R_b) should be as small as possible. Wiklund et al. (Wiklund et al., 2004) also found that the length of the resonating field, L, should be smaller than the radius of curvature of the curved reflector, R_b. Furthermore Wiklund et al. suggested that to minimise the

lateral losses the lateral radii of the nodes closest to the plane reflecting surface of the transducer, w_t, and of the node closest to the curved reflector, w_r, of the resonant field must also be less than the radius of the respective reflecting surfaces. The lateral radii of the nodes are given as

$$w_r = \left(\frac{\lambda^2 R_a^2 L}{\pi^2 (R_a - L)} \right)^{\frac{1}{4}} \tag{197}$$

$$w_t = \left(\frac{\lambda^2 L (R_t - L)}{\pi^2} \right)^{\frac{1}{4}} \tag{198}$$

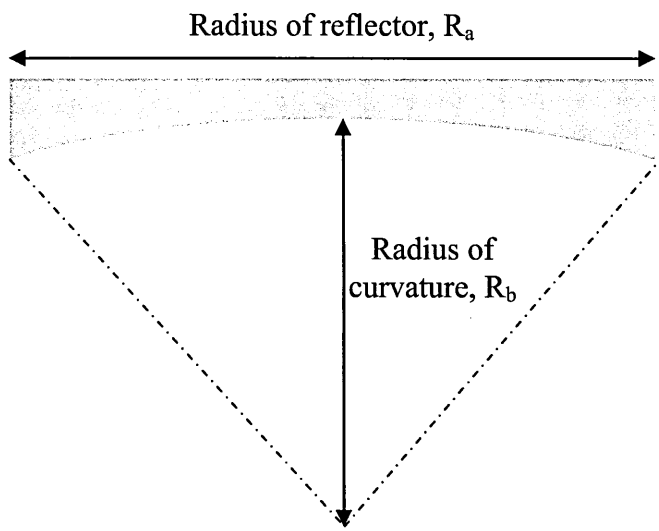

Figure 6-15: Diagram to show the measurements of the reflectors

Several spherically curved reflectors were used to find which gave both enough power to the resonant field and enough stability (Table 6-9). Although guidelines recommended a small radius of curvature the reflector that was observed to give the most stable levitation was reflector 5. The diameter of the reflector of reflector 1 does not meet the criteria set out in by the constraints given in relation to equations (197)

and (198) as the radius length of the resonant field was typically 4 cm. For the other reflectors the radii of the lateral nodes were calculated to be w_r = 2.0 cm and w_t = 1.0 cm.

Table 6-9: Table to show the properties of reflectors used

Reflector	1	2	3	4	5	6
R_a / cm	4	7	7	7	7	7
R_b / cm	3	5	12	18	24	∞

A signal generator with adjustable frequency (Thurlby Thandar Instruments, TG1010) was used to produce the oscillating signal which was then amplified by a 200 W power amplifier, the amplified was built in-house from a potted amplifier circuit bought from BK Electronics (MF200). The transducer formed part of an LCR circuit which was oscillated by this signal. The series and parallel tuning inductors for the circuit were made by wrapping enamelled copper wire around spools with hollow cores small enough to insert ferrite cores (10 mm diameter and 100 mm length ferrite rod bought from Rapid) and the resistors were 1 Ω Arcol (Aluminium Clad) heat sink resistors. The inductors were made so that by moving the ferrite cores in and out of the tubes it allowed for a range of possible inductances, the centre of the ranges were chosen to be the modelled values of the respective inductances. Building the inductors so that they were tuneable was found to be useful as during experimentation there was a drift in the frequency and inductance that would result in a resonant transducer; this was probably due to heating of the transducer.

The frequency of the signal generator was adjusted to find the resonant frequency and the relative strength of the acoustic signal was measured by a small piezo-electric

crystal embedded in the reflector (6 mm diameter and 2 mm think disc transducer of material C-5400 bought from Channel Industries). The microphone was recessed into a bored cavity in the reflector, the wires were taken back through a hole in the reflector so that they did not disrupt the standing field. An oscilloscope (Tektronix TDS 500B) was used to observe the voltage across the transducer and microphone.

Initial attempts at levitation of polystyrene balls are shown in Figure 6-16. The balls were made of expanded polystyrene and were approximately 2-3 mm in diameter. The balls were trapped in the antinodes of the field and could be held for long periods of time (during experimentation they were levitated for over one hour). The maximum number of balls levitated at any one time was 14.

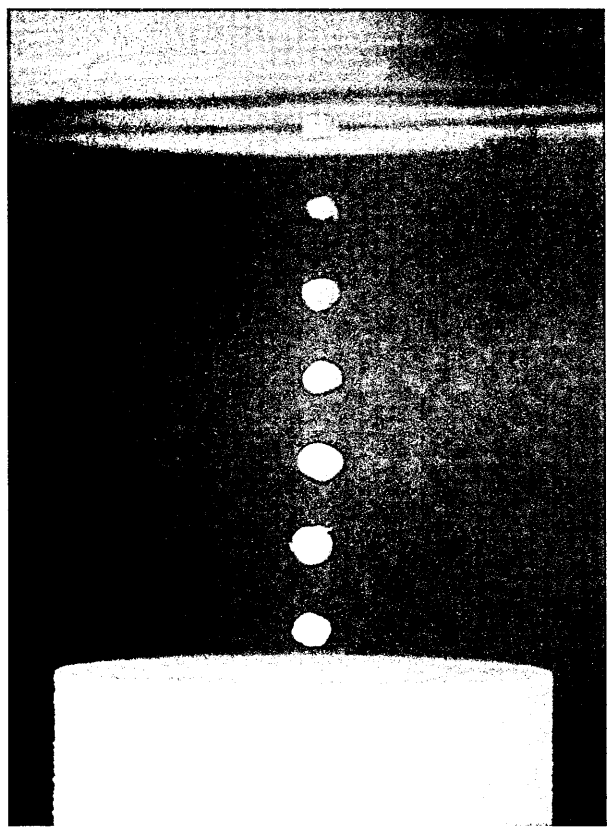

Figure 6-16: First Attempts at ultrasonic levitation

6.4 The Chamber

A chamber needed to be designed so that the trap could be enclosed in an infra-red inactive atmosphere so that spectra could be taken. The chamber must be large enough so that the reflected sound waves from the chamber have attenuated sufficiently so as not to affect the standing sound field used for levitation. The chamber chosen was a 6 port stainless steel vacuum chamber (Figure 6-17). The chamber was first evacuated using a rotary pump and the pressure measured using a pirani gauge.

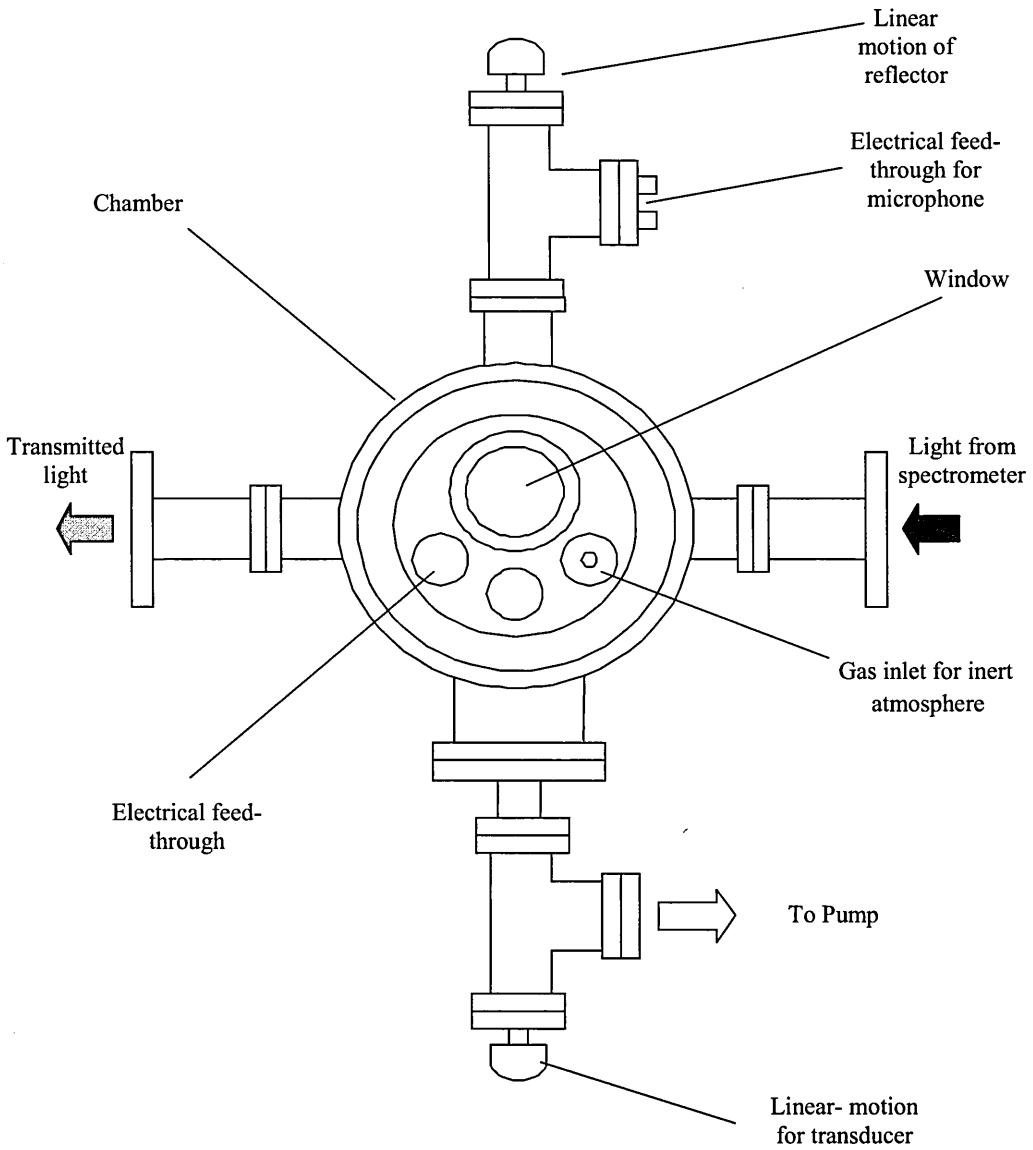

Figure 6-17: A diagram of the vacuum chamber used to contain the acoustic trap

The transducer needed to be held in a fixed position in the chamber whilst being allowed to vibrate freely in the vertical direction. To ensure that as much of the sound energy radiated into the chamber as little contact as possible must be made with materials of similar acoustic impedance. A clamp was designed and made in-house that tightened around the circumference of the steel end and which was in contact with the transducer by means of a thin rubber ring. This clamp was glued onto a platform. As the impedance matching of the front face with the levitating gas was so poor the design of this clamp was important as we had to ensure that as little energy was lost through the back face. As the transducer was not touching the platform its back face was air backed and because it was steel it had a much poorer impedance matching than the front face. It was necessary to have as little contact with the transducer as possible and so the narrow rubber ring made sure that the transducer was held as lightly as possible without allowing it to move. Fixing the transducer by its circumference at the very bottom of the back face meant that the transducers resonance and oscillation was damped by as little as possible.

Both the transducer platform and reflector were mounted onto linear feed-throughs so that the levitating aerosol could be placed in the path of the beam of infrared light when the chamber was attached to the spectrometer and detector. Figure 6-18 shows how the transducer and reflector were mounted on their linear feed-throughs.

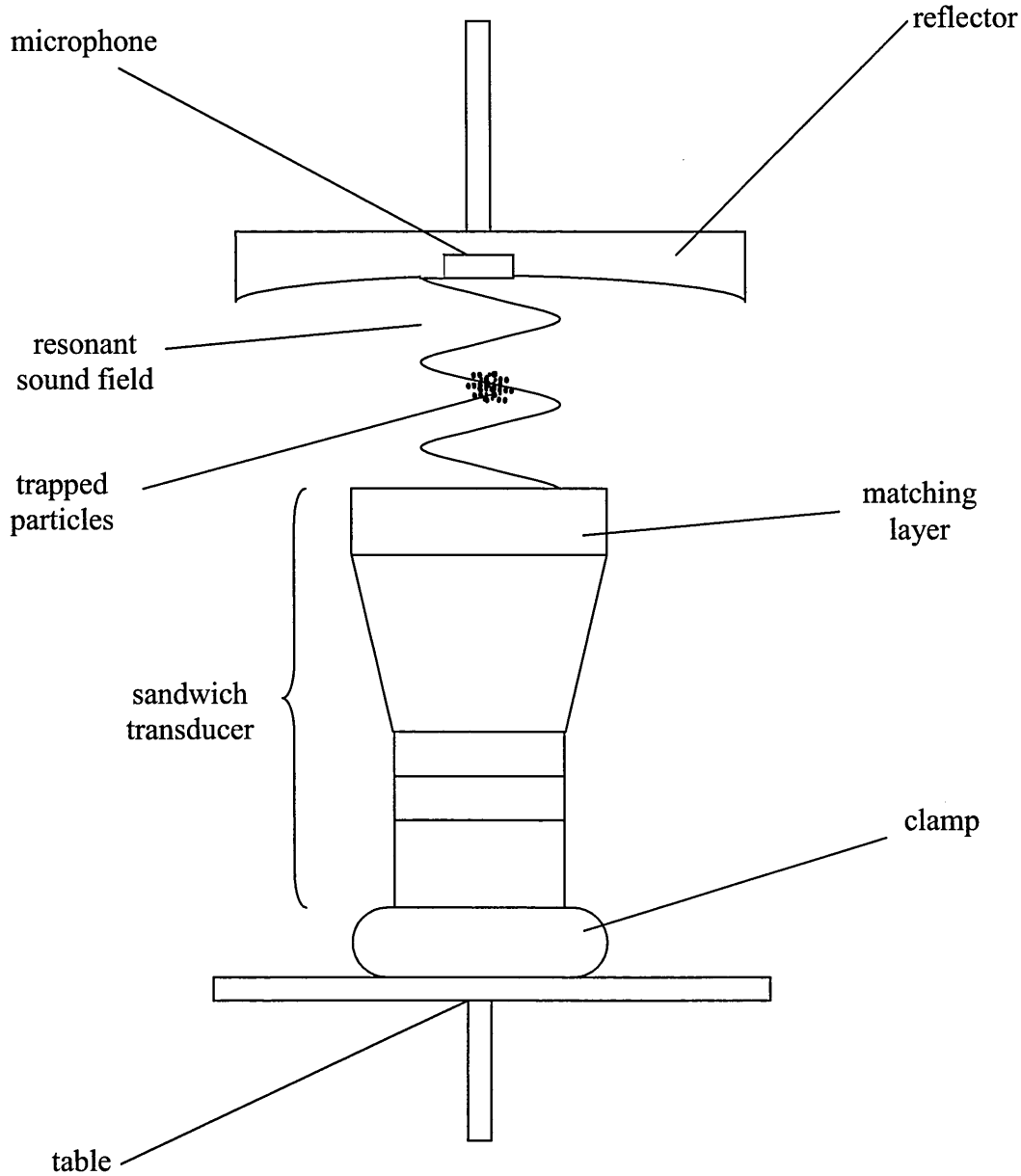

Figure 6-18: Diagram of Acoustic Trap

The chamber was lit by three 3 V, 5 mm diameter, white light LEDs which were mounted inside the chamber at a distance of approximately 10 cm from the edges of the reflector so that a web camera (Logitech Quickcam Pro) which was mounted outside the chamber looking through a window could be used to obtain video images of the samples during levitation. To enhance contrast of the volcanic ash a disc of white PTFE was placed vertically behind the transducer. Spectra were taken with the

LED lights on and off to ensure that the wavelengths of light emitted by the LEDs were not picked up by the infra red detectors.

It was noticed that the samples were clumping when subjected to an acoustic field; Sarabia et al. (Riera-Franco de Sarabia et al., 2003) had suggested that if there is a high humidity the particles are more likely to clump so we added a heating mechanism to drive off the water (Figure 6-19). This mechanism was made in-house and consisted of four heat sink resistors (Arcol 15 W, 22 Ω ± 5 %) screwed onto a copper block (2.5 × 2.5 × 2 cm) which was in turn attached to the reflector and wired in series. A current was then passed through the resistors causing them to heat up causing the water in the sample to evaporate. The chamber was then pumped down removing the water vapour. An NTC thermistor (Honeywell Unicurve, 192-501DET-A01, tolerance ±0.2 °C) was used to measure the temperature in the chamber and temperatures in excess of 100 °C were readily achievable. The thermistor was allowed to hang freely from any surface so that it could measure the gas temperature and was at least 5 cm away from the standing wave during operation so as not to disrupt it.

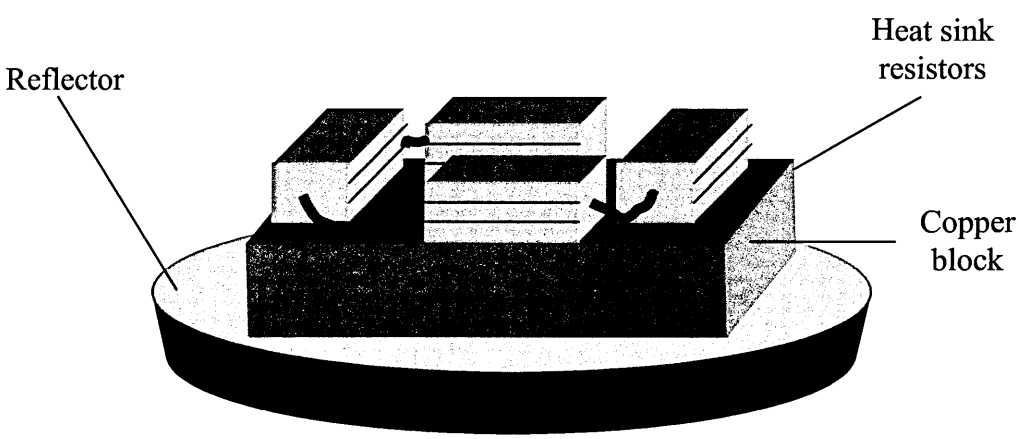

Figure 6-19: A diagram of the heating mechanism.

It was also possible to cool the cell by flowing cooled ethanol through stainless steel five spiral loops of tubing attached to the copper block. The ethanol flowed through a closed loop, which is coiled through a bath of ethanol which in turn cooled by liquid nitrogen. The set-up for this is shown in Figure 6-20. The temperature of the bath is measured with a platinum resistance thermometer (PRT, PT100 Pico Technology) and the addition of nitrogen is regulated using a PID controller (Tempatron PID 330). Using this method it was possible to cool the chamber to -50 °C.

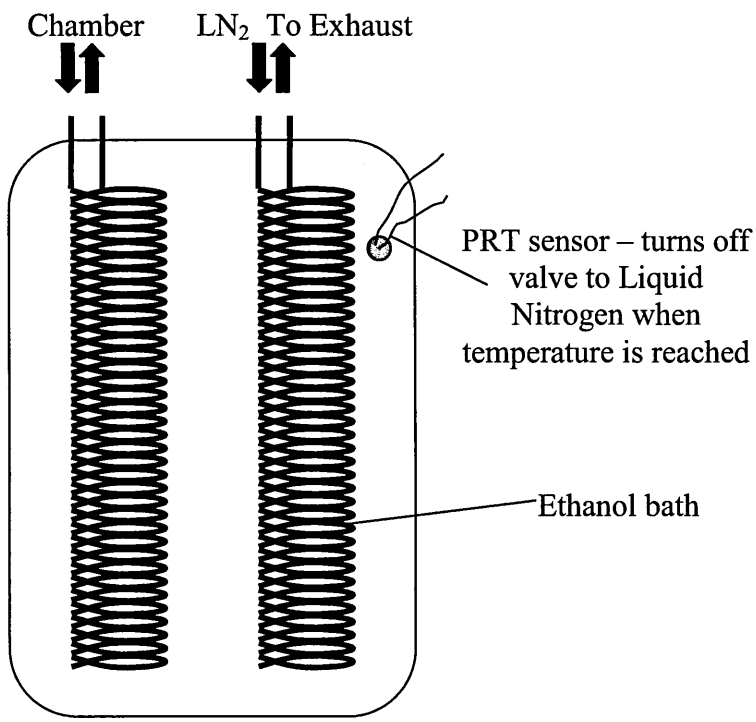

Figure 6-20: A diagram to show how the chamber was cooled

The front and back ports of the chamber were fitted with potassium bromide (KBr) windows to stop aerosol contamination spreading into the spectrometer or detector. The top and bottom ports were used for the linear feedthroughs to both the transducer and reflector. One of the side ports was used for access to the chamber to place and collect samples. The other side port held the electrical feedthrough (needed for power supply to the transducer, LEDs, thermistor and the heating element), the feedthrough

for the cooled ethanol, a window through which the webcam recorded the samples and a feedthrough to allow the chamber to be filled with gas. Figure 6-21 and Figure 6-22 below show the trap installed at the Rutherford Appelton Laboratories.

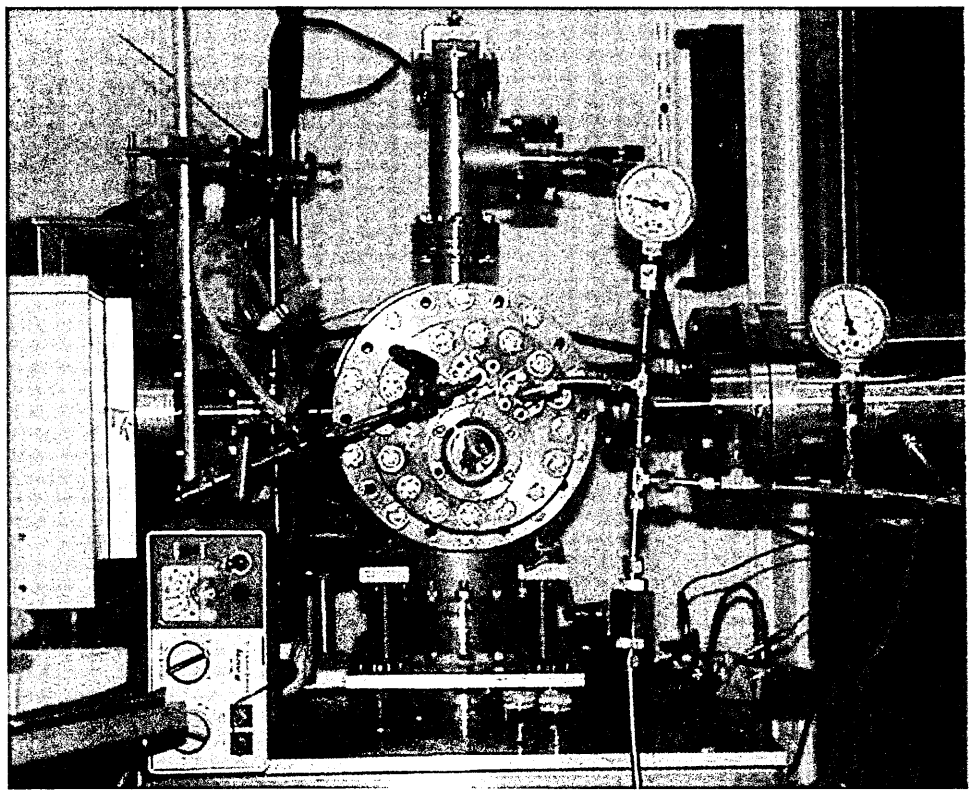

Figure 6-21: The acoustic trap installed at RAL

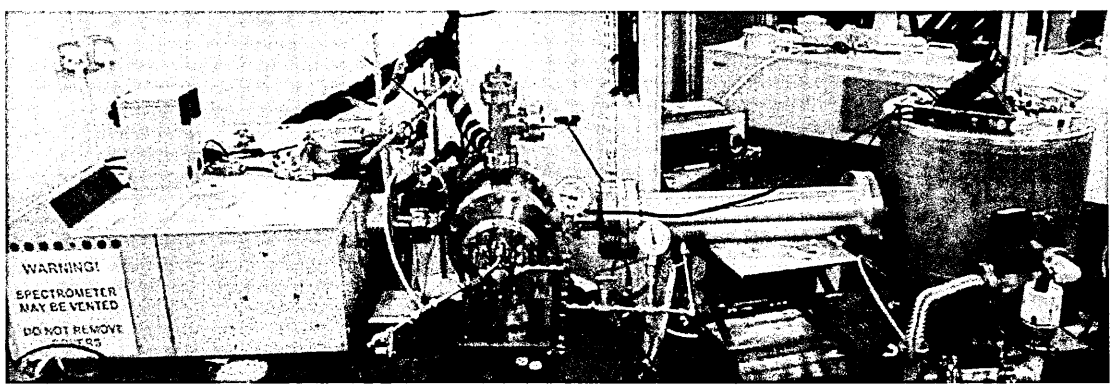

Figure 6-22: the acoustic trap attached to spectrometer and detector at RAL

Chapter 7: Aerosol Spectroscopy

This chapter describes results of the application of this chamber to FT-IR spectroscopy of aerosols and how the data collected can be used to obtain values for the complex refractive index at many wavelengths.

7.1 Preparation of Samples

Our samples were soot, sand and two volcanic ashes, one being a basalt (low percentage of silicate: ≈50 %) and the other being a Rhyolite (High percentage of silicate, ≈75 %). The volcanic samples were donated by Prof. Stephen Self, Department of Environment, Earth and Ecosystems at the Open University. The basaltic sample (07-07-91-04) was from an eruption in the Sunset Crater, Arizona, U.S.A. in AD 1065. The rhyolitic (NZ 82-4) sample is ash from the Taupo Caldera, New Zealand, a huge eruption about 26,000 years old. The sample was a natural ash sample from an eruption that involved mixing of basalt magma with seawater. Table 7-1 shows the major oxide composition of the volcanic ash samples.

Table 7-1: Major mineral composition of the volcanic ash samples

	% oxide by weight	
Oxide	**Rhyolite**	**Basalt**
SiO_2	71.79	50
TiO_2	0.42	
Al_2O_3	14.69	
Fe_2O_3	3.05	
MnO	0.10	
MgO	0.63	
CaO	2.53	
Na_2O	4.15	
K_2O	2.55	
P_2O_5	0.09	

The soot sample was collected from inside the chimney of a domestic coal fire and the sand sample is builders' sharp sand from a local builders' merchant. The samples were then milled using an agate TEMA grinding mill as shown in Figure 7-2. Agate was used because although it was not as hard as tungsten carbide it introduces less contamination. To clean the grinding mill between samples sand was crushed for 6 minutes and removed before washing it with warm water and drying with compressed air.

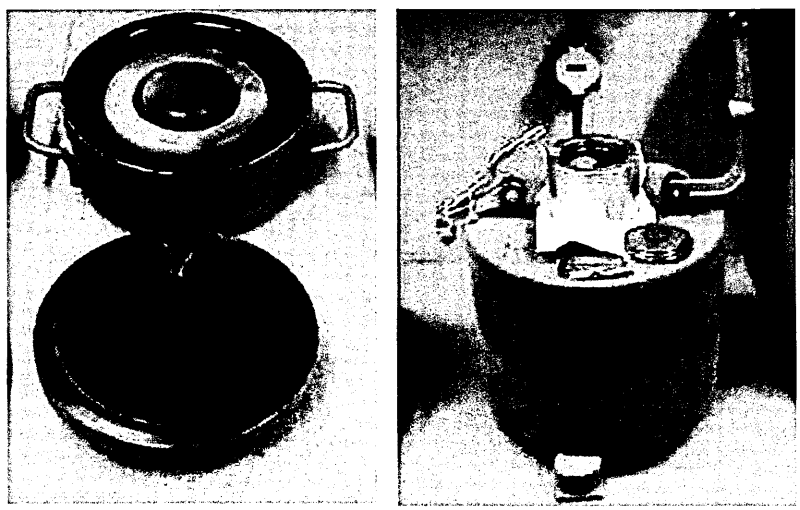

Figure 7-1: A picture of an agate grinding mill similar to the one used (TEMA, 2012)

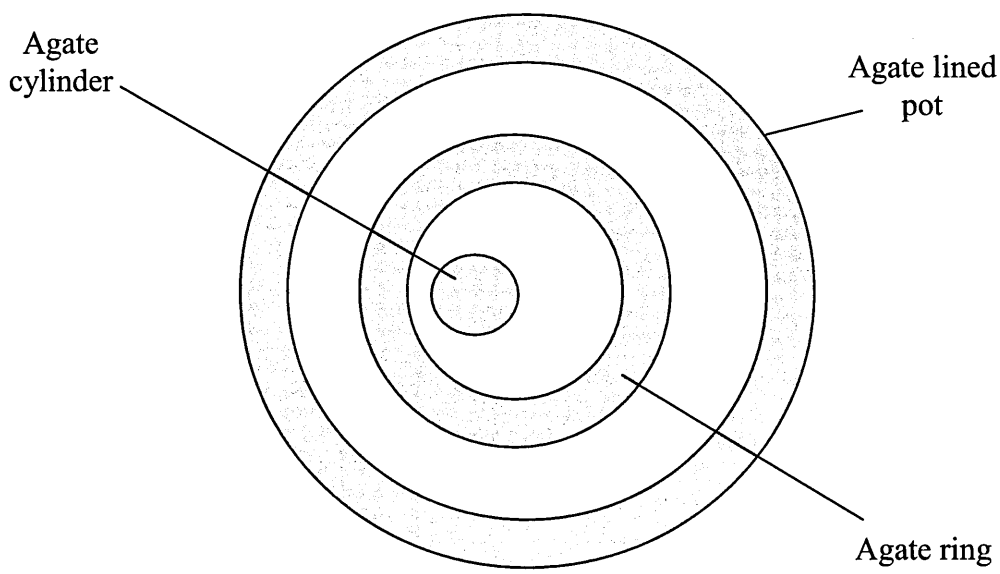

Figure 7-2: TEMA grinding mill used for crushing samples

Roughly 50 g of ash were distributed equally between the layers, the TEMA grinding mill then vibrates and as it does the agate ring and cylinder move independently which crushes the sample to micrometer range particles. Samples were left for between 15 and 45 minutes depending on how long they took to obtain fine texture as felt by hand.

The most readily available method to size the dust samples was a graduated sieve. The samples were sieved into four size bands corresponding to the smallest sizes of graduated sieve available below 100 μm: <32 μm, 32-45 μm, 45-63 μm and 63-90 μm and >90 μm. The mass proportions of each of the size ranges after sieving are shown in Table 7-2.

Table 7-2: The percentage of the total mass of the samples in each size range after sieving

	% of total mass after sieving			
Size range / μm	**soot**	**Sand**	**Basalt**	**Rhyolite**
<32	24.2	0.4	7.7	10.0
32-45	11.7	1.0	3.0	7.2
45-63	16.8	1.5	5.9	9.6
63-90	12.2	1.4	3.6	10.0
>90	34.9	95.7	79.7	63.1

Each of the first three size ranges were investigated spectroscopically. This smallest size range that this method produced was <32 μm, but it was felt that this size range was too broad and large to represent the types of aerosol we were interested in. Also to obtain maximum entrainment of particles within our sound field and reduce agglomeration we are looking for a maximum size of particle of 0.6 μm. Another method was developed to obtain a smaller size range. The outline of the method was

that a long section of plastic pipe 2 m long and about 5 cm in diameter was held in a vertical position and filled with water. Stokes' law of the frictional force on spherical objects with small Reynolds numbers (i.e. very small particles) falling through a continuous viscous fluid was then used to determine the frictional force on a 10 μm particle of each sample. We are able to use the Stokes' law approximation as the Reynolds numbers of our aerosols flowing through water are very small (approximately 0.005 for a 10 μm particle flowing through water).

$$F = 6\pi\mu RV \tag{1}$$

where F is the drag force on the particle, μ is the dynamic viscosity of the fluid, R is the radius of the particle and V is the velocity that the particle is travelling. The velocity of the particle was assumed to be the terminal velocity of the particle through the medium which given by

$$V_T = \frac{2}{9}\frac{\left(\rho_p - \rho_f\right)}{\mu} gR^2 \tag{2}$$

where V_T is the particles terminal velocity, g is the acceleration due to gravity and ρ denotes the densities of the particle and fluid. These equations are used for rigid, spheres travelling in a viscous liquid. Volcanic ash is not spherical and as such a dynamical shape correction factor needs to be used to predict the velocities with precision. Riley (Riley et al., 2003) conducted research to identify which easily measurable parameters of volcanic ash are the best at predicting shape and dynamic properties of volcanic ash. It showed that the diameters of ash particles were 10–120 % larger than ideal spheres at the same terminal velocity, indicating that irregular particle shape greatly increases drag. Since we are looking to impose an upper limit on our aerosol distribution size we have calculated the terminal velocity of a 5 μm diameter sphere (of the same density as each of our samples) and determined the time

that it would take it to fall 1.8 m through the tube, these values are given in Table 7-3. We know that the volcanic ash samples of the same equivalent volume would travel more slowly but we can know that, even with the maximum increase in drag, the ash aerosol particles that have passed 1.8 m depth would have a larger diameter than 10 μm.

Table 7-3: The time taken for a 5 μm particle of each of the samples to fall 1.8 m through water calculated using Stokes law.

Sample	Time for 5 μm particle to fall 1.8 m / minutes
Soot	1032
Sand	1307
Rhyolite	1189
Basalt	1962

A hole was then drilled 1.8 m down the tube and blocked with a bung. A diagram of this apparatus is shown in Figure 7.3. Each of the samples in turn was tipped into the top of the tube and after the respective times the bung was opened and the water from ***above*** the bung collected, this water should contain only particles on 10 μm or less. The collected sample was then left to settle in a shallow, covered container. Most of the water was then decanted away and the remainder was then left to evaporate. The sample was then dried by applying gentle heat and lightly ground to loosen the particles. Before use the samples were ultrasonically agitated to separate them.

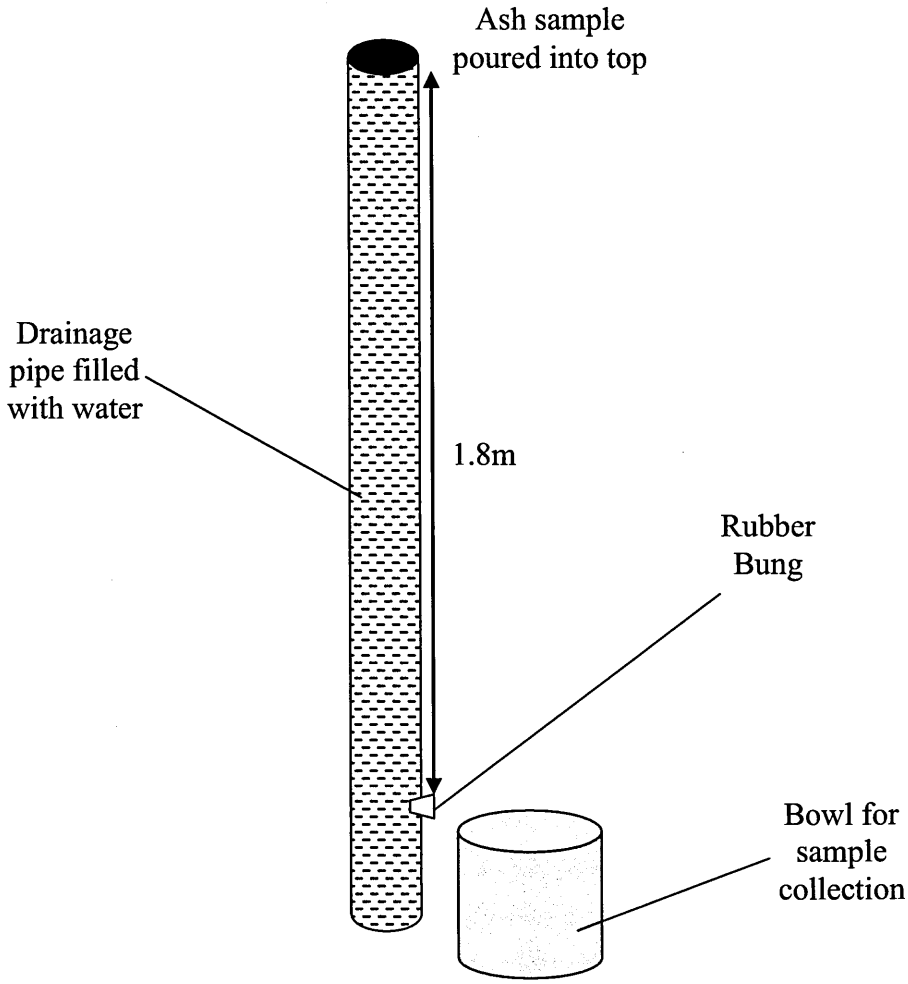

Figure 7-3: A Diagram to show the apparatus used to separate the samples using Stokes law.

7.2 Obtaining absorption spectra

The infra red aerosol spectra were measured on a Bruker IFS 120HR Fourier transform infrared (FTIR) spectrometer in the Molecular Spectroscopy Facility (MSF) at Rutherford Appleton Laboratory (RAL). This spectrometer has a resolution of up to 0.0015 cm^{-1} and operates over a wide spectral range (far IR to UV) (Newnham et al., 1996). During the work the spectrometer was configured with a broadband silicon carbide globar source operating at approximately 1000 K and a germanium/potassium bromide (Ge/KBr) beamsplitter. During sampling one hundred scans were obtained

and co-added. The radiation was detected using a broadband mercury-cadmium-teluride (MCT) detector (500-2000 cm^{-1}).

Several methods of inserting the aerosol into the trap were trialled,

- We used the method outlined by Gonzalez (Gonzalez et al., 2003) whereby a the aerosol was put onto an inclined, flat glass plane above the ultrasonic field and then subjected to a weak 20 kHz frequency oscillation which caused the aerosol to fall into the trap. This method worked well for large particles but the small particles were not drawn into the trap as easily.
- We also tried to insert the aerosol by means of a small (1 cm diameter), slightly dipped stainless steel platform next to the trap. The aerosol would be placed on the platform and a small Swagelock nozzle directed towards it. The nozzle would connected first to a needle valve and then to a pipe overpressure with nitrogen. When the aerosol was desired the needle valve would be opened and the resulting gust would blow some of the aerosol particulates into the trap. This method worked well for large particles but the small particles would be made airborne but not get drawn into the trap.
- The best method we found was to place small amounts of the sample (a few mg) were placed onto the top of the transducer, which was then lifted into the standing field when the transducer was switched on. This proved the best for trapping small particles but also allowed up to heat our sample using the reflecting mirror as a heat source as discussed earlier.

The chamber was then sealed and pumped down using a rotary pump and then refilled with infrared transparent nitrogen gas. A background sample was taken and then the

sample was levitated by switching on the transducer (Figure 7-4). In Figure 7-4 you can see three trapped nodes of volcanic ash.

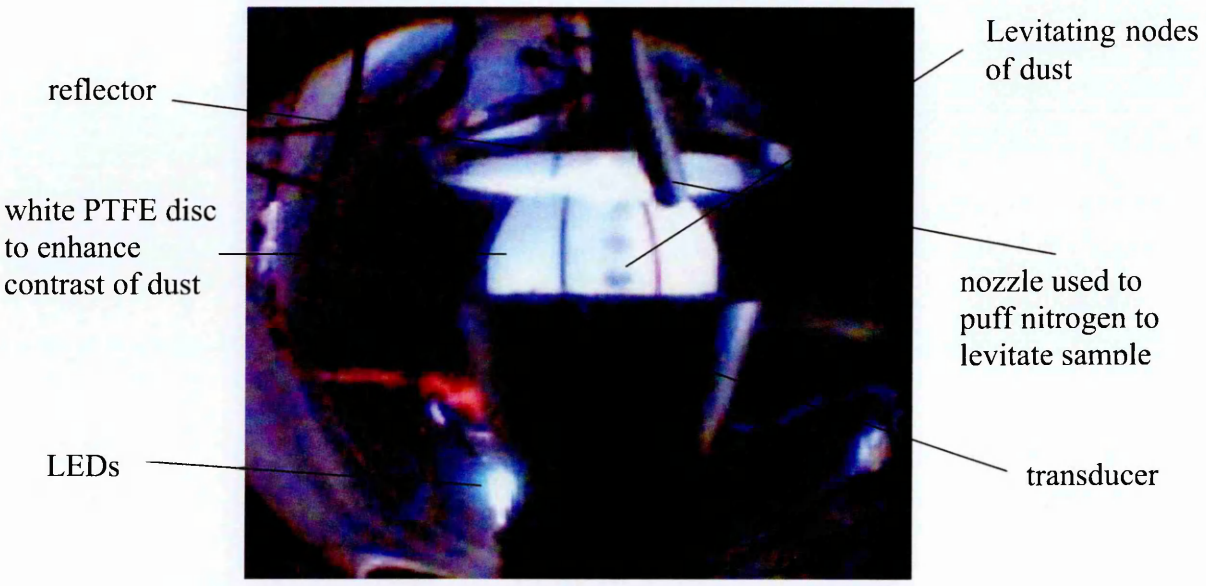

Figure 7-4: Images of dust levitating in the chamber

After measurement the sample was collected by vacuum suction: a small piece of fine mesh filter paper was clamped in place over a piece of stainless steel Swagelok tube. This tube was held under a small negative pressure by attaching it to a small diaphragm pump. A needle valve was placed between the filter and the tube under pressure, the needle valve was opened just enough so that the suction would remove the sample from the acoustic field. The Swagelok tube was found to be too large to insert into the acoustic field as it disrupted it before the sample could be collected. A glass Pasteur pipette with a fine needle nose was fitted to the pipe which collected the sample without disrupting the field. The mass of the filter paper was found beforehand and measured again after so that the mass of the sample could be determined.

Spectroscopic measurements were performed and examples of the absorbance spectra measured are shown in Figure 7-5 - Figure 7-8. These spectra are as expected with the silicate containing species rhyolite (Figure 7-5), sand (Figure 7-6) and basalt (Figure 7-8) showing the characteristic absorption feature of silicon dioxide at approximately 0.11 μm^{-1}. The absorbance of the soot (Figure 7-7) is also as expected with a broadly featureless spectrum showing broadband absorption.

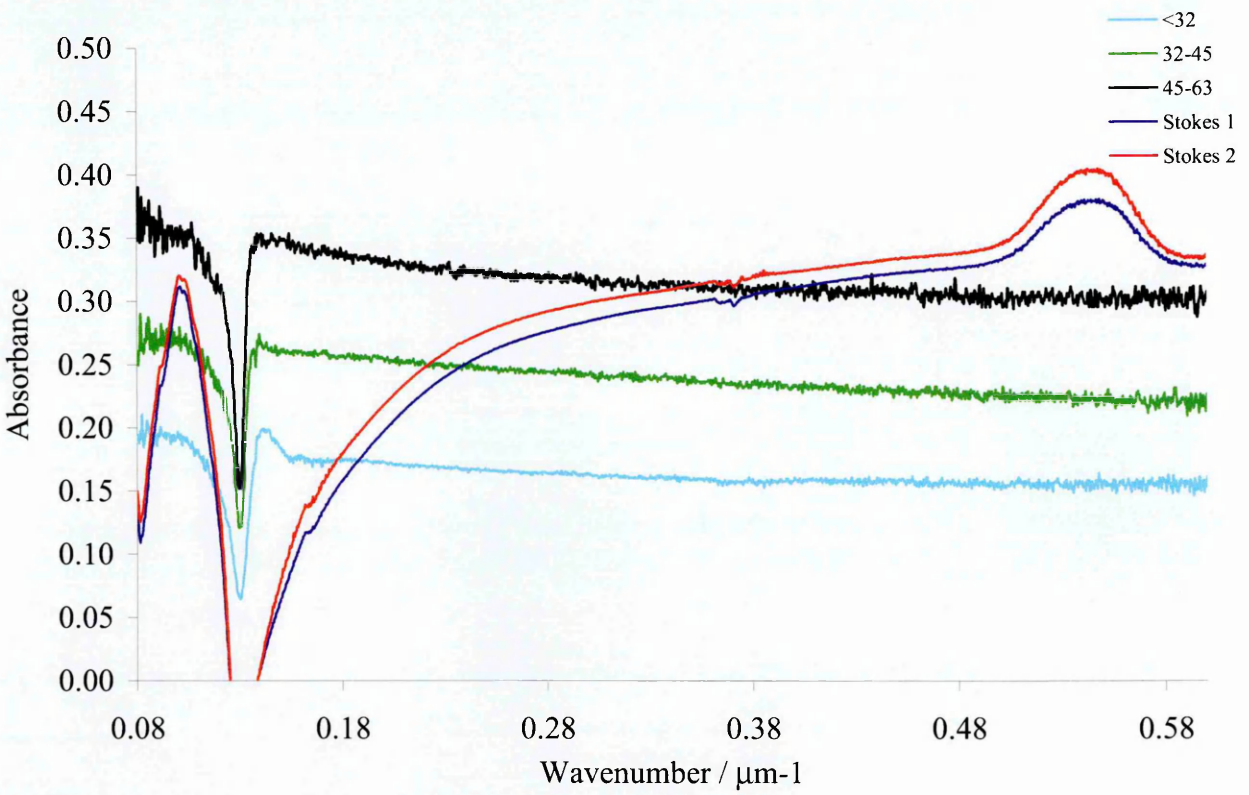

Figure 7-5: The absorbance spectra of the rhyolitc sample from (0.08 – 0.060) μm^{-1} for samples of the different size ranges < 32µm, 32 – 45 µm, 45 – 63 µm and two spectra of samples that have been selected for size by the stokes method

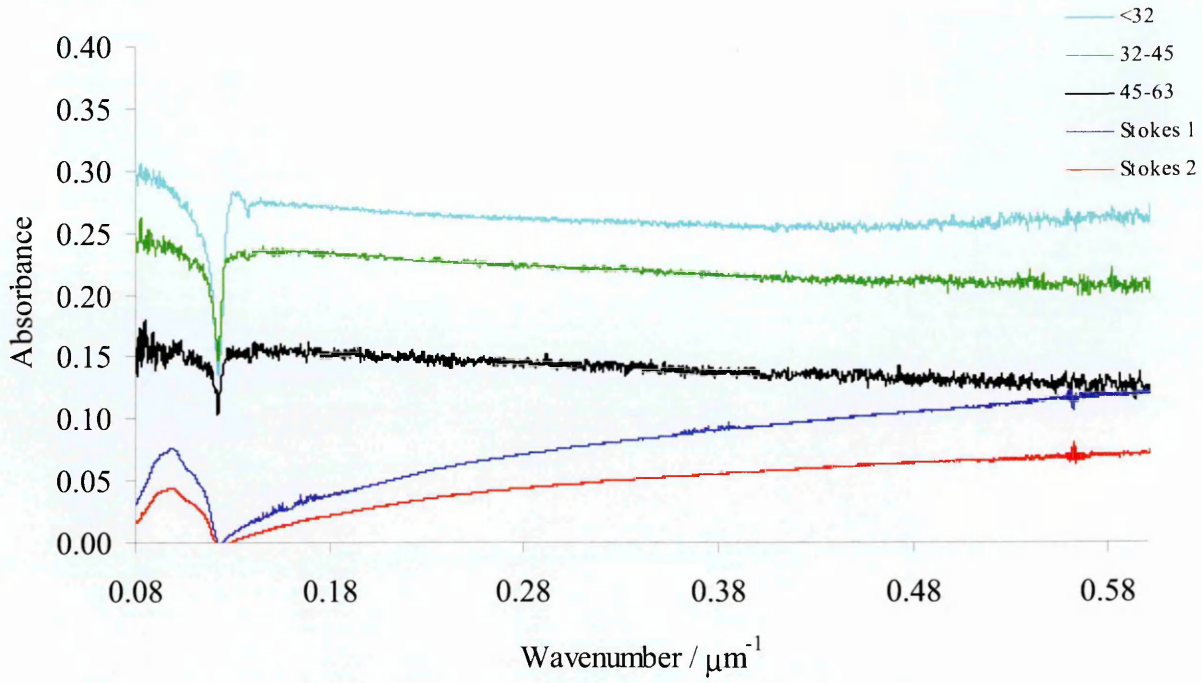

Figure 7-6: Absorbance spectra of the basaltic sample from (0.08 – 0.060) μm^{-1} for samples of the different size ranges < 32μm, 32 – 45 μm, 45 – 63 μm and two spectra of samples that have been selected for size by the stokes method

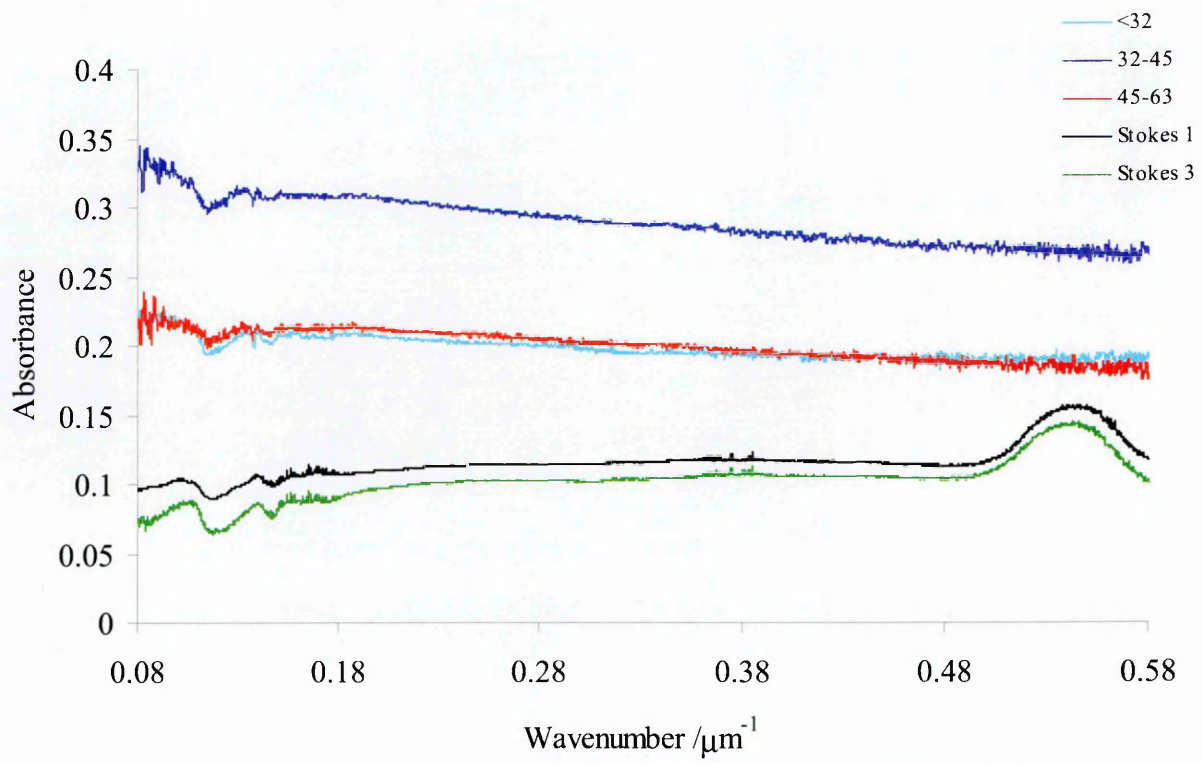

Figure 7-7: Absorbance of the soot sample from (0.08 – 0.060) μm^{-1} for samples of the different size ranges < 32μm, 32 – 45 μm, 45 – 63 μm and two spectra of samples that have been selected for size by the stokes method

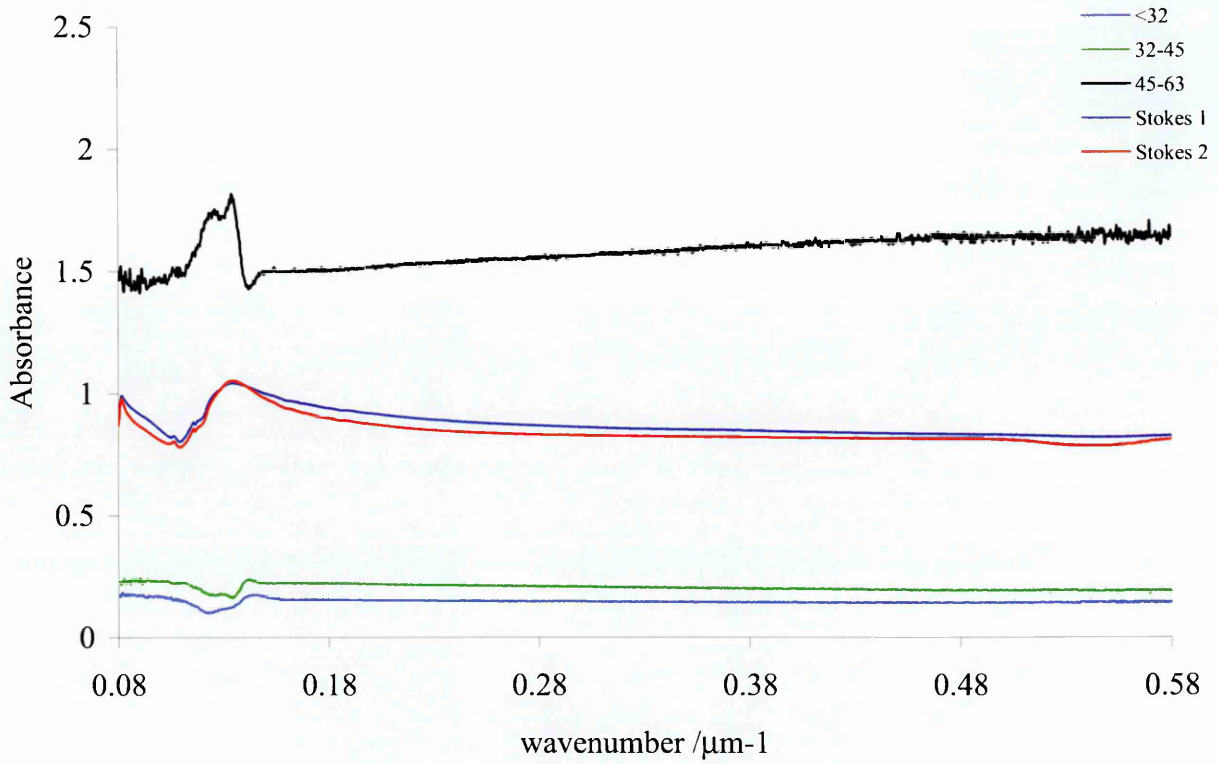

Figure 7-8: Absorbance spectrum of sand sample from (0.08 – 0.060) μm^{-1} for samples of the different size ranges < 32 µm, 32 – 45 µm, 45 – 63 µm and two spectra of samples that have been selected for size by the stokes method

7.3 Determining the properties of the trapped aerosol

First the mass of each of the samples was found using a sensitive microbalance, the masses trapped in the nodes varied for each sample from 0.05 mg to 10.09 mg. To find the size distribution of the aerosols we decided to image them using a scanning electron microscope (SEM). Since our samples are non-conducting they have to be coated with a conducting material to prevent charge build up before they can be imaged using the scanning electron microscope. The coating chosen was gold which had to be between 2-20 nm thick to prevent charging. To coat the samples we mounted the samples onto the stubs using a sticky carbon film. The plasma coating was laid down under a 5×10^{-2} mbar argon plasma atmosphere. The gold electrode was

held at a distance on 7 cm over our sample and the current between the electrodes was 20 mA. The samples were left to coat for 90 s in a 2 kV potential difference.

The SEM used was a Zeiss supra 55Vp, each sample was imaged at 12 magnifications in the range of 70 to 20000, example images can be seen in Figure 7-9 - Figure 7-12.

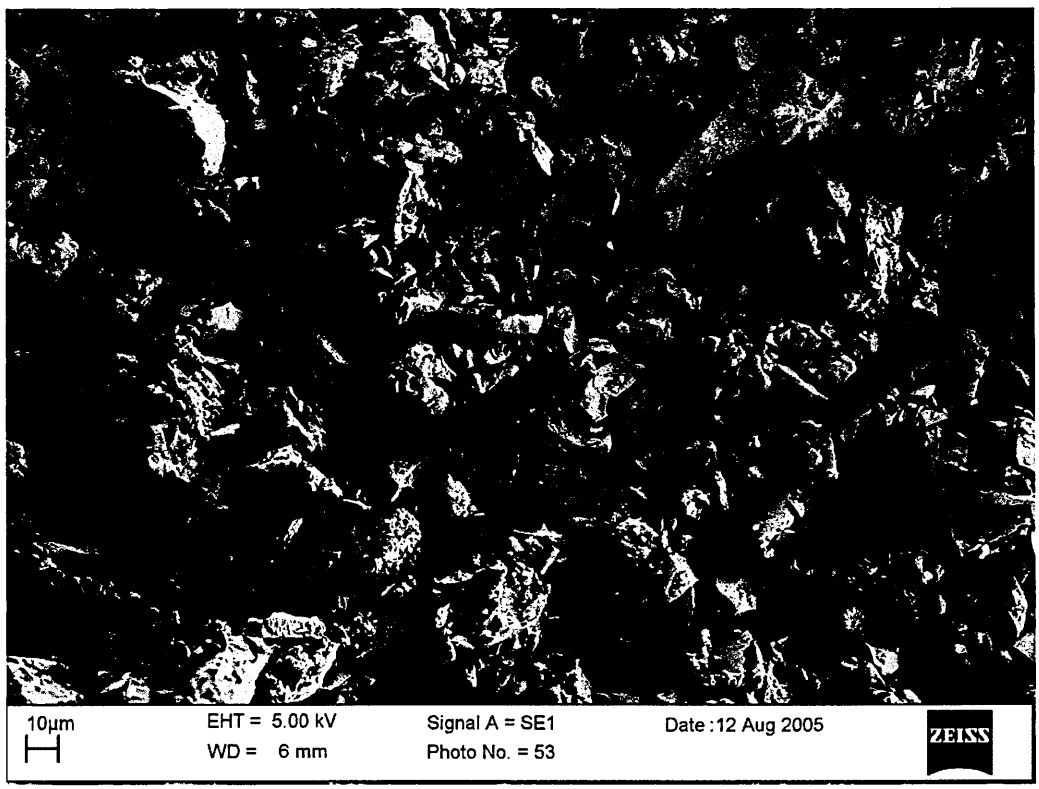

Figure 7-9: Scanning electron microscope images of a rhyolite type volcanic ash this sample has not been in the trap.

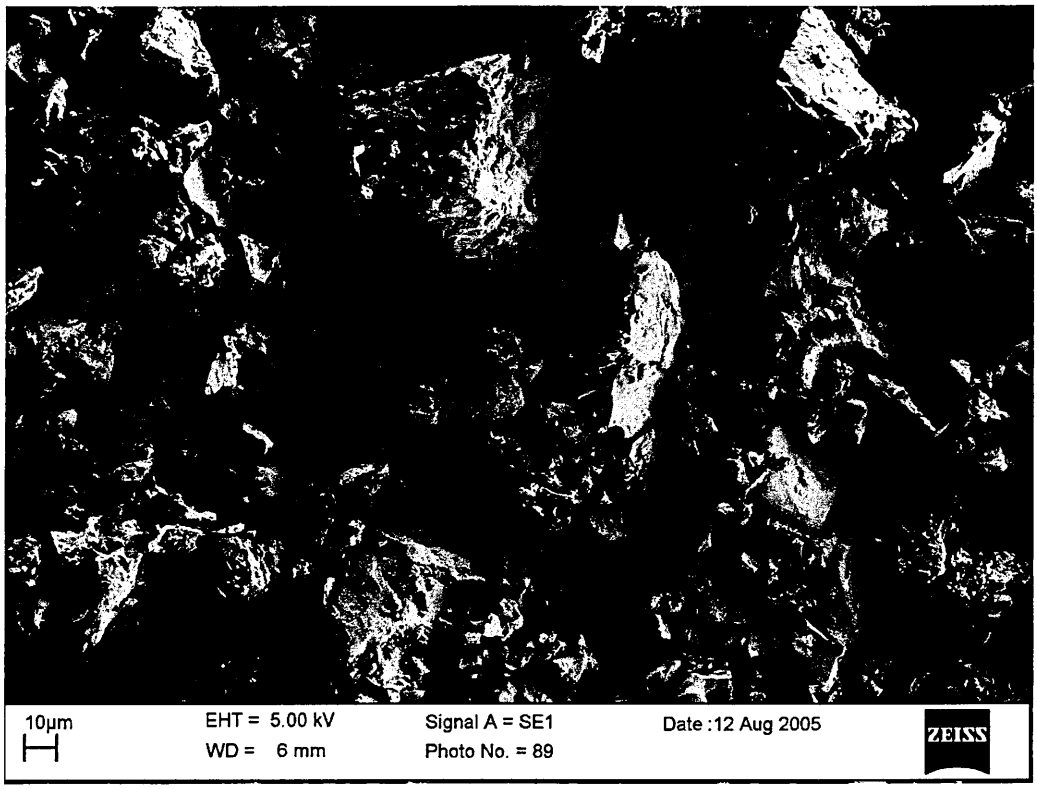

Figure 7-10: Scanning electron microscope images of a basaltic type volcanic ash this sample has not been in the trap.

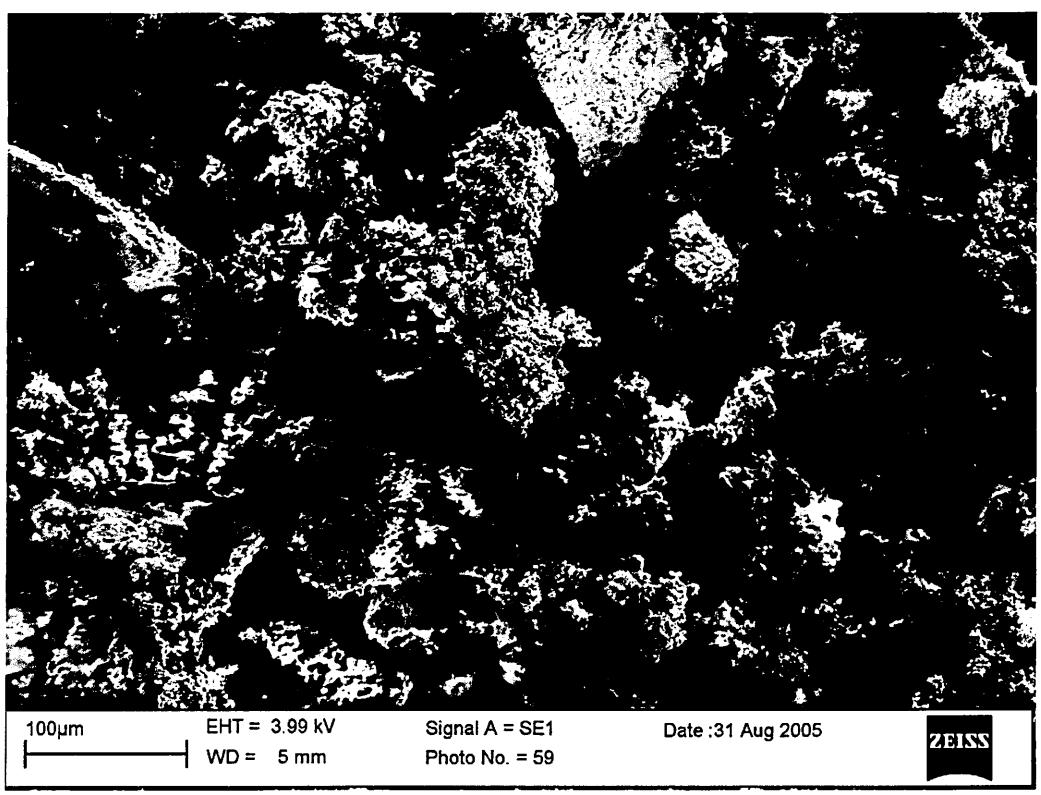

Figure 7-11 Scanning electron microscope images of the soot this sample has not been in the trap, this image has saturated spots as the carbon black was a good insulation and localised charging was seen.

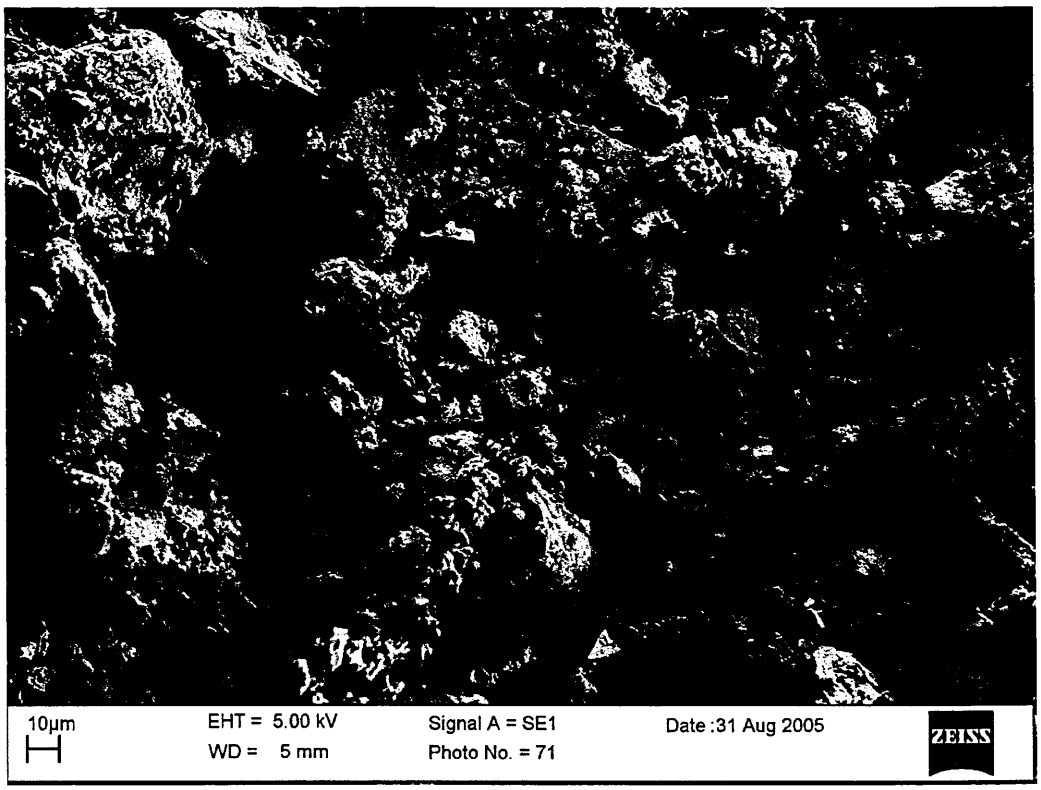

Figure 7-12: Scanning electron microscope images of a sand sample this sample has not been in the trap.

Each sample that had been in the trap and whose spectrum had been taken was then imaged with the SEM at each of the 12 magnifications. You can see from the images that the size range of the sample is much narrower after trapping.

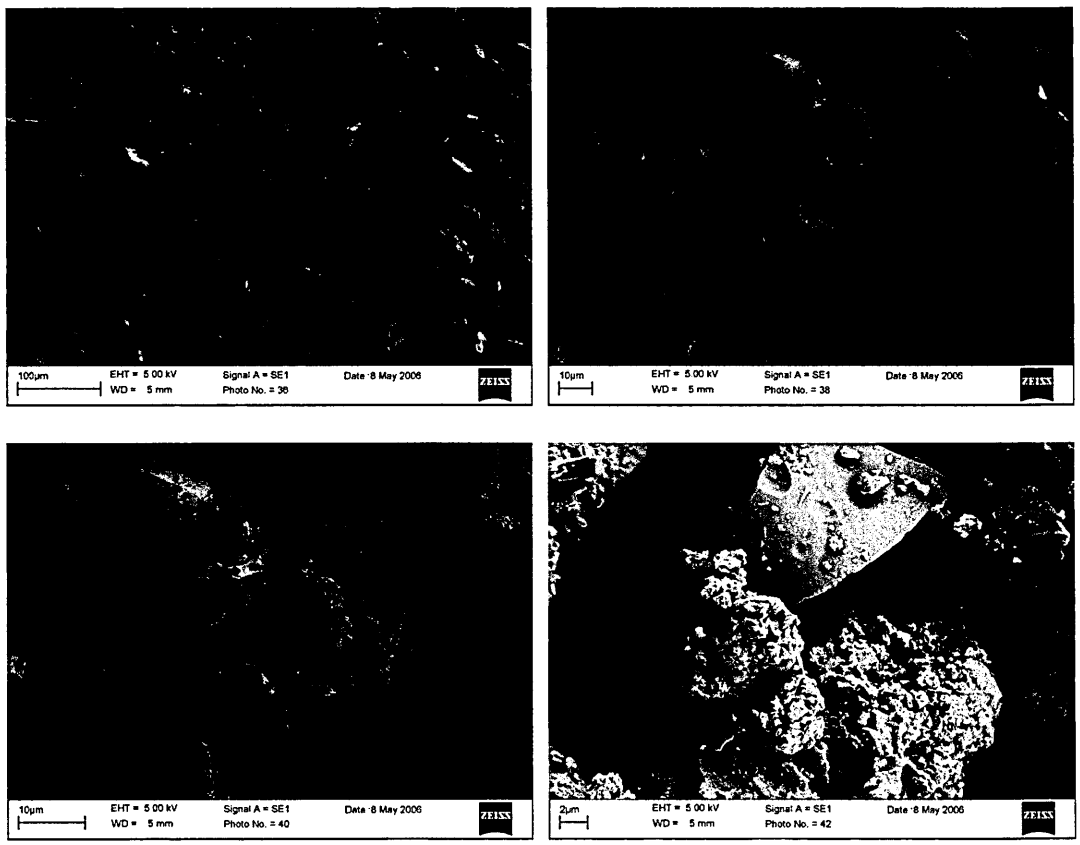

Figure 7-13: SEM images of the rhyolitic dust sample after levitation in the trap

Initially we had decided to use the edge detection software ImageJ (Schneider et al., 2012) to count the numbers of particles at each size but it was discovered that the SEM pictures did not offer enough contrast to make this possible. Figure 7-14 is an SEM image of the rhyolitic volcanic ash sample after levitation and Figure 7-15 is a screen capture of he output of the size distribution analysis of the software. The black and white image on the screen capture in the SEM image with the detected edges superimposed and as you can see the texture of the volcanic ash resulted in a vast overestimation of the particles. The table on the left of the image shows the results of the measurements of each particle detected in number of pixels. The graph on the right shows the distribution of the particle sizes detected.

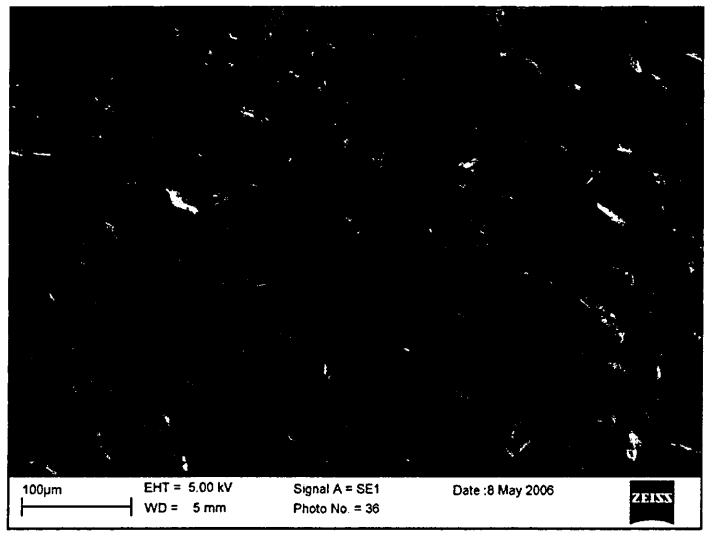

Figure 7-14: SEM image of the rhyolitic volcanic ash after levitation

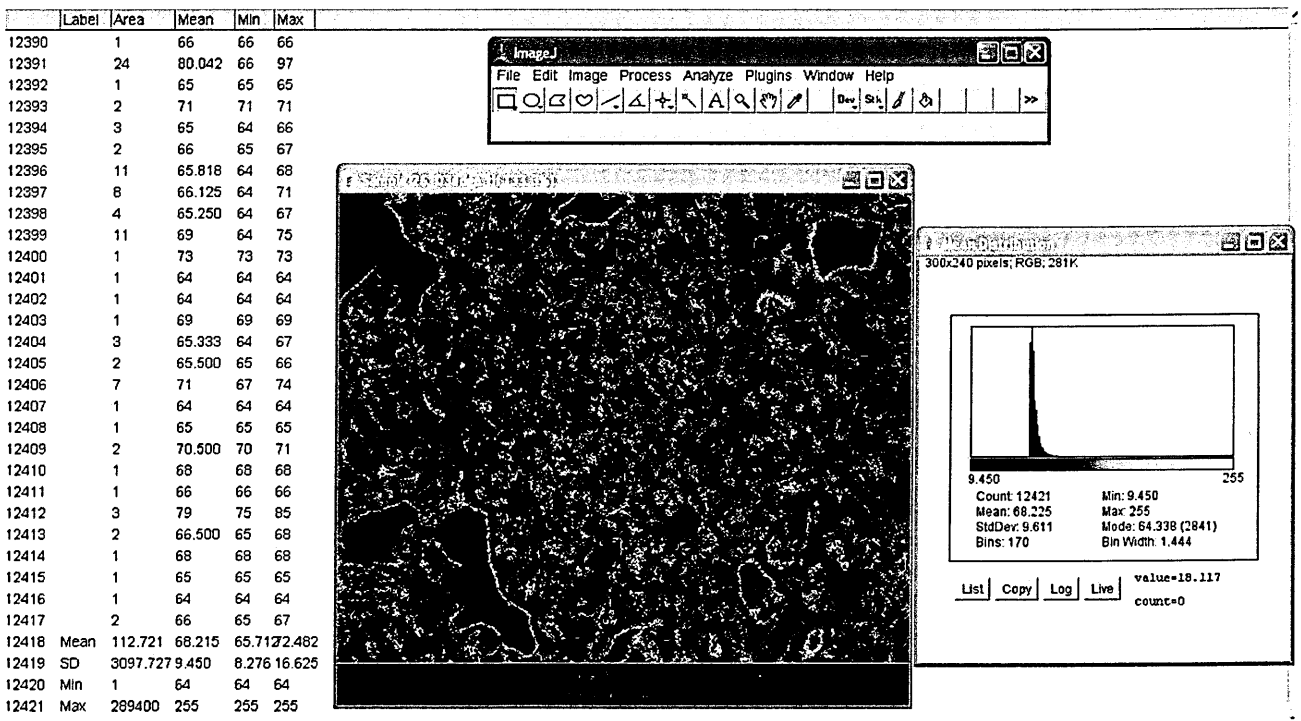

	Label	Area	Mean	Min	Max
12390		1	66	66	66
12391		24	80.042	66	97
12392		1	65	65	65
12393		2	71	71	71
12394		3	65	64	66
12395		2	66	65	67
12396		11	65.818	64	68
12397		8	66.125	64	71
12398		4	65.250	64	67
12399		11	69	64	75
12400		1	73	73	73
12401		1	64	64	64
12402		1	64	64	64
12403		1	69	69	69
12404		3	65.333	64	67
12405		2	65.500	65	66
12406		7	71	67	74
12407		1	64	64	64
12408		1	65	65	65
12409		2	70.500	70	71
12410		1	68	68	68
12411		1	66	66	66
12412		3	79	75	85
12413		2	66.500	65	68
12414		1	68	68	68
12415		1	65	65	65
12416		1	64	64	64
12417		2	66	65	67
12418	Mean	112.721	68.215	65.71	72.482
12419	SD	3097.727	9.450	8.276	16.625
12420	Min	1	64	64	64
12421	Max	269400	255	255	255

Figure 7-15: Screen capture of the edge detection software and its size distribution analysis of the SEM image in Figure 7-14.

The size distribution of the particles in each picture (670 images) was subsequently manually counted. A length scale was developed for each image magnification and the number of particles that fell in the decided size ranges was counted. The size ranges are shown in Table 7-4.

Table 7-4: Size ranges used for counting dust particles.

Size ranges for particle counts / μm										
<0.1	0.1-1	1-5	5-10	10-25	25-50	50-75	75-100	100-200	200-300	300-400

The number of particles in each size range in each of the twelve images for a sample was counted. The results of each count were then normalised to account for the different areas that the images at different magnifications show, this allowed us to calculate the relative numbers of particles in each size range. An average particle volume is calculated for each size range assuming that the numbers of particles of a particular diameter within each size range were equally distributed. Using the average particle volume for each size range and the density of the material the average mass of a particle for each size range was found. Each average particle mass was then multiplied by the relative numbers of particles in each size range to find the relative total mass of each particle range. If this is then normalised to the total mass collected the absolute numbers of the particle distribution in each size band can then be calculated. This was then used to produce a histogram of the particle size distribution for each sample (Figure 7-18).

Videos, taken of the trap during each experiment, have been used to determine the volume of the node and the path length of the spectrometer beam through the aerosol. Several frames were extracted from the videos and, close-up snap shots of each node extracted. Stills from one of the videos can be seen in Figure 7-16.

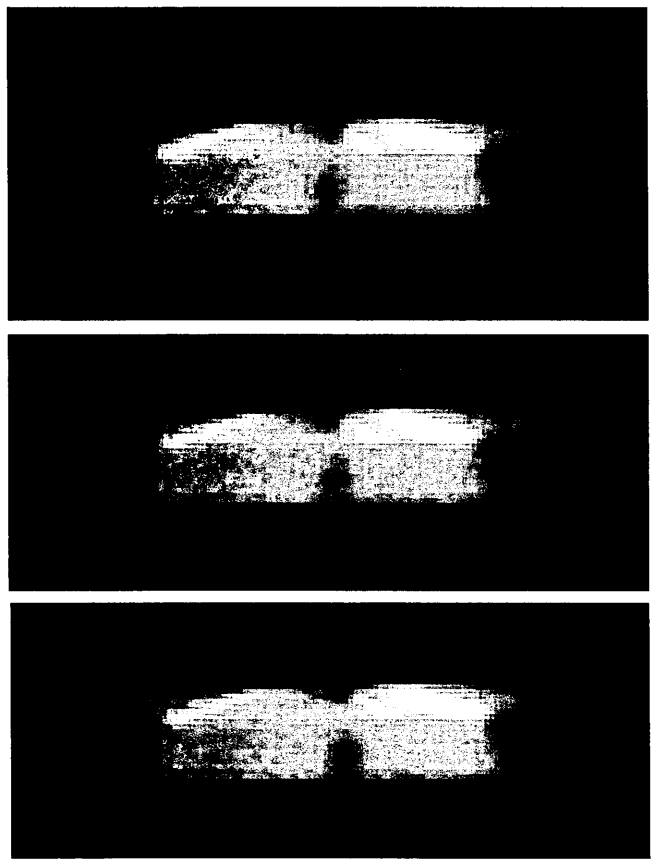

Figure 7-16: Stills taken from a movie of the dust trapped in the acoustic trap each of the still is taken about 15 s apart.

Two methods were then used to extract information about the path length through the aerosol clouds and the volume of the aerosol cloud.

1. Using Edge Detection

In this method a MATLAB routine (Appendix 1) was written that extracted stills from the videos and allowed the region of the node to be selected by user input. The image is then analysed by the software to produce a distribution of the numbers of pixels of each particular colour (Figure 7-17). The image of the smaller region around the node is then outputted onto the screen. The pixel colour that determines the edge of the node is chosen by user input and the software creates a continuous edge around the node corresponding to pixels of that colour.

The number of pixels within the node area counted. The number of pixels represents the cross sectional area projected by the node, the true area of the node is then found by comparing the relative lengths, in pixels, of the diameter of the transducer with the known diameter of the transducer. From this the ratio of the radii of the two nodes in the sound field that had trapped dust was calculated assuming an ellipsoid and the ratio of the volumes calculated. The average ratio of the nodes for seven frames was taken. The ratio of the volumes of the nodes range from 0.3-0.5 however this method was not found to be as reproducible as the second method and so was discontinued.

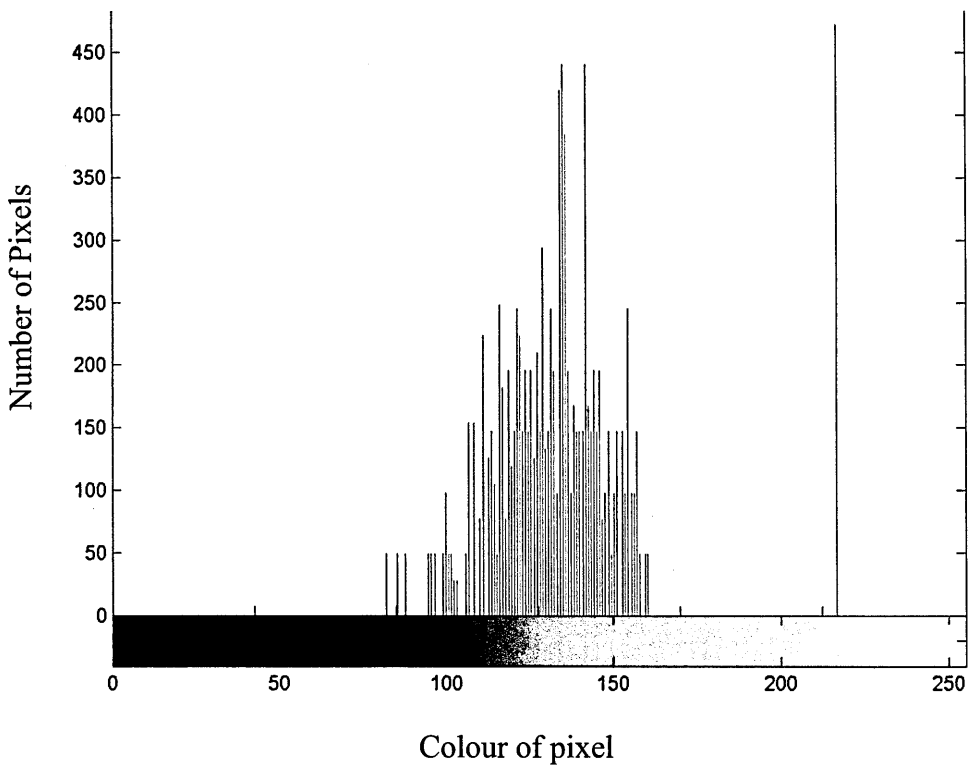

Figure 7-17: Histogram of pixel colour around the node closest to the transducer

2. Using a Modelled Ellipsoid

In this method a MATLAB routine (Appendix 2) was written that extracted still from the video and the user selected the region of the nodes to zoom in on. The

user would then input cursor marks to indicate the antipodal points of the ellipsoidal shape of each of the two nodes containing dust and the edges of the transducer. The length in pixels of each dimension of each node and the transducer are found by comparing the co-ordinates of the cursor marks for both the transducers and nodes. The true diameter is of the nodes is then found by comparing the relative lengths, in pixels, of the diameter of the transducer with the known diameter of the transducer. Once the lengths of the semi-major and semi-minor axes of the ellipse can be found it can then be translated into a volume by modelling each of the nodes as an ellipsoid.

Once the volumes of the node and the numbers of particles in each size range have been calculated the number density of the aerosol cloud can be calculated to do this a MATLAB routine was then written that fitted a lognormal curve to the histogram of our particle size data (Appendix 3). The histograms of the dust counts along with the lognormal fits to our data for one sample of each of the size ranges are shown in Figure 7-18 - Figure 7-21 and the size parameters for one sample of each size range resulting from the routines are given in Table 7-5- Table 7-8. The lognormal fits to the data show good agreement however the limited number of size ranges means that the fit parameters are not very precisely defined. If this method were to be repeated the ranges would be made much smaller. The size ranges of the aerosols measured matched closely with the graduated sieve ranges. The size range seen in the Stokes sized sample matched closely with what was predicted by the Stokes drift approximation i.e. that we had chosen our time so that we selected particles smaller than 5 μm in radius.

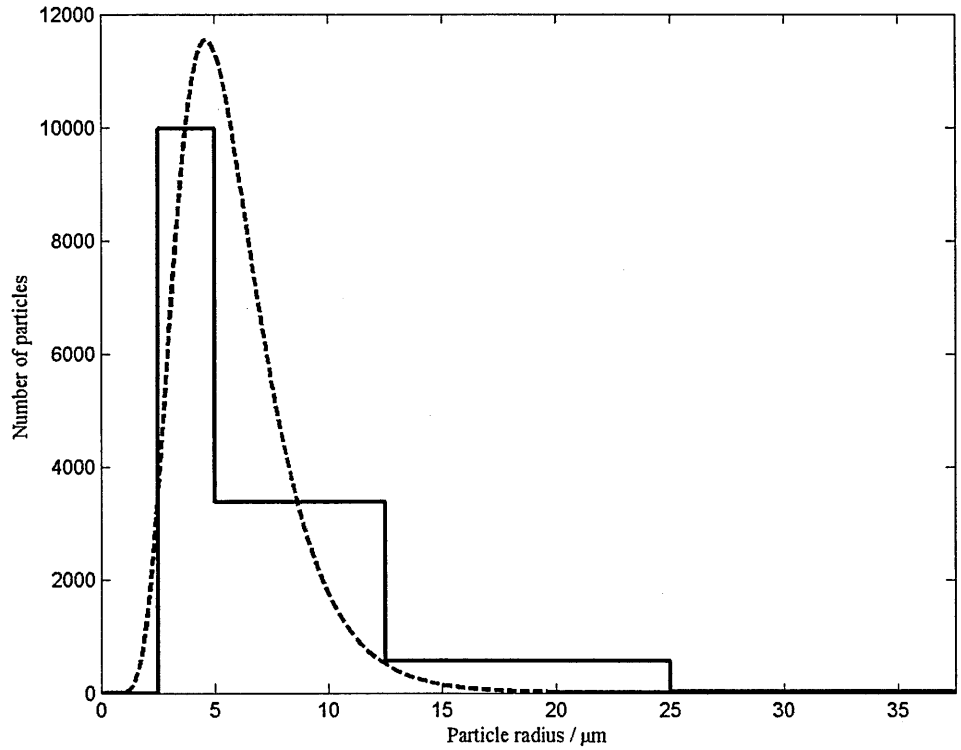

Figure 7-18: Histogram of the size distribution of particles in the <32 mm rhyolitc sample (with lognormal fit shown as a dashed line)

Table 7-5: A table of the aerosol parameters obtained from the routines for the <32 mm rhyolitic sample

Parameter	**Value**
Mass in node	7.9×10^{-7} kg
Volume of Node	1.72×10^{-8} m^3
Volume Number Concentration	3.35×10^{6} / cm^3
Mean Volume of Particle	8.5×10^{-16} m^3
Median Radius	5.4 μm
Standard Deviation (s.d. Ln(r))	0.38

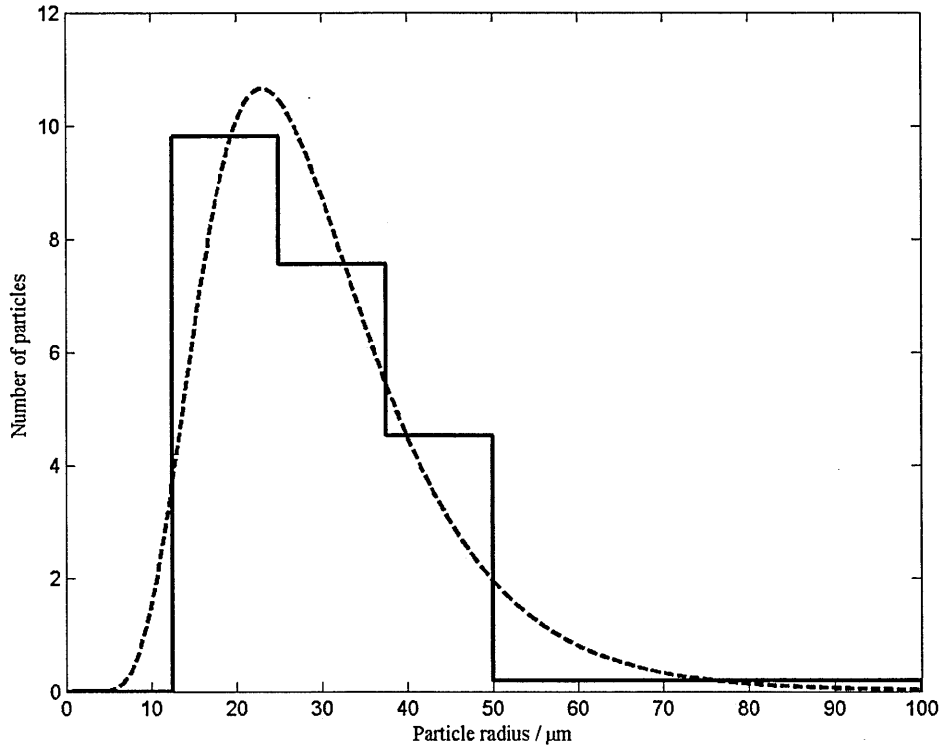

Figure 7-19: Histogram of the size distribution of particles in the 32 – 45 mm rhyolitc sample (with lognormal fit shown as a dashed line)

Table 7-6: A table of the aerosol parameters obtained from the routines for the 32 45 mm rhyolitic sample

Parameter	Value
Mass in node	0.13×10^{-6} kg
Volume of Node	1.58×10^{-8} m^3
Volume Number Concentration	1.85×10^{4} / cm^3
Mean Volume of Particle	1.14×10^{-13} m^3
Median Radius	27.5 μm
Standard Deviation (s.d. Ln(r))	0.436

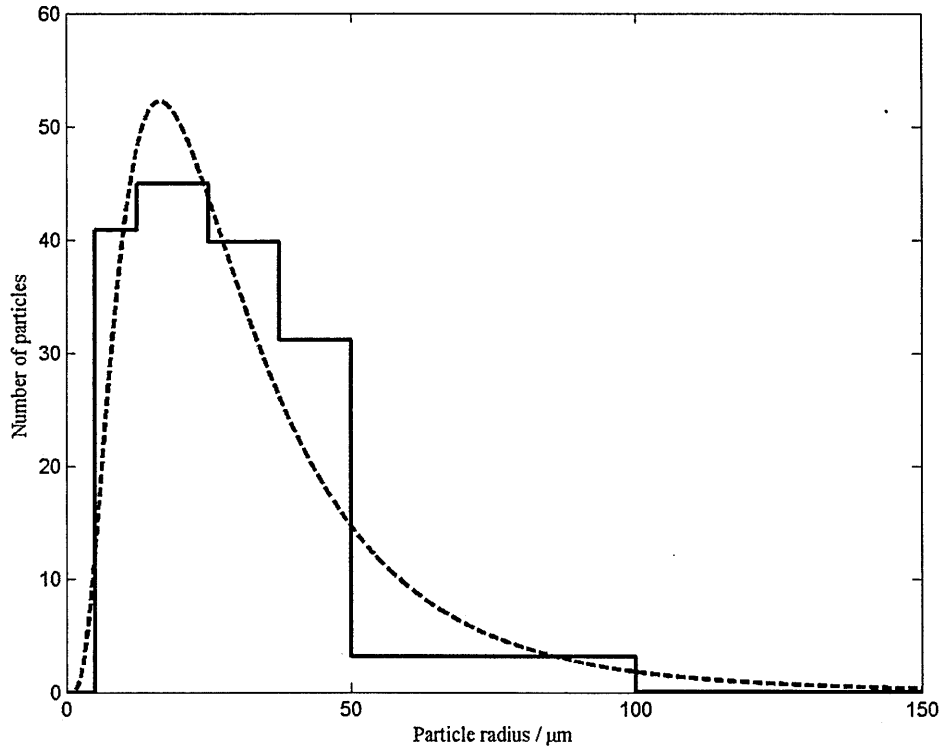

Figure 7-20: Histogram of the size distribution of particles in the 45 – 63 mm rhyolitc sample (with lognormal fit shown as a dashed line)

Table 7-7: A table of the aerosol parameters obtained from the routines for the 45 – 63 mm rhyolitic sample

Parameter	**Value**
Mass in node	1.29×10^{-6} kg
Volume of Node	1.70×10^{-8} m^3
Volume Number Concentration	1.13×10^{5} / cm^3
Mean Volume of Particle	1.66×10^{-13} m^3
Median Radius	26.9 μm
Standard Deviation (s.d. Ln(r))	0.69

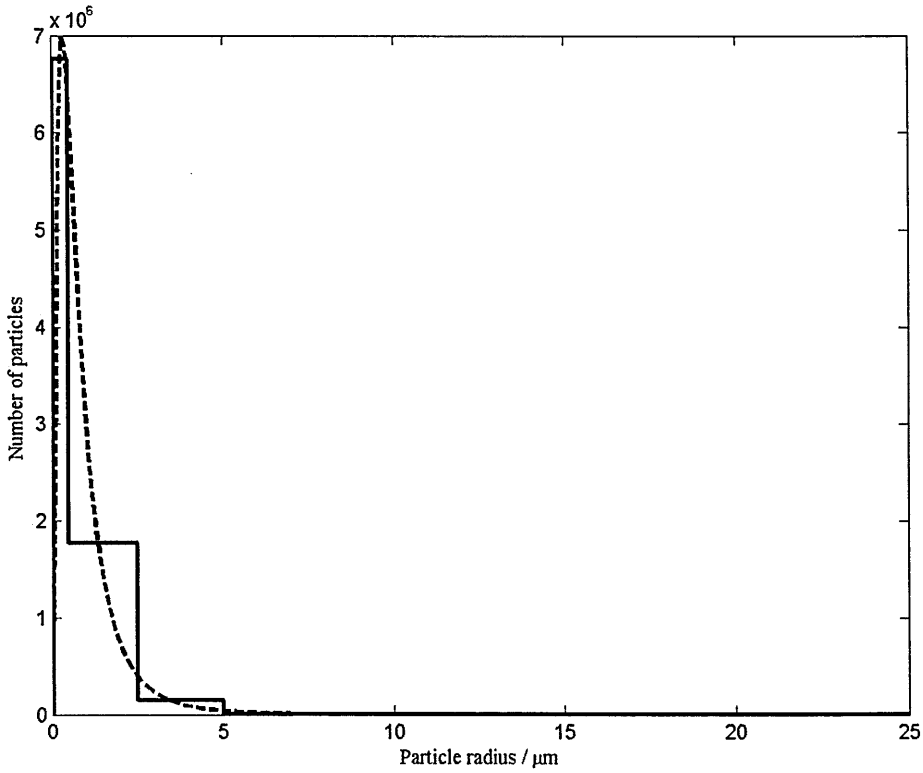

Figure 7-21: Histogram of the size distribution of particles in the Stokes sized rhyolitc sample (with lognormal fit shown as a dashed line)

Table 7-8: A table of the aerosol parameters obtained from the routines for the Stokes rhyolitic sample

Parameter	**Value**
Mass in node	1.00×10^{-6} kg
Volume of Node	1.01×10^{-8} m^3
Volume Number Concentration	7.02×10^{8} / cm^3
Mean Volume of Particle	3.66×10^{-18} m^3
Median Radius	0.7 μm
Standard Deviation (s.d. Ln(r))	0.402

7.4 Modelling the spectra to obtain complex refractive indices

The useful information as far as climate prediction is concerned is the complex refractive index. To extract this from the experimental data we used a Fortran routine called Miex (Wolf and Voshchinnikov, 2004). This program calculates the extinction cross section of the aerosol, using Mie scattering theory, which would be calculated using the following user inputs:

- The real and complex components of the refractive index, $m = n+ik$ of a material relative to the surrounding medium
- The number density of the aerosol
- The parameters of the lognormal distribution characterising the size distribution of the aerosol, defined using a dimensionless size parameter

$$x = \frac{2\pi a}{\lambda} \tag{3}$$

where a is the radius of the particle and λ is the wavelength of the radiation. This program has been specifically written to describe the scattering of particles where the dust grains are assumed to be homogeneous spheres. This program calculates the Mie coefficients and efficiency factors for single particles based on the method described by Voshchinnikov (Wolf and Voshchinnikov, 2004). The calculations of the angular functions are based on the standard approach (see (Wiscombe, 1980). The particle size distributions were accounted for by a proper averaging of the single parameters (efficiency factors etc.).

The program is not ideally suited to the work in this thesis as it calculates the extinction cross section from the refractive indices, the calculation needed to analyse the data in this thesis is the reverse, to calculate the real and complex refractive

indices from the spectroscopic data. To accomplish this, the Miex program was put into a loop by the author (Appendix 4). In this loop, the program was run thousands of times with 100 different values of the real (n) and complex (k) refractive indices for each wavelength. The output of each loop was the extinction crossection spectra that would be seen for those values of n and k. A least square fit approach was then used to determine which of the crossection data for a particular input value of n and k fitted the experimentally determined crossection data the best. This was the assumed to be our best estimate for the values of n and k.

The range of values of the real and complex refractive index and the increments between them was determined by equation, starting from a measured set of real and complex refractive indices from Jena-St Petersburg database of optical constants (2011) e.g. for the real part of the refractive index the values went from half of the value of the input number to twice the value of the input number. The experimental data was then matched so that for every value of the real and complex refractive index at a particular wavelength in the input data there was a matching data set for the experimentally determined extinction cross- sections for each of the sample runs with different aerosol size parameters. For each sample the program then created a 3 dimensional array of data with wavelength represented on one dimension and 100 different values of the real and complex refractive index along the second and third dimensions respectively. The array was then filled with the calculated value of extinction cross-section for the matching wavelength and specific value of the real and complex refractive index for each sample in turn. The best value for the real and complex refractive index was chosen to be the one that gave the closest match to the

all of the arrays i.e. the real and complex refractive index that resulted in extinction cross-sections that matched the experimental data most closely.

Samples of the results for the real and complex refractive index for the silicatious samples compared to the input refractive indices are shown in Figure 7-22 and Figure 7-23 respectively. Samples of the results for the real and complex refractive index for the soot sample compared to the input refractive indices are shown in
Figure 7-24 and Figure 7-25 respectively. The results obtained were erratic and due to the large uncertainty in some of our input parameters we can have little confidence in the results. The values for the real part of the complex refractive index seem to behave predictably and produce smooth continuous outputs but the imaginary part swings wildly by orders of magnitude between the wavelengths. In order to be more confident in the results of this program the input parameters from some of the experimentally determined constants need to be more accurately measured, in particular the characterisation of the aerosol size parameters needs to be better defined.

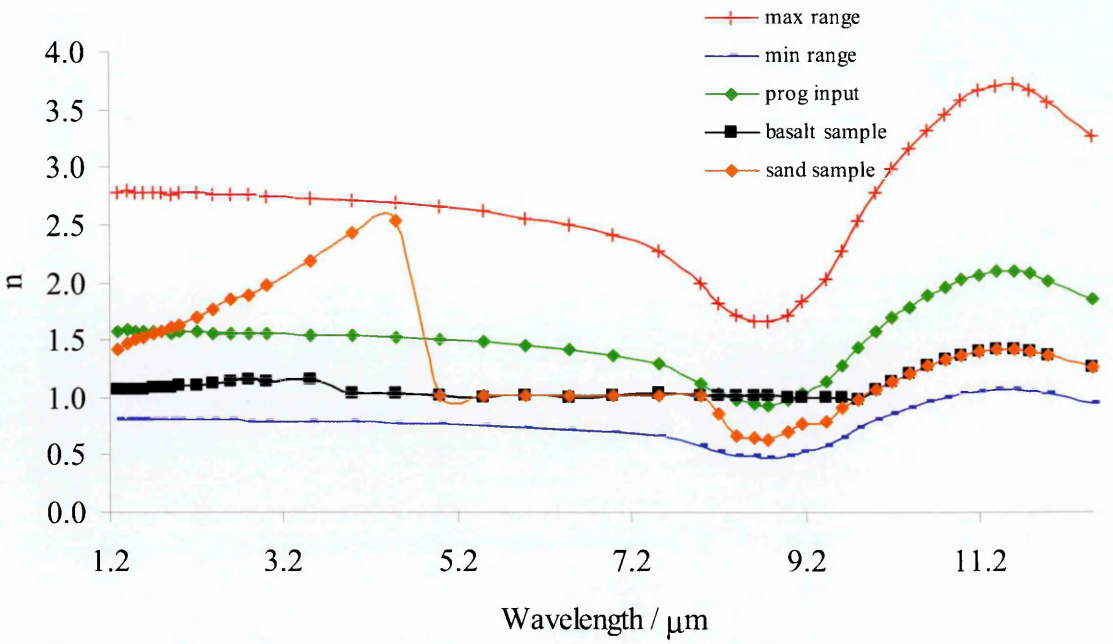

Figure 7-22: A graph to show the value of the real refractive index of the silicatious samples obtained from the program compared to values from the database. The program input is the refractive index from the data base, the max and min range are the extent of the ranges of values of refractive index calculated and the basalt sample and the sand sample are the program outputs of the best fit values of refractive index to our data.

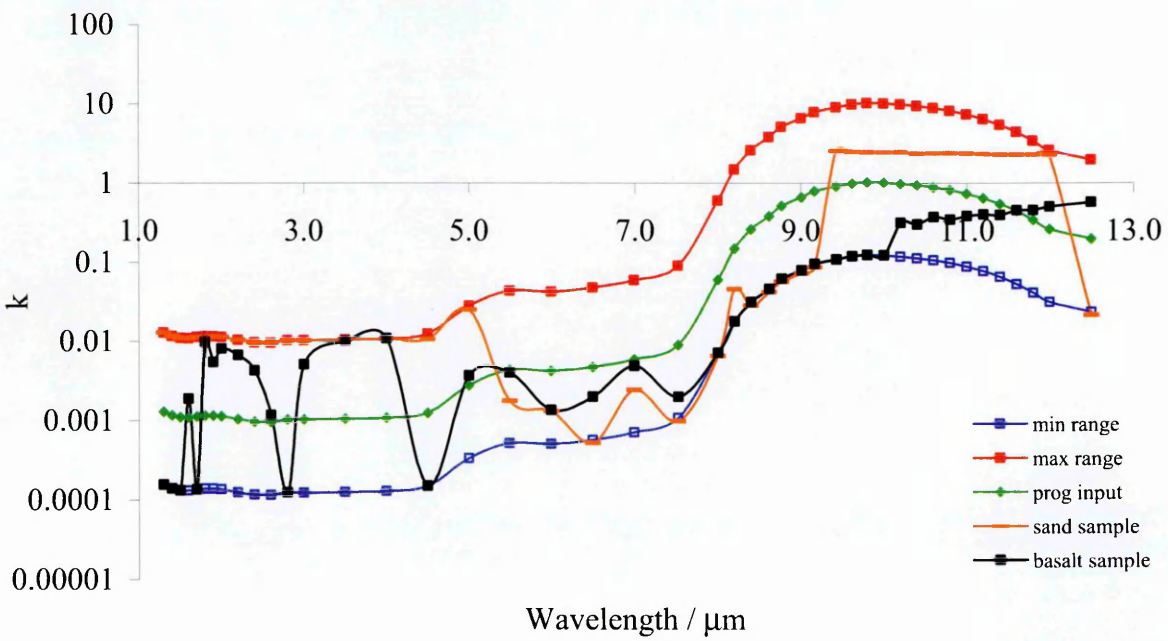

Figure 7-23: A graph to show the value of the complex refractive index of the silicatious samples obtained from the program compared to values from the database. The program input is the refractive index from the data base, the max and min range are the extent of the ranges of values of refractive index calculated and the basalt sample and the sand sample are the program outputs of the best fit values of refractive index to our data.

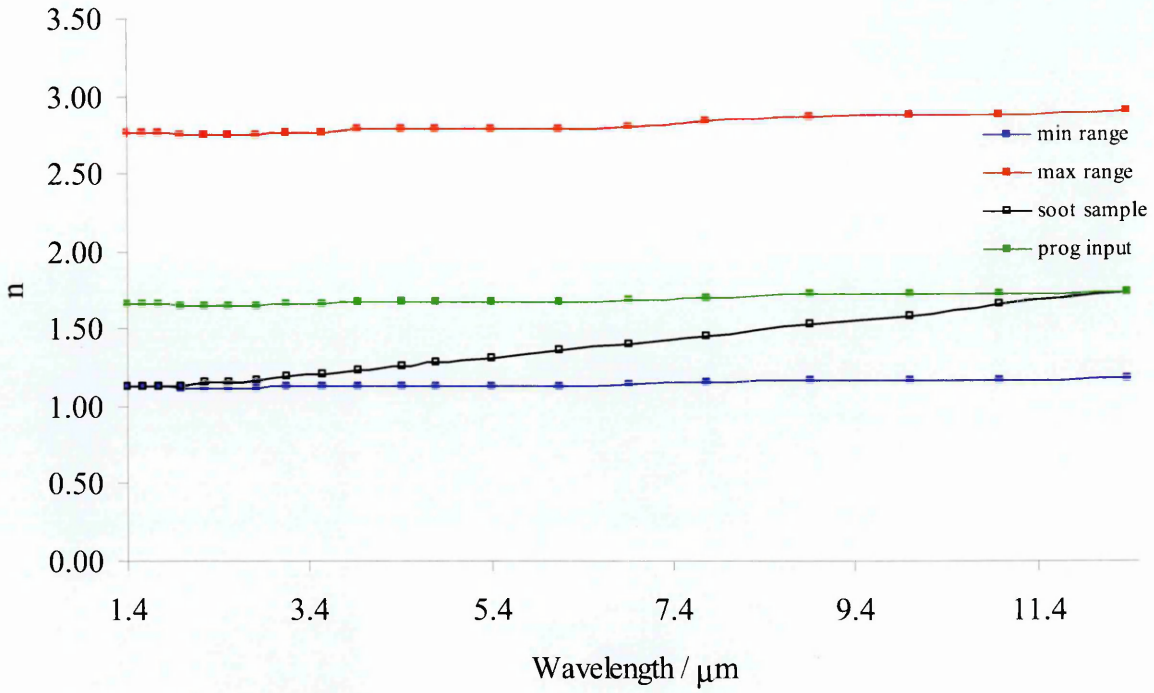

Figure 7-24: A graph to show the value of the real refractive index of the soot sample obtained from the program compared to values from the database. The program input is the refractive index from the data base, the max and min range are the extent of the ranges of values of refractive index calculated and the soot sample is the program outputs of the best fit values of refractive index to our data.

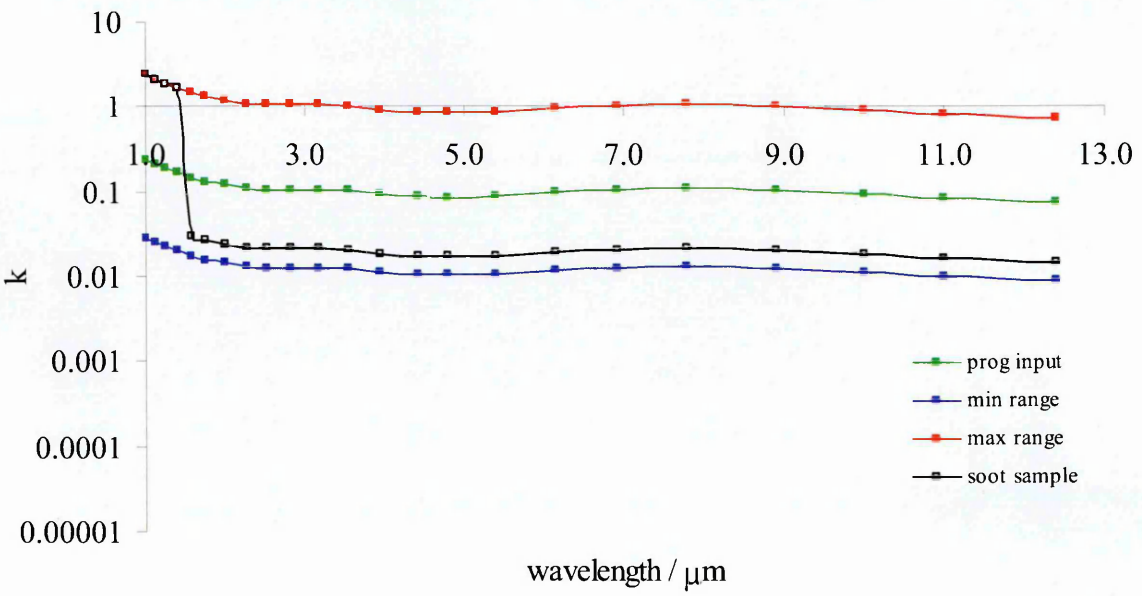

Figure 7-25: A graph to show the value of the complex refractive index of the soot sample obtained from the program compared to values from the database. The program input is the refractive index from the data base, the max and min range are the extent of the ranges of values of refractive index calculated and the soot sample is the program outputs of the best fit values of refractive index to our data.

To check the closeness of the fit the fitted values of the real and complex refractive index determined in the program were put back into the Miex program to find out what values for the cross section they would give (Figure 7-26). The spectral fits show close agreement for each size range however there is an unexpected feature at just below 8 μm which is due to the erratic outputs from the program.

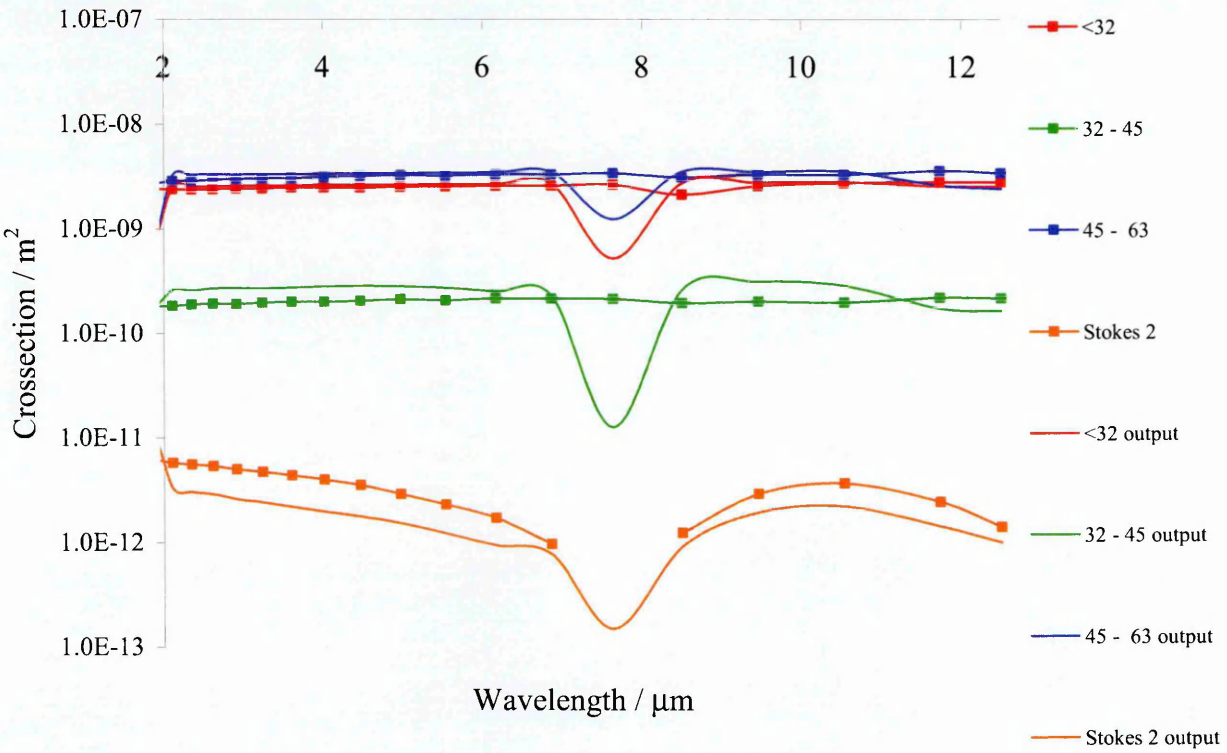

Figure 7-26: A graph to show the value of the cross section for each of the size ranges of the basaltic sample obtained from the program compared to values from experiment. The experimentally determined cross sections and the cross sections determined by h program for each size range as shown in the same colour with the experimental data showing the data points used.

7.5 Making the trap compatible for levitation of mimic interstellar medium icy grains.

The trapping and growth of ice particles in stationary fields has been previously reported (Bauerecker and Neidhart, 1998a, Bauerecker and Neidhart, 1998b). Heterogeneous chemistry in ice analogues caused by ultraviolet light has been a key

area of research within the group I am part of at the Open University and I was a contributor to experimental work undertaken that was subsequently published (Holtom et al., 2006, Mason et al., 2005).

Over 100 molecules have been identified in the interstellar medium (T=10 K, $\rho=10^6$ H atoms/cm^{-3}) however there is thought to be too much complexity for these molecules to have been formed in gas phase reactions in the low temperature and low pressure environments of the interstellar medium (Ehrenfreund et al., 2003). The chemistry is thought to happen by

- Direct mechanisms – collisions between gas phase atoms and grain mantle
- Indirect mechanisms – diffusion of reagents across surface encounter and react (mediated by photons, phonons, electrons).

The molecules are thought to have been formed during chemistry on "dust grains". These silicatious or carbonatious dust grains are thought to be covered in an icy mantle due to accretion of approximately 1 atom per day, at these temperatures accretion is thought to happen with unit efficiency. Hydrogen, carbon, oxygen and nitrogen atoms have been shown to be mobile on the surfaces down to 10-30 K.

The chemistry that occurs will be sensitive to the ice crystal structure or phase. Currently ice analogues are deposited onto substrates and irradiated with, photons, ions and electrons to investigate possible new chemical pathways. To monitor this chemistry spectroscopy is performed in the bulk but there is doubt as to whether this is representative of the "grains". It is hoped that an acoustic trap can be incorporated into an interstellar chemistry experiment to coagulate icy grains, initiate chemical

reactions by irradiation and investigate how the particle size and structure affects the chemistry.

We have managed to trap both liquid and solid ice water samples within the trap (Figure 7-27 and Figure 7-28) with the intent to coating the dust samples with ice and water and discovering how this changes the optical properties.

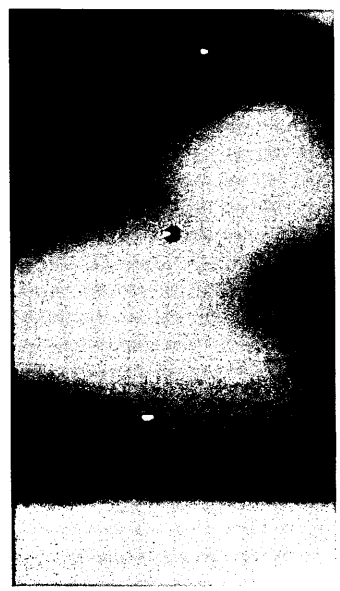

Figure 7-27: Water droplets trapped in the ultrasonic trap

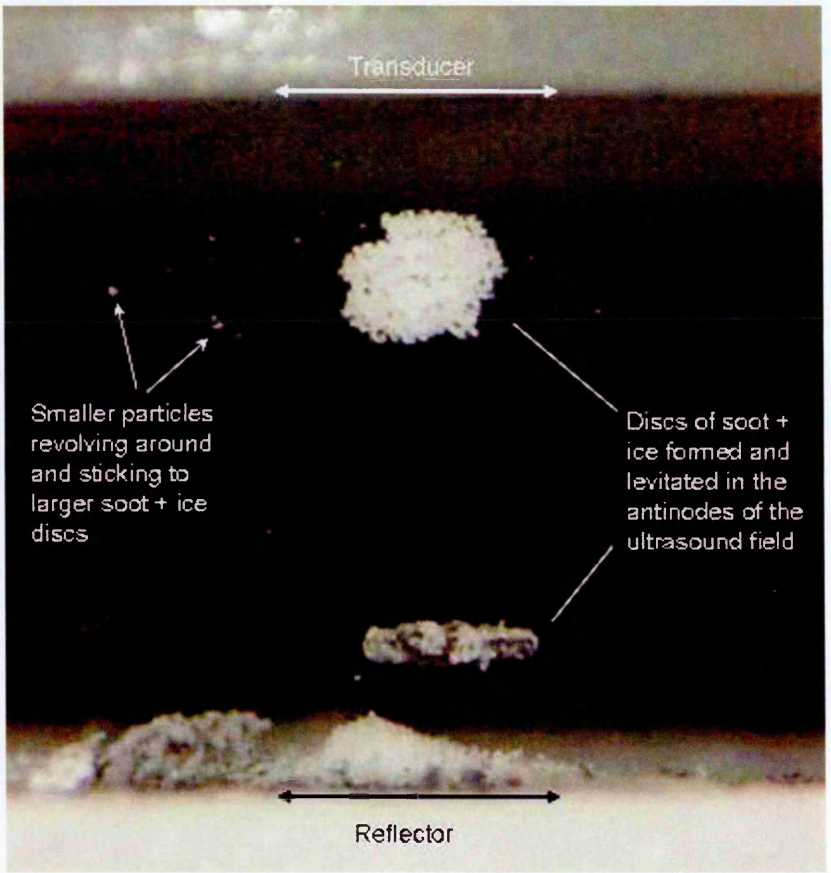

Figure 7-28: Matrix of Ice and Soot trapped in the ultrasonic trap

Investigative transmission spectra have been taken of the trapped ice and water samples, the spectra can be seen in Figure 7-29.

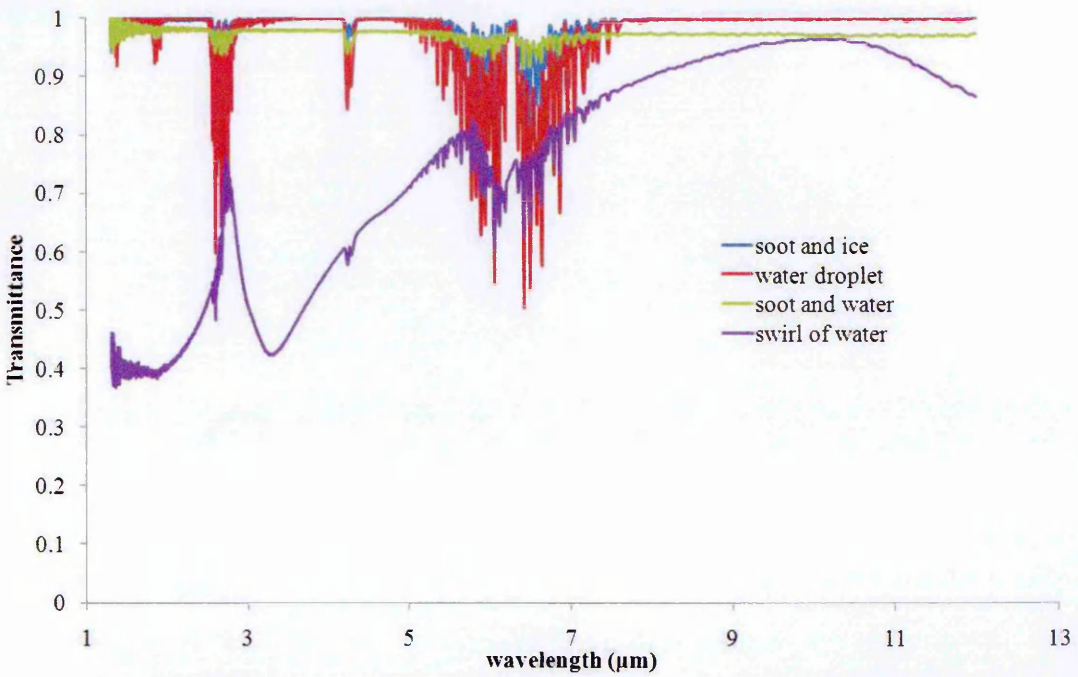

Figure 7-29: Transmittance of ice/dust analogues taken on an FT-IR spectrometer.

7.6 Ideal trap configuration

In order to improve the quality of results obtained there are several improvement suggested.

- Ideally construction of a new chamber with a wide angle window so that reflection spectroscopy rather than transmission spectroscopy could be done so that the absorption and scattering coefficients can be measured without complete reliance on computer modelling to separate the contributions.
- Larger radius reflector and a higher trapping node chosen that is at a greater distance from the PZT sandwich transducer to minimise near field effects and to improve the stability of the node.
- Creating of a transducer with a curved surface to maximise the trapping forces.
- Using a larger sandwich transducer with a lower resonant frequency to create a lower frequency standing wave to increase acoustic entrainment for the size range we are interested in (<10 μm). In addition to this it might be beneficial to have several of these transducers attached to a single front plate quarter wave matching plate. This would generate a large surface area with smaller total acoustic impedance but also would produce nodes with a longer path length. This would allow spectra to be obtained from aerosols with a lower number density which would act to minimise agglomeration of the aerosol particles b reducing the acoustic wake effect.
- Using an aerosol generator and aerosizer for easier production of relevantly sized aerosols (<10 μm) and more reliable sizing measurements. In addition to this the production of an aerosol with a narrow size distribution would be preferable so that the trap could be configured to maximise entrainment of those particles so that as little orthoknetic motion was possible. This would

mean that there would not be as much change in the size distribution of the aerosol over time meaning that higher resolution spectra could be obtained.

- High temperature setting epoxy, to construct the transducer as the sound transmission processes the epoxy resin, changing its properties causing a loss of intensity in the sound field.
- Quarter wave plate matching with graduated layers to increase the intensity of the sound field by increasing the proportion of the energy transmitted from the PZT sandwich transducer into the chamber.
- Feedback tuning of the resonant field: during operation it was noticed that the precise frequency of the resonance changed, this was probably due to warming of the transducer. Although this was only by up to 10 Hz it was enough to reduce the levitating power of the sound field such that the aerosol was dropped. Ideally a feedback loop would be inserted from the microphone either into the signal generator or to the linear feedthroughs which would then adjust the frequency or height of the reflector to maintain resonance.

Chapter 8: Conclusions

"Joy in looking and comprehending is nature's most beautiful gift."

Albert Einstein

8.1 Conclusions

Characterisation of the mechanisms and consequences of global warming is one of the most important topics in modern science. It requires a detailed investigation of the infrared properties of the constituents of the terrestrial atmosphere: gaseous, particulate and liquid. In this thesis Fourier-Transform Infra-Red (FTIR) Spectroscopy was used to provide data on the absorption cross sections needed to evaluate the radiative forcing of substances present in the terrestrial atmosphere. Also presented was a novel method for the investigation of the real and refractive indices needed to evaluate the radiative forcing of aerosols present in the terrestrial atmosphere such as soot from wood fires, sand and volcanic ash.

In this thesis we have presented the results of a study of the infrared transmission spectroscopy of the gas CF_3I over a range of different temperatures and pressures of the gas. The peaks in the spectrum were identified and assigned including the assignment of two previously unseen peaks, the calculated integrated absorption intensities (IAIs) of these peaks are then reported. The simple approximation proposed by Pinnock et al. (1995) to estimate the radiative forcing of an optically thin gas in the atmosphere is then applied to our data and the results presented. The analysis section of this chapter discusses the limitations and rigorousness of

assumptions made in this chapter for example those of the Pinnock approximations e.g. that the gases are optically thin and those of the IAI calculations e.g that the gas behaves ideally.

In this thesis there was also an investigation of the interactions of aerosols with electromagnetic radiation and the subsequent effects it may have on the Earth's radiation budget. Aerosols may affect the terrestrial radiation budget in two ways: i) they may induce global cooling due to scattering and reflection of incident solar radiation and ii) global warming due to absorption of terrestrial infrared radiation. To asses the net contribution of these aerosols one must know the concentration and location of any aerosol and also absorption and scattering coefficients. Studying the spectroscopy of aerosols has proven to be a difficult problem since aerosols settle out quickly under the influence of gravity and so have short residence times in aerosol chambers thus radiative properties of aerosols provide one of the largest uncertainties in atmospheric modelling.

In this thesis an 'acoustic trap' has been developed to counteract gravity allowing us to record spectra of some common atmospheric aerosols: volcanic ash, coal soot and sand. This thesis detailed the specifics of the design of our ultrasonic trap and how it was made suitable for collecting spectra of particulate aerosols. The trapping chamber had to be able to be evacuated, filled with an infrared inactive gas which was able to be heated and cooled, contain the trap itself and allow for the retrieval of our samples. Significant technical difficulties were overcome in the design of this trap. The results of the application of this chamber to FT-IR spectroscopy of aerosols and how the data was collected and how it could be used to obtain values for the complex refractive

index at many wavelengths. An analysis of the techniques used was given and an array of ideas for further improvement and application of the ultrasonic levitator were proposed. This research has been largely an initial test of feasibility of the suitability of the ultrasonic trap for these purposes; although there are several improvements that need to be made in both the design of the trap and of the method of analysis before reliable results can be obtained I believe that it will prove to be a useful addition to the current methods available for the analysis of atmospheric aerosols.

Chapter 9: Bibliography

ALEXEEV, A. & GUTFINGER, C. (2003) Particle drift in a resonance tube - a numerical study. *The Journal of the Acoustical Society of America,* 114, 1357-1365.

ALVAREZ-ARENAS, T. E. G. (2004) Acoustic Impedance Matching of Piezoelectric Transducers to the Air. *IEEE Transactions on Ultrasonics, Ferroelectrics, and Frequency Control* 51, 624-633.

ATKINSON, R., BAULCH, D. L., COX, R. A., HAMPSON, R. F., KERR, J. A. & TROE, J. (1992) Evaluated Kinetic and Photochemical Data for Atmospheric Chemistry Supplement-Iv - Iupac Subcommittee on Gas Kinetic Data Evaluation for Atmospheric Chemistry. *Journal of Physical and Chemical Reference Data,* 21, 1125-1568.

BAILEY, S., D. BRINKER, H. CURTIS, P. JENKINS, AND D. SCHEIMAN (1997) Solar Cell Calibration and Measurement Techniques. *NASA Technical Memorandum.* Cleveland, OH, USA, NASA.

BALKANSKI, Y. J., JACOB, D. J., GARDNER, G. M., GRAUSTEIN, W. C. & TUREKIAN, K. K. (1993) Transport and Residence Times of Tropospheric Aerosols Inferred from a Global Three-Dimensional Simulation of 210Pb. *Journal Geophysical Research,* 98, 20573-20586.

BANWELL, C. N. & MCCASH, E. M. (1995) *Fundamentals of molecular spectroscopy,* London, McGraw-Hill.

BAUERECKER, S. & NEIDHART, B. (1998a) Cold Gas Traps for Ice Particle Formation. *Science,* 282, 2211-2212.

BAUERECKER, S. & NEIDHART, B. (1998b) Formation and growth of ice particles in stationary ultrasonic fields. *The Journal of Chemical Physics,* 109, 3709-3712.

BRASSEUR, G. U. Y. & HITCHMAN, M. H. (1988) Stratospheric Response to Trace Gas Perturbations: Changes in Ozone and Temperature Distributions. *Science,* 240, 634-637.

BUTTERWORTH, S. (1914) On Electrically-maintained Vibrations. *Proceedings of the Physical Society of London,* 27, 410.

CADY, W. G. (1922) The piezo-electric resonator. *Proceedings of the Institute of Radio Engineers,* 10, 83–114.

CAKMUR, R. V., MILLER, R. L., PERLWITZ, J., GEOGDZHAYEV, I. V., GINOUX, P., KOCH, D., KOHFELD, K. E., TEGEN, I. & ZENDER, C. S. (2006) Constraining the magnitude of the global dust cycle by minimizing the difference between a model and observations. *Journal Geophysical Research,* 111, D06207.

CHA, B. S., LEE, S., KANASHIMA, T., OKUYAMA, M. & TANAKA, T. (2011) Influences of perforation ratio in characteristics of capacitive micromachined ultrasonic transducers in air. *Sensors and Actuators A Physical,* 171, 191-198.

CHRISTIDIS, N., HURLEY, M. D., PINNOCK, S., SHINE, K. P. & WALLINGTON, T. J. (1997) Radiative forcing of climate change by CFC-11

and possible CFC- replacements. *Journal of Geophysical Research-Atmospheres,* 102, 19597-19609.

COCHRAN, A., REYNOLDS, P. & HAYWARD, G. (1998) Progress in stacked piezocomposite ultrasonic transducers for low frequency applications. *Ultrasonics,* 36, 969-977.

CZYZ, H. (1990) On the concentration of aerosol particles by means of drift forces in a standing wave field. *Acustica,* 70, 23-28.

DOINIKOV, A. A. (1994) Acoustic Radiation Pressure on a Rigid Sphere in a Viscous Fluid. *Proceedings of the Royal Society A,* 447, 447-466.

DOMARKAS, V. & KAZYS, R. (1975) *Piezoelectric transducers for measuring devices,* Vilnius, Mintis.

DONG, S., LIPKENS, B. & CAMERON, T. M. (2006) The effects of orthokinetic collision, acoustic wake, and gravity on acoustic agglomeration of polydisperse aerosols. *Journal of Aerosol Science,* 37, 540-553.

DUAN, Y. Y., SHI, L., SUN, L. Q., ZHU, M. S. & HAN, L. Z. (2000) Thermodynamic Properties of Trifluoroiodomethane (CF_3I). *International Journal of Thermophysics,* 21, 393-404.

DUCK, F. (2009) The Electrical Expansion of Quartz by Jacques and Pierre Curie. *Ultrasound,* 17, 197-203.

EHRENFREUND, P., FRASER, H. J., BLUM, J., CARTWRIGHT, J. H. E., GARCIA-RUIZ, J. M., HADAMCIK, E., LEVASSEUR-REGOURD, A. C., PRICE, S., PRODI, F. & SARKISSIAN, A. (2003) Physics and chemistry of

icy particles in the universe: answers from microgravity. *Planetary and Space Science,* 51, 473-494.

FEYNMAN, R. P., LEIGHTON, R. & SANDS, M. (1971) *Lectures on Physics: Commemorative Issue Vol 2,* Reading, Addison Wesley.

FIEBERG, J. E., SZABO, A. & WHITE, J. M. (1996) Electron-stimulated chemistry of CF3I adsorbed on Ag(111) C-F bond cleavage and C-C coupling. *Journal of the Chemical Society-Faraday Transactions,* 92, 4739-4748.

FRECKLETON, R. S., HIGHWOOD, E. J., SHINE, K. P., WILD, O., LAW, K. S. & SANDERSON, M. G. (1998) Greenhouse gas radiative forcing: Effects of averaging and inhomogeneities in trace gas distribution. *Quarterly Journal of the Royal Meteorological Society,* 124, 2099-2127.

GANN, R. G., HARRIS, R. H., HORKAY, F., MCKENNA, G. B., NYDEN, M. R., PEACOCK, R. D., RICKER, R. E., STOUDT, M. R. & WALDRON, W. K. (1994) Compatibility of Halon Alternatives for in-Flight Fire Suppression. *Abstracts of Papers of the American Chemical Society,* 208, 287.

GAO, J. R., CAO, C. D. & WEI, B. (1999) Containerless Processing of Materials by Acoustic Levitation. *Advances in Space Research,* 24, 1293-1297.

GLASS, S., DHOOGE, P. & NIMITZ, J. (1999) Gas Phase Combustion Suppression of Various Fuels by CF3I. *Proceedings of the 1999 Halon Options Technical Working Conference.* University of New Mexico, Albuquerque, NM.

GONZALEZ, I., GALLEGO-JUAREZ, J. A. & RIERA, E. (2003) The influence of entrainment on acoustically induced interactions between aerosol particles - an experimental study. *Journal of Aerosol Science,* 34, 1611-1631.

GOR'KOV, L. P. (1962) On the Forces Acting on a Small Particle in an Acoustical Field in an Ideal Fluid. *Soviet Physics Doklady,* 6, 773-775.

HANSEN, J., SATO, M. & RUEDY, R. (1997) Radiative forcing and climate response. *Journal of Geophysical Research-Atmospheres,* 102, 6831-6864.

HARRIES, J. E., BRINDLEY, H. E., SAGOO, P. J. & BANTGES, R. J. (2001) Increases in greenhouse forcing inferred from the outgoing longwave radiation spectra of the Earth in 1970 and 1997. *Nature,* 410, 355-357.

HAWKES, J. J., CEFAI, J. J., BARROW, D. A., COAKLEY, W. T. & BRIARTY, L. B. (1998) Ultrasonic manipulation of particles in microgravity. *Journal of Physics D: Applied Physics,* 31, 1673.

HAYWOOD, J. & SCHULZ, M. (2007) Causes of the reduction in uncertainty in the anthropogenic radiative forcing of climate between IPCC (2001) and IPCC (2007). *Geophysical Research Letters,* 34, 20701.

HAYWOOD, J. M., DONNER, L. J., JONES, A. & GOLAZ, J.-C. (Eds.) (2009) *Global indirect radiative forcing caused by aerosols: IPCC (2007) and beyond, in Clouds in the Perturbed Climate System,* Cambridge, MIT Press.

HE, Y. B., HOLLENSTEIN, H., QUACK, M., RICHARD, E., SNELS, M. & BURGER, H. (2002) High resolution analysis of the complex symmetric CF_3

stretching chromophore absorption in CF_3I. *Journal of Chemical Physics,* 116, 974-983.

HIGHWOOD, E. J. & SHINE, K. P. (2000) Radiative forcing and global warming potentials of 11 halogenated compounds. *Journal of Quantitative Spectroscopy & Radiative Transfer,* 66, 169-183.

HILL, R. (1980) A theory for optimization in the use of acoustic emission transducers. *Journal of the Acoustical Society of America,* 67, 673.

HOFFMANN, T. L. (2000) Environmental implications of acoustic aerosol agglomeration. *Ultrasonics,* 38, 353-357.

HOLTOM, P. D., DAWES, A., MUKERJI, R. J., DAVIS, M. P., WEBB, S. M., HOFFMAN, S. V. & MASON, N. J. (2006) VUV photoabsorption spectroscopy of sulfur dioxide ice. *Physical Chemistry Chemical physics,* 8, 714-718.

HOUGHTON, J. T. & GROUP, I. P. O. C. C. W. (1995) *Climate change, 1994: radiative forcing of climate change and an evaluation of the IPCC IS92 emission scenarios*, Cambridge University Press.

HUANG, S. (2004) Merging information from different resources for new insights into climate change in the past and future. *Geophysical Research Letters,* 31, L13205.

IEEE (1976) Standard on Piezoelectricity IN INSTITUTE, A. N. S. (Ed.), IEEE.

IPCC (1990) Climate Change: The Intergovernmental Panel on Climate Change Scientific Assessment. IN HOUGHTON, J. T., JENKINS, G. J. & EPHRAUMS, J. J. (Eds.) New York.

IPCC (2001) The Scientific Basis. Contribution of Working Group I to the Third Assessment Report of the Intergovernmental Panel on Climate Change. IN J.T., H., DING, Y., GRIGGS, D. J., NOGUER, M., LINDEN, P. J. V. D., X. DAI, K. M. & JOHNSON, C. A. (Eds.) NY, IPCC.

IPCC (2007) *Climate Change 2007: The Physical Science Basis. Contribution of Working Group I to the Fourth Assessment Report of the Intergovernmental Panel on Climate Change,* Cambridge, United Kingdom and New York, NY, USA, Cambridge University Press.

JAIN, A., BRIEGLEB, B., MINSCHWANER, K. & WUEBBLES, D. (2000) Radiative forcings and global warming potentials of 39 greenhouse gases. *Journal Geophysical Research,* 105, 20773-20790.

KENDALL, P. A., MASON, N. J., BUCHANAN, G. A., MARSTON, G., TEGEDER, P., DAWES, A., EDEN, S., LIMÃ£O-VIEIRA, P. & NEWNHAM, D. A. (2003) Temperature dependent high-resolution infrared photoabsorption cross-sections of trifluoromethyl sulphur pentafluoride. *Chemical Physics,* 287, 137-142.

KING, L. V. (1934) On the Acoustic Radiation Pressure on Spheres. *Proceedings of the Royal Society of London. Series A, Mathematical and Physical Sciences,* 147, 212-240.

KRITZ, J. (1961) A High-Efficiency Transducer for Transmission to Air. *Journal of the Acoustical Society of America,* 8, 1570-1570.

LEIGHTON, T. G. (1997) *The Acoustic Bubble,* London, Academic Press.

LOHMANN, U., ROTSTAYN, L., STORELVMO, T., JONES, A., MENON, S., QUAAS, J., EKMAN, A. M. L., KOCH, D. & RUEDY, R. (2010) Total aersol effect: radiative forcing or radiative flux perturbation? *Atmospheric Chemistry Physics,* 10, 3235-3246.

LUTHER, F. M. & FOUQUART, Y. (1985) *Intercomparison of radiation codes in climate models (ICRCCM),* Geneva.

MANN, M. E. & JONES, P. D. (2003) Global surface temperatures over the past two millennia. *Geophysical Research Letters,* 30, 1820.

MANTHEY , W. (1992) Ultrasonic transducers and transducer arrays for applications in air. *Measurement Science and Technology,* 3, 249.

MASON, N. J., DAWES, A., DRAGE, E. A., WEBB, S. M., MCPHEAT, R. & HAYES, G. (2008) The spectroscopy and chemical dynamics of microparticles explored using an ultrasonic trap. *Faraday Discussions,* 137, 367-376.

MASON, N. J., DAWES, A., MUKERJI, R., DRAGE, E. A., VASEKOVA, E., WEBB, S. M. & LIMÃ£O-VIEIRA, P. (2005) Atmospheric chemistry with synchrotron radiation. *Journal of Physics B: Atomic, Molecular and Optical Physics,* 38, S893-S911.

MCGEE, P., F. CLEVELAND, F.,MILLER, S. (1952) Infrared Spectral Data and Tentative Assignments for CF3Br and CF3I. *Journal of Chemical Physics,* 20, 1044.

MENON, S., HANSEN, J., NAZARENKO, L. & LUO, Y. (2002) Climate Effects of Black Carbon Aerosols in China and India. *Science,* 297, 2250-2253.

MILLS, I. M. & WHIFFEN, D. H. (1959) Integration theorems on vibrational intensities. *Journal of Chemical Physics,* 30, 1916-1620.

MISRA, A., SEES, J., HALL, L., LEVY, R. A., ZAITSEV, V. B., ARYUSOOK, K., RAVINDRANATH, C., SIGAL, V., KESARI, S. & RUFIN, D. (1998) Plasma etching of dielectric films using the non-global-warming gas CF3I. *Materials Letters,* 34, 415-419.

MORGANELECTROCERAMICS (2009) Guide to Piezoelectric & Dielectric Ceramic. Windsor, Morgan Electro Ceramics.

MORGANELECTROCERAMICS (2012) TP-235 The Design of Piezoelectric Sandwich Transducers *Technical Publications.* Morgan Electro Ceramics.

MUTSCHKE, H. (2011) Jena-St Petersburg database of optical constants

NEWNHAM, D., BALLARD, J. & PAGE, M. (1996) Infrared band strengths of HFC-134a vapour. *Journal of Quantitative Spectroscopy & Radiative Transfer,* 55, 373-381.

NISHIHIRA, M. & IMANO, K. (2004) Simulation study of acoustic intermediate layer and electrical source impedance in an ultrasonic pulse system. *Acoustical Science and Technology,* 25, 203-206.

NIST (2011) Thermophysical Properties of Fluid Systems. NIST.

OHTAKE, H., ISHIHARA, H., FUSE, T., KOSHIISHI, A. & SAMUKAWA, S. (2003) Highly selective and high rate SiO2 etching using argon-added C2F4/CF3I plasma. *Journal of Vacuum Science & Technology B,* 21, 2142-2146.

ONDA (2012) ONDA Corporation.

ORESKES, N. (2004) The Scientific Consensus on Climate Change. *Science,* 306, 1686-1686.

PARKER, D. E. (2006) A Demonstration That Large-Scale Warming Is Not Urban. *Journal of Climate,* 19, 2882-2895.

PICKETT, H. M. (1991) The fitting and prediction of vibration-rotation spectra with spin interactions. *Journal of Molecular Spectroscopy,* 148, 371-377.

PILINIS, C. & LI, X. (1998) Particle shape and internal inhomogeneity effects on the optical properties of tropospheric aerosols of relevance to climate forcing. *Journal Geophysical Research,* 103, 3789-3800.

PINNOCK, S., HURLEY, M. D., SHINE, K. P., WALLINGTON, T. J. & SMYTH, T. J. (1995) Radiative Forcing of Climate by Hydrochlorofluorocarbons and Hydrofluorocarbons. *Journal of Geophysical Research-Atmospheres,* 100, 23227-23238.

POPE, V. D., GALLANI, M. L., ROWNTREE, P. R. & STRATTON, R. A. (2000) The impact of new physical parametrizations in the Hadley Centre climate model: HadAM3. *Climate Dynamics,* 16, 123-146.

RAMASWAMY, V., SCHWARZKOPF, M. D. & RANDEL, W. J. (1996) Fingerprint of ozone depletion in the spatial and temporal pattern of recent lower-stratospheric cooling. *Nature,* 382, 616-618.

RATTIGAN, O. V., SHALLCROSS, D. E. & COX, R. A. (1997) UV absorption cross-sections and atmospheric photolysis rates of CF3I, CH3I, C2H5I and CH2ICl. *Journal of the Chemical Society-Faraday Transactions,* 93, 2839-2846.

RAYLEIGH, J. W. S. (1878) The explanation of certain acoustical phenomena. *Nature,* 18, 319-321

RIERA-FRANCO DE SARABIA, E., ELVIRA-SEGURA, L., GONZÃ¡LEZ-GÃ³MEZ, I., RODRÄ±Ì□GUEZ-MAROTO, J. J., MUÃ±OZ-BUENO, R. & DORRONSORO-AREAL, J. L. (2003) Investigation of the influence of humidity on the ultrasonic agglomeration of submicron particles in diesel exhausts. *Ultrasonics,* 41, 277-281.

RILEY, C. M., ROSE, W. I. & BLUTH, G. J. S. (2003) Quantitative shape measurements of distal volcanic ash. *Journal Geophysical Research,* 108, 2504.

SANABIA, J. E., MOORE, J. H. & TOSSELL, J. A. (2002) CF3I on a silicon surface: Adsorption, temperature-programmed desorption, and electron-stimulated desorption. *Journal of Chemical Physics,* 116, 10402-10410.

SATHEESH, S. & KRISHNAMOORTHY, K. (2005) Radiative effects of natural aerosols: A review. *Atmospheric Environment* 39, 2089-2110.

SCHNEIDER, C. A., RASBAND, W. S. & ELICEIRI, K. W. (2012) NIH Image to ImageJ: 25 years of image analysis. *Nature Methods,* 9, 671-675.

SCHWARTZ, J. & NEAS, L. M. (2000) Fine Particles Are More Strongly Associated than Coarse Particles with Acute Respiratory Health Effects in Schoolchildren. *Epidemiology,* 11, 6-10.

SCOTT, D. S. (1975) A new approach to the acoustic conditioning of industrial aerosol emissions. *Journal of Sound and Vibration,* 43, 607-619.

SEINFELD, J. H., PANDIS, S. N. & ZELLNER, R. (2000) Atmospheric Chemistry and Physics, from Air Pollution to Climate Change. *Journal of Atmospheric Chemistry,* 37, 212-214.

SHERIDAN, J. & GORDY, W. (1950) Interatomic Distances in CF_3Br, CF_3I, and CF_3CN. *Physical Review,* 77, 292-293.

SIGURDSSON, H. (1990) Evidence of volcanic loading of the atmosphere and climate response. *Global and Planetary Change,* 3, 277-289.

SMITH, K., NEWNHAM, D., PAGE, M., BALLARD, J. & DUXBURY, G. (1996) Infrared band strengths and absorption cross-sections of HFC-32 vapour. *Journal of Quantitative Spectroscopy & Radiative Transfer,* 56, 73-82.

SOLOMON, S., BURKHOLDER, J. B., RAVISHANKARA, A. R. & GARCIA, R. R. (1994) Ozone Depletion and Global Warming Potentials of CF_3I. *Journal of Geophysical Research-Atmospheres,* 99, 20929-20935.

SVILAINIS, L. & MOTIEJŪNAS, G. (2006) Power amplifier for ultrasonic transducer excitation. *Ultragarsas,* 58, 30-36.

TAKEKAWA, H., MINOURA, H. & YAMAZAKI, S. (2003) Temperature dependence of secondary organic aerosol formation by photo-oxidation of hydrocarbons. *Atmospheric Environment,* 37, 3413-3424.

TEGEN, I. & MILLER, R. (1998) A general circulation model study on the interannual variability of soil dust aerosol. *Journal Geophysical Research,* 103, 25975-25995.

TEMA (2012) Laboratory disc mill.

TEMKIN, S. (1994) Gasdynamic agglomeration of aerosols. I. Acoustic waves. *Physics of Fluids,* 6, 2294.

UNFCCC (1991) United Nations Framework Convention on Climate Change. United Nations.

WEBB, S. M., JAKSCH, D., MCPHEAT, R. A., DRAGE, E., VASEKOVA, E., LIMAO-VIEIRA, P., MASON, N. J. & SMITH, K. M. (2005) High-resolution, temperature dependant, Fourier transform infrared spectroscopy of CF_3I. *Journal of Quantitative Spectroscopy & Radiative Transfer,* 94, 425-438.

WEBB, S. M. & MASON, N. J. (2004) Single-bubble sonoluminescence: creating a star in a jar. *European Journal of Physics,* 25, 101-113.

WIKLUND, M., TOIVONEN, J., TIRRI, M., HANNINEN, P. & HERTZ, H. M. (2004) Ultrasonic enrichment of microspheres for ultrasensitive biomedical analysis in confocal laser-scanning fluorescence detection. *Journal of Applied Physics,* 96, 1242-1248.

WILKINS, E. T. (1954) Air pollution aspects of the London fog of December 1952. *Quarterly Journal of the Royal Meteorological Society,* 80, 267-271.

WISCOMBE, W. J. (1980) Improved Mie scattering algorithms. *Applied Optics,* 19, 1505-1509.

WOLF, S. & VOSHCHINNIKOV, N. V. (2004) Mie scattering by ensembles of particles with very large size parameters. *Computer Physics Communications,* 162, 113-123.

XIE, W. J., CAO, C. D., LU, Y. J. & WEI, B. (2002) Levitation of Iridium and Liquid Mercury by Ultrasound. *Physical Review Letters,* 89, 104304.

XIE, W. J. & WEI, B. (2001) Parametric study of single-axis acoustic levitation. *Applied Physics Letters,* 79, 881-883.

Chapter 10: Appendices

10.1 Appendix 1: Matlab routine for finding node volume by colour

```
C:\MATLAB6p5\work\aerosol_data_processing\d...\pixel_count.m        Page 1
30 July 2012                                                      01:11:08

%program to extract a frame from an avi movie

%opens movie and removes from the avi structure file the number of frames
mov=aviread('D:\pictures_dust\video 94.avi');
file_info=aviinfo('D:\pictures_dust\video 94.avi');
numframes=file_info(1).NumFrames;
str1='SAND_63-90';

for framenum=50:round((numframes-1)/4):numframes;
str2=num2str(framenum);
n=framenum
%frame removed, converted to an image and displayed

frame=mov(framenum);
%clear mov;
[image,map1]=frame2im(frame);
clear frame;

%cropping node1

imshow(image,map1);
[ex,why,rgb]=impixel1;
saveas(gcf,['C:\Documents and Settings\sarah webb\My Documents\Acoustic_Trap\SAND\pixel ↙
_count\image_',str1,'_',str2,'.jpeg']);
%zoom(2);
node1=imcrop;
imshow (node1), title ('RGB image of the node closest to the transducer');

%image is shown and select area of node one with cross hair

saveas(gcf,['C:\Documents and Settings\sarah webb\My Documents\Acoustic_Trap\SAND\pixel ↙
_count\n1RGB_',str1,'_',str2,'.jpeg']);
close gcf;

%cropping node2 (same as before)

imshow(image,map1), title ('RGB image of the node furthest from the transducer');
zoom(2);
node2=imcrop;
imshow (node2);
saveas (gcf,['C:\Documents and Settings\sarah webb\My Documents\Acoustic_Trap\SAND\pixe ↙
l_count\n2RGB_',str1,'_',str2,'.jpeg']);

close gcf;
clear image;
clear map1;

%turns RGB image to an grayscale image which imhist accepts as input, also
%inserts a colour bar on the grayscale image so that the cut-off intensity
%of node edge may be found

[RGBn1, map2]=imread(['C:\Documents and Settings\sarah webb\My Documents\Acoustic_Trap\ ↙
SAND\pixel_count\n1RGB_',str1,'_',str2,'.jpeg']);
imshow (RGBn1,map2);
RGBn1a=imcrop;
%[x,map2]=rgb2ind(RGBa,4);
clear RGBn1;
%imshow (x,map2)
%clear RGBa
grayn1=rgb2gray(RGBn1a);
imshow (grayn1), title ('Grayscale image of the node closest to the transducer');
```

```
pixval on;
saveas (gcf,['C:\Documents and Settings\sarah webb\My Documents\Acoustic_Trap\SAND\pixe ↙
l_count\n1gray_',str1,'_',str2,'.jpeg']);

%draws a histogram of the pixels

figure, imhist(grayn1,255), title ('Histogram of pixel colour around node closest to th ↙
e transducer');
set(gca, 'YLimMode', 'auto','XLimMode','Auto')
%set(gca)
saveas (gcf,['C:\Documents and Settings\sarah webb\My Documents\Acoustic_Trap\SAND\pixe ↙
l_count\n1hist_',str1,'_',str2,'.jpeg']);
histn1= imhist(grayn1,255);
%figure, imhist(y,255);

%asks user for an input on the command line (intensity cut off for edge of
%node) and then counts how many pixels are within the node and how many are
%in the total image

user_entry = input('pixel intensity cut-off for node 1 =');
n1pix=sum(histn1(1:user_entry,1));
n1vol=(pi*4/3)*((sqrt(n1pix/pi))^3);
Tn1pix=sum(histn1);
clear RGBn1a;

%same for node 2

[RGBn2, map3]=imread(['C:\Documents and Settings\sarah webb\My Documents\Acoustic_Trap\ ↙
SAND\pixel_count\n2RGB_',str1,'_',str2,'.jpeg']);
imshow (RGBn2,map3), title ('RGB image of the node furthest from the transducer');
RGBn2a=imcrop;
%[x,map2]=rgb2ind(RGBa,4);
clear RGBn2;
%imshow (x,map2)
%clear RGBa
grayn2=rgb2gray(RGBn2a);
imshow (grayn2),  title ('Grayscale image of the node furthest from the transducer');
pixval on;
saveas (gcf,['C:\Documents and Settings\sarah webb\My Documents\Acoustic_Trap\SAND\pixe ↙
l_count\n2gray_',str1,'_',str2,'.jpeg']);

%draws a histogram of the pixels

figure, imhist(grayn2,255), title ('Histogram of pixel colour around node furthest from ↙
 the transducer');
set(gca, 'YLimMode', 'auto','XLimMode','Auto')
saveas (gcf,['C:\Documents and Settings\sarah webb\My Documents\Acoustic_Trap\SAND\pixe ↙
l_count\n2hist_',str1,'_',str2,'.jpeg']);
histn2= imhist(grayn2,255);
%figure, imhist(y,255);

%asks user for an input on the command line (intensity cut off for edge of
%node) and then counts how many pixels are within the node and how many are
%in the total image

user_entry1 = input('pixel high intensity (white)cut-off for node 2 = ');
user_entry2 = input('pixel low intensity (black)cut-off for node 2 = ');
n2pix=sum(histn2(user_entry2:user_entry1,1));
n2vol=(pi*4/3)*((sqrt(n2pix/pi))^3);
Tn2pix=sum(histn2);
clear RGBn2a;
```

```
clear image;

prop(1,framenum)=n1vol/(n1vol+n2vol);

end

avfrac=(sum(prop))/4

clear mov
```

10.2 Appendix 2: Matlab routine for finding the ellipse volume by modelling and ellipsoid


```
%program to extract a frame from an avi movie


str1 = input('Enter dust name: ','s');
str3 = input('Enter size range: ','s');
mass = input('Mass of dust (kg): ');
loca=input('Location of video files: ','s');
vid=input('Video file name: ','s')

if loca=='cut'
    str4 = ['C:\Documents and Settings\sarah webb\My Documents\Acoustic_Trap\cut videos ↙
\',vid,'.avi']
elseif loca=='cds'
    str4 = ['D:\pictures_dust\',vid,'.avi']
elseif loca=='new'
    str4 = ['C:\Documents and Settings\sarah webb\My Documents\Acoustic_Trap\new_sample ↙
s\ral_SLA\videos\',vid,'.avi']
else
    loca='location name not recognised'
    break
end

%opens movie and removes from the avi structure file the number of frames
%C:\Documents and Settings\sarah webb\My Documents\Acoustic_Trap\cut videos\video40cut. ↙
avi
%D:\pictures_dust\video 85.avi
mov=aviread(str4);
file_info=aviinfo(str4);
numframes=file_info(1).NumFrames;


for framenum=5:round((numframes-1)/3):numframes;
str2=num2str(framenum);
n=framenum
%frame removed, converted to an image and displayed

frame=mov(framenum);
%clear mov;
[image,map1]=frame2im(frame);
clear frame;

%crops picture to node area plus transducer

imshow(image,map1);

saveas(gcf,['C:\Documents and Settings\sarah webb\My Documents\Acoustic_Trap\',str1,'\e ↙
llipse_vol\image_',str1,'_',str3,'_',str2,'.jpeg']);
%zoom(2);
node1=imcrop;
imshow (node1), title ('RGB image of the nodes in the transducer');

% pick pixels at each extreme of the transducer and nodes

[ex,why,rgb]=impixel;
saveas(gcf,['C:\Documents and Settings\sarah webb\My Documents\Acoustic_Trap\',str1,'\e ↙
llipse_vol\zoom_',str1,'_',str3,'_',str2,'.jpeg']);
close gcf;
clear image
%works out absolute length of pixel and therefore absolute length of nodes
pixlength=5.9e-2/(ex(2)-ex(1))
```

```
an1=pixlength*(ex(4)-ex(3))
%bn1=pixlength*(why(6)-why(5))
n1vol=(4/3)*pi*(an1/2)^3

an2=pixlength*(ex(6)-ex(5))
%bn2=pixlength*(why(10)-why(9))
n2vol=(4/3)*pi*(an2/2)^3

prop(1,framenum)=n1vol/(n1vol+n2vol);
prop(1,framenum+1)=an1

clear node1
end

clear mov

prop2=nonzeros(prop);
name=['C:\Documents and Settings\sarah webb\My Documents\Acoustic_Trap\',str1,'\ellipse ↙
_vol\particle_vols_',str1,'_',str3,'.txt']

%works out average of mass ratios and prints to file
avfrac=(sum(prop2(1:2:5)))/3;
avlen=(sum(prop2(2:2:6)))/3;
n1volav=(4/3)*pi*((avlen/2)^3);
nodemass=avfrac*mass;
prop2(7)=avfrac;
prop2(8)=nodemass;
prop2(9)=n1volav
prop2(10)=avlen
fid = fopen(name,'w');
fprintf(fid,'%5.3e \r\n',prop2);
fclose(fid);
```

10.3 Appendix 3: Histogram fitting Matlab routine


```
%program to fit lognormal distribution to exp data and plot over histogram
%of data and output parameters

%get user inputs for program from command line

%general inputs
str1 = input('Enter dust name: ','s');
str2 = input('Enter size range: ','s');
mass = input('Mass of dust (kg): ');
density = input ('Density of sample (kg/m^3): ');
volum=input('Volume of node (m^3): ');


%no. of particles in size ranges'
y1 = input('number in size range <0.1: ');
y2 = input('number in size range 0.1-1: ');
y3 = input('number in size range 1-5: ');
y4 = input('number in size range 5-10: ');
y5 = input('number in size range 10-25: ');
y6 = input('number in size range 25-50: ');
y7 = input('number in size range 50-75: ');
y8 = input('number in size range 75-100: ');
y9 = input('number in size range 100-200: ');
y10 = input('number in size range 200-300: ');
y11 = input('number in size range 300-400: ');
y12 = input('number in size range 400-500: ');
y13 = input('number in size range 500-600: ');


x=[0.0,0.1,1,5,10,25,50,75,100,200,300,400,500,600];
y=[y1,y2,y3,y4,y5,y6,y7,y8,y9,y10,y11,y12,y13];
% <0.1,0.1-1,1-5 ,5-10,10-25,25-50

%selecting density


%if strcmpi(str1,'soot')==1
 %   density=2000
 %elseif strcmpi(str1,'sand')==1
 %   density=2650
 %elseif strcmpi(str1,'0707')==1
 %   density=2900
    %elseif str3=='sand'
    %elseif strcmpi(str1,'NZ82')==1
    %density=2500
    %else
   % result='dust name not recognised'
   % break
   %end

%converting absolute numbers in size bins to histogram heights
sz=size(x,2)-1;
height=zeros(1,sz);
radius=x./2

for n=1:sz;
    height(1,n)=y(n)/(radius(n+1)-radius(n));
    height(1,sz+1)=height(1,sz);
    width(n)=radius(n);
    width(sz+1)=radius(sz+1);
    acwidth(n)=(radius(n+1)-radius(n));
```

```
    mean_rad(1,n)=(((radius(1,n+1)-radius(1,n))/2)+radius(1,n));
    mean_vol(1,n)=(4/3)*pi*((mean_rad(1,n).*1e-6).^3);
    mean_vol_rad(1,n)=(((radius(1,n).^4)+(radius(1,n+1).^4))/2).^0.25;
    act_mean_vol(1,n)=(4/3).*pi.*(mean_vol_rad(1,n).*1e-6).^3;
    %mean_rad(1,n)=x(1,n)

end

weight_mean_vol=sum(act_mean_vol.*y)/sum(y)


%fitting to a lognormal distribution
[i,j,s] = find(height);
ex1=[0:0.1:radius(max(j)+1)];
exy=transpose(ex1);

co3=0.389;
fit_x=transpose(mean_rad);
fit_vol=(4/3).*pi.*(fit_x.^3);
fit_y=transpose(height(1:sz))/sum(y);
%(sum(height(1:sz).*acwidth));

%obtaining parameters from maximum likelihood parameters
%lnx=log(fit_x);
%topfact=height.*lnx;
%topfact2=sum(topfact);
%mew=topfact/sum(y);
%tpfct=(lnx-mew)^2
%tpfct2=sum(tpfct2);
%row=sqrt(tpfct2/sum(y))

%from least squares
mod = fittype('(co3./(x.*co2)).*exp(-((log(x)-co1).^2)./(2*(co2^2)))','coeff',{'co1','c ↙
o2'},'prob','co3');

opts = fitoptions(mod);
opts.Lower = [log(0.05),0.01];
opts.Upper = [log(500),1e4];
opts.MaxIter = 500;
opts.DiffMaxChange: 500;

fresult = fit(fit_x,fit_y,mod,opts,'prob',co3);
[M,v]=lognstat(fresult.co1,fresult.co2);

%calculating output parameters

meanvol=(4/3)*pi*(M*1e-6)^3;
meanvol2=(sum(mean_vol.*y))/sum(y);


 total_v=mass/density ;
 no_part=total_v/weight_mean_vol;
 no_bs=no_part/sum(y);
 ac_no=height*no_bs;

 %plotting and writing outputs
stairs (width,ac_no);
xlabel('Particle radius / \mum','FontName','Times New Roman','FontSize',10);
ylabel('Number of particles ','FontName','Times New Roman','FontSize',10)
set(gca,'XLim',[0,radius(max(j)+1)]);
set(findobj('Type','line'),'Color','k','LineWidth',2);
```

```
hold on ;

why = lognpdf(exy,fresult.col,fresult.co2);

factfact=sum(y.*no_bs);
fact=why.*(factfact);
%why1=transpose(why);
plot(exy,fact);
h = findobj(gca,'Type','line');
set(h(1),'Color','k','LineWidth',2,'LineStyle','--');
maxrad=exp(fresult.col);
no_conc=(sum(ac_no(1:sz).*acwidth))/(volum*1e6);
fresult


saveas(gcf,['C:\Documents and Settings\yvette\My Documents\sarah\Acoustic_Trap2\',str1, ↙
'\size dist\hist_',str2,'_log_new.jpeg']);

%hold off

P= logncdf(exy,fresult.col,fresult.co2);
%plot(exy,P); grid;
k=find(0.45< P & P<0.55);
median=mean(exy(k));

j=find(why);
spread=max(exy(j))-min(exy(j));

name=['C:\Documents and Settings\yvette\My Documents\sarah\Acoustic_Trap2\',str1,'\size ↙
 dist\variable_',str2,'_new.mat'];
save (name, 'mass','volum','fresult','median','spread','no_conc');
no_conc
hold off
%clear all
```

10.4 Appendix 4; Miex Program with adaptations to put it into a loop

```
                                    miex_logn_loop.f90
!
********************************************************************************
**********
! ADAPTED AND PUT INTO LOOP BY
!
_____________________________________________________
!                                                    (Sarah Webb)
!
================================================================================
==========
!
********************************************************************************
**********
! MIEX: MIE SCATTERING CODE FOR LARGE GRAINS
!
_____________________________________________________
!                                                    Contact information:
swolf@mpia.de (Sebastian Wolf)
!
================================================================================
==========
! GENERAL CODE DESCRIPTION
! ------------------------
!
! Based on Mie scattering theorie, the following quantities for
!
!       (a) single grain sizes / chemical components
!   and (b) mixtures of chemically different grains with a size distributions
!
! can be calculated:
!
!   * Scattering matrix elements S11, S12, S33, and S34
!   * Extinction effiency factor          (Qext) & Extinction cross section
(Cext)
!   * Scattering effiency factor          (Qsca) & Scattering cross section
(Csca)
!   * Absorption effiency factor          (Qabs) & Absorption cross section
(Cabs)
!   * Backscattering effiency factor      (Qbk)  & Backscattering cross section
(Cbk)
!   * Radiation pressure effiency factor (Qpr)
!   * Albedo
!   * Scattering assymetry factor (g).
!
!
_____________________________________________________
! The optical data of the grains have to be provided in files with the following
tabular form
!   * first  row: wavelength [micron]
!   * second row: n (=real[ri])
!   * second row: k (=imag[ri]).
!
! Rem.: For astrophysical applications, such tables can be found, e.g., at
!       http://www.astro.uni-jena.de/Users/database/entry.html
!       ("Jena-Petersburg Database of Optical Constants"). See, also,
!       N.V.Voshchinnikov: "Optics of Cosmic Dust",
!                          Astrophysics and Space Physics Review 12,  1 (2002)
!       for further references.
!
!
================================================================================
==========
! SUBROUTINES / MODULES
! ---------------------
!
! (1) Module 'datatype'     : data type definitions
! (2) Module 'mie_routines'
!     (2.1) aa2      : calculations of the ratio of derivative to the function
                                    Page 1
```

```
for Bessel functions
!                       of half order with complex argument: J'(n)/J(n)
!     (2.2) shexqnn2 : derive quantities (listed above) for a single size
parameter
!                       and chemical composition`
!
*****************************************************************************
*********************

!
=============================================================================
====================
! Definition of the data type to be used for floating point operations:
! - r1: real*4  (FORTRAN 77: "real")
! - r2: real*8  (FORTRAN 77: "double precision")
!
=============================================================================
====================
module datatype
  implicit none
  integer, parameter, public ::  r1=selected_real_kind(1)  ! real*4
  integer, parameter, public ::  r2=selected_real_kind(9)  ! real*8 (double
precision)
end module datatype


!
=============================================================================
====================
! Collection of subroutines
!
=============================================================================
====================
module mie_routines
  private :: aa2
  public  :: shexqnn2
contains
  !
=============================================================================
==================
  ! Subroutine for calculations of the ratio of derivative to the function for
Bessel functions
  ! of half order with complex argument: J'(n)/J(n). The calculations are given
by the recursive
  ! expression ``from top to bottom'' beginning from n=num.
  ! *  a=1/x (a=2*pi*a(particle radius)/lambda - size parameter).
  ! *  ri - complex refractive index.
  ! *  ru-array of results.
  ! - this routine is based on the routine 'aa' published by
  !       N.V.Voshchinnikov: "Optics of Cosmic Dust",
  !                          Astrophysics and Space Physics Review 12,  1
(2002)
  !
=============================================================================
==================
  subroutine aa2( a, ri, num, ru )
    use datatype

    implicit none

    ! variables for data
exchange.....................................................................
    real(kind=r2), intent(in)                  :: a
    complex(kind=r2), intent(in)               :: ri
    integer, intent(in)                        :: num
    complex(kind=r2), dimension(:), intent(out) :: ru

    ! local
variables.....................................................................
```

```
.........
    integer :: i, i1, j, num1
    complex(kind=r2) :: s, s1

!-------------------------------------------------------------------------------
-----------------
    ! initialisierung: not necessary (+ slowes the code down remarkably)
    ! ru(:) = (0.0, 0.0)

    s       = a / ri
    ru(num) = real(num+1,kind=r2) * s
    num1    = num - 1
    do j=1, num1
       i     = num - j
       i1    = i + 1
       s1    = i1 * s
       ru(i) = s1 - 1.0_r2 / (ru(i1) + s1)
    end do
  end subroutine aa2


!===============================================================================
====================
  ! shexqnn2
  ! --------
  ! - for a given size parameter 'x' and (complex) refractive index 'ri' the
following quantities
  !   are determined:
  !   * Qext      - extinction effiency
  !   * Qsca      - scattering effiency
  !   * Qabs      - absorption effiency
  !   * Qbk       - backscattering effiency
  !   * Qpr       - radiation pressure effiency
  !   * albedo    - Albedo
  !   * g         - g scattering assymetry factor
  !   * SA1, SA2 - scattering amplitude function
  ! - further input parameters
  !   * doSA = .true.  ->  calculation of the scattering amplitudes
  !   * nang ... half number of scattering angles theta in the intervall
0...PI/2
  !               (equidistantly distributed)
  ! - this routine is based on the routine 'shexqnn' published by
  !       N.V.Voshchinnikov: "Optics of Cosmic Dust",
  !                          Astrophysics and Space Physics Review 12,  1
(2002)

!===============================================================================
====================
  subroutine shexqnn2( ri, x, Qext, Qsca, Qabs, Qbk, Qpr, albedo, g, ier, SA1,
SA2, doSA, nang )
    use datatype

    implicit none

    ! variables for data
exchange.....................................................................
    complex(kind=r2), intent(in)                :: ri
    real(kind=r2), intent(in)                   :: x
    real(kind=r2), intent(out)                  :: Qext, Qsca, Qabs, Qbk, Qpr,
albedo, g
    integer, intent(out)                        :: ier
    complex(kind=r2), dimension(:), intent(out) :: SA1, SA2
    logical, intent(in)                         :: doSA
    integer, intent(in)                         :: nang

    ! local
variables.....................................................................
.........
```

```
    integer       :: iterm, nterms, num, iu0, iu1, iu2, iang2, iang
    real(kind=r2) :: r_iterm, factor, eps, pi, ax, besJ0, besJ1, besJ2, besY0,
besY1, besY2, b, an, &
          y, ass, w1, qq, fac, an2, P, T, Si, Co, z, xmin
    complex(kind=r2) :: ra0, rb0, ra1, rb1, r, ss, s1, s2, s3, s, rr

    real(kind=r2), dimension(0:1)               :: fact
    real(kind=r2), dimension(:), allocatable    :: mu, fpi, fpi0, fpi1, ftau
    complex(kind=r2), allocatable, dimension(:) :: ru

!-------------------------------------------------------------------------------
-----------------
    ! Maximum number of terms to be considered
    nterms = 20000000

    ! Accuracy to be achieved
    eps    = 1.0e-20_r2

    ! Minimum size parameter
    xmin   = 1.0e-6_r2


!-------------------------------------------------------------------------------
-----------------
    ! initialization
    allocate( ru(1:nterms), mu(1:nang), fpi(1:nang), fpi0(1:nang), fpi1(1:nang),
ftau(1:nang) )
    ier     = 0
    Qext    = 0.0_r2
    Qsca    = 0.0_r2
    Qabs    = 0.0_r2
    Qbk     = 0.0_r2
    Qpr     = 0.0_r2
    albedo  = 0.0_r2
    g       = 0.0_r2
    fact(0) = 1.0_r2
    fact(1) = 1.0e+250_r2
    factor  = 1.0e+250_r2

    ! null argument
    if (x <= xmin) then
       ier = 1
       print *, "<!> Error in subroutine shexqnn2:"
       print *, "    - Mie scattering limit exceeded:"
       print *, "      current size parameter: ", x
    else
       pi = 4.0_r2 * atan(1.0_r2) ! PI = 3.14...
       ax = 1.0_r2 / x
       b  = 2.0_r2 * ax**2
       ss = (0.0_r2, 0.0_r2)
       s3 = (0.0_r2,-1.0_r2)
       an = 3.0_r2

       ! define the number for subroutine aa2 [Loskutov (1971)]
       y   = sqrt( RI * conjg(ri) )  *  x
       num = 1.25 * y + 15.5

       if      ( y<1.0_r2 ) then
          num = 7.5 * y + 9.0
       else if ( (y>100.0_r2) .and. (y<50000.0_r2) ) then
          num = 1.0625 * y + 28.5
       else if ( y>=50000.0_r2 ) then
          num=1.005*y+50.5
       end if

       if(num > nterms) then
          ier = 2
          print *, "<!> Error in subroutine shexqnn2:"
          print *, "    - Maximum number of terms  : ", nterms
```

```
         print *, "    - Number of terms required : ", num
         print *, "    ** Solution: Increase default value of the variable
'nterm' **"
      else
         ! logarithmic derivative to Bessel function (complex argument)
         call aa2(ax,ri,num,ru)

         !
!-------------------------------------------------------------------------------
----------
         ! FIRST TERM
         !
!-------------------------------------------------------------------------------
----------
         ! initialize term counter
         iterm = 1

         ! Bessel functions
         ass = sqrt( pi / 2.0_r2 * ax )
         w1  = 2.0_r2/pi * ax
         Si  = sin(x)/x
         Co  = cos(x)/x

         ! n=0
         besJ0 =  Si / ass
         besY0 = -Co / ass
         iu0   = 0

         ! n=1
         besJ1 = ( Si * ax - Co) / ass
         besY1 = (-Co * ax - Si) / ass
         iu1   = 0
         iu2   = 0

         ! Mie coefficients
         s   = ru(1) / ri + ax
         s1  = s * besJ1 - besJ0
         s2  = s * besY1 - besY0
         ra0 = s1 / (s1 - s3 * s2)   ! coefficient a_1

         s   = ru(1) * ri + ax
         s1  = s * besJ1 - besJ0
         s2  = s * besY1 - besY0
         rb0 = s1 / (s1 - s3 * s2)   ! coefficient b_1

         ! efficiency factors
         r    = -1.5_r2 * (ra0-rb0)
         Qext = an * (ra0 + rb0)
         Qsca = an * (ra0 * conjg(ra0)  +  rb0 * conjg(rb0))

         ! scattering amplitude functions
         if (doSA) then
            do iang=1, nang
               mu(iang) = cos( (real(iang,kind=r2)-1.0_r2) *
(pi/2.0_r2)/real(nang-1,kind=r2) )
            end do

            fpi0(:) = 0.0_r2
            fpi1(:) = 1.0_r2
            SA1(:)  = cmplx( 0.0_r2, 0.0_r2 )
            SA2(:)  = cmplx( 0.0_r2, 0.0_r2 )

            r_iterm = real(iterm,kind=r2)  ! double precision
            fac     = (2.0*r_iterm + 1.0_r2) / (r_iterm * (r_iterm+1.0_r2))

            do iang=1, nang
               iang2      = 2 * nang - iang

               fpi(iang)  = fpi1(iang)
```

```
                ftau(iang) = r_iterm * mu(iang) * fpi(iang)  -  (r_iterm+1.0) *
fpi0(iang)

                P          = (-1.0)**(iterm-1)
                SA1(iang)  = SA1(iang)   +   fac * (ra0*fpi(iang)  +
rb0*ftau(iang))

                T          = (-1.0)**iterm
                SA2(iang)  = SA2(iang)   +   fac * (ra0*ftau(iang) +
rb0*fpi(iang) )

                if  ( iang /= iang2 )  then
                   SA1(iang2) = SA1(iang2)   +   fac * (ra0*fpi( iang)*P +
rb0*ftau(iang)*T)
                   SA2(iang2) = SA2(iang2)   +   fac * (ra0*ftau(iang)*T +
rb0*fpi( iang)*P)
                end if
             end do

             iterm   = iterm + 1
             r_iterm = real(iterm, kind=r2)

             do iang=1, nang
                fpi1(iang) = ((2.0*r_iterm-1.0) / (r_iterm-1.0))   *   mu(iang)
*  fpi(iang)
                fpi1(iang) = fpi1(iang)   -   r_iterm * fpi0(iang)/(r_iterm-1.0)
                fpi0(iang) = fpi(iang)
             end do
          else
             ! start value for the next terms
             iterm = 2
          end if

          !
----------------------------------------------------------------------------
----------
          ! 2., 3., ... num
          !
----------------------------------------------------------------------------
----------
          z = -1.0_r2

          do
             an  = an + 2.0_r2
             an2 = an - 2.0_r2

             ! Bessel functions
             if(iu1 == iu0) then
                besY2 = an2 * ax * besY1 - besY0
             else
                besY2 = an2 * ax * besY1 - besY0 / factor
             end if
             if(dabs(besY2) > 1.0e+300_r2) then
                besY2 = besY2 / factor
                iu2   = iu1 + 1
             end if
             besJ2 = (w1 + besY2 * besJ1) / besY1

             ! Mie coefficients
             r_iterm = real(iterm,kind=r2)

             s   = ru(iterm) / ri + r_iterm * ax

             s1  = s * besJ2 / fact(iu2) - besJ1 / fact(iu1)
             s2  = s * besY2 * fact(iu2) - besY1 * fact(iu1)
             ra1 = s1 / (s1 - s3 * s2)                          ! coefficient a_n,
(n=iterm)

             s   = ru(iterm) * ri + r_iterm * ax
```

```
            s1  = s * besJ2 / fact(iu2) - besJ1 / fact(iu1)
            s2  = s * besY2 * fact(iu2) - besY1 * fact(iu1)
            rb1 = s1 / (s1 - s3 * s2)                          ! coefficient b_n,
(n=iterm)

            ! efficiency factors
            z  = -z
            rr = z * (r_iterm + 0.5_r2) * (ra1 - rb1)
            r  = r + rr
            ss = ss + (r_iterm - 1.0_r2) * (r_iterm + 1.0_r2) / r_iterm * (ra0
* conjg(ra1)  &
                + rb0 * conjg(rb1)) &
                + an2 / r_iterm / (r_iterm - 1.0_r2) * (ra0 * conjg(rb0))
            qq   = an * (ra1 + rb1)
            Qext = Qext + qq
            Qsca = Qsca + an * (ra1 * conjg(ra1) + rb1 * conjg(rb1))

            ! leaving-the-loop criterion
            if ( dabs(qq / qext) < eps ) then
               exit
            end if

            ! Bessel functions
            besJ0 = besJ1
            besJ1 = besJ2
            besY0 = besY1
            besY1 = besY2
            iu0   = iu1
            iu1   = iu2
            ra0   = ra1
            rb0   = rb1

            ! scattering amplitude functions
            if (doSA) then
               r_iterm = real(iterm,kind=r2)
               fac     = (2.0 * r_iterm+1.0) / (r_iterm * (r_iterm+1.0))

               do iang=1, nang
                  iang2      = 2 * nang - iang

                  fpi(iang)  = fpi1(iang)
                  ftau(iang) = r_iterm * mu(iang) * fpi(iang)  -  (r_iterm+1.0)
* fpi0(iang)

                  P          = (-1.0)**(iterm-1)
                  SA1(iang)  = SA1(iang)   +   fac * (ra0*fpi(iang) +
rb0*ftau(iang))

                  T          = (-1.0)**iterm
                  SA2(iang)  = SA2(iang)   +   fac * (ra0*ftau(iang) +
rb0*fpi(iang))

                  if  ( iang /= iang2 ) then
                     SA1(iang2) = SA1(iang2)   +   fac * (ra0*fpi(iang)*P  +
rb0*ftau(iang)*T)
                     SA2(iang2) = SA2(iang2)   +   fac * (ra0*ftau(iang)*T +
rb0*fpi( iang)*P)
                  end if
               end do

               iterm   = iterm + 1
               r_iterm = real(iterm,kind=r2)

               do iang=1, nang
                  fpi1(iang) = ((2.0*r_iterm-1.0) / (r_iterm-1.0))   *
mu(iang)  *  fpi(iang)
                  fpi1(iang) = fpi1(iang)   -   r_iterm *
fpi0(iang)/(r_iterm-1.0)
                  fpi0(iang) = fpi(iang)
```

```
            end do
         else
            iterm = iterm + 1
         endif

         if ( iterm==num ) then
            exit
         else
            cycle
         end if
      end do

      ! efficiency factors (final calculations)
      Qext   = b * Qext
      Qsca   = b * Qsca
      Qbk    = 2.0_r2 * b * r * conjg(r)
      Qpr    = Qext - 2.0_r2 * b * ss
      Qabs   = Qext - Qsca
      albedo = Qsca / Qext
      g      = (Qext - Qpr) / Qsca
    end if
  end if
  deallocate( ru, mu, fpi, fpi0, fpi1, ftau )
 end subroutine shexqnn2
end module mie_routines

!
================================================================================
====================
! Main Program
!
================================================================================
====================
program mie
 use datatype
 use mie_routines

 implicit none

 logical :: doSA, svsep
 integer :: icomp, ilam, nlam, ncomp, nrad, ask1, ask2, ask3, nang, nang2,
irad, ier, iang, en, kay, &
   intm, intn, into , nit, nfile, nfil , factcomp

 real(kind=r2) :: radmin, radmax, mu, row, radminlog, radmaxlog, steplog,
refmed, rad, rad1, delrad, &
      pi, x, qextx, qscax, qabsx, qbkx, qprx, albedox, gscattx, wqsc, wqscx,
weisum, wrad, weight, &
      wradx, angx, nfact, kfact
 real(kind=r2), allocatable, dimension(:) :: lambda, abun, albedo, gscatt,
S11x, S12x, S33x, S34x, &
      qext, qsca, qabs, qbk, qpr, &
      cext, csca, cabs, cbk, cpr, &
      minsq, bestn, bestk, minrad, &
      maxrad, mufil, rowfil
 real(kind=r2), allocatable, dimension(:,:) :: n, k, S11, S12, S33, S34, cexp
,leastsq, bestce
 real(kind=r2), allocatable, dimension(:,:,:) :: Cextal, difference
 complex(kind=r2) :: ri
 complex(kind=r2), allocatable, dimension(:) :: S1x, S2x


 character(len=8) :: fresult , datfile, fitparam
 character(len=8), allocatable, dimension(:) :: fname
 character(len=2) :: str
 !
--------------------------------------------------------------------------------
-----------------
```

```
  !print *
  !print *,
"=============================================================================="
  !print *, "
    "
  !print *, "     MIE SCATTERING     MIEX V1.04
    "
  !print *, "
_____________________ "
  !print *, "                                                    Contact:
swolf@mpia.de "
  !print *,
"=============================================================================="
  !print *
  print *,
"------------------------------------------------------------------------------"
  print *, "
    "
  print *, "                  MIE SCATTERING     MIEX V1.04
    "
  print *, "         (adapted to give best fit RI to experimental data)
    "
  print *, "
    "
  print *, "
    "
  print *,
"------------------------------------------------------------------------------"


!-------------------------------------------------------------------------------
--------------------
  ! 0. General settings

!-------------------------------------------------------------------------------
--------------------
  ! Real refractive index of the surrouding medium
  print *, "Real refractive index of the surrouding medium    : "; read *,
refmed


!-------------------------------------------------------------------------------
--------------------
  ! 1. Get main parameters

!-------------------------------------------------------------------------------
--------------------
  print *, "Number of wavelengths                             : "; read *, nlam
  print *, "Number of n and k iterations                      : "; read *, nit
  ncomp=1
  print *, "Name of the exp data files (lambda/Cext(all files for dust); 8
characters" &
  ; read  *, datfile
  print *, "Number of Cext data in file" ; read  *, nfile

  allocate( fname(1:ncomp), lambda(1:nlam), n(1:ncomp,1:nlam),
k(1:ncomp,1:nlam), abun(1:ncomp), &
       qext(1:nlam), qsca(1:nlam), qabs(1:nlam), qbk(1:nlam), qpr(1:nlam), &
       cext(1:nlam), csca(1:nlam), cabs(1:nlam), cbk(1:nlam), cpr(1:nlam), &
       albedo(1:nlam), gscatt(1:nlam), cexp(1:nfile,1:nlam),
difference(1:nfile,1:nit,1:nit),   &
       leastsq(1:nit,1:nit), bestn(1:nlam),bestk(1:nlam),minrad(1:nfile), &
       maxrad(1:nfile), mufil(1:nfile), rowfil(1:nfile),minsq(1:2),
bestce(nfile,nlam))
  allocate ( Cextal(1:nfile,1:nit,1:nit) )

  lambda(:) = 0.0_r2
  n(:,:)    = 0.0_r2
```

```
  k(:,:)    = 0.0_r2
  abun(:)   = 0.0_r2

  qext(:)   = 0.0_r2
  qsca(:)   = 0.0_r2
  qabs(:)   = 0.0_r2
  qbk(:)    = 0.0_r2
  qpr(:)    = 0.0_r2

  cext(:)   = 0.0_r2
  csca(:)   = 0.0_r2
  cabs(:)   = 0.0_r2
  cbk(:)    = 0.0_r2
  cpr(:)    = 0.0_r2
  Cextal(:,:,:)=0.0_r2
  cexp(:,:)=0.0_r2
  difference(:,:,:)=0.0_r2
  leastsq(:,:)=0.0_r2
  albedo(:) = 0.0_r2
  gscatt(:) = 0.0_r2
  minsq(:) =0.0_r2
  bestn(:)=0.0_r2
  bestk(:)=0.0_r2
  minrad(:)=0.0_r2
  maxrad(:)=0.0_r2
  mufil(:)=0.0_r2
  rowfil(:)=0.0_r2
  bestce(:,:)=0.0_r2

!-------------------------------------------------------------------------------
--------------------

  print *, "Name of the dust data files (lambda/n/k data); 8 characters"
  print *, " [all data files have to contain the refractive]"
  print *, " [index the same wavelength distribution       ]"

  do icomp=1,ncomp
     print *, "     ", icomp, ". component : "; read  *, fname(icomp)
  end do

  if (ncomp>1) then
     print *, "<?> Relative abundances of the different components [%]"
     do icomp=1,ncomp
        print *, "     ", icomp, ". component : "; read  *, abun(icomp)
     end do
  else
     abun(:) = 100.0_r2
  end if
  abun(:) = abun(:)/100.0_r2

  print *, "-1- Single grain size"
  print *, "-2- Grain size distribution                    : "
  read *, ask1
  if (ask1==1) then
     print *, " Grain radius [micron]                      : "
     read  *,radmin
     radmax = radmin
     nrad   = 1
     mu  = log(radmin)
     row = 0.0_r2
  else
    print *, "    File name for fit parameters [8 characters]          : "
     read  *,fitparam
!$$$$$$      print *, "    Minimum grain radius [micron]               : "
!$$$$$$      read  *,radmin
!$$$$$$      print *, "    Maximum grain radius [micron]               : "
!$$$$$$      read  *,radmax
!$$$$$$      print *, "    mu (mean) [micron]                          : "
```

```
!$$$$$$      read  *,mu
!$$$$$$      print *, "    row (standard deviation of LogN dist)       : "
!$$$$$$      read  *,row
     print *, "    Number of radius size bins                          : "
     read  *,nrad
  end if

  print *, "Calculate scattering matrix elements (0=n/1=y): "
  read *, ask2
  if (ask2==1) then
     print *, "Number of scattering angles in the interval"
     print *, " [0°,180°];  odd number!"
     print *, " [example: '181' -> step width = 1°]          : "
     read *, nang2
     nang = (nang2-1)/2 + 1
     doSA = .true.
  else
     nang  = 1
     nang2 = 1
     doSA = .false.
  end if

  print *, "Project name (8 characters)                    : "
  read *,fresult

  !print *, "Save results in separate files (0=n/1=y)      : "
  !read *, ask3
  !if (ask3==0) then
  !   svsep = .false.
  !else
  !   svsep = .true.
  !end if

  svsep = .false.

!-------------------------------------------------------------------------------
--------------------
  ! 2. Read data files & Prepare the calculations

!-------------------------------------------------------------------------------
--------------------
  print *
  print *,"<i> Calculation started ..."

  ! read lambda/n/k database
  do icomp=1, ncomp
     open(unit=1, file="./ri-data/"//fname(icomp), action="read",
status="unknown", form="formatted")
     do ilam=1,nlam
        read(unit=1,fmt=*) lambda(ilam), n(icomp,ilam), k(icomp,ilam)
     end do
     close(unit=1)
  end do

open(unit=1, file="./ri-data/"//datfile, action="read", status="unknown",
form="formatted")
!$$$$$$ do nfil=1,nfile
!$$$$$$      do ilam=1,nlam
        read(unit=1,fmt=*) cexp
!$$$$$$      end do
!$$$$$$ end do
     close(unit=1)
     !print *,lambda
     !print *,cexp(2,1)

open(unit=1, file="./ri-data/"//fitparam, action="read", status="unknown",
form="formatted")

        do nfil=1,nfile
```

```
      read(unit=1,fmt=*) minrad(nfil),maxrad(nfil),mufil(nfil), rowfil(nfil)
    end do
    close(unit=1)
    !print *, minrad
    !print *, maxrad
    !print *, mufil
    !print *, rowfil

   allocate( S1x(1:nang2), S2x(1:nang2), &
       S11(1:nang2,1:nlam), S12(1:nang2,1:nlam), S33(1:nang2,1:nlam),
S34(1:nang2,1:nlam), &
       S11x(1:nang2),       S12x(1:nang2),       S33x(1:nang2),
S34x(1:nang2) )

  S11(:,:) = 0.0_r2
  S12(:,:) = 0.0_r2
  S33(:,:) = 0.0_r2
  S34(:,:) = 0.0_r2


!------------------------------------------------------------------------------
-------------------
  ! 3. Run the Mie scattering routines

!------------------------------------------------------------------------------
-------------------
  do ilam=1, nlam



!start do loops for n ank k
do nfil=1,nfile

  radmin=minrad(nfil)
  radmax=maxrad(nfil)
  mu=mufil(nfil)
  row=rowfil(nfil)


  ! define radial step width
  radminlog = log10(radmin)
  radmaxlog = log10(radmax)
  if  (nrad>1) then
     steplog = (radmaxlog - radminlog) / real(nrad-1,kind=r2)
  else
     steplog = 0.0_r2
  endif

  pi = 4.0_r2 * atan(1.0_r2) ! PI = 3.14...


do en=1,nit
do kay =1,nit

  qext(:)   = 0.0_r2
  qsca(:)   = 0.0_r2
  qabs(:)   = 0.0_r2
  qbk(:)    = 0.0_r2
  qpr(:)    = 0.0_r2

  cext(:)   = 0.0_r2
  csca(:)   = 0.0_r2
  cabs(:)   = 0.0_r2
  cbk(:)    = 0.0_r2
  albedo(:) = 0.0_r2
  gscatt(:) = 0.0_r2
```

```
            weisum = 0.0_r2
         wrad   = 0.0_r2
         wqsc   = 0.0_r2

      do icomp=1, ncomp
         do irad=1, nrad
            ! initialize some arrays
            S1x(:)  = (0.0_r2,0.0_r2)
            S2x(:)  = (0.0_r2,0.0_r2)
            S11x(:) = 0.0_r2
            S12x(:) = 0.0_r2
            S33x(:) = 0.0_r2
            S34x(:) = 0.0_r2

            ! current radius / radius interval
            rad  = 10.0**(radminlog + (irad-1)*steplog)
            rad1 = 10.0**(radminlog +  irad   *steplog)
            if  (nrad>1) then
               delrad = rad1 - rad
            else
               delrad = 1.0_r2
            endif

            ! size parameter
            x = 2.0_r2*pi * rad * refmed / lambda(ilam)

            ! complex refractive index
            !print*,lambda(ilam)
            !print*,n(icomp,ilam)
            !print*,k (icomp,ilam)

            !nfact= (n(icomp,ilam)/5)+ (1.2*en*(n(icomp,ilam)/nit))
            !kfact= (k(icomp,ilam)/10)+ (3*kay*(k(icomp,ilam)/nit))
            nfact=0.3+((en-1)*((2.5-0.3)/nit))
            kfact=0.001+((kay-1)*((1-0.001)/nit))
            !print *, en, kay, n(icomp,ilam),nfact, k(icomp,ilam),kfact

            ri = cmplx( nfact, kfact )  /  refmed

            !print*,nfact
            !print*,kfact

            ! derive the scattering parameters
            call shexqnn2( ri, x, qextx, qscax, qabsx, qbkx, qprx, albedox,
gscattx, ier, S1x, S2x, &
                  doSA, nang )

            if (ier==1 .or. ier==2) then
               print *,"Program stopped."
               stop
            end if

            ! update average values
            weight = abun(icomp) * delrad * (1/(rad*row*2.5068)) *
exp(-((LOG(rad)-mu)**2)/(2*(row**2)))
            weisum = weisum + weight

            wradx  = pi*(rad/1.0e+6_r2)**2         * weight
            wqscx  = pi*(rad/1.0e+6_r2)**2 * qscax * weight

            wrad   = wrad + wradx
            wqsc   = wqsc + wqscx

            cext(  ilam)  =  cext(  ilam)  +  qextx * wradx
            csca(  ilam)  =  csca(  ilam)  +  qscax * wradx
            cbk(   ilam)  =  cbk(   ilam)  +  qbkx  * wradx
            cabs(  ilam)  =  cabs(  ilam)  +  qabsx * wradx
```

```
            qext(  ilam)  =  qext(  ilam)  +  qextx * wradx
            qsca(  ilam)  =  qsca(  ilam)  +  qscax * wradx
            qbk(   ilam)  =  qbk(   ilam)  +  qbkx  * wradx
            qabs(  ilam)  =  qabs(  ilam)  +  qabsx * wradx

            gscatt(ilam)  =  gscatt(ilam)  +  gscattx * wqscx

            S11x(:) =           0.5_r2 * abs(S2x(:)) * abs(S2x(:))
            S11x(:) = S11x(:) + 0.5_r2 * abs(S1x(:)) * abs(S1x(:))
            S12x(:) =           0.5_r2 * abs(S2x(:)) * abs(S2x(:))
            S12x(:) = S12x(:) - 0.5_r2 * abs(S1x(:)) * abs(S1x(:))
            S33x(:) = real(  S2x(:) * conjg(S1x(:)), kind=r2 )
            S34x(:) = aimag( S2x(:) * conjg(S1x(:)) )

            S11(:,ilam) = S11(:,ilam) + S11x(:)*weight
            S12(:,ilam) = S12(:,ilam) + S12x(:)*weight
            S33(:,ilam) = S33(:,ilam) + S33x(:)*weight
            S34(:,ilam) = S34(:,ilam) + S34x(:)*weight
          end do !end irad

        factcomp = icomp
        end do              !end icomp
        !print *, factcomp



        cext(  ilam) = cext(  ilam) / weisum
        csca(  ilam) = csca(  ilam) / weisum
        cbk(   ilam) = cbk(   ilam) / weisum
        cabs(  ilam) = cabs(  ilam) / weisum

        qext(  ilam) = qext(  ilam) / wrad
        qsca(  ilam) = qsca(  ilam) / wrad
        qbk(   ilam) = qbk(   ilam) / wrad
        qabs(  ilam) = qabs(  ilam) / wrad

        S11( :,ilam) = S11( :,ilam) / weisum
        S12( :,ilam) = S12( :,ilam) / weisum
        S33( :,ilam) = S33( :,ilam) / weisum
        S34( :,ilam) = S34( :,ilam) / weisum

        albedo(ilam) = csca(ilam)/cext(ilam)
        gscatt(ilam) = gscatt(ilam) / wqsc

!writing Cext to an array
Cextal(nfil,en,kay)= cext(ilam)
      !end n ank k do loops
      end do              !end kay
      end do              !end en
      print *, "Finished file loop (nfile (8) in total)"
      end do              !end nfile

!least squares fit to go here

!read in exp data

    do intm=1,nfile
    do intn=1,nit
    do into=1,nit

difference(intm,intn,into)=
abs((Cextal(intm,intn,into)-Cexp(intm,ilam))/(Cexp(intm,ilam)+Cextal(intm,intn,i
nto)))

    end do
    end do
    end do
```

```
leastsq=Sum(difference, dim=1)

write (str, '(I2)') ilam

open(unit=1, file="./results/leastsq"//str// "_"//fresult//".txt",
action="write", status="unknown", form="formatted")

  write(unit=1,fmt=*) "# leastsq for wavlength  : ", lambda(ilam)
  write(unit=1,fmt=*)
  write(unit=1,fmt=*) "# for each n and k itteration the differenc between exp
and model"
  write(unit=1,fmt=*) leastsq
  close(unit=1)

minsq= minloc(leastsq)
!print *,difference
!print *,leastsq


    !bestn(ilam)=(n(factcomp,ilam)/5)+(1.2*minsq(1)*(n(factcomp,ilam)/nit))
    !bestk(ilam)=(k(factcomp,ilam)/10)+(3*minsq(2)*(k(factcomp,ilam)/nit))
        bestn=0.3+((minsq(1)-1)*((2.5-0.3)/nit))
    bestk=0.001+((minsq(2)-1)*((1-0.001)/nit))
!print *,minsq, bestn(ilam), bestk(ilam)

    do intm=1,nfile
    bestce(intm,ilam)=Cextal(intm,minsq(1),minsq(2))
    end do
     !print *, n(1,1), n(2,1),n(1,2)
         !print *,  n(factcomp,ilam),minsq(1),
bestn(ilam),k(factcomp,ilam),minsq(2), bestk(ilam)
     !print *, "Finished lambda loop (nlam in total)"

  end do                !end ilam
       !print *, bestce
    !print *, size(n), size(k), ncomp


!-------------------------------------------------------------------------------
--------------------
  ! 4. Save the results

!-------------------------------------------------------------------------------
--------------------
  open(unit=1, file="./results/"//fresult//".txt", action="write",
status="unknown", form="formatted")

  write(unit=1,fmt=*) "# *** PROJECT_PARAMETERS ***"
  write(unit=1,fmt=*)
  write(unit=1,fmt=*) "# Number_of_wavelengths           : ", nlam
  write(unit=1,fmt=*) "# Number_of_chemical_components   : ", ncomp
  write(unit=1,fmt=*) "# Relative_abundances_[%]         : "
  do icomp=1,ncomp
     write(unit=1,fmt=*) "# ", icomp, ". component: ",
real(abun(icomp)*100.0_r2,kind=r1)
  end do
  write(unit=1,fmt=*) "# Name(s) of the dust data file(s) :"
  do icomp=1,ncomp
     write(unit=1,fmt=*) "# ", icomp, ". component: ", fname(icomp)
  end do
  write(unit=1,fmt=*) "# Minimum grain radius [micron]    : ",
real(radmin,kind=r1)
  write(unit=1,fmt=*) "# Maximum grain radius [micron]    : ",
real(radmax,kind=r1)
  write(unit=1,fmt=*) "# mean radius                      : ", real( mu,kind=r1)
  write(unit=1,fmt=*) "# standard deviation               : ", real(
row,kind=r1)
```

```
  write(unit=1,fmt=*) "# Number of size bins              : ", nrad
  if (doSA) then
     write(unit=1,fmt=*) "# Number of scattering angles      : ", nang2
  end if
  write(unit=1,fmt=*)
  write(unit=1,fmt=*)

!-------------------------------------------------------------------------------
-------------------
write(unit=1,fmt=*) "# *** RESULTS ***"
  write(unit=1,fmt=*)
  write(unit=1,fmt=*) "# Wavelength_[micron] Best_n_value best_k_value"
  do ilam=1,nlam
      write(unit=1,fmt=*) lambda(ilam), bestn(ilam), bestk(ilam)
  end do
close(unit=1)

open(unit=1, file="./results/calcext_"//fresult//".txt", action="write",
status="unknown", form="formatted")
write(unit=1,fmt=*) "# *** Calc Cext ***"
  write(unit=1,fmt=*)
  write(unit=1,fmt=*) "# Wavelength_[micron] Cext"
  do intm=1,nfile
    write(unit=1,fmt=*) "file number",intm
    do  ilam=1,nlam
      write(unit=1,fmt=*) lambda(ilam), bestce(intm,ilam)
    end do
  end do
close(unit=1)

!$$$$$$   write(unit=1,fmt=*) "# *** RESULTS ***"
!$$$$$$   write(unit=1,fmt=*)
!$$$$$$   write(unit=1,fmt=*) "# 1. Wavelength [micron], Extinction efficiency
factor / cross section [m^2]"
!$$$$$$   do ilam=1,nlam
!$$$$$$       write(unit=1,fmt=*) lambda(ilam), qext(ilam), cext(ilam)
!$$$$$$   end do
!$$$$$$   write(unit=1,fmt=*)
!$$$$$$
!$$$$$$   write(unit=1,fmt=*) "# 2. Wavelength [micron], Scattering efficiency
factor / cross section [m^2]"
!$$$$$$   do ilam=1,nlam
!$$$$$$       write(unit=1,fmt=*) lambda(ilam), qsca(ilam), csca(ilam)
!$$$$$$   end do
!$$$$$$   write(unit=1,fmt=*)
!$$$$$$
!$$$$$$   write(unit=1,fmt=*) "# 3. Wavelength [micron], Backscattering
efficiency factor/cross section [m^2]"
!$$$$$$   do ilam=1,nlam
!$$$$$$       write(unit=1,fmt=*) lambda(ilam), qbk(ilam), cbk(ilam)
!$$$$$$   end do
!$$$$$$   write(unit=1,fmt=*)
!$$$$$$
!$$$$$$   write(unit=1,fmt=*) "# 4. Wavelength [micron], Absorption efficiency
factor / cross section [m^2]"
!$$$$$$   do ilam=1,nlam
!$$$$$$       write(unit=1,fmt=*) lambda(ilam), qabs(ilam), cabs(ilam)
!$$$$$$   end do
!$$$$$$   write(unit=1,fmt=*)
!$$$$$$
!$$$$$$   write(unit=1,fmt=*) "# 5. Wavelength [micron], Albedo"
!$$$$$$   do ilam=1,nlam
!$$$$$$       write(unit=1,fmt=*) lambda(ilam), albedo(ilam)
!$$$$$$   end do
!$$$$$$   write(unit=1,fmt=*)
!$$$$$$
!$$$$$$   write(unit=1,fmt=*) "# 6. Wavelength [micron], Scattering asymmetry
factor g"
!$$$$$$   do ilam=1,nlam
```

```
!$$$$$$       write(unit=1,fmt=*) lambda(ilam), gscatt(ilam)
!$$$$$$    end do
!$$$$$$    write(unit=1,fmt=*)
!$$$$$$
!$$$$$$    write(unit=1,fmt=*) "# 7. Radiation pressure efficiency factor Qpr"
!$$$$$$    do ilam=1,nlam
!$$$$$$       write(unit=1,fmt=*) lambda(ilam), qext(ilam) -
gscatt(ilam)*qsca(ilam)
!$$$$$$    end do
!$$$$$$    write(unit=1,fmt=*)
!$$$$$$
!$$$$$$    write(unit=1,fmt=*) "# 8. Wavelength [micron], theta [degree],
F11-F12-F33-F34 "
!$$$$$$    if (doSA) then
!$$$$$$       do ilam=1,nlam
!$$$$$$          do iang=1,nang2
!$$$$$$             ! angx: scattering angle [°]
!$$$$$$             angx = real(iang-1,kind=r2) * 180.0_r2/real(nang2-1,kind=r2)
!$$$$$$             write(unit=1,fmt=*) lambda(ilam), angx, S11(iang,ilam)
!$$$$$$             write(unit=1,fmt=*) lambda(ilam), angx, S12(iang,ilam)
!$$$$$$             write(unit=1,fmt=*) lambda(ilam), angx, S33(iang,ilam)
!$$$$$$             write(unit=1,fmt=*) lambda(ilam), angx, S34(iang,ilam)
!$$$$$$          end do
!$$$$$$       end do
!$$$$$$    else
!$$$$$$       write(unit=1,fmt=*) "# not calculated."
!$$$$$$    end if
!$$$$$$    close(unit=1)
!$$$$$$
!$$$$$$
!-------------------------------------------------------------------------------
--------------------
!$$$$$$    if (svsep) then
!$$$$$$       ! 1. Extinktion efficiency factor
!$$$$$$       open(unit=1, file="./results/"//fresult//".qext", action="write",
status="unknown", &
!$$$$$$            form="formatted")
!$$$$$$       do ilam=1,nlam
!$$$$$$          write(unit=1,fmt=*) lambda(ilam), qext(ilam)
!$$$$$$       end do
!$$$$$$       close(unit=1)
!$$$$$$
!$$$$$$       ! 2. Extinktion cross section [m^2]
!$$$$$$       open(unit=1, file="./results/"//fresult//".cext", action="write",
status="unknown", &
!$$$$$$            form="formatted")
!$$$$$$       do ilam=1,nlam
!$$$$$$          write(unit=1,fmt=*) lambda(ilam), cext(ilam)
!$$$$$$       end do
!$$$$$$       close(unit=1)
!$$$$$$
!$$$$$$       ! 3. Scattering efficiency factor
!$$$$$$       open(unit=1, file="./results/"//fresult//".qsca", action="write",
status="unknown", &
!$$$$$$            form="formatted")
!$$$$$$       do ilam=1,nlam
!$$$$$$          write(unit=1,fmt=*) lambda(ilam), qsca(ilam)
!$$$$$$       end do
!$$$$$$       close(unit=1)
!$$$$$$
!$$$$$$       ! 4. Scattering cross section [m^2]
!$$$$$$       open(unit=1, file="./results/"//fresult//".csca", action="write",
status="unknown", &
!$$$$$$            form="formatted")
!$$$$$$       do ilam=1,nlam
!$$$$$$          write(unit=1,fmt=*) lambda(ilam), csca(ilam)
!$$$$$$       end do
!$$$$$$       close(unit=1)
!$$$$$$
```

```
!$$$$$$       ! 5. Backscattering effiency factor
!$$$$$$       open(unit=1, file="./results/"//fresult//".qbk", action="write",
status="unknown", &
!$$$$$$            form="formatted")
!$$$$$$       do ilam=1,nlam
!$$$$$$          write(unit=1,fmt=*) lambda(ilam), qbk(ilam)
!$$$$$$       end do
!$$$$$$       close(unit=1)
!$$$$$$
!$$$$$$       ! 6. Backscattering cross section [m^2]
!$$$$$$       open(unit=1, file="./results/"//fresult//".cbk", action="write",
status="unknown", &
!$$$$$$            form="formatted")
!$$$$$$       do ilam=1,nlam
!$$$$$$          write(unit=1,fmt=*) lambda(ilam), cbk(ilam)
!$$$$$$       end do
!$$$$$$       close(unit=1)
!$$$$$$
!$$$$$$       ! 7. Absorption efficieny factor
!$$$$$$       open(unit=1, file="./results/"//fresult//".qabs", action="write",
status="unknown", &
!$$$$$$            form="formatted")
!$$$$$$       do ilam=1,nlam
!$$$$$$          write(unit=1,fmt=*) lambda(ilam), qabs(ilam)
!$$$$$$       end do
!$$$$$$       close(unit=1)
!$$$$$$
!$$$$$$       ! 8. Absorption cross section [m^2]
!$$$$$$       open(unit=1, file="./results/"//fresult//".cabs", action="write",
status="unknown", &
!$$$$$$            form="formatted")
!$$$$$$       do ilam=1,nlam
!$$$$$$          write(unit=1,fmt=*) lambda(ilam), cabs(ilam)
!$$$$$$       end do
!$$$$$$       close(unit=1)
!$$$$$$
!$$$$$$       ! 9. Albedo
!$$$$$$       open(unit=1, file="./results/"//fresult//".alb", action="write",
status="unknown", &
!$$$$$$            form="formatted")
!$$$$$$       do ilam=1,nlam
!$$$$$$          write(unit=1,fmt=*) lambda(ilam), albedo(ilam)
!$$$$$$       end do
!$$$$$$       close(unit=1)
!$$$$$$
!$$$$$$       ! 10. Scattering asymmetry factor g
!$$$$$$       open(unit=1, file="./results/"//fresult//".g", action="write",
status="unknown", &
!$$$$$$            form="formatted")
!$$$$$$       do ilam=1,nlam
!$$$$$$          write(unit=1,fmt=*) lambda(ilam), gscatt(ilam)
!$$$$$$       end do
!$$$$$$       close(unit=1)
!$$$$$$
!$$$$$$       ! 11. Qpr
!$$$$$$       open(unit=1, file="./results/"//fresult//".qpr", action="write",
status="unknown", &
!$$$$$$            form="formatted")
!$$$$$$       do ilam=1,nlam
!$$$$$$          write(unit=1,fmt=*) lambda(ilam), qext(ilam) -
gscatt(ilam)*qsca(ilam)
!$$$$$$       end do
!$$$$$$       close(unit=1)
!$$$$$$
!$$$$$$       ! 12. Scattering Matrix elements S11, S12, S33, and S34
!$$$$$$       if (doSA) then
!$$$$$$          ! 11.1. S11
!$$$$$$          open(unit=1, file="./results/"//fresult//".f11", action="write",
status="unknown", &
```

```
!$$$$$$              form="formatted")
!$$$$$$           do ilam=1,nlam
!$$$$$$              write(unit=1,fmt=*) lambda(ilam)
!$$$$$$              do iang=1,nang2
!$$$$$$                 ! angx: scattering angle [°]
!$$$$$$                 angx = real(iang-1,kind=r2) *
180.0_r2/real(nang2-1,kind=r2)
!$$$$$$                 write(unit=1,fmt=*) angx, S11(iang,ilam)
!$$$$$$              end do
!$$$$$$           end do
!$$$$$$           close(unit=1)
!$$$$$$
!$$$$$$           ! 11.2. S12
!$$$$$$           open(unit=1, file="./results/"//fresult//".f12", action="write",
status="unknown", &
!$$$$$$                form="formatted")
!$$$$$$           do ilam=1,nlam
!$$$$$$              write(unit=1,fmt=*) lambda(ilam)
!$$$$$$              do iang=1,nang2
!$$$$$$                 ! angx: scattering angle [°]
!$$$$$$                 angx = real(iang-1,kind=r2) *
180.0_r2/real(nang2-1,kind=r2)
!$$$$$$                 write(unit=1,fmt=*) angx, S12(iang,ilam)
!$$$$$$              end do
!$$$$$$           end do
!$$$$$$           close(unit=1)
!$$$$$$
!$$$$$$           ! 11.3. S33
!$$$$$$           open(unit=1, file="./results/"//fresult//".f33", action="write",
status="unknown", &
!$$$$$$                form="formatted")
!$$$$$$           do ilam=1,nlam
!$$$$$$              write(unit=1,fmt=*) lambda(ilam)
!$$$$$$              do iang=1,nang2
!$$$$$$                 ! angx: scattering angle [°]
!$$$$$$                 angx = real(iang-1,kind=r2) *
180.0_r2/real(nang2-1,kind=r2)
!$$$$$$                 write(unit=1,fmt=*) angx, S33(iang,ilam)
!$$$$$$              end do
!$$$$$$           end do
!$$$$$$           close(unit=1)
!$$$$$$
!$$$$$$           ! 11.4. S34
!$$$$$$           open(unit=1, file="./results/"//fresult//".f34", action="write",
status="unknown", &
!$$$$$$                form="formatted")
!$$$$$$           do ilam=1,nlam
!$$$$$$              write(unit=1,fmt=*) lambda(ilam)
!$$$$$$              do iang=1,nang2
!$$$$$$                 ! angx: scattering angle [°]
!$$$$$$                 angx = real(iang-1,kind=r2) *
180.0_r2/real(nang2-1,kind=r2)
!$$$$$$                 write(unit=1,fmt=*) angx, S34(iang,ilam)
!$$$$$$              end do
!$$$$$$           end do
!$$$$$$           close(unit=1)
!$$$$$$        end if
!$$$$$$     end if

!-------------------------------------------------------------------------------
--------------------
  ! 5. Clean-up

!-------------------------------------------------------------------------------
--------------------
  deallocate( fname, lambda, n, k, abun, qext, qsca, qabs, qbk, qpr, cext, csca,
cabs, cbk, cpr, &
       albedo, gscatt, S1x, S2x, S11, S12, S33, S34, S11x, S12x, S33x, S34x,
```

```
cexp, Bestn, Bestk, &
      difference, leastsq, Cextal)

  print *,"    ... done."
  print *

end program mie
```